UNIVERSITAT POLITÈCNICA DE CATALUNYA BARCELONATECH

Levitation and control of particles with internal degrees of freedom

Gerard Planes Conangla

ICFO

PhD Dissertation

Levitation and control of particles with internal degrees of freedom

Supervisor:
Prof. Romain Quidant

Author:
Gerard Planes Conangla

Co-supervisor:
Prof. Andreas W. Schell

April 16, 2020

Abstract

Levitodynamics is a fast growing field that studies the levitation and manipulation of micro- and nanoobjects, fuelled by both fundamental physics questions and technological applications. Due to the isolated nature of trapped particles, levitated systems are highly decoupled from the environment, and offer experimental possibilities that are absent in clamped nanomechanical oscillators. In particular, a central question in quantum physics is how the transition between the classical and quantum world materializes, and levitated objects represent a promising avenue to study this intermediate regime.

In the last years, most levitation experiments have been restricted to optically trapped silica nanoparticles in vacuum, controlling the particle's position with intensity modulated laser beams. However, the use of optical traps severely constrains the experiments that can be performed, because few particle materials can withstand the optical absorption and resulting heating in vacuum. This completely prevents the use of objects with internal degrees of freedom, which—coupled to mechanical variables—offer a clear path towards the study of quantum phenomena at the macroscale.

In this thesis, we address these issues by considering other types of trap and feedback schemes, achieving excellent control on the dynamics of optically active nanoparticles. With stochastic calculus, simulations and experiments, we study the dynamics of trapped particles in different regimes, considering also a hybrid quadrupole-optical trapping scheme. Then, using a Paul trap of our own design, we demonstrate the trapping, interrogation and feedback cooling of a nanodiamond hosting a single NV^- center in vacuum, a clear candidate to perform quantum physics experiments at the single spin level. Finally, we discuss and implement an optimal controller to cool the center of mass motion of an optically levitated nanoparticle. The feedback is realized by exerting a Coulomb force on a charged particle with a pair of electrodes, and thus requires no optics.

Resum

La levitodinàmica és un camp de la física en ràpida expansió que estudia la levitació i manipulació de micro- i nano-objectes, empesa per la possibilitat de solucionar trencaclosques de física fonamental i de desenvolupar noves aplicacions tecnològiques. Gràcies al gran aïllament de les partícules en levitació, l'evolució dels sistemes levitodinàmics està molt desacoplada del seu entorn. Per consegüent, permeten fer experiments que no serien possibles en nanooscil·ladors mecànics sobre substrat. En particular, una qüestió central en física consisteix en entendre com es produeix la transició entre els mons clàssic i quàntic; els objectes en levitació permeten estudiar aquest règim intermedi de manera innovadora.

En els últims anys, la majoria d'experiments de levitodinàmica s'han limitat a atrapar òpticament partícules de sílice en el buit, tot controlant la posició de la partícula amb feixos làser modulats. Tot i així, l'ús de trampes òptiques suposa un obstacle a l'hora d'exportar aquests experiments a règims més diversos perquè, a baixes pressions, pocs materials són capaços de suportar les altes temperatures resultants de l'absorció de llum làser. Això impedeix l'ús d'objectes amb graus de llibertat interns, que –acoplats a variables mecàniques– suposen un full de ruta clar per estudiar fenòmens quàntics a escala macroscòpica.

En aquesta tesi, adrecem aquestes qüestions tot considerant altres tipus de trampa i tècniques de feedback, i assolim un control excellent de la dinàmica de nanopartícules òpticament actives en levitació. Mitjançant càlcul estocàstic, simulacions i experiments, estudiem la dinàmica de les partícules en règims diversos, àdhuc considerant un esquema híbrid de trampa de Paul-òptica. A continuació, utilitzant una trampa de Paul, demostrem experimentalment l'atrapament, interrogació i feedback-*cooling* en el buit d'un nanodiamant que conté un únic NV^- center, un clar candidat per a la realització d'experiments de física quàntica amb un únic spin. Finalment, estudiem i implementem un control·lador òptim per a refredar el centre de massa d'una partícula òpticament levitada. El feedback es realitza exercint una força de Coulomb sobre una partícula carregada positivament mitjançant un parell d'electrodes, i per tant no requereix elements òptics.

Acknowledgements

First, and foremost, I must thank my supervisor, Prof. Romain Quidant. I will be forever indebted to you for your guidance and support. Thank you for giving me the chance to take risks, for your good spirits and for bringing me along in this exciting and ambitious project, considering I had never aligned a laser before.

Second, I want to thank Prof. Andreas W. Schell, who somehow decided to leave the veggie-friendly Japan and join the project to become my other supervisor. Thank you for your never-ending insistence on being systematic, clarity, and precision, but also for thinking out of the box and for teaching me—by example—not to trust anything (or anyone).

This list would not be complete without mentioning also Prof. Raúl Rica, my third (although unofficial) supervisor, who gently introduced me to the lab and to the wonderful world of trapped Brownian particles at the beginning of my PhD. After he left for Granada, he continued to help me way more than he was supposed to, and for that you will always have my gratitude.

My fellow levitation colleagues have each had a large influence on this work, starting with the first generation of students (Pau and Francesco), postdocs (Vincenzo, Nadine, Giacomo, Jan, Raúl and Andreas), and new generation of PhDs (Marc and Andrés). Sharing this time and working alongside you has been truly inspiring and enjoyable.

To close the ICFO chapter, I would like to acknowledge all the ICFO staff, and in particular the people of the mechanical workshop, human resources, IT department and electronic workshop. You made my life way easier.

My family is the main reason behind the decision to start a PhD, through their help and encouragement. Gràcies, papes, pel suport constant, per l'educació excel·lent i per la paciència durant tots aquests anys d'estudi que m'han permès arribar fins aquí. Gràcies, Marina i Núria, pels anys que hem passat plegats, pels anys que vindran i, en definitiva, per completar aquesta família fantàstica. Teniu un futur brillant.

My last thank-you is for Irene, for accompanying me since the beginning of this ride. You are the best result of this thesis.

Contents

1

Introduction

1.1 Accessing individual quantum systems

Quantum mechanics emerged at the beginning of the 20th century to explain phenomena that collided with the traditional assumptions of classical mechanics and electromagnetism. Although it began as a completely phenomenological set of postulates, it provided a framework to understand black-body radiation [1], the photoelectric effect [2] and the spectral lines of atomic hydrogen [3]. Thanks to the work of Heisenberg, Schrödinger, Dirac and Von Neumann (among others), by 1935 it was an established and rigorous theory, described by Hermitian operators on Hilbert spaces [4, 5, 6, 7].

Since then, experimental control of quantum systems has been pursued widely. Atomic physics helped provide a test bed for quantum mechanics, studying the spectral lines of atomic ensembles and their interaction with radiation. The advent of spectrally pure, tunable radiation sources [8] in the 1960s, such as microwave oscillators and lasers, dramatically improved the precision of these experiments.

Shortly after its inception, it was realized that quantum mechanics should also apply to individual particles. If these particles were then coupled to macroscopic systems, the predictions of the theory lead to extremely bizarre consequences, as the the thought experiment of the cat that is dead and alive at the same time perfectly exemplifies [9]. That caused great distress to many physicists, among them Schrödinger, who wrote:

> "We never experiment with just one electron or atom or (small) molecule. In thought experiments, we sometimes assume that we do; this invariably entails ridiculous consequences [...]" [10]

In spite of this, in the mid 1950s the seminal work of Wolfgang Paul, Hans Dehmelt, et al. [**?**] made possible the first realizations of single particle

traps. Although electrostatic trapping of charged particles is impossible[1], they recognized that particles could still be trapped in a saddle point of a time-varying electric potential. The invention of ion traps constituted a turning point in the history of physics. They offered a means to study and test quantum mechanics with single constituents of matter, instead of with ensembles.

The first single electron was trapped in 1973 by Wineland et al. [11] using a Penning trap [12], and single ions followed seven years later [13, 14], allowing the first studies of light-matter interaction at the single atom level. Notorious examples include Doppler cooling of ion clouds [15, 16], in 1978, and sideband cooling, first proposed in 1975 [17] and attained 14 years later by Diedrich et al. with a single $^{198}Hg^{+}$ ion [18]. These advances allowed physicists to work with single entities at the ground state, the first step to address their quantum levels. This allowed the observation of quantum jumps [19], of which Schrödinger had said 60 years before:

> "If we are going to stick to this damned quantum-jumping, then I regret that I ever had anything to do with quantum theory." [20]

Around the same time, Ashkin proposed to use light as a trapping mechanism for neutral particles. Using radiation pressure from a laser beam, he was able to trap dielectric microparticles in liquid in 1970 [21]. In 1978, he proposed a method to stably trap, cool and manipulate single atoms [22] that would inspire the first atom-trapping experiments of 1985 [23, 24, 25]. In parallel, Ashkin also obtained an optical trap created with a single, tightly focused, laser beam [26]. This scheme is now known as "optical tweezers", and became a standard technique in biophysics and biology [27, 28, 29] to manipulate and position micro-objects in liquid environments.

1.2 Quantum systems at a bigger scale

Outside of the life sciences, the trapping of large dielectric particles initially attracted little interest. This course of action would remain dormant until the turn of the century when, with microscopic systems, the limits of quantum mechanics started to be pushed towards larger masses.

One of the major motivations behind the research in small physical systems is of a fundamental nature. For instance, in quantum mechanics we seek to understand the evolution of the wave function, which gener-

[1] Due to the electrostatic potential being harmonic and satisfying the maximum principle.

ally evolves deterministically[2]. Yet, actual measurements always find the physical system in a definite state. To account for this discrepancy, the original formulation of quantum mechanics divided the world into a quantum system, evolving unitarily with the Schrödinger equation, and measuring devices, that projected this wave into a single of its possible states. This division, however, is arbitrary. In the words of John S. Bell:

> "The concepts *system*, *apparatus*, *environment*, immediately imply an artificial division of the world, and an intention to neglect, or take only schematic account of, the interaction across the split. [...] The first charge against *measurement*, in the fundamental axioms of quantum mechanics, is that it anchors there the shifty split of the world into *system* and *apparatus*. A second charge is that the word comes loaded with meaning from everyday life, meaning which is entirely inappropriate in the quantum context." [30]

Another important question that is still being explored is how the transition between the classical and quantum world materializes. Thanks to the experiments with single ions and atoms, it is now agreed upon that the microscopic world obeys the laws of quantum mechanics. At the same time, classical physics describes extremely well the evolution of systems big enough to be visible. Thus, a natural question to ask is what theory should be used in the intermediate regime. When is a system big enough to be macroscopic? Does quantum mechanics extend to such systems as well? These questions can be studied by working with devices that, although small, are made of millions of atoms.

The study of small systems also opens up the possibility to develop new technologies. Richard Feynman argued in his 1960 lecture "There's plenty of room at the bottom" [31] that there is a niche of opportunities in the miniaturization and manipulation of the micro world. At the time the lecture went largely unnoticed, but today it is cited by articles, grants and proposals[3]. The reason behind this recent interest is the emergence of nanotechnology, that has brought about the possibility to create and manipulate structures barely visible with an optical microscope, yet much bigger than single molecules. A prime example is the transistor, which in terms of impact is one of the most important inventions of the 20th century [32, 33].

The same fabrication techniques can also be used to create miniaturized optical cavities [34], mechanical oscillators [34], or superconducting

[2]According to the Schrödinger equation as a linear superposition of different states.
[3]This manuscript is no different.

circuits [35], which can be used in technological applications but also for fundamental physics research. The latter reached a turning point in 2010, when microelectromechanical systems (MEMS) reached the ground state of a macroscopic oscillator for the first time [36, 37, 38], indicating that quantum mechanics might be a good representation of macroscopic reality. This opened up possibilities to study quantum mechanics at larger scales than was possible with single ions [39, 40, 41, 42].

These ground state cooling experiments [36, 37, 38] are excellent examples of electro- and optomechanical systems, where an electromagnetic oscillator interacts with a mechanical oscillator. Electro- and optomechanical systems have been very productive in the last years, in part due to the large range of different effects that can be understood with the same simple formalism [34][4]. The role of the mechanical oscillator can be taken by devices as diverse as membrane resonators [43], cantilevers [36] or carbon nanotubes [44, 45].

As of today, the most well-known optomechanical system is the Laser Interferometer Gravitational-Wave Observatory (LIGO), a large-scale experiment made with several km long Fabry-Perot interferometers. The LIGO entered the spotlight of modern research after its conceptual fathers were awarded the Nobel prize in 2017, following the detection of a black hole merger [46]. One year later, Arthur Ashkin was also recognized with a Nobel prize for his invention of the optical tweezers [26, 27, 28, 47]. These two fields, optomechanics and optical tweezers, might seem completely disparate at first sight. However, the motion of a trapped particle in vacuum can be often modelled as a harmonic oscillator. Therefore, levitated particles offer an alternative platform to realize mechanical oscillators with very low mechanical dissipation [48], and may be used in experiments on quantum control with yet larger particles.

The seminal work of Ashkin already demonstrated the levitation of a microparticle in high vacuum in 1976 [49]. One year later [50], he also reported on feedback stabilization of its center of mass (CoM). After this pioneering works, the interest in levitating particles in vacuum remained dormant for years, but it was revived 10 years ago with the proposals to bring an optically levitated nanoparticle to the ground state [51, 52, 53].

1.3 Levitation of micro and nanoobjects

In 2010, a study of the transition between the ballistic and Brownian regimes [54] resumed the experimentation of levitated particles in vacuum.

[4] In terms of relevance, the optomechanical Hamiltonian can be compared to the Jaynes-Cummings Hamiltonian.

Since then, both theoretical and experimental work with levitated particles has grown extensively.

At high vacuum, levitated particles have single mechanical modes with $\mathcal{Q}$ factors exceeding 10^8 [55], close to state-of-the-art MEMS [56, 57]. Thus, they offer a promising avenue to study quantum mechanics in domains that are particularly challenging for systems on a substrate. They are unique in the possibility to perform free fall experiments, studies of the particle's rotation, and to engineer the trapping potentials dynamically. Furthermore, concepts such as wave-matter interference [40, 58], the generation of cat states [52] or the validity of collapse models [58, 59] are particularly suited to experiments with levitated objects. However, investigating these questions requires precise quantum control. For levitated particles, that still remains in the future.

A path to achieve such control is the use of particles with internal degrees of freedom. For instance, electron spins in the crystal lattice of a levitated particle can potentially be coupled to the CoM or to other mechanical degrees of freedom of the particle. If these spins can be accessed, their state could be coherently transferred to the mechanical variables, leading to the realization of superposition states at the macroscale.

Yet, at the beginning of this work this possibility was facing difficulties. Because optical tweezers are very convenient to deploy[5], most recent levitation experiments in vacuum made use of optically trapped nanoparticles. Still, the absence of an efficient heat dissipation mechanism restricts optical trapping in vacuum to just a few nanoparticle materials[6] [60], preventing the use of objects with internal degrees of freedom—such as solid-state emitters or spins—and also of other materials with large responses to light. The reason for this is that at low pressures black body radiation becomes the major contributor to internal energy loss; for many materials its rate is too slow and when the bulk temperature increases the particle degrades.

This is the case of optically trapped nanodiamonds, whose levitation faces issues already at ~ 50 mbar [61, 62]. Nanodiamonds are an extremely interesting material to levitate, since they host many color center defects with atom-like properties. Among these defects, the most well known is the nitrogen vacancy (NV) center, a defect with an electron spin and very convenient features[7]. Unfortunately, due to the mentioned difficulties, their levitation in vacuum has remained largely unexplored.

A different strategy to bring nanodiamonds to vacuum is the use of ion traps, which avoid heat by its use of electric fields. The approach is com-

[5] Technically easy setups and good nanoparticle position signals.

[6] The most common of them being SiO_2.

[7] Electron transitions in the visible, hyperfine transitions at an easy to work with frequency (2.87 GHz), and the possibility to initialize and read-out the spin state optically.

plementary to optical tweezers, because the collection lens—necessary for motion or fluorescence detection of the particle—can also be used to create an optical trap if necessary. Since 2010, Paul traps have been used extensively to levitate nanoparticles. A few examples of this are the experiments of A. Kuhlicke with NV centers at ambient pressure [63], P. Nagornykh with graphene microflakes [64], I. Alda with a surface trap [65], or J. Millen, with a Paul trap in a Fabry-Perot cavity [66].

CoM cooling has also been pursued extensively in levitated systems since, as previously discussed, the first step in many proposed quantum experiments is bringing the system into the ground state of the motion. Ongoing efforts can be divided in two directions: cavity cooling [67, 68, 69] and feedback cooling [55, 70]. Up to this time, parametric feedback cooling (PFC) [55] is still the standard technique for motion control of optically levitated nanoparticles [71]. Yet, because PFC is inherently nonlinear, it becomes inefficient at small oscillation amplitudes, leading to difficulties to decrease further the CoM energy [71]. Likewise, laser light, which is the common mechanism to exert forces onto the levitated particles, is a limiting factor when working with particles that degrade at high temperatures.

Control theory, and optimal control in particular, may offer new strategies to improve the cooling of levitated objects. Furthermore, the use of electric fields presents a laser-free alternative to apply forces on trapped particles, that can be easily implemented with standard electronic instruments. By taking advance of the compensation electrodes, electric feedback cooling could be implemented in Paul traps and optical tweezers experiments in a completely analogous way.

At the beginning of this work, the use of linear, optimal control feedback schemes to cool nanoparticles had remained unexplored. Similarly, no single NV^- had yet been detected in a levitated nanodiamond in vacuum. Its levitation, control and interrogation would mark an important milestone, since this step is a fundamental requirement to realize single spin control and coupling to mechanical variables.

1.4 Outline of the thesis

In this thesis, we describe our work on the manipulation of trapped particles with internal degrees of freedom in vacuum. To avoid heating issues, we consider other types of trap beyond the common optical tweezers, and implement a novel feedback scheme, achieving excellent control on the dynamics of the trapped nanoparticle.

Our results offer new possibilities to work with truly isolated macroscopic systems at the quantum level, and do so in two main directions: firstly, by demonstrating and proposing new ways to trap and interact with internal energy levels, even in the case of particles hosting a single emitter; secondly, by realizing a novel, easy to implement and very efficient feedback technique that, by relying on electric fields, can be implemented with minimal optical requirements.

The thesis is divided in five main chapters, followed by a short Outlook and a set of Annexes. The latter contains many details that are either common in "Levitodynamics" or physics in general (in which case there is no need to force the reader to go through them) or out of the scope of the chapters. In any case, when it is required, references to specific parts of the Annexes are included in the main text.

An overview of the chapters is detailed hereunder:

1. **Chapter 1**: Introduction.

2. **Chapter 2**: Fundamentals of particle trapping and details for two types of particle traps: the Paul trap and the optical tweezers. For both of them, the equations of motion are derived and solved, taking into account Brownian effects due to the interaction of the particle with gas molecules. Details of the experimental realization of the traps are also included.

3. **Chapter 3**: Study of the dynamics of the CoM of a Brownian particle levitated in a Paul trap, mostly focusing on the overdamped regime. It includes a comparison of the theory with numerical simulations and experimental data from the Paul trap.

4. **Chapter 4**: Realization of a hybrid quadrupole-optical trap. The dynamics of the trapped particles are studied both theoretically and experimentally, and include the trapping of gold nanoparticles.

5. **Chapter 5**: Demonstration of the trapping, interrogation and feedback cooling of a nanodiamond hosting a single NV^- center in vacuum, a clear candidate to perform quantum physics experiments at the single spin level.

6. **Chapter 6**: implementation and results of a linear-quadratic regulator to cool the CoM motion of an optically levitated nanoparticle. The feedback, realized with an FPGA, exerts a Coulomb force on a charged particle with a pair of electrodes. The cooling technique achieves lower CoM temperatures and shorter transients than previous optical schemes.

7. **Chapter 7**: Outlook.

8. **Annexes**:

    a) A review of stochastic calculus, the formalism required to perform calculations with dynamic stochastic processes.

    b) A review of the harmonic oscillator model. Notes on force sensing and accelerometers are also included.

    c) Short review of optics, to be used as reference for the concepts mentioned in the main text.

    d) Common techniques for trapped particles, including signal calibration and calculations of the temperature/energy.

    e) Details of the calculations with the WKB method in chapter 3.

    f) Fundamentals of control theory. To be used as a reference for chapter 6.

2

Nanoparticle levitation

In this chapter, the fundamentals of particle trapping are introduced for two types of particle traps: the Paul trap and the optical tweezers. For both of them, the equations of motion are derived and solved, taking into account Brownian effects due to the interaction of the particle with gas molecules. We also include details of the experimental realization of the traps.

2.1 Introduction

A *particle trap* is a combination of force fields that capture and confine particles of diverse nature. If left to freely evolve, the dynamics of a small particle will constantly be perturbed by external forces, such as gravity, collisions with molecules, or electrostatic fields, and those forces need to be counteracted by the trap. There are several ways to accomplish this, arising from different physical principles and resulting in a large variability of features among different designs. For instance, some traps can control and change the position of the particles. Others can be adapted to work at different environments: particles can be trapped in liquid, in a gas or even made to "levitate" in vacuum, often in an environment that remains highly isolated from external influences.

Particle traps have a large number of scientific applications [12, 29, 72, 73, 74], among them mass spectrometry, basic physics research or—in the case of atoms and ions—the control of quantum states. Different types of trap exist [26, 75, 76], but in this work only two have been used and studied

in detail: the *Paul trap*, a member of the family of quadrupole ion traps—used to trap charged particles—, and the *optical tweezers*, a particular type of dipole trap—used for neutral or dielectric particles.

In a particle trap, the effect of the trapping fields results in "stable" trapping[1]. This can be restated in a more precise way if one uses mathematical terms: in a particle trap, the trap center is a critical point of the dynamical system defined by the center of mass (CoM) equations of motion[2], and this critical point is stable[3].

The crux of the matter is then the following: how does one engineer a field that leads to stable trapping? Restraining ourselves to the domain of classical physics, ideally a trap should satisfy the following conditions:

1. As stated before, the point particle should be kept in a critical stable point. Therefore, in the case of a perturbation, the trap would push the particle back to the center.

2. The force should be created by a conservative field, resulting in a well-defined energy.

3. If possible, the potential of the field should be quadratic in every axis. In this case, the equation of motion becomes linear.

The last condition is not strictly necessary, but it vastly simplifies the study of the system. A quadratic trap potential takes the expression

$$\Phi_0(x, y, z) = \frac{k_x x^2}{2} + \frac{k_y y^2}{2} + \frac{k_z z^2}{2}, \tag{2.1}$$

where $k_i > 0$. $\Phi_0(x, y, z)$ will then have a stable critical point at $(x, y, z) = (0, 0, 0)$, where we would like to load our particle. From Newton's second law, this would result in the equation of motion of a harmonic oscillator (see Annex B). As we shall see in the following sections, however, these conditions are not always satisfied.

[1] Otherwise it cannot be called a trap.

[2] A 3-dimensional system with x, y and z as parameters.

[3] In other words, the eigenvalues of the differential of the linearised system around the critical point are all negative.

2.2 Quadrupole ion traps

A quadrupole trap is a device that uses electric fields to trap charged particles. Whether the particle is an electron, an ion or a nanoparticle with a net charge, the functioning principle is the same: the charged particle feels a force from an electromagnetic field following Lorentz's law. Hence, the particle's CoM equations of motion can be obtained by solving Newton's second law.

However, creating a charged particle trap is not straightforward. In electrostatics in vacuum, the electric potential satisfies Laplace's equation

$$\Delta\Phi = 0 \tag{2.2}$$

inside its domain. Functions that satisfy Laplace's equation are known as *harmonic functions*, and they obey the following

Theorem 1 (Maximum principle)**.** *Let f be a function such that $\Delta f = 0$ on some domain Ω (such f is known as a harmonic function). Then, either f is constant or it does not attain a maximum (minimum) within Ω. Any local maximum (minimum) will be found on the boundary $\partial\Omega$, and any critical point inside Ω will be a saddle point.*

In other words, *any* potential containing a maximum or a minimum (and therefore, a locally stable critical point) will not be a harmonic function. For instance, the previously introduced potential, $\Phi_0(x, y, z)$, can't be harmonic since

$$\Delta\Phi_0(x, y, z) = k_x + k_y + k_z > 0. \tag{2.3}$$

The maximum principle goes beyond quadratic potentials, however. And unfortunately, since electrostatic potentials are always harmonic functions, a local minimum is impossible to achieve, whether the potential is locally quadratic, quartic or of higher degree.

At this point, creating a trap for charged particles would appear to be a lost cause. There is a workaround, nevertheless, if one relaxes the assumptions a little. What is needed to "trap" a particle is not necessarily a minimum, but rather a stable (i.e., bounded) orbit of the equations of motion. Wolfgang Paul was the first to design a device that was able to keep charged particles in "dynamic confinement", and for his insight (and experimental realizations) he was awarded the Nobel prize in 1989[4].

The *Paul* trap uses electrodes in a quadrupole disposition to create an electric potential with a local saddle point. A particle in this saddle (or

[4]That's also why a family of ion traps are known as Paul traps.

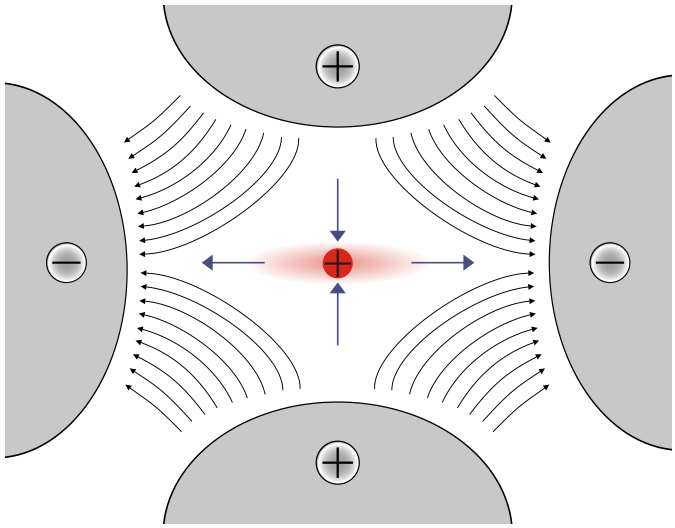

Figure 2.1: **Quadrupole ion trap scheme**: sketch of a quadrupole ion trap with a particle of positive charge (dark red). The electric field E (black arrows) is generated by a quadrupole of endcaps. The polarity of the endcaps will oscillate between positive and negative for every AC cycle.

hyperbolic) critical point will be unstably trapped, since any perturbation will eject the particle along the unstable manifold. However, the equation of motion has some stable solutions when the static boundary conditions for the electric potential are replaced by oscillating boundary conditions, $V(t) = A \cdot \cos(\omega t)$. Intuitively, the integral curves around this critical point will oscillate and alternate between being attractive and being repulsive.

2.2.1 Quadrupole ion trap equations

The ideal Paul trap with rotational symmetry creates a potential of the form

$$\Phi(x, y, z) = \frac{U_0 + V_0 \cos \omega t}{2d^2}(2z^2 - x^2 - y^2), \qquad d = \sqrt{\frac{r_0^2}{2} + z_0^2}, \tag{2.4}$$

where z_0 and r_0 are the distances from the center to the inner (upper and lower) and ring end caps respectively[5] (see Fig. 2.2). For a particle of charge

[5]Notice that, in general, we may consider DC and AC terms.

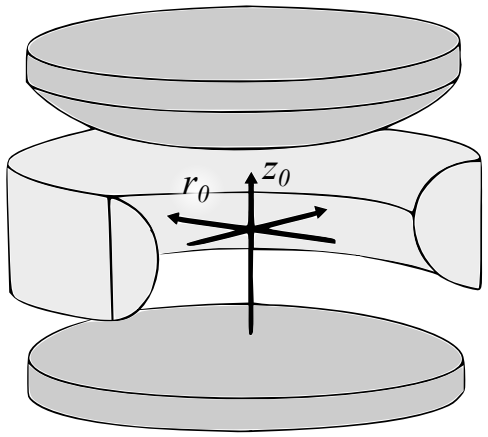

Figure 2.2: **Ring Paul trap**: sketch of a Paul trap with rotational symmetry. The parameters r_0 and z_0 are the distance from the center to the ring and upper/lower caps, respectively.

Q and mass m this potential gives rise to the equations of motion[6]

$$\ddot{x} - \frac{Q}{md^2}(U_0 + V_0 \cos \omega t)x = 0, \tag{2.5}$$

$$\ddot{y} - \frac{Q}{md^2}(U_0 + V_0 \cos \omega t)y = 0, \tag{2.6}$$

$$\ddot{z} + \frac{2Q}{md^2}(U_0 + V_0 \cos \omega t)z = 0. \tag{2.7}$$

By an appropriate change of variables, with

$$a_x = a_y = \frac{-4QU_0}{md^2\omega^2}, \quad a_z = \frac{8QU_0}{md^2\omega^2}, \tag{2.8}$$

$$q_x = q_y = \frac{2QV_0}{md^2\omega^2}, \quad q_z = \frac{-4QV_0}{md^2\omega^2}, \quad \tau = \frac{\omega}{2}t, \tag{2.9}$$

these equations can be transformed to the classical *Mathieu equations*

$$\ddot{u}_i + (a_i - 2q_i \cos 2\tau)u_i = 0. \tag{2.10}$$

These (one for every axis) form a linear set of ordinary differential equations (ODEs), non autonomous but involving only periodic functions on t. Thus, according to Floquet's theorem, there exists a basis of the space of solutions consisting on functions of the form

$$w_1(\tau) = e^{\mu\tau}\phi(\tau) \quad w_2(\tau) = e^{-\mu\tau}\phi(-\tau), \tag{2.11}$$

[6]This is just a trivial application of Newton's second law and Lorentz force.

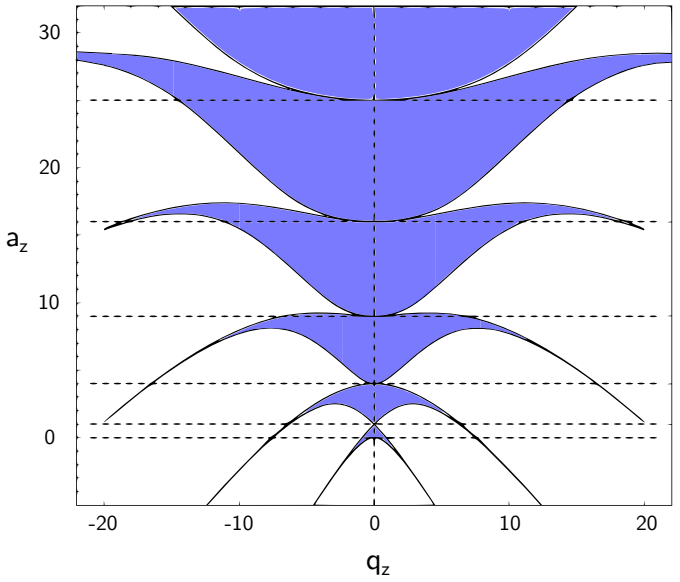

Figure 2.3: **Mathieu stability diagram**: stability diagram for Mathieu's equation for axial direction z (shaded regions are stable, white unstable).

where ϕ is a π-periodic function and the Lyapunov characteristic exponent is $\mu = \alpha + i\beta$, with $\alpha(a,q)$, $\beta(a,q) \in \mathbb{R}$. Therefore, $w(z)$ has the pseudo-periodic property[7]

$$w(z+\pi) = e^{\mu\pi} w(z). \tag{2.12}$$

The stability of the solutions depends on the values α and β. Clearly, if $\alpha \neq 0$, either $w_1(\tau)$ or $w_2(\tau)$ will increase exponentially, and the general solution (a linear combination of both) will be unstable. As per β, integer values lead to degeneracy of eigenvalues, and thus to an independent solution that grows linearly with τ, hence unstable. For this reason, $\beta(a,q) = n \in \mathbb{N}$ defines the boundaries between stable and unstable regions. The common operating regime of Paul traps can be seen in figure 2.4; in the case of (linear) damping, a similar change of variables allows us to recover the original Mathieu equations, with an identical region of stability, though enlarged and slightly shifted.

The stable solutions of the Mathieu equation can be expressed in the form of a Fourier series. A specially interesting case is the so called adiabatic approximation. In this regime, the particle motion averaged over the high

[7]For a more complete and in-depth treatment of this, we refer to the "Charged particle traps" book. For a detailed description of the Mathieu functions, see the NIST webpage `http://dlmf.nist.gov/`.

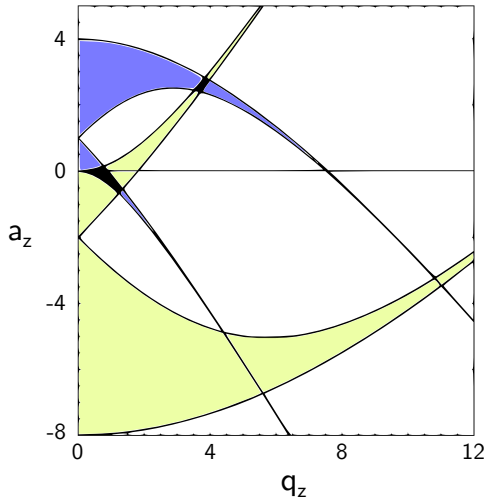

Figure 2.4: **Paul trap stability diagram**: z axis (blue) and r axis (light yellow). The stability region of the equation of motion is the intersection (marked in black) of the stability diagrams in the r and z directions (see Fig. 2.3), because the particle needs to be stable in *every* direction. The limit of the first stability region for $a = 0$ is found at $q \simeq 0.9080463$.

frequency oscillation is governed by an effective potential energy

$$U_{\text{eff}} = \frac{Q^2 E_\omega^2(r)}{4m\omega^2}. \tag{2.13}$$

For this approximation to be valid in the Paul trap, it is required that $a, q \ll 1$. Then, β, which can be exactly calculated as a continued fraction in terms of a and q can be approximated[8] as

$$\beta \approx \sqrt{a + \frac{q^2}{2}}. \tag{2.14}$$

As a rule of thumb, this is valid as long as $q_{x,y} < 0.2$, $q_z < 0.4$. For values bigger than this, or for more accuracy, the fourth order approximation

$$\beta \simeq \sqrt{a - \frac{(a-1)q^2}{2(a-1)^2 - q^2} - \frac{(5a+7)q^4}{32(a-1)^3(a-4)}} \tag{2.15}$$

or more sophisticated methods [77] can be used. If a and q are small, then the coefficients of the Fourier expansion become rapidly smaller with increasing n, and the particle motion simplifies to

$$u_i(t) = G\left(1 - \frac{q_i}{2}\cos\omega t\right)\cos\Omega_i t, \tag{2.16}$$

[8]This is known as the Dehmelt's approximation.

with $\Omega = \frac{\beta\omega}{2}$ known as the *secular* or *macromotion* frequency; therefore, because we are working in a stability region confined by $\beta_z = 1$, the secular motion will always satisfy $\Omega \leq \frac{\omega}{2}$. Since it is assumed that $\beta \ll 1$, the secular motion is slow compared with the superimposed *micromotion* (or driving frequency) ω. For the special case of $a = 0$ (i.e., no DC field applied in the Paul trap electrodes)

$$\Omega_{x,y} \simeq \frac{q\omega}{2\sqrt{2}} = \frac{2QV_0}{md^2\omega^2} \cdot \frac{\omega}{2\sqrt{2}} = \frac{QV_0}{\sqrt{2}md^2\omega}, \qquad \Omega_z \simeq \frac{\sqrt{2}QV_0}{md^2\omega} = 2 \cdot \Omega_{x,y}, \tag{2.17}$$

where Dehmelt's approximation [12] has been used. Thus, from eqs. (2.17) it is seen that increasing the driving frequency leads to a decrease of the secular motion. To increase[9] Ω, the options would be either to increase the voltage $\uparrow V_0$, get a higher charge to mass ratio $\uparrow Q/m$, decrease the trap frequency $\downarrow \omega$ or make the trap smaller. In any case, for the trap to be stable we will need to always to keep track of the q_z parameter, making sure that $q_z < 0.908$.

As a final note, it should be stressed that the regime of secular oscillations is only possible in vacuum. We experimentally observe that, at ambient pressure, damping due to air drag doesn't allow the particle to oscillate in this effective potential, although the trap stability region is enlarged [78]. A rigorous treatment of this case can be found at section "Stochastic dynamics in a Paul trap".

2.2.2 Design and simulation of the Paul trap

The first step in the design of a Paul trap is engineering a saddle electric potential (a hyperbolic paraboloid). Paul's original solution achieved this by using hyperboloid shaped electrodes: an external one-sheet hyperboloid and an internal two-sheet hyperboloid (one of which is grounded, usually the external one, and the other connected to an AC source). This leads to an *exactly* quadratic potential with a saddle point in the middle[10], and therefore to linear equations of motion. However, it was soon realized that this geometry could be considerably modified with negligible changes in the particle dynamics, since the equations can be linearised close to the critical point by taking only the first few terms of the power series expansion of the potential. This led to some of today's most used ion trap geometries:

[9] There are several reasons why this might be desirable: to avoid low frequency noise, to get higher $Q = \frac{f}{\Gamma}$, to better resolve motional frequencies or to have deeper effective potentials.

[10] As can be seen by solving the partial differential equation with the electrodes as boundary conditions; see Ref. [12].

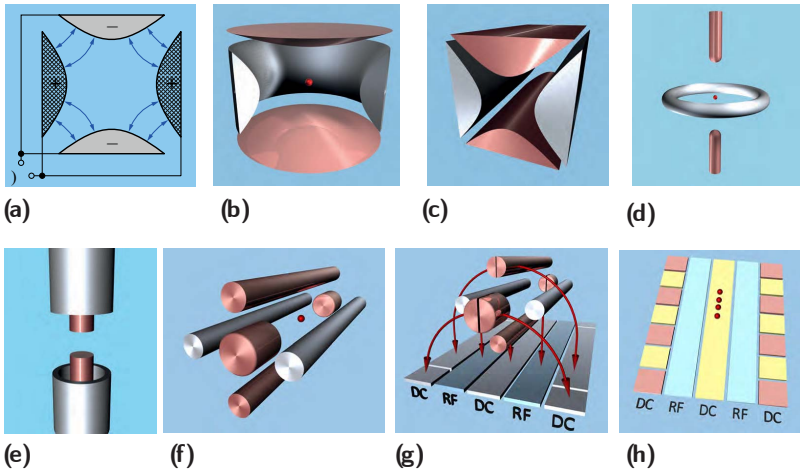

Figure 2.5: **Trap geometries**: (a) Perfectly hyperbolic electrodes. (b) Classic Paul trap. (c) Hyperbolic linear trap; confinement in the axial dimension is provided by the addition of electrodes held at a positive DC voltage. (d-e) Different geometries of (topologically) ring traps and (f-g-h) topologically linear traps. Reproduced from Brownnutt et. al [79] with permission from the authors, Copyright© 2011 by American Physical Society. All rights reserved.

- The *end-cap trap*, made with concentric cylinders with revolution symmetry. Because it has a single point with zero field (the center of symmetry), it is used to trap single ions or particles.

- The *linear trap*, with its axial symmetry, designed for the trapping of several particles at once, and usually with some kind of lateral caps for axial confinement.

- Surface or planar designs, suited for on-chip or integrated traps.

Pictures of these designs can be found in Figure 2.5.

In this thesis we have mainly worked with an end-cap Paul trap (portrayed in Fig. 2.6), which we have designed, simulated, built and incorporated into the experimental setup. We have chosen this design because it offers a high level of confinement when compared to linear traps (which have a weak axial potential) while allowing for excellent optical access to the trapped particle, due to a largely free solid angle on the radial direction.

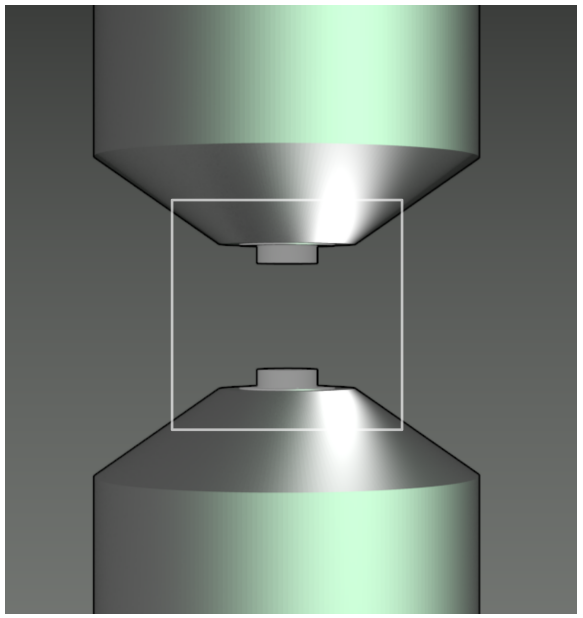

Figure 2.6: **Paul trap design**: (a) Artistic representation of our end-cap Paul trap design. The inner rods can be observed at the center of the revolution axis. The white rectangle at the middle of the picture signals the region that is simulated in Fig. 2.7.

To simulate the Paul trap field[11] several steps have been carried out:

1. We chose the trap geometry, given the experiment constraints. As stated, we are interested in working with single trapped particles with internal degrees of freedom. For these needs the end-cap trap was the best option.

2. We defined Laplace's equation with the chosen geometry as the boundary conditions. One should always try to exploit the symmetries of the problem, since every continuous symmetry transforms a n dimensional problem to a $n-1$ dimensional problem, which will be less computationally intensive. For 3D or revolution symmetry problems, such as the end-cap Paul trap, the finite element method (FEM) is probably the best option, taking special care to use a finer mesh close to the trapping region[12].

[11] The procedure is general enough to be applied in any quadrupole ion trap design.

[12] For planar traps, the NIST group has a very efficient Python code at GitHub. See `https://github.com/nist-ionstorage/electrode`.

3. For each electrode, we simulated the electric potential inside the domain by setting the voltage in that electrode (i.e., the boundary conditions of V) to 1 and the rest to zero. By the linearity of the equation, a linear combination of these solutions will satisfy any set of boundary conditions as long as the voltage is constant at every electrode, and will therefore be a solution of the complete signal. If

$$\begin{cases} \Delta V_i(x) = 0 \quad x \in \Omega \\ V_i = 1 \quad x \in \partial\Omega_i, \quad V_i = 0 \quad \partial\Omega_{k\neq i} \end{cases} \tag{2.18}$$

and

$$\begin{cases} \Delta V_j(x) = 0 \quad x \in \Omega \\ V_j = 1 \quad x \in \partial\Omega_j, \quad V_j = 0 \quad \partial\Omega_{k\neq j} \end{cases} \tag{2.19}$$

then, $U(x) = a \cdot V_i(x) + b \cdot V_j(x)$ will satisfy

$$\begin{cases} \Delta U(x) = 0 \quad x \in \Omega \\ U(x) = a \quad x \in \partial\Omega_i, \quad U(x) = b \quad x \in \partial\Omega_j, \quad U(x) = 0 \quad \partial\Omega_{k\neq i,j} \end{cases} \tag{2.20}$$

4. We tested a wide range of problem parameters. As it has been seen, $U_{\text{eff}}(r) \propto E_\omega^2(r)$, so a good figure of merit is obtaining $U_{\text{eff}}(r)$ as close to a paraboloid as possible.

5. In general, once the design is final, the electric potential at any time can be obtained (due to the aforementioned linearity) by multiplying with the appropriate cosine factor.

We have performed FEM simulations of the end-cap trap in COMSOL and compared the solution to the linear case in MATLAB. The final design is made of two inner steel rods (1 mm in diameter), connected to the high voltage driving, and two outer steel cylinders that are grounded; the inner and outer parts are separated by a ceramic MACOR[13] tube. The two assembled steel electrodes are separated by 1.4 mm and mounted on a MACOR holder, which in turn is screwed over a three axis piezoelectric stage[14]. Fig. 2.7 shows a simulation of the trap design at the region marked with a rectangle in Fig. 2.6, and Fig. 2.8 a picture of the trap inside the vacuum chamber.

[13] Trademark for a machinable glass-ceramic, developed and sold by Corning Inc.

[14] I acknowledge the help of ICFO's mechanical workshop, and especially of Xavi, in building the trap.

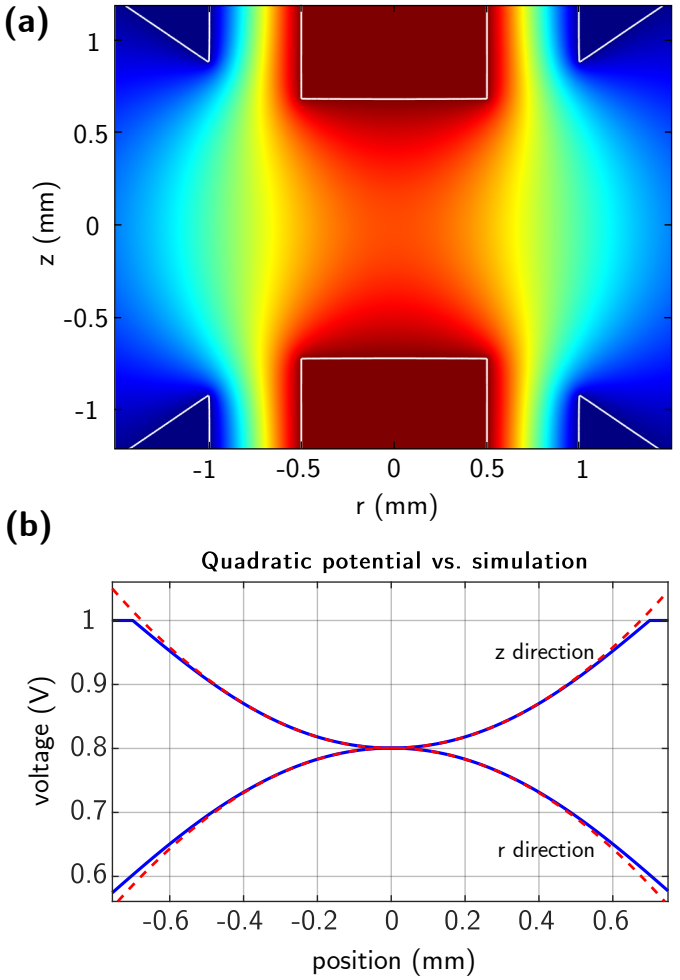

Figure 2.7: **Paul trap simulation**: (a) FEM simulation of the electric potential at the trapping region (see Fig. 2.6 for reference). The inner rod boundary condition is set to 1 V and the outer cylinder is set to 0 V. The FEM simulation has been performed in COMSOL and imported to MATLAB for analysis. (b) Comparison of the electric potential along the two main directions r and z with a purely quadratic potential. At the center of the trap, where the particle is confined, there is barely any difference between the two.

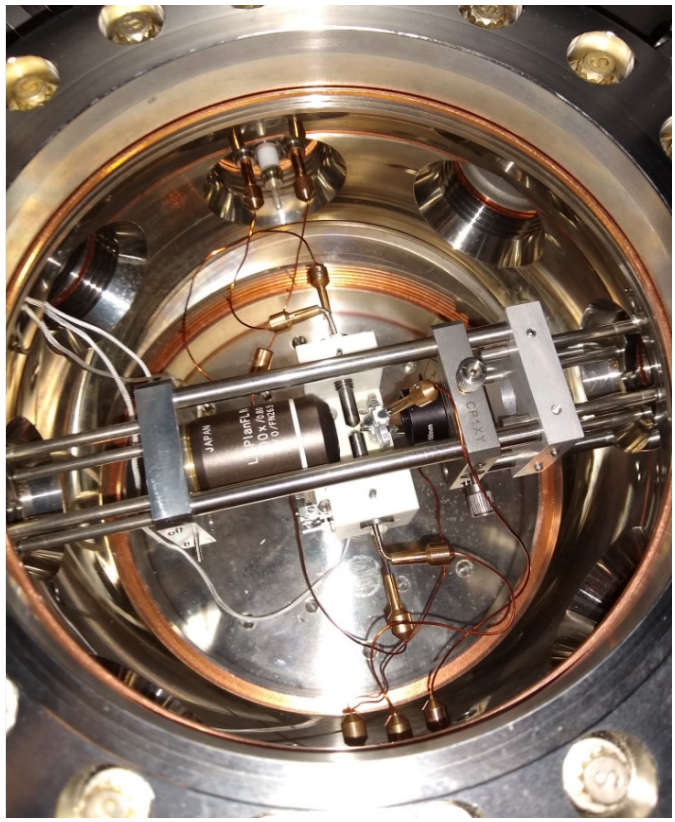

Figure 2.8: **Picture of the vacuum chamber**: photography of the vacuum chamber, showing the Paul trap in a white ceramic holder with its electric connections. On the left (objective (OBJ)) and right (collection lens) the optics components can be seen. On the upper left part of the chamber, below the trap, three white cables control the position of the piezoelectric stages.

Although in principle the design has perfect revolution symmetry around its axis center, when the trap is realized slight mechanical misalignments or differences in the assembly may lead to different secular frequencies in the radial directions of a trapped particle. However, in our experiment we haven't accessed pressures that are low enough to differentiate these two frequencies in the measured PSDs (since, at low pressures, the resonance peaks are thinner and it is easier to tell them apart). In Chapter 5 we discuss an alternative design of the trap with cuts in the steel jackets, resulting in different effective geometrical factors. With this change in the geometry, we induce different secular frequencies and try to perform parametric feedback cooling.

2.3 Optical dipole traps

Optical dipole traps rely on the electric dipole interaction with far red-detuned light to trap neutral particles in a light field, such as dielectric micro and nanoparticles or atoms. The possibility of trapping neutral particles with this force was first considered by Letokhov [80], who suggested that atoms might be one-dimensionally confined at the nodes or antinodes of a standing wave tuned far below or above the atomic transition frequency. Later, A. Ashkin, who had already used the radiation pressure to trap microparticles in 1970 [21] and pioneered the field of atom trapping [24, 25], demonstrated the trapping of micron-sized particles in a single beam laser light with the combined action of radiation pressure and the dipole force [26]. That was the first reported use of a single-beam gradient force trap, the modern *optical tweezers*.

Optical tweezers are therefore a particular implementation of optical dipole traps. They are scientific instruments that use a single, highly focused laser beam to provide an attractive (or repulsive) force in 3 dimensions which depends on the relative refractive index between particle and surrounding medium. They are able to trap and manipulate small particles, whose size is in the range of some hundreds of nanometers to microns, including dielectric and absorbing particles, and have been particularly successful in studying a variety of biological systems [29].

In the most general case, the optical force acting on a rigid object is described by integrating Maxwell's stress tensor over a surface enclosing the object [81]. The derivation of Maxwell's stress tensor requires the knowledge of the total (incident and scattered) vectorial electromagnetic field on the integration surface, and may become very complicated for arbitrarily shaped objects. In the following section we will derive the optical force in a simplified scenario.

2.3.1 Optical dipole trap equations

To see how a dielectric particle can be trapped with light, let us focus on the Rayleigh regime [81]: this means that a fundamental assumption we make is that the particle is "significantly" smaller than the wavelength of the trapping light[15], which we assume is monochromatic. Nevertheless, trapping can occur when the particle is of comparable size or even significantly larger than the laser wavelength. For a detailed description of these other regimes, see Volpe et al. [82].

[15]Here "significantly" is not well defined, but we can assume that the particle diameter is $\sim \lambda/10$ or smaller.

According to the Lorentz formula, a point particle with charge Q in the presence of an electromagnetic field will experience the force

$$\mathbf{F} = Q\left(\mathbf{E} + \frac{\mathrm{d}\mathbf{x}}{\mathrm{d}t} \times \mathbf{B}\right), \tag{2.21}$$

where variables in bold represent 3-dimensional vectors $\mathbf{x} = (x, y, z)$. A generic dielectric particle may not have a net charge but, since we are in the Rayleigh regime by assumption, we may approximate the particle by a dipole. Then, the previous expression can be expanded as

$$\begin{aligned}\mathbf{F} &= Q\left(\mathbf{E}(\mathbf{x}_1) - \mathbf{E}(\mathbf{x}_2) + \frac{\mathrm{d}(\mathbf{x}_1 - \mathbf{x}_2)}{\mathrm{d}t} \times \mathbf{B}\right) \\ &\simeq Q\left(\mathbf{E}(\mathbf{x}_1) + ((\mathbf{x}_1 - \mathbf{x}_2)\cdot\nabla)\,\mathbf{E} - \mathbf{E}(\mathbf{x}_1) + \frac{\mathrm{d}(\mathbf{x}_1 - \mathbf{x}_2)}{\mathrm{d}t} \times \mathbf{B}\right) \\ &= Q\left(((\mathbf{x}_1 - \mathbf{x}_2)\cdot\nabla)\,\mathbf{E} + \frac{\mathrm{d}(\mathbf{x}_1 - \mathbf{x}_2)}{\mathrm{d}t} \times \mathbf{B}\right),\end{aligned} \tag{2.22}$$

where in the second equality we used a Taylor expansion of order 1. We now rewrite (2.22) in terms of the electric dipole moment,

$$\mathbf{p} = Q\mathbf{d} = Q(\mathbf{x}_1 - \mathbf{x}_2). \tag{2.23}$$

We also assume the particle response is linear, $\mathbf{p} = \alpha\mathbf{E}$, where α is the particle polarizability in vacuum[16]

$$\alpha = 4\pi\epsilon_0 a^3 \frac{n^2 - 1}{n^2 + 2} \tag{2.24}$$

and, in the last expression, a is the particle's radius and n its refractive index. Thus we obtain

$$\begin{aligned}\mathbf{F} &= (\mathbf{p}\cdot\nabla)\,\mathbf{E} + \frac{\mathrm{d}\mathbf{p}}{\mathrm{d}t} \times \mathbf{B} \\ &= \alpha\left[(\mathbf{E}\cdot\nabla)\,\mathbf{E} + \frac{\mathrm{d}\mathbf{E}}{\mathrm{d}t} \times \mathbf{B}\right].\end{aligned} \tag{2.25}$$

Finally, we apply the vector calculus identity $(\mathbf{E}\cdot\nabla)\,\mathbf{E} = \nabla\left(\frac{1}{2}E^2\right) - \mathbf{E} \times (\nabla \times \mathbf{E})$ and Faraday's law, $\nabla \times \mathbf{E} = -\frac{\partial \mathbf{B}}{\partial t}$. Thus, equation (2.25) becomes

$$\begin{aligned}\mathbf{F} &= \alpha\left[\frac{1}{2}\nabla E^2 - \mathbf{E} \times (\nabla \times \mathbf{E}) + \frac{\mathrm{d}\mathbf{E}}{\mathrm{d}t} \times \mathbf{B}\right] \\ &= \alpha\left[\frac{1}{2}\nabla E^2 - \mathbf{E} \times \left(-\frac{\mathrm{d}\mathbf{B}}{\mathrm{d}t}\right) + \frac{\mathrm{d}\mathbf{E}}{\mathrm{d}t} \times \mathbf{B}\right] \\ &= \alpha\left[\frac{1}{2}\nabla E^2 + \frac{\mathrm{d}}{\mathrm{d}t}\left(\mathbf{E} \times \mathbf{B}\right)\right].\end{aligned} \tag{2.26}$$

[16]The expression varies slightly when the particle is immersed in a medium with refractive index different than one [82].

The right hand part of this last equation is proportional to the Poynting vector, and since the power of the laser is constant when sampling over frequencies much smaller than the frequency of the laser's light, the derivative of this term averages to zero and the force can be written as

$$\mathbf{F} = \frac{1}{2}\alpha \nabla E^2. \tag{2.27}$$

This is known as the *optical gradient force*, and it shows that, at the end of the day, trapping a dielectric particle is just a matter of engineering the correct optical potential. However, in reality the laser beam also inflicts another type of force, known as the *scattering force*, which works against the gradient force in the axial direction of the trap. The reason why the scattering force hasn't appeared in the previous calculations is precisely due to the ad-hoc nature of the derivation, which is only meant as a means to gain some intuition. More rigorous derivations of the dipole force, which are out of the scope of the thesis, can be found in many excellent reviews [81, 82]. For now, it is enough to know that the dipole force can be written as the sum of two terms,

$$\mathbf{F}_{\text{opt}} = \mathbf{F}_{\text{grad}} + \mathbf{F}_{\text{scat}}, \tag{2.28}$$

$$\mathbf{F}_{\text{grad}} = \frac{1}{2}\alpha' \nabla E^2, \tag{2.29}$$

$$\mathbf{F}_{\text{scat}} = \alpha'' \omega \mu_0 \langle S \rangle - i\frac{\alpha''}{2} \nabla \times (\mathbf{E} \times \mathbf{E}^*), \tag{2.30}$$

where $\alpha = \alpha' + i\alpha''$, ω is the field angular frequency, μ_0 is the magnetic permeability and $\langle S \rangle$ is the Poynting vector.

In practice, the scattering force acts as a force in the direction of the laser beam, resulting in a particle equilibrium position that is displaced slightly downstream of the intensity maximum. For low numerical aperture (NA) lenses, the scattering force is larger than the gradient force, and as a result they are unable to trap particles. This is why most optical tweezers, made of lenses or objectives (OBJs), work with NAs of at least 0.8.

2.3.2 Gaussian beam and linear approximation

To gain some intuition on how an optical trap scales with the system parameters, we may approximate the trap by a Gaussian beam optical potential in the three axes. Then, we can approximate even more by considering that the particle motion is confined around the optical maximum, thus ending up with harmonic oscillator dynamics (see Annex B for details on the model).

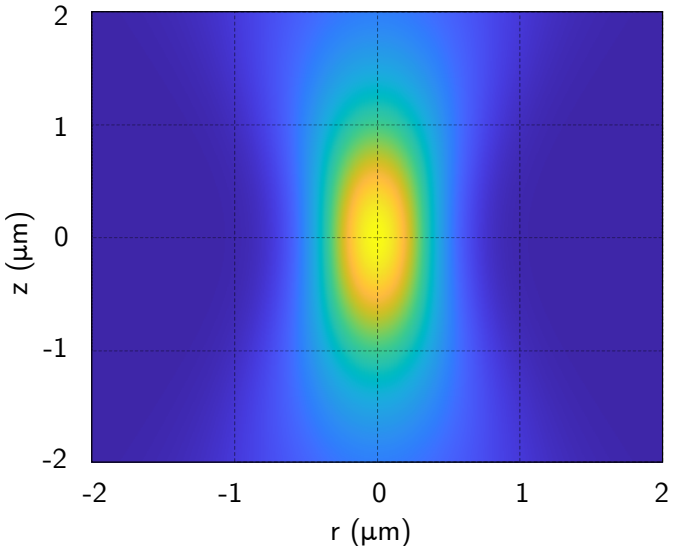

Figure 2.9: **Gaussian beam**: Intensity of a simulated Gaussian beam around focus. The light wavelength is $\lambda = 1064$ nm and the NA $= 0.8$. To compensate for the error of using the Gaussian beam at large NAs, a correction factor $c_\mathrm{f} = 1.5$ is introduced in $w_0 = \frac{\lambda}{\pi \mathrm{NA}} c_\mathrm{f}$. The intensity values at the r and z cross-sections can be found in Fig. 2.10.

As before, though, one must remember that this is a very unrigorous approach, that can only be justified as a quest for intuition. As we have seen, single beam optical traps require large NAs to trap particles (otherwise the scattering force is too large and the gradient force too weak). However, the Gaussian beam is the solution to the Helmholtz equation that is found by applying the paraxial approximation, which breaks down precisely at large NAs. In other words, we will be using an approximation in a regime where it should not be applied. One can then introduce ad-hoc factors to "correct" for the induced errors, and this turns out to be a very fruitful approach to simulate the dynamics, but it remains an approximation nonetheless.

Being aware of this, we can proceed with the computations. The Gaussian beam (see Annex C) takes the expression

$$I(r,z) = I_0 \left(\frac{w_0}{w(z)} \right)^2 e^{-\frac{2r^2}{w^2(z)}}, \tag{2.31}$$

where $w(z) = w_0 \sqrt{1 + \left(\frac{z}{w_0/\mathrm{NA}} \right)^2}$, $w_0 = \frac{\lambda}{\pi \cdot \mathrm{NA}}$ and NA is the numerical aperture of the hypothetical lens creating the trap; the constant I_0 can be found by measuring the laser beam with a power meter, as $P_0 = \frac{1}{2} \pi I_0 w_0^2$. Notice that we are ignoring polarization effects that would break the symmetry in

the r direction in two different x and y axis. A plot of the Gaussian beam for NA = 0.8 can be found in Fig. 2.9. Its second order Taylor expansion at the focus is

$$I(r,z) = \frac{2P_0}{\pi}\left(\frac{\pi\cdot \mathrm{NA}}{\lambda}\right)^2 - \frac{8P_0}{\pi}\left(\frac{\pi\cdot \mathrm{NA}}{\lambda}\right)^4 \frac{r^2}{2} - \frac{4P_0\lambda^2}{\pi^3}\left(\frac{\pi\cdot \mathrm{NA}}{\lambda}\right)^6 \frac{z^2}{2} + \mathcal{O}(r^3, z^3). \tag{2.32}$$

Then, the (linear) dipole force will be

$$\mathbf{F} = \frac{1}{2}\alpha\nabla E^2 = \frac{2\pi a^3}{c}\left(\frac{n^2-1}{n^2+2}\right)\nabla I(\mathbf{r}) \simeq \begin{pmatrix} k_r r \\ k_z z \end{pmatrix},$$

where

$$\begin{pmatrix} k_r \\ k_z \end{pmatrix} = -\frac{2\pi a^3}{c}\left(\frac{n^2-1}{n^2+2}\right)\cdot \begin{pmatrix} \left(\frac{8P_0}{\pi}\frac{\pi\cdot \mathrm{NA}}{\lambda}\right)^4 \\ \frac{4P_0\lambda^2}{\pi^3}\left(\frac{\pi\cdot \mathrm{NA}}{\lambda}\right)^6 \end{pmatrix}, \tag{2.33}$$

the intensity $I = c\epsilon_0|E^2|$, a is the particle radius and n the refractive index of the nanoparticle material. Both the Gaussian beam force and its linear approximation are plotted in Fig. 2.10.

Thus, a particle trapped in a focused beam can be often approximated as a harmonic oscillator. This is a basic assumption in almost every optomechanics [34, 67] experiment where the levitated particle takes on the mechanical oscillator's role. Here, damping due to collisions with air molecules is also modelled with a constant term, obtaining a linear constant coefficient ODE for the position of the particle $x(t)$

$$m\ddot{x} + \gamma\dot{x} + kx = F(t). \tag{2.34}$$

In the equation, $k = m\omega_0^2$ is the strength of the restoring force, γ the damping coefficient[17], and $F(t)$ an external driving force, possibly stochastic.

We need to keep in mind, though, that however useful in developing an intuition, this is still a model, and may not always represent reality satisfactorily. For instance, it has been reported that thermal driving is enough to induce nonlinearities in the dynamics of optically trapped particles in vacuum [83]. The assumptions of the model that is being used should always be clear in case they need to be extended or reconsidered.

[17] For instanced modelled with Stoke's drag law $\gamma = 6\pi\,\eta\, r$ (r the particle's radius and η the dynamic viscosity of the fluid).

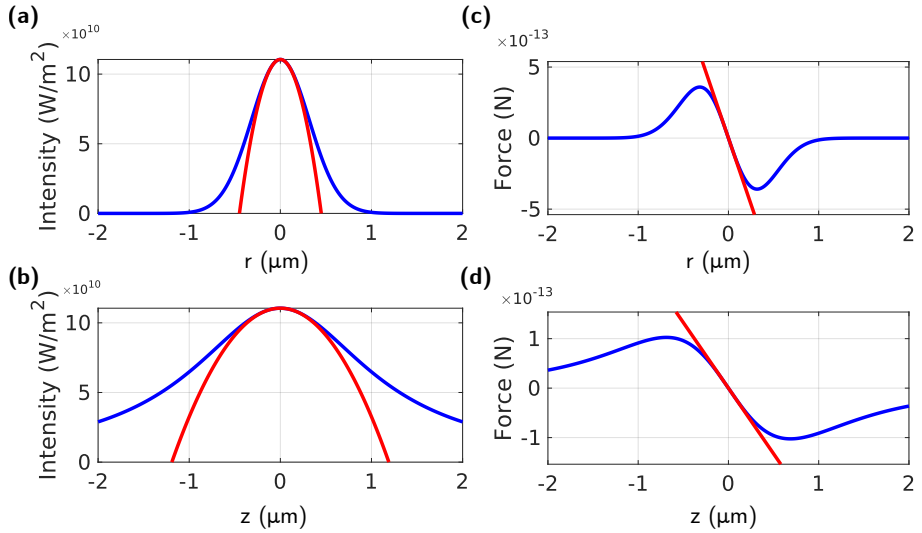

Figure 2.10: **Gradient force in a Gaussian beam**. (a) Intensity section in the r direction of the simulated Gaussian beam in Fig. 2.10, along with its quadratic potential approximation. (b) Intensity section in the z direction of the simulated Gaussian beam in Fig. 2.10, along with its quadratic potential approximation. (c) Restoring force in the r direction of the previous optical potential and its linear approximation. (d) Restoring force in the z direction of the previous optical potential and its linear approximation.

2.4 Stochastic dynamics in a harmonic oscillator trap

Often, as is the case for optically trapped particles, the dynamics of the center of mass (CoM) are well approximated by the harmonic oscillator model (an overview of which can be found at Annex B). However, when the particles under study are small, with diameters below ~ 50 μm, one needs to go a step beyond the classical noise-free model and take into account the intrinsic randomness of the system due to the interaction of the particle with gas or liquid molecules. These *Brownian dynamics* [84] are achieved by adding a stochastic driving force $F(t) = \sigma\eta(t)$ to the equation of motion

$$m\ddot{x} + \gamma\dot{x} + m\omega_0^2 x = \sigma\eta(t), \tag{2.35}$$

with $\eta(t)$ a zero mean and unit standard deviation white noise and $\sigma = \sqrt{2k_B T\gamma}$, expression obtained from a fluctuation-dissipation theorem (see D.20). A proper treatment of the equation requires the use of the Wiener function and Itô calculus (see Annex A). However, thinking of it as white noise generally provides a good intuition of its effect on the dynamics.

Even though the stochastic equation without further approximations can be solved in all generality, it is useful to consider the "overdamped" regime first, in which the inertia term is discarded.

2.4.1 Overdamped regime

It is common to discard the second order term of the stochastic differential equation when it is "small" compared to the other terms[18]. In this case the equation takes the form of an Ornstein-Uhlenbeck (OU)[19] process

$$\gamma\dot{x} + kx = \sigma\eta(t), \tag{2.36}$$

with γ the damping constant and $k = m\omega_0^2$ the restoring force. In Itô's notation

$$\mathrm{d}X_t = -aX_t\,\mathrm{d}t + b\,\mathrm{d}W_t, \tag{2.37}$$

with $a = \frac{k}{\gamma} > 0$, $b = \frac{\sigma}{\gamma}$. The solution of this stochastic differential equation (SDE) is

$$X_t = X_0 e^{-at} + b\int_0^t e^{-a(t-s)}\mathrm{d}W_s. \tag{2.38}$$

The autocorrelation of the process can be obtained by using Itô's isometry on the last expression

$$\begin{aligned} R(t,s) &= \mathbb{E}\left[\int_0^t f(u)\,\mathrm{d}W_u \int_0^s f(v)\,\mathrm{d}W_v\right] \\ &= b^2 e^{-a(s+t)}\cdot\mathbb{E}\left[\int_0^t e^{au}\,\mathrm{d}W_u \int_0^s e^{av}\,\mathrm{d}W_v\right] \\ &= b^2 e^{-a(s+t)}\cdot\mathbb{E}\left[\int_0^{\min(t,s)} e^{au}e^{au}\,\mathrm{d}u\right] \\ &= \frac{b^2}{2a}e^{-a(s+t)}(e^{2\min(s,t)} - 1) = \frac{b^2}{2a}\left(e^{-a|t-s|} - e^{-a(t+s)}\right). \end{aligned}$$

When $|t-s| = 0$, the autocorrelation equals the variance of X_t,[20]

$$\mathbb{E}(X_t^2) = \frac{b^2}{2a}\left(1 - e^{-2at}\right) = \frac{k_\mathrm{B}T}{m\omega_0^2}\left(1 - e^{-2at}\right). \tag{2.39}$$

[18] This can be made rigorous as a perturbative problem, a *regular perturbation* problem. However, this is not always the case when the parameter is multiplying the highest order term of the equation. See Ref. [85] for more details

[19] See Annex A.

[20] Equivalently this can also be written as $\langle X_t^2\rangle$.

For small t, the variance takes the expression

$$\lim_{t\to 0}\mathbb{E}(X_t^2) = \frac{2k_\mathrm{B}T}{\gamma}t + \mathcal{O}(t^2) = \frac{\sigma^2}{\gamma^2}t + \mathcal{O}(t^2), \tag{2.40}$$

while for long times

$$\lim_{t\to\infty}\mathbb{E}(X_t^2) = \frac{k_\mathrm{B}T}{m\omega_0^2}, \tag{2.41}$$

as is expected from the equipartition theorem. As t and s increase, the second exponential summand of the process autocorrelation becomes arbitrarily small. The remaining part is a function of $\tau \equiv t - s$ only; thus, we can apply the Wiener-Khinchin theorem (see Annex A.1.2) to get an analytical expression of the power spectrum of the process:

$$S(f) = \mathcal{F}\left(\frac{b^2}{2a}e^{-a|\tau|}\right) = \frac{b^2}{a^2 + 4\pi^2 f^2} \tag{2.42}$$

$$S(\omega) = \frac{\sigma^2}{k^2 + \gamma^2\omega^2} = \frac{\sigma^2/m^2}{\omega_0^4 + \Gamma^2\omega^2}, \tag{2.43}$$

where in the last expression we have reintroduced the mass, as it will help in identifying similarities between this and the full second order system power spectrum, and $\Gamma = \gamma/m$ is the normalized damping.

As expected by Parseval's theorem, the integral of the power spectral density (PSD) is

$$\mathbb{E}(X_t^2) = \frac{1}{2\pi}\int S(\omega)\mathrm{d}\omega = \frac{1}{2\pi}\int \frac{\sigma^2/m^2}{\omega_0^4 + \Gamma^2\omega^2}\mathrm{d}\omega = \frac{k_\mathrm{B}T}{m\omega_0^2},$$

recovering again the value expected by the equipartition theorem.

Observation: expression (2.42) of the power spectral density has two clear different regimes: at low frequencies, the a^2 term in the denominator dominates and the spectrum is almost flat. At large f, a^2 is negligible and the other term dominates. In a log-log scale representation, the power spectrum looks like two straight lines (first an horizontal line and then a decreasing line); the frequency at which the behaviour changes is known as the *corner frequency*, $\omega_c = a = \frac{k}{\gamma} = \frac{\omega_0^2}{\Gamma}$.

2.4.2 Full 2nd order equation

The full equation takes the expression

$$m\ddot{x} + \gamma\dot{x} + kx = \sigma\eta(t). \tag{2.44}$$

Performing a change of variables, $x = e^{\frac{-\gamma}{2m}t}x_1$, we get

$$m\ddot{x}_1 + \left(k - \frac{\gamma^2}{4m}\right)x_1 = \sigma e^{\frac{\gamma}{2m}t}\eta(t), \tag{2.45}$$

thus eliminating $\dot{x}$. Setting $a = \frac{k}{m} - \frac{\gamma^2}{4m^2}$, $b = \frac{\sigma}{m}$ and rewriting the equation as a first order linear system with

$$X = \begin{pmatrix} x_2 \\ v_2 \end{pmatrix}, \tag{2.46}$$

where $v_2 = \dot{x_2}$, we get in Itô's notation

$$\mathrm{d}X = \begin{pmatrix} 0 & 1 \\ -a & 0 \end{pmatrix} \cdot X\mathrm{d}t + \begin{pmatrix} 0 \\ be^{\frac{\gamma}{2m}t} \end{pmatrix} \cdot \mathrm{d}W_t. \tag{2.47}$$

The solution of a linear homogeneous SDE is

$$X_t = e^{\int_0^t A(t)\mathrm{d}t} \cdot X_0 + e^{\int_0^t A(t)\mathrm{d}t} \cdot \int_0^t e^{-\int A(s)\mathrm{d}s}\sigma(s)\mathrm{d}W_s, \tag{2.48}$$

where $A(t)$ is the (generally vector) coefficient of X. For this SDE a fundamental matrix solution of the associated homogeneous noise-free system is

$$\Phi(t) = \begin{pmatrix} \cos\sqrt{a}t & \sin\sqrt{a}t/\sqrt{a} \\ -\sqrt{a}\sin\sqrt{a}t & \cos\sqrt{a}t \end{pmatrix}. \tag{2.49}$$

The determinant of this matrix is 1, so its inverse matrix will be

$$\begin{aligned}\Phi^{-1}(t) = e^{-\int A(\tau)\mathrm{d}\tau} &= \det\Phi(t)^{-1} \cdot \begin{pmatrix} \cos\sqrt{a}t & -\sin\sqrt{a}t/\sqrt{a} \\ \sqrt{a}\sin\sqrt{a}t & \cos\sqrt{a}t \end{pmatrix} \\ &= \begin{pmatrix} \cos\sqrt{a}t & -\sin\sqrt{a}t/\sqrt{a} \\ \sqrt{a}\sin\sqrt{a}t & \cos\sqrt{a}t \end{pmatrix}\end{aligned}$$

and hence we can solve the complete system. We are interested in the first component of X, the position (as we will be calculating the PSD of the trajectory of the particle)

$$\begin{aligned}x_1(t) = &\begin{pmatrix} \cos\sqrt{a}t & \sin\sqrt{a}t/\sqrt{a} \end{pmatrix} \cdot \begin{pmatrix} x_1(0) \\ v_1(0) \end{pmatrix} + \\ &\begin{pmatrix} \cos\sqrt{a}t & \sin\sqrt{a}t/\sqrt{a} \end{pmatrix} \cdot \int_0^t be^{\frac{\gamma}{2m}r} \cdot \begin{pmatrix} -\sin\sqrt{a}r/\sqrt{a} \\ \cos\sqrt{a}r \end{pmatrix} \mathrm{d}W_r.\end{aligned}$$

Finally, $x_1(t) = e^{\frac{\gamma t}{2m}} x(t)$, so

$$\begin{aligned} x(t) =& e^{-\frac{\gamma t}{2m}} \begin{pmatrix} \cos\sqrt{a}t & \sin\sqrt{a}t/\sqrt{a} \end{pmatrix} \cdot \begin{pmatrix} x(0) \\ v(0) + \frac{\gamma}{2m} x(0) \end{pmatrix} + \\ & e^{-\frac{\gamma t}{2m}} \begin{pmatrix} \cos\sqrt{a}t & \sin\sqrt{a}t/\sqrt{a} \end{pmatrix} \cdot \int_0^t b e^{\frac{\gamma}{2m} r} \cdot \begin{pmatrix} -\sin\sqrt{a}r/\sqrt{a} \\ \cos\sqrt{a}r \end{pmatrix} \mathrm{d}W_r. \end{aligned} \tag{2.50}$$

We see that, after a transient time, only the term depending on $\mathrm{d}W_r$ remains, so the first moment of the process is zero. Now, applying Itô's isometry as before to calculate the covariance we get

$$\begin{aligned} R(t,s) = \mathbb{E}\left[\int_0^t f(u)\,\mathrm{d}W_u \int_0^s f(v)\,\mathrm{d}W_v\right] = b^2 e^{-\frac{\gamma(t+s)}{2m}} \cdot \begin{pmatrix} \cos\sqrt{a}t & \sin\sqrt{a}t/\sqrt{a} \end{pmatrix} \cdot \\ \cdot \mathbb{E}\left[\int_0^{\min(t,s)} e^{\frac{\gamma}{m}u} \begin{pmatrix} \frac{\sin^2\sqrt{a}u}{a} & -\frac{\sin\sqrt{a}u\cos\sqrt{a}u}{\sqrt{a}} \\ -\frac{\sin\sqrt{a}u\cos\sqrt{a}u}{\sqrt{a}} & \cos^2\sqrt{a}u \end{pmatrix} \mathrm{d}u\right] \cdot \begin{pmatrix} \cos\sqrt{a}s \\ \sin\sqrt{a}s/\sqrt{a} \end{pmatrix}. \end{aligned}$$

This is a quite uninteresting calculation. As in the one-dimensional OU process, one gets a term which only depends on the difference $|t-s| = \tau$, and another which is multiplied by $e^{-|t+s|}$, that quickly vanishes. Setting $t = s$ we recover the variance,

$$\mathbb{E}[X_t^2] = \frac{k_\mathrm{B}T}{m\omega_0^2}\left(1 - e^{-\Gamma t}\left(\frac{\omega_0^2}{\omega_1^2} - \frac{\Gamma^2}{4\omega_1^2}\cos(2\omega_1 t) + \frac{\Gamma}{2\omega_1}\sin(2\omega_1 t)\right)\right), \tag{2.51}$$

where we have defined $\omega_1 = \sqrt{\omega_0^2 - (\Gamma/2)^2} = \sqrt{a}$ and used the normalized damping constant $\Gamma = \frac{\gamma}{m}$. As in the overdamped case,

$$\lim_{t\to\infty} \mathbb{E}[X_t^2] = \frac{k_\mathrm{B}T}{m\omega_0^2},$$

as expected from the equipartition theorem. However, more interesting is the behaviour at short times,

$$\lim_{t\to 0} \mathbb{E}[X_t^2] = \frac{2\Gamma k_\mathrm{B}T}{3m} t^3 + \mathcal{O}(t^4).$$

Observation: this value of the variance assumes that x_0, v_0, initial conditions of the problem, are known. This *may not be the case* for a real experiment in the lab. For instance, assume we have a particle in an optical tweezer, and we want to calculate the mean square displacement (MSD),

$$\mathbb{E}[(x(t) - x(0))^2] = \mathbb{E}[x^2(t) + x^2(0) - 2x(0)x(t)]. \tag{2.52}$$

Then we distinguish two cases:

1. $x(0)$ is known, e.g. $x(0) = 0$. Then

$$\mathbb{E}[x^2(t) + x^2(0) - 2x(0)x(t)] = \mathbb{E}[x^2(t)] = \mathcal{O}(t^3). \tag{2.53}$$

2. $x(0)$ is not known (or is uncontrolled), and we do the ensemble average. Then

$$\begin{aligned}\mathbb{E}[x^2(t) + x^2(0) - 2x(0)x(t)] &= \mathbb{E}[x^2(t)] + \mathbb{E}[x^2(0)] - 2\mathbb{E}[x(0)x(t)] \\ &= \frac{2k_{\mathrm{B}}T}{m\omega_0^2} - 2R(t) = \mathcal{O}(t^2).\end{aligned}$$

We see, therefore, that the leading term of the series expansion of the MSD is different in each case. This is an important distinction that is not clear in Tongcang Li et. al. [54].

If in the autocorrelation integral we keep only the term with τ dependency (since the term multiplied by $e^{-|t+s|}$ will quickly decay), after some simplification one gets

$$R(\tau) = \frac{b^2m^2e^{\frac{-\Gamma|\tau|}{2}}\left(2\sqrt{a}m\cos(\sqrt{a}|\tau|) + \gamma\sin(\sqrt{a}|\tau|)\right)}{\sqrt{a}(\gamma^3 + 4a\gamma m^2)}. \tag{2.54}$$

Worth mentioning is the value of the time constant of the exponential factor, $\frac{2}{\Gamma}$: this value is proportional to the time needed for the autocorrelation to get below a given threshold[21], otherwise known as *losing the coherence* of the oscillation. A usual criterion is 3 time constants, with the autocorrelation decreasing to below $e^{-3} < 5\%$. The number of oscillations of the system during this time is

$$3\frac{2/\Gamma}{1/f} = \frac{3 \cdot 2 \cdot f}{\Gamma} \simeq \frac{\omega}{\Gamma} \triangleq \mathcal{Q}. \tag{2.55}$$

[21] Which is arbitrarily set.

Thus, the $\mathcal{Q}$-factor can be understood as the number of oscillations of the system under the presence of Brownian noise before the autocorrelation gets below 5%[22].

From the expression of the autocorrelation we see that $R(t,\tau) = R(\tau)$: therefore, the process is wide-sense stationary and the conditions to apply the Wiener-Khinchin theorem are satisfied (see Annex A.1.2). The Fourier transform of this autocorrelation function is the PSD

$$S(f) = \frac{16b^2}{\Gamma^4 + 8(a + 4\pi^2 f^2)\Gamma^2 + 16(a - 4\pi^2 f^2)^2} \tag{2.56}$$

which, after replacing the variables and some rearranging takes the simpler and more familiar expression

$$S(\omega) = \frac{\sigma^2/m^2}{(\omega_0^2 - \omega^2)^2 + \Gamma^2\omega^2}, \tag{2.57}$$

where we have replaced the unitary ordinary frequency Fourier transform (in terms of f) by the non-unitary angular frequency Fourier transform. Thus, it is readily seen that this is the frequency response of a harmonic oscillator to a flat-spectrum (white noise) driving force.

As in the overdamped case,

$$\mathbb{E}(X_t^2) = \frac{1}{2\pi}\int \frac{\sigma^2/m^2}{(\omega_0^2 - \omega^2)^2 + \Gamma^2\omega^2}\mathrm{d}\omega = \frac{k_\mathrm{B}T}{m\omega_0^2} \tag{2.58}$$

as expected by the equipartition theorem.

2.5 Conclusions

In summary, in this chapter we have discussed the conditions that a device needs to satisfy to constitute a particle trap, and have studied two cases: the Paul trap, used for charged particles, and the optical tweezers, for particles that can be approximated as dipoles. We have also described in detail how to design and simulate a particular type of Paul trap, in our case with an end-cap geometry.

The equations of motion of a trapped particle can often be approximated with a harmonic oscillator model and, when this is possible, it helps tremendously in developing an intuition of the particle's dynamics. For both traps, we have explained under which conditions the harmonic oscillator is a good representation of the system. Finally, we have taken into account the Brownian effects that result from the interaction of the particle with

[22]The number of "coherent" oscillations.

gas molecules. To include them in our analysis, we have used stochastic calculus and Itô integrals instead of the more common Fourier transforms. This has the advantage of making fully visible the transient behaviour of the processes.

A fully stochastic treatment of the Paul trap equation still remains, since in this chapter we have *first* approximated the equation with an effective potential and then included the noise term. The case where the noise is considered since the beginning will be studied in the next chapter.

3

Stochastic dynamics in a Paul trap

In this chapter, we study the dynamics of the center of mass of a Brownian particle levitated in a Paul trap, an example of non harmonic oscillator dynamics[a]*. We mostly focus on the overdamped regime, comparing theory with numerical simulations and experimental data from our Paul trap. We find an exact analytical solution to the stochastic equation of motion, expressions for the standard deviation of the motion, and thermalization times by using the WKB method. Finally, we prove the power spectral density of the motion can be approximated by that of an Ornstein-Uhlenbeck process and use that to calibrate the motion of a trapped particle. The contents of this section are based on Ref. [86].*

[a] At least, not without the proper approximations. As we have seen before, with the adiabatic approximation the dynamics become equivalent to those of a particle oscillating in an effective potential.

3.1 Introduction

The invention of the quadrupole ion trap in the late 1950s had a tremendous impact in physics [75], since it allowed the trapping of ions and, thus, gave rise to the manipulation of individual quantum objects under well-controlled conditions for the first time [87]. Naturally, after the first demonstrations of ion trapping appeared, the study of the ion dynamics in quadrupole traps increased at a vertiginous pace [88, 89, 90]. Despite this, due to the very restrictive experimental conditions required for ion trapping,

the pressure regimes dominated by damping and Brownian noise [91, 92] did not receive much attention until optical tweezers detection techniques were adapted to nanoparticles levitated in Paul traps [64, 65]. Furthermore, many recent studies with micro and nanoparticles in Paul traps were mainly focused on the determination of the trapped object's optical properties [93, 94, 95, 96] or in detecting small signals from internal degrees of freedom [61, 63, 97, 98]. These experiments would benefit from a good understanding of the particle dynamics, since minimizing the variance of the position greatly improves the particles' signal collection.

The work detailed in this chapter tries to bridge this gap, by doing a theoretical and experimental study of the dynamics of a particle levitated in a Paul trap, starting from its stochastic differential equation. We find the exact solution to the equation, expressions for the standard deviation σ_y of the motion and thermalization times by using the WKB method [99] under two different limits. We then show that a naïve description of the dynamics based on the overdamped approximation—typically used by the optical tweezers community—is not valid in the case of a Paul trap. Finally, we also prove that the motion's power spectral density (PSD) can be approximated by that of an Ornstein-Uhlenbeck (OU) process [100]. We include a comparison of all the theory results with simulations and provide an application example, using the expressions to calibrate the motion of a trapped particle.

3.2 Theory

3.2.1 Analytical solution

The CoM motion along an axis of a classical particle levitated in a quadrupole trap can be described [12] by the stochastic differential equation of motion

$$m\ddot{y} + \gamma\dot{y} - \epsilon\cos\omega_{\mathrm{d}}t \cdot y = \sigma\eta(t), \tag{3.1}$$

where we have neglected DC electric fields. Here, m is the particle mass [101], γ is the constant damping due to the interaction with residual gas molecules, ω_{d} is the trap driving frequency, epsilon is defined as

$$\epsilon \triangleq \frac{QV}{d^2},$$

where Q is the particle charge, V the trap voltage and d is the characteristic size of the trap (related to the distance between electrodes), and finally $\sigma\eta(t)$ is a stochastic force, with $\eta(t)$ being a unit intensity Gaussian white noise

and $\sigma = \sqrt{2k_{\mathrm{B}}T\gamma}$ [102]. We notice that at the pressure regimes of this work (ambient to low vacuum), the quadratic region of the electric potential in the trap is much larger than the particle confinement. Therefore, the dynamics along the different axes are uncoupled, and the 1D equation that we have just presented is a good description for the motion along all of them [83].

An explicit expression for $y(t)$ can be obtained as follows. We introduce the normalized damping $\Gamma = \gamma/m$ and perform the change of variables $y = e^{-\frac{\Gamma}{2}t}y_1$, obtaining:

$$m\ddot{y}_1 - \left(\frac{m\Gamma^2}{4} + \epsilon\cos\omega_{\mathrm{d}}t\right)y_1 = \sigma e^{\frac{\Gamma}{2}t}\eta(t). \tag{3.2}$$

Introducing a dimensionless time $\tau = \omega_{\mathrm{d}}t/2$ and defining

$$y_2 = \frac{m\omega_{\mathrm{d}}}{2}y_1,$$

we get to:

$$\begin{aligned}\ddot{y}_2 - \left(\frac{\Gamma^2}{\omega_{\mathrm{d}}^2} + 2\cdot\frac{2\epsilon}{m\omega_{\mathrm{d}}^2}\cos(2\tau)\right)y_2 = \\ \frac{2\sigma}{\omega_{\mathrm{d}}}e^{\frac{\Gamma}{\omega_{\mathrm{d}}}\tau}\eta\left(\frac{2\tau}{\omega_{\mathrm{d}}}\right).\end{aligned} \tag{3.3}$$

Notice that with $a = -\Gamma^2/\omega_{\mathrm{d}}^2, \quad q = 2\epsilon/m\omega_{\mathrm{d}}^2$ we obtain the Mathieu equation at the left hand side of equation (3.3), plus a noise term:

$$\begin{aligned}\ddot{y}_2 + (a - 2\cdot q\cos(2\tau))\,y_2 = \\ \frac{2\sigma}{\omega_{\mathrm{d}}}e^{\frac{\Gamma}{\omega_{\mathrm{d}}}\tau}\eta\left(\frac{2\tau}{\omega_{\mathrm{d}}}\right).\end{aligned} \tag{3.4}$$

We can now rewrite this equation as a first order linear system with $Y = (y_2, v_2)^\top$, where $v_2 = \dot{y_2}$. In Itô's notation [1].

$$\begin{aligned}\mathrm{d}Y = \begin{pmatrix}0 & 1\\ -a + 2q\cos(2\tau) & 0\end{pmatrix}\cdot Y\mathrm{d}\tau + \\ \begin{pmatrix}0\\ \sqrt{\frac{2}{\omega_{\mathrm{d}}}}\sigma e^{\frac{\Gamma}{\omega_{\mathrm{d}}}\tau}\end{pmatrix}\cdot \mathrm{d}W_\tau\end{aligned}. \tag{3.5}$$

[1] In the noise differential we used $\eta\left(\frac{2\tau}{\omega_{\mathrm{d}}}\right)\frac{2}{\omega_{\mathrm{d}}}\mathrm{d}\tau = \eta(t)\mathrm{d}t = \mathrm{d}W_t = \sqrt{\frac{2}{\omega_{\mathrm{d}}}}\mathrm{d}W_\tau$. The time change formula for Itô integrals was used, see Oksendal [100], Theorem 8.5.7.

The fundamental matrix solution of the associated homogeneous noise-free system is given by the Mathieu cosine and sine functions [2]:

$$\Phi(\tau) = \begin{pmatrix} \mathrm{c}_{a,q}(\tau) & \mathrm{s}_{a,q}(\tau) \\ \dot{\mathrm{c}}_{a,q}(\tau) & \dot{\mathrm{s}}_{a,q}(\tau) \end{pmatrix}. \tag{3.6}$$

Here, we refer to the Mathieu functions as solutions of Mathieu's differential equation

$$\ddot{y} + (a - 2q\cos(2\tau))y = 0, \tag{3.7}$$

where a and q are constant parameters. The stability of the solutions depends on the values of these parameters, as seen before. Since it is a linear 2nd order differential equation, two independent solutions generate the linear space of all solutions of the homogeneous problem. More specifically, the Mathieu functions $\mathrm{c}_{a,q}(\tau)$ and $\mathrm{s}_{a,q}(\tau)$ are defined as the solutions of (3.7) with initial conditions $(y, \dot{y}) = (1, 0)$ (for $\mathrm{c}_{a,q}(\tau)$) and $(y, \dot{y}) = (0, 1)$ (for $\mathrm{s}_{a,q}(\tau)$), in clear analogy to the standard $\cos(\tau)$ and $\sin(\tau)$ functions.

Now, with Liouville's formula [3] we see that the determinant of this matrix is 1. Therefore its inverse is

$$\begin{aligned} \Phi^{-1}(\tau) &= \det \Phi(\tau)^{-1} \cdot \begin{pmatrix} \dot{\mathrm{s}}_{a,q}(\tau) & -\mathrm{s}_{a,q}(\tau) \\ -\dot{\mathrm{c}}_{a,q}(\tau) & \mathrm{c}_{a,q}(\tau) \end{pmatrix} \\ &= \begin{pmatrix} \dot{\mathrm{s}}_{a,q}(\tau) & -\mathrm{s}_{a,q}(\tau) \\ -\dot{\mathrm{c}}_{a,q}(\tau) & \mathrm{c}_{a,q}(\tau) \end{pmatrix} \end{aligned} \tag{3.8}$$

and hence we can solve the complete system (see Annex A). Solving for the particle's position we obtain

$$\begin{aligned} y_2\left(\frac{2\tau}{\omega_\mathrm{d}}\right) = \begin{pmatrix} \mathrm{c}_{a,q}(\tau) & \mathrm{s}_{a,q}(\tau) \end{pmatrix} \cdot \begin{pmatrix} y_2(0) \\ v_2(0) \end{pmatrix} + \begin{pmatrix} \mathrm{c}_{a,q}(\tau) & \mathrm{s}_{a,q}(\tau) \end{pmatrix} \\ \cdot \int_0^\tau \sqrt{\frac{2}{\omega_\mathrm{d}}} \sigma e^{\frac{\Gamma}{\omega_\mathrm{d}} u} \cdot \begin{pmatrix} -\mathrm{s}_{a,q}(u) \\ \mathrm{c}_{a,q}(u) \end{pmatrix} \mathrm{d}W_u, \end{aligned} \tag{3.9}$$

which is the solution of (3.5). Undoing the time change and setting $y_2 = \frac{\omega_\mathrm{d} m}{2} e^{\frac{\Gamma t}{2}} y$ we obtain

$$\begin{aligned} y(t) = e^{-\frac{\Gamma t}{2}} \begin{pmatrix} \mathrm{c}_{a,q}(\omega_\mathrm{d} t/2) & \mathrm{s}_{a,q}(\omega_\mathrm{d} t/2) \end{pmatrix} \cdot \begin{pmatrix} y(0) \\ \frac{2}{\omega_\mathrm{d}} v(0) + \frac{\Gamma}{\omega_\mathrm{d}} y(0) \end{pmatrix} + \\ \frac{2}{\omega_\mathrm{d} m} \begin{pmatrix} \mathrm{c}_{a,q}(\omega_\mathrm{d} t/2) & \mathrm{s}_{a,q}(\omega_\mathrm{d} t/2) \end{pmatrix} \cdot \int_0^t \sigma e^{\frac{\Gamma}{2}(r-t)} \cdot \begin{pmatrix} -\mathrm{s}_{a,q}(\omega_\mathrm{d} r/2) \\ \mathrm{c}_{a,q}(\omega_\mathrm{d} r/2) \end{pmatrix} \mathrm{d}W_r \end{aligned} \tag{3.10}$$

[2] For a detailed discussion of the Mathieu equation and functions' properties, see `http://dlmf.nist.gov/28.2`.

[3] It is also called the Wronskian of the system.

which is an explicit analytical solution of equation (3.1) and coincides with the solution provided in Ref. [103]. Notice that the initial condition terms decay exponentially and do not affect the long term behaviour of the equation.

3.2.2 Approximate solution

Even though the solution in (3.10) is exact, it is difficult to obtain useful parameters from it—such as its moments' asymptotic behaviour—without numerical methods. At high pressures, one may be tempted to perform the same approximation as in the previous section by discarding the highest order term (inertia); this is common procedure in *overdamped* optical tweezers systems. In the Paul trap case, this approximation leads to a solvable, easy to evaluate analytical solution. However, even though at first sight the expression looks reasonable, the solution thus obtained is incorrect, since the approximation in which it is based changes the asymptotic behaviour of the dynamics. If inertia ($m\ddot{y}$) is neglected, Equation 3.1 becomes

$$\gamma\dot{y} - \epsilon\cos\omega_{\mathrm{d}}t \cdot y = \sigma\eta(t). \tag{3.11}$$

We will refer to this as the *naïve* overdamped approximation. The solution to this equation is:

$$y(t) = e^{-\frac{\epsilon}{\gamma\omega_{\mathrm{d}}}\sin\omega_{\mathrm{d}}t}\left(y(0) + \frac{\sigma}{\gamma}\int_0^t e^{\frac{\epsilon}{\gamma\omega_{\mathrm{d}}}\sin\omega_{\mathrm{d}}r}\mathrm{d}W_r\right). \tag{3.12}$$

Assuming $y(0) = 0$ for simplicity, we may apply Itô's isometry in (3.12), finding the following expression for the process variance:

$$\mathbb{E}[y^2(t)] = e^{-\frac{2\epsilon}{\gamma\omega_{\mathrm{d}}}\sin\omega_{\mathrm{d}}t}\left(\frac{\sigma^2}{\gamma^2}\int_0^t e^{\frac{2\epsilon}{\gamma\omega_{\mathrm{d}}}\sin\omega_{\mathrm{d}}s}\mathrm{d}s\right) \tag{3.13}$$

which grows with time as $\mathcal{O}(t)$. This behaviour is qualitatively different from the one obtained with the solution to the full equation and indicates that, in this case, the singular perturbation problem requires a more sophisticated approach than just neglecting the highest order term.

Some physical intuition on why the approximation fails can be gained noticing that in the absence of inertia or noise, no net force acts on average over a cycle of the driving field. By linearity, superimposing a Brownian motion leads to a uniformly growing variance, thus avoiding a stable trapping regime.

We thus provide an alternative approximate solution by following the WKB procedure to find the short and long term behaviour of the physically relevant process variance $\langle y^2(t)\rangle$.

With the WKB computations, one seeks a solution of the form

$$y(\tau) = e^{-\tau/2\kappa} \exp\left(\frac{S_0}{\kappa} + S_1 + \dots\right) \tag{3.14}$$

as a series in terms of κ, known as the "small parameter". Since the choice of κ has a certain degree of arbitrariness, we provide calculations for two κ alternatives. We then follow our analysis by further approximation, dropping small terms of the series, and find that both choices lead to a result of the same form. Numerical simulations serve as a final check for the validity of the expressions.

For the first series, we use the particle mass m as the small parameter κ. In the second case, we rewrite eq. (3.1) as

$$\kappa^2 \ddot{y} + \kappa \dot{y} - \beta' \cos(2\tau) y = \frac{m\sigma}{\gamma^2} \sqrt{\frac{\omega_\mathrm{d}}{2}} \eta(\tau), \tag{3.15}$$

which is a reformulation of (3.1) where $\tau = \frac{\omega_\mathrm{d} t}{2}$ as before, $\beta' = \frac{m\epsilon}{\gamma^2}$ and $\kappa = \frac{m\omega_\mathrm{d}}{2\gamma}$ is the new small parameter.

At this point we introduce a set of parameter values, in accordance with our experimental setup:

- $T = 295$ K (ambient temperature).
- Particle radius: we assume 100 nm $\leq r \leq$ 1000 nm. From the radius, $m = \frac{4}{3} r^3 \rho$, where ρ is the material density. Assuming silica, this results in $m \in [10^{-17}\, 10^{-15}]$ kg.
- $\gamma = 6\pi\nu r$, where $\nu = 18.6 \cdot 10^{-6}$ Pa·s is the viscosity of air at ambient pressure. This gives $\gamma = 3.5 \cdot 10^{-11}$ kg/s. $\sigma = \sqrt{2 k_\mathrm{B} T \gamma}$ is obtained from the fluctuation-dissipation theorem (D.20), $\sigma = 5.3 \cdot 10^{-16}$.
- $\omega_\mathrm{d}/2\pi \in [0.5,\, 20]$ kHz
- Q is the net number of charges in the particle (assume $50 \leq Q \leq 1000$), V the electric potential at the electrodes ($500 \leq V \leq 2000$ volts) and d^2 a constant factor that takes into account the geometry of the trap (0.1 nm $< d <$ 1 mm). From these we calculate $\epsilon = \frac{QV}{d^2}$. $\epsilon \in [4 \cdot 10^{-9} \quad 3 \cdot 10^{-5}]$

For these, $\kappa \ll 1$ and thus ensure the validity of the method. The derivations provided are completely general except when an approximation relies on the specific values of the chosen parameters, in which case it is explicitly indicated.

The details of the WKB calculations, which are a bit tedious, can be found in Annex E. Instead, we proceed directly to discuss the results. Stating the problem with the initial conditions $y(0) = v(0) = 0$ for greater clarity, the solution of the equation of motion is then found to be approximately:

$$y(t) \approx \frac{\sigma}{\gamma} \int_0^t e^{\lambda(t-s)} \, \mathrm{d}W_s. \tag{3.16}$$

Here, W_t is a Wiener process, the time integral of the white noise η driving the equation of motion (see the Annex A)

$$W_t = \int_0^t \eta_s \, \mathrm{d}s, \tag{3.17}$$

and λ is the larger of the two characteristic Floquet exponents. λ can be thought of as a thermalization rate: the time it takes for the particle to reach "equilibrium" is proportional to $1/|\lambda|$. However, one should recall that the Paul trap equation is non-autonomous and, therefore, the concepts from the theory of stationary processes, when they apply, are only approximations.

The value of λ depends on the way the limit is taken and how many terms of the series expansion are considered (see Annex E), but in both cases it is a negative number with a small absolute value that can be approximated as

$$\lambda \approx -\frac{m\epsilon^2}{2\gamma^3}. \tag{3.18}$$

Our numerical tests show that this is a good approximation when the equation parameters are similar to actual nanoparticle experiments [64, 65, 66, 97, 98], for pressures between a few millibars and ambient.

According to the Itô isometry [100], the variance of the approximate solution equals

$$\mathbb{E}[y^2(t)] = \left(\frac{\sigma}{\gamma}\right)^2 \int_0^t e^{2\lambda(t-s)} \, \mathrm{d}s = \left(\frac{\sigma}{\gamma}\right)^2 \frac{1 - e^{2\lambda t}}{2\,|\lambda|}. \tag{3.19}$$

It follows that

$$\mathbb{E}[y^2(t)] \simeq \frac{\sigma^2}{2\gamma^2\,|\lambda|} \tag{3.20}$$

for $t \gg 1/|\lambda|$ and that the variance converges to this value in the limit $t \to \infty$. For short times the diffusion term dominates and it grows linearly

$$\mathbb{E}\left[y(t)^2\right] \approx \left(\frac{\sigma}{\gamma}\right)^2 t. \tag{3.21}$$

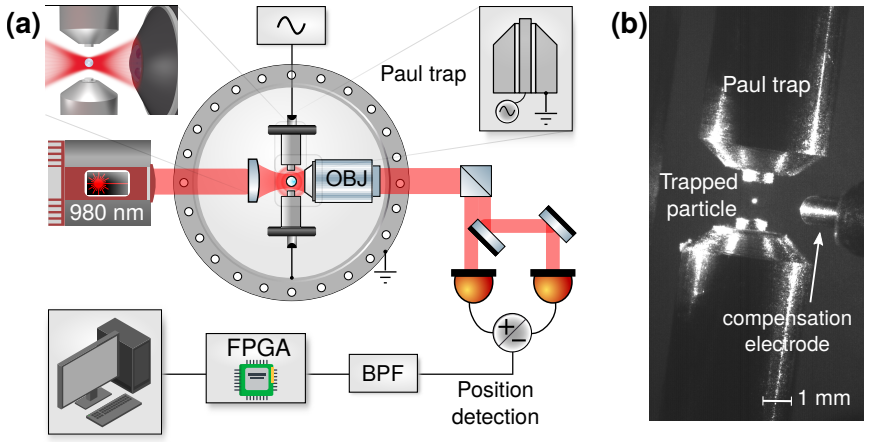

Figure 3.1: **Experimental setup** (a) Setup sketch. A Paul trap, driven by a high voltage sinusoidal signal, levitates a charged nanoparticle that is illuminated from the left with a 980 nm diode laser. The scattered light is collected with an objective (OBJ) and sent to a quadrant photodiode (QPD) to detect the motion. The measured signals are band-pass filtered (BPF) and sent to a Field-Programmable Gate Array (FPGA), where they are further pre-processed and sent to a computer. (b) Picture of the trap inside the vacuum chamber viewed from above, showing the end-cap Paul trap electrodes and one of the compensation electrodes.

The actual duration of this regime depends on the exact physical parameters. By taking values from common nanoparticle experiments [64, 65, 66, 97, 98], we find it should lie in the 10^{-2} s to several seconds range (see Fig. 3.2).

Expression (3.16) is approximately equal to the stationary solution of the OU equation [100]

$$\mathrm{d}x_t = \lambda x_t + \frac{\sigma}{\gamma}\,\mathrm{d}W_t, \tag{3.22}$$

which also describes optically trapped particles in the overdamped regime. Therefore, the covariance of the process $y(t)$ is approximately equal to the covariance of the stationary OU process, found in the previous section:

$$\mathbb{E}\left[y(t)y(u)\right] \approx \frac{\sigma^2}{2\gamma^2\,|\lambda|}e^{\lambda|u-t|}. \tag{3.23}$$

By the Wiener-Khinchin theorem (Annex A.1.2), the approximate power

spectral density (PSD) of $y(t)$ is

$$S_y(\omega) = \int_{-\infty}^{\infty} e^{-i\omega t} \frac{\sigma^2}{2\gamma^2 |\lambda|} e^{\lambda|t|} \, \mathrm{d}t \tag{3.24}$$

$$= \left(\frac{\sigma}{\gamma}\right)^2 \frac{1}{\lambda^2 + \omega^2}. \tag{3.25}$$

We can provide a more detailed argument to this expression by using explicit bounds on the error of the WKB approximation. For simplicity, we assume that $y(0) = \dot{y}(0) = 0$; the following calculation can be easily generalized to the case of arbitrary initial conditions. We define the PSD as

$$S(\omega) = \lim_{T' \to \infty} \frac{1}{T'} \mathbb{E} \left| \int_0^{T'} x(t) e^{-i\omega t} \, \mathrm{d}t \right|^2. \tag{3.26}$$

The expression for the expected value in (3.26), *before* the limit is taken, provides corrections to (3.24), which go to zero as $T' \to \infty$. The calculation relies on the Itô isometry and tedious but elementary integration. Its result is:

$$S_{T'}(\omega) = \frac{\sigma^2}{\gamma^2} \frac{1}{\omega^2 + \lambda^2} \left(1 + \frac{A_{T'}}{T'}\right) \tag{3.27}$$

where

$$\begin{aligned} A_{T'} = &\frac{e^{2\lambda T'} - 1}{2\lambda} - \\ &\frac{2}{\lambda^2 + \omega^2} \left[\lambda \left(e^{\lambda T'} \cos \alpha T' - 1\right) + \omega e^{\lambda T'} \sin \omega T'\right]. \end{aligned} \tag{3.28}$$

It is clear that the correction $\frac{A_{T'}}{T'}$ goes to zero, at the rate $\frac{1}{T'}$ (since the characteristic exponent λ is negative).

From (3.24), we clearly see that our parameter $|\lambda|$ corresponds to the cut-off frequency of the trap [104].

3.3 Experimental methods

3.3.1 Setup

The experimental setup is displayed in Fig. 3.1. We use a rotationally symmetric end-cap Paul trap to levitate charged nanoparticles (silica and polystyrene). It is designed to provide optical access and a linear electric field in a large volume around the trapping region. The Paul trap is made of two assembled steel electrodes separated by 1.4 mm mounted on a ceramic

holder. The oscillating field is created by a high voltage signal (sinusoidal with frequency between 1–30 kHz, amplitude of 0.6–2 kV_{pp}).

The nanoparticles, originally suspended in ethanol, are loaded into the trap with a custom made electrospray at ambient pressure. This ensures that particles are highly charged ($50 < n < 1000$ of net e^+ charges in this study, depending on the particle). The Paul trap is mounted on a piezo stage inside a vacuum chamber, giving access to pressures below ambient conditions. A laser, focused with an aspheric lens with low effective numerical aperture (NA < 0.1), illuminates the particle. Its scattering signal is collected in forward detection with an OBJ (0.8 NA) and directed to a quadrant photodiode (QPD) (see Annex D for details), giving signals proportional to the particle motion in the 3 perpendicular directions $x(t)$ (parallel to trap axis), $y(t)$ (gravity direction) and $z(t)$ (beam propagation). These signals are sent to an FPGA and recorded in a computer.

3.3.2 Details of the numerical simulation

We have developed functions and libraries in C++ to generate sample paths of a vector process (of arbitrary dimension) defined by a stochastic differential equation

$$\mathrm{d}\mathbf{X} = \mathbf{a}(t, \mathbf{X})\,\mathrm{d}t + \mathbf{b}(t, \mathbf{X})\,\mathrm{d}W.$$

The simulation of X_t is performed with a modified Runge-Kutta method for stochastic differential equations [105] (strong order 1, deterministic order 2), detailed at the end Annex A. This particular method does not require any non-zero derivatives of the diffusion term $\mathbf{b}(t, \mathbf{X})$. Other methods (e.g. the Milstein method) have strong order 1 but reduce to the Euler-Maruyama method (strong order 0.5) when $\mathbf{b}(t, \mathbf{X})$ is a constant.

Since the realizations of the process have a certain degree of randomness, each of them will be different and many traces (usually around $n = 1000$) need to be generated to estimate the process statistical moments

$$\mathbb{E}[f(X_t)] \simeq \frac{1}{n} \sum_i f(X_t^i).$$

This is usually quite intensive in terms of processing power and computer memory. For this reason, the main computation is coded in C++, while MATLAB and Python are used for post-processing. The code and libraries can be freely downloaded from https://github.com/gerardpc/sde_simulator.

3.4 Results and discussion

With the code we have simulated the stochastic differential equation to check the validity of the approximate solution (3.16) and the expression (3.24) of the motion's PSD.

We have also measured position traces from a real trapped particle, computed the PSD, and compared the results to the model to calibrate the position signal (i.e., find the factor to convert a signal in volts to meters). Finally, we have studied the dependence of $\sigma_y \triangleq \sqrt{\mathbb{E}[y^2(t)]}$ on the experimental parameters ω_d and $Q \times V$ for long t to ascertain the best regimes for trapping in terms of particle confinement.

The behaviour of $\mathbb{E}[y^2(t)]$ for common nanoparticle experimental parameters is displayed in Fig. 3.2. Subfigures (a) to (d) compare the diffusive regime ($t \ll 1/|\lambda|$) of the process variance to the expression (3.21) for different parameter choices. In all of our numerical experiments $\mathbb{E}[y^2(t)]$ closely follows the $\frac{\sigma^2}{\gamma^2}t$ trend. However, in some of them a small oscillation at ω_d can be seen, which is not present in our model due to the approximations of the WKB method. These realizations of the process start with initial conditions in the origin $x(0) = 0$, $v(0) = 0$, and represent the behaviour we would expect from a cooled nanoparticle (for instance with feedback cooling through the compensation electrodes [106]) after the cooling is turned off at $t = 0$.

Fig. 3.2 (e) and (f) show the long term trend of the position variance ($t > |\lambda|$). The diffusive regime and the asymptotic "equilibrium" value found in (3.20) are marked with red dashed lines, and the simulations are found to follow these closely (the higher the number of averaged traces, the smaller the variance of the simulation and the better the resemblance with the model). We found a surprisingly long thermalization time for the particle motion to reach equilibrium, that we have verified with numerical simulations. Depending on the experimental conditions, it might take seconds (as is the case of Fig. 3.2 (f)) or even tens of seconds for common values extracted from the literature. This is in stark contrast with optical dipole traps. At ambient or low vacuum pressure regimes, a cooled optically trapped nanoparticle reaches equilibrium in the timescale of microseconds. The results indicate that one should be cautious when taking data from a trapped particle on a Paul trap, since the process memory might be longer than expected and the results could still be affected by the initial conditions.

Another interesting finding is that, in this regime, $\mathbb{E}[y^2(t)]$ does not converge to the value expected from the equipartition theorem if one naïvely uses the effective potential approximation for quadrupole traps. For a simple harmonic oscillator, $\mathbb{E}[y^2(t)] = k_\mathrm{B}T/m\Omega^2$ (see Annex D), and using the

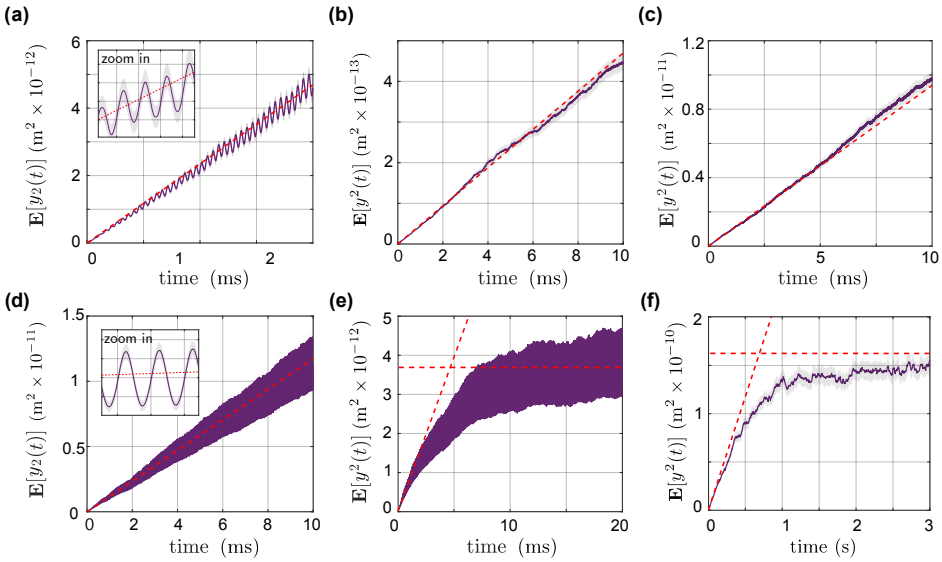

Figure 3.2: **Variance and reheating** Comparison of numerical simulations of the variance (in purple) with the analytical expressions (in red dashed lines) found in the theory section. Sub-figures (a) to (d) show simulations of $\mathbb{E}[y^2(t)]$ (starting from $(x, v) = (0, 0)$ at $t = 0$) for $t \ll 1/|\lambda|$ in a range of typical experimental values, proving the validity of the expressions for common nanoparticle experiments. The insets in (a) and (d) show the oscillatory behaviour of the variance due to the trap driving, along with confidence intervals of ± 1 standard error (these margins can't be seen in some of the figures, due to the oscillations being much larger than the uncertainty). Figures (b) and (c), although similar at first sight, show very different speeds in a reheating experiment. The last two sub-figures, (e) and (f), show simulations of $\mathbb{E}[y^2(t)]$ for $t > 1/|\lambda|$: thermalization around an equilibrium value can be observed. The two figures portray a case where the oscillations dominate (e) and a case where the oscillations are small with respect to the equilibrium value (f). Again, the gray area around the variance (in purple) represents ± 1 standard error. **Simulation details**: $T = 295$ K, Paul trap with $f = 20$ kHz, $V = 1000$ V. (a) Pressure $p = 101$ mbar, particle with $r = 100$ nm, $Q = 100$ e^+. (b) Pressure $p = 1010$ mbar, particle with $r = 500$ nm, $Q = 500$ e^+. (c) As (a) but $p = 1010$ mbar. (d) As (c) but $r = 20$ nm. (e) $r = 100$ nm, $Q = 500$ e^+, $p = 300$ mbar and $V = 2000$ V. (f) As (e) but $p = 1010$ mbar and $V = 1000$ V.

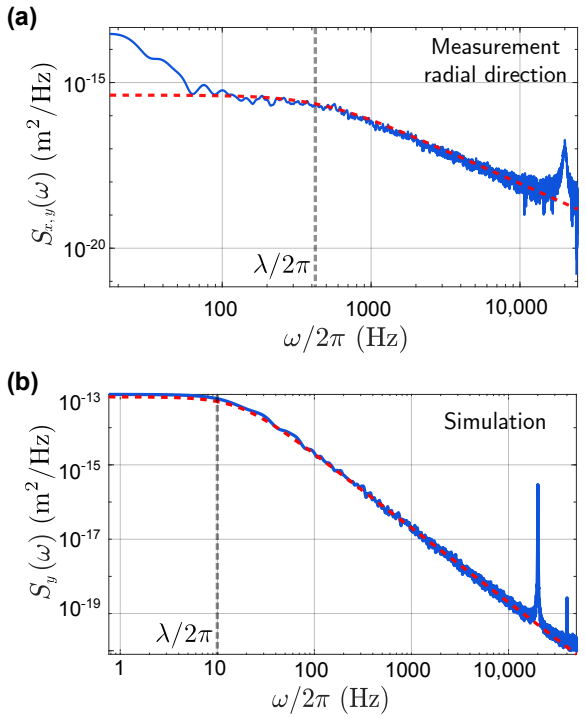

Figure 3.3: **Motion spectral densities** Comparison of measurements and numerical simulations of the power spectral densities (PSD), in blue, with the analytical expressions (in red dashed lines) found in the theory section. (a) Measurement of the PSD $S_{x,y}(\omega)$ in the trap radial directions x, y for a polystyrene particle of 243 nm in diameter (Paul trap with $V = 1000$ V and $f = 20$ kHz, $p = 100$ mbar $\pm 30\%$ gauge uncertainty). A fit of the expression found in (6.8) is superimposed, with amplitude and corner frequency as free parameters. The fitted corner frequency, $\lambda/2\pi \simeq 420$ Hz, is marked with a grey dashed line in the figure. From eq. (3.18) we recover a value of ϵ compatible with the pressure, voltage and frequency of the trap. (b) Simulation of the process with the expression in (6.8) superimposed (dashed red line) but no free parameters (using the values of the simulation: $V = 1000$ V, $f = 20$ kHz, $p = 1010$ mbar, resulting in $\lambda/2\pi \simeq 10$ Hz). Excellent agreement between model and simulation is found except at $\omega = \omega_{\mathrm{d}}$, since the trap driving is suppressed in the Ornstein-Uhlenbeck model.

expression for the secular frequency of a weakly damped Paul trap [107]

$$\Omega = \frac{\omega_\mathrm{d}}{2}\sqrt{\frac{q^2}{2} - \frac{\Gamma^2}{\omega_\mathrm{d}^2}} \tag{3.29}$$

one finds that

$$\mathbb{E}[y^2(t)] = \frac{k_\mathrm{B}T}{m\Omega^2} = \frac{8k_\mathrm{B}T}{m\omega_\mathrm{d}^2\left(q^2 - \frac{2\Gamma^2}{\omega_\mathrm{d}^2}\right)}. \tag{3.30}$$

From Eq. (3.29), we see that the secular approximation breaks down if $2\Gamma^2/\omega_\mathrm{d}^2 > q^2$, as it is typically the case at ambient pressure. However, Eq. (3.20) shows—with the support of numerical simulations—that

$$\mathbb{E}[y^2(t)] \simeq \frac{\sigma^2\gamma}{m\epsilon^2} = \frac{8k_\mathrm{B}T}{mq^2\omega_\mathrm{d}^2}\left(\frac{\Gamma^2}{\omega_\mathrm{d}^2}\right). \tag{3.31}$$

A refined approximation to the variance was given in Ref. [91]:

$$\mathbb{E}[y^2(t)] \simeq \frac{8k_\mathrm{B}T}{mq^2\omega_\mathrm{d}^2}\left(1 + \frac{\Gamma^2}{\omega_\mathrm{d}^2}\right) I_0^2\left[\frac{q}{\sqrt{1 + \frac{\Gamma^2}{\omega_\mathrm{d}^2}}}\right], \tag{3.32}$$

where I_0 is the zeroth order modified Bessel function.

The approximation in (3.31), of course, is not valid for any choice of values in parameter space, since we have used several approximations based on our own experiment. Nonetheless, it is a good approximation for nanoparticles in Paul traps at ambient and similar pressure regimes, as long as the condition $\Gamma \gg \omega_\mathrm{d}$ is fulfilled and the stability criteria of the Mathieu equation are met [91], i.e., q is not too large[4] (in particular, $q \lesssim \sqrt{1 + \Gamma^2/\omega_\mathrm{d}^2}$, since in this case $I_0 \simeq 1$). Eq. 3.32 has a minimum at $q_\mathrm{min} = 1.518\sqrt{1 + \Gamma^2/\omega_\mathrm{d}^2}$, which finds the optimal set of parameters to maximize the confinement:

$$\mathbb{E}[y^2(t)]_\mathrm{min} = \frac{8k_\mathrm{B}T}{m\omega_\mathrm{d}^2}. \tag{3.33}$$

Therefore, we see that our approximation is valid when the parameters of the system are tuned close to the optimal situation. In practice, when a particle is injected into our trap we trap many more particles at once. The one that we keep is the one with—visibly—the smallest motion amplitude.

[4]Note that in this case q, introduced in Chapter 2, may be above 0.9, because the presence of damping displaces the stability region of the Mathieu equation. See Major et al. [12] for reference.

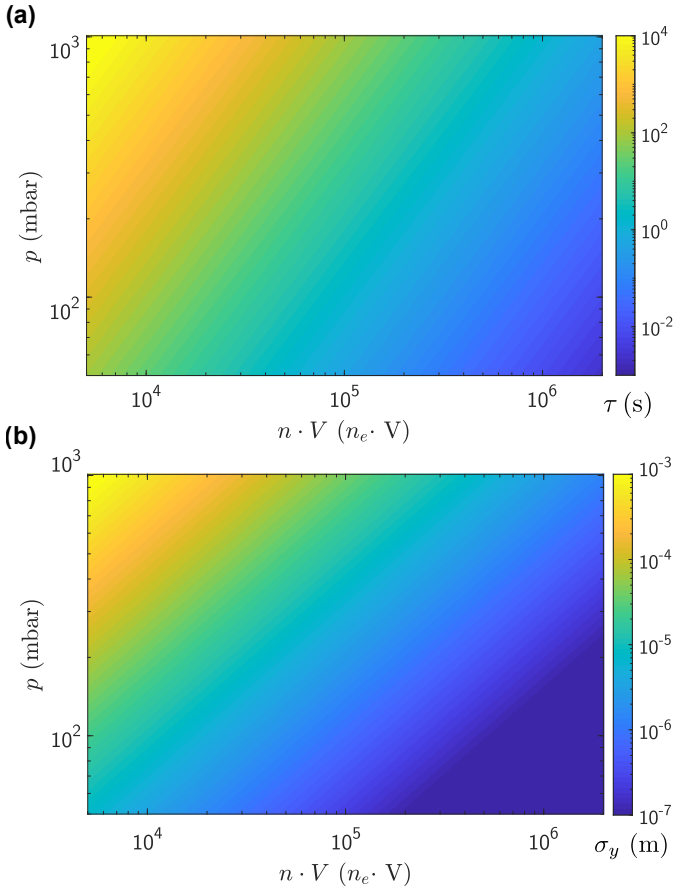

Figure 3.4: $\sqrt{\mathbb{E}[y^2(t)]}$ **in equilibrium** (a) Dependence of the characteristic time to reach equilibrium, $\tau = 1/|\lambda|$, with the pressure p and trap amplitude $Q \cdot V$, for a particle with radius $r = 100$ nm (initial conditions $(x, v) = (0, 0)$). In the plot axis, n_e is the trapped particle's net number of electron charges. (b) Dependence of the confinement $\sigma_y \triangleq \sqrt{\mathbb{E}[y^2(t)]}$ with the pressure p and trap amplitude $Q \cdot V$ after equilibrium has already been reached (i.e., $t \gg \tau$), for a particle with radius $r = 100$ nm. The confinement scales with the mass as $1/\sqrt{m}$, as can be seen from eq. (3.31).

At high pressures there is no secular oscillation: the motion is highly damped and the only observed oscillation is due to the *micromotion* driving at ω_d [65], responsible for the peak at ω_d in Figs. 3.3 (a) and (b). However, as we have seen, the overdamped approximation cannot be straightforwardly applied. This is in stark contrast with optical tweezers: for an optically trapped particle in a regime where viscous forces dominate over inertia (i.e., at low Reynolds numbers), the acceleration term ($m\ddot{y}$) can be neglected. It is assumed that the particle achieves a terminal velocity instantaneously at every new position during its motion [82]. The approximation cannot be performed in Paul traps, where inertia has a key role on the ponderomotive force; this, in turn, is the responsible for the trapping mechanism [108]. Any attempt to neglect inertia would result in a vanishing ponderomotive force, and the inclusion of the noise term in the equation of motion would produce a solution where the particle diffuses away from the trap center (see Approximate solution). Instead, the solution we present here, based on eq. (6.8), represents a situation similar to the overdamped optical trap, whose PSD of the position is characterized by a cut-off frequency $\omega_k = k/\gamma$, where k is the stiffness of the trap [104]. In our description, the cut-off frequency is given by the parameter $|\lambda|$, so that the effective stiffness of the damped Paul trap is given by:

$$k = \frac{m\epsilon^2}{2\gamma^2} = \frac{Q^2V^2}{2md^4\Gamma^2}, \tag{3.34}$$

where the first equality clarifies the key effect of the mass on the trapping mechanism, i.e., a massless particle experiences zero restoring or ponderomotive force.

Figs. 3.3 (a) and (b) show the motion PSD of the process (in blue) compared with the OU model (eq. (6.8), red-dotted line) on a log–log scale. Subfigure (g) presents an actual measurement of a trapped particle, showing a corner frequency around 400 Hz, after which the spectrum decays as $1/\omega^2$. The red line is a fit to eq. (6.8), which can be used to calibrate the particle's motion at ambient pressure. Experimentally, careful consideration is required on how this measurement is performed. The common detection technique, also adopted in this work, consists in focusing a laser on the particle and collecting the scattering light. This induces an optical force which can noticeably modify the dynamics. In our experiment, we have resorted to an extremely low effective NA to minimize the effect of the dipole potential. In Fig. 3.3 (b), a simulation of the process is compared to the model without any free parameters. The agreement is excellent except for the micromotion peak at ω_d, which is averaged out in the model (as is expected when using an OU model). The peak's energy is however a

negligible contribution to the total $\mathbb{E}[y^2(t)]$ and, hence, the PSD expression can be safely used for calibration.

Fig. 3.4 displays the dependence of σ_y and the thermalization characteristic time with the parameters that are accessible in the laboratory, namely pressure and voltage. The functional dependence was introduced in equations (3.18) and (3.31), and a relevant absence in those expressions is the trap frequency: at the 50 mbar to 1010 mbar pressure regime we find that ω_d has a negligible effect in the particle confinement. At the same time, σ_y is approximately proportional to the pressure.

3.5 Conclusions

In conclusion, we have solved the general stochastic differential equation of a nanoparticle in a Paul trap, found a calibration method for the motion PSD of a levitated nanoparticle at ambient/low vacuum pressures, and applied it to a real experiment. The PSD expression has been obtained by computing an alternative (approximate) solution to the equation of motion with the WKB method. With it, we have proved that $y(t)$ resembles an OU process at pressures close to ambient conditions, and studied $\langle y^2(t)\rangle$ for short and long times.

We have complemented our theory results with thorough numerical experiments that validate the derived analytical expressions. We have also used our code to study the dependence of the particle confinement with the Paul trap parameters.

Our findings caution against naïvely assuming that the effective potential model can be applied to any set of experimental parameters. Also, as we have found out, particles may equilibrate to the thermal bath very slowly; assuming that they thermalize faster than measurement time without the proper checks might lead to wrong conclusions.

If these two points are under control, the next step for any levitation experiment is the calibration of the particle's motion, and the results of this chapter provide a novel method to do so for particles in Paul traps. Our results can also be readily applied to estimate and optimize the particle confinement, which would be especially relevant in experiments that crucially depend on the particles' signal collection.

4

Hybrid trapping regimes

The levitation of particles in vacuum allows the study of the physical properties of extremely isolated objects. In this chapter, we study a hybrid nanoparticle trap by combining a Paul trap with a weak but highly focused optical beam. We investigate the dynamics of trapped particles in the combined potential, and assess the suitability of the trap as a platform to levitate particle species that would otherwise suffer from heat photo-damage.

4.1 Introduction

One of the major drivers of modern research is the possibility to transform laboratory experiments into technology that can be used by society. In physics, the development of novel applications starts by understanding the fundamental properties and components of the system under consideration. Its investigation requires good isolation from external elements and good spatial localization. This poses a challenge for microscopic devices, because they are commonly studied in a substrate and the system's signal and properties are strongly influenced by the environment [109]. Moreover, when the object is small, measuring a signal may become challenging due to the presence of neighbouring noise sources. To overcome these difficulties, the use of particle traps, that levitate objects in isolation, has become common practice in different fields [49, 110, 111, 112].

The trapping of micro- and nanoparticles can be achieved by different means. Paul or radio-frequency (RF) traps use a combination of AC and

DC electric fields for the confinement of charged particles [75]. Their use for the study of micro and nanoparticles is nowadays widespread [95, 96, 98, 112, 113, 114, 115]. For instance, there is a large field devoted to the study of the optical properties of atmospheric aerosols—and of liquid droplets in particular [93, 94]. Another possibility is the use of optical tweezers—or, more generally, optical dipole traps—, that can trap dielectric particles near the maximum of a light intensity distribution, like the focus of a strongly focused laser beam [21, 26, 116]. Although mostly used to trap dielectric microparticles suspended in a liquid [29], optical tweezers also allow the levitation of micro and nanoparticles in air or vacuum [54, 61]. Both techniques also allow the precise optical detection of the motion of the trapped particles, a central concern in the emerging field of levitation optomechanics [48].

Nevertheless, to study micro- and nanoobjects that interact with light very strongly, such as highly absorbing materials or particles with internal degrees of freedom, these two trapping techniques suffer from serious drawbacks. Optical tweezers, on the one hand, require high intensities to trap, with typical powers of $\sim$ 100 mW in levitodynamics experiments. Such powers induce heat to even low absorbing materials [60], which can lead to high bulk temperatures and particle photo-damage already at pressures of a few tens of millibars [62]. Thus, although they remain the best option to interact with the particle's degrees of freedom and control its dynamics, they cannot be used at low pressures with most object materials, and unfortunately this is the most interesting regime for fundamental studies. On the other hand, Paul traps have low particle confinement [65], and although they do not induce heat to the trapped particles, they offer modest detection signals and interaction strength to interrogate the levitated object. Hybrid traps, which combine two types of fields, present a possible workaround and have already demonstrated their flexibility with magneto-gravitational traps, combining magnetic and gravitational fields [117, 118, 119], and in a Paul trap in combination with a Fabry-Perot cavity [66, 120].

In this chapter, we describe our implementation and characterization of a hybrid nanoparticle trap that combines a Paul trap with a weak but highly focused optical beam. We demonstrate that this system is versatile both for levitating and optically interrogating particles, especially those that suffer from optical absorption. In particular, we have validated the system with gold nanoparticles, nanodiamonds and crystals hosting rare earth ions. We have also studied numerically and experimentally the particle dynamics in terms of its position distribution in equilibrium, which we have used to reconstruct the trapping potential.

4.2 Experimental setup and methods

The experimental setup is displayed in Fig. 4.1. The end-cap Paul trap is designed to provide optical access and a linear electric field in a large volume around the trapping region. It allows the levitation of charged nanoparticles of various different materials, and we have experimented with silica, gold, diamond and Er+ doped crystals. The Paul trap (driven by a signal of frequency between 1 kHz – 30 kHz, and an amplitude of 0.6 kV_{pp} – 2 kV_{pp}) is mounted on a piezo stage inside the vacuum chamber, giving access to pressures down to 10^{-6} mbar.

The nanoparticles are prepared in ethanol suspensions and then loaded into the trap with a custom made electrospray at ambient pressure. The electrospray ensures that particles are highly charged ($50 < n < 1000$ of net e^+ charges in this study, depending on the particle). To detect the presence of trapped particles during the particle loading process, we use a weakly focused 980 nm diode laser that illuminates the trapping volume (focus spot $> 10\mu$m). Once a single particle is on the trap, a 532 nm laser is turned on, adding the optical potential to the hybrid trap. The scattered 532 nm light is collected and directed to a quadrant photodiode, returning electric signals that are proportional to the particle motion in the 3 perpendicular directions $x(t)$ (parallel to trap axis), $y(t)$ (gravity direction) and $z(t)$ (beam propagation). These signals are sent to an FPGA and recorded in a computer. Additionally, if the particle has internal transitions or interacts strongly with the 532 nm laser light (e.g. highly absorbing materials like our gold nanorods), the fluorescence can also be collected and sent to a light-tight box. There, we can measure it with a fluorescence camera or a spectrometer.

When a particle is in levitation, stray DC fields may push it away from the center of the Paul trap. The most common protocol to cancel these fields consists on creating an opposite DC voltage with the compensation electrodes, by checking that excess micromotion—a forced oscillation at the trap driving frequency that can be seen as a peak in the motion's power spectral density (PSD)—is minimized. However, by adding a DC electric field with the electrodes, a particle at the center of the optical trap will move away from the focus. In other words, cancelling stray DC fields *and* pushing the particle away from the focus have the same effect in detection: one cannot say if a reduction in the micromotion peak is due to the particle moving away from the detection beam or due to a proper compensation of the DC fields. To decouple these two effects, we have chosen to detect and move the particle with the same system: a $4f$ pair of lenses. Once the particle is trapped with the 532 nm laser, a $4f$ system can adjust the angle at which the laser beam enters the back of the trapping objective.

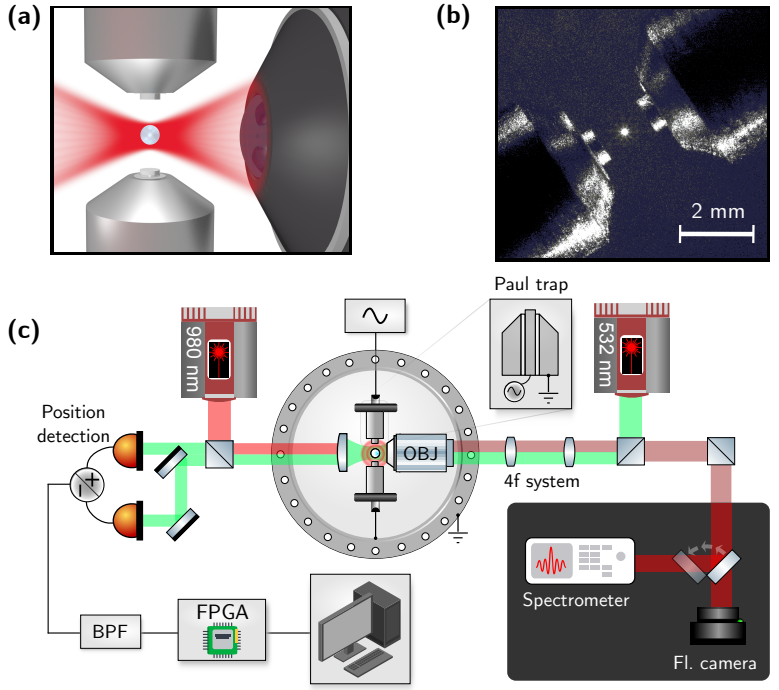

Figure 4.1: **Experimental setup** (a) Artistic representation of the hybrid trapping scheme. A charged nanoparticle sits at the minimum of the combined effective potential. The Paul trap end-cap concept allows for good optical access to the particle's signal. (b) Photo of the trap inside the vacuum chamber viewed from above, showing a levitated particle in the hybrid trap. (c) Setup sketch. A Paul trap, driven by a high voltage sinusoidal signal, levitates a charged nanoparticle. The particle is illuminated from the left with a weakly focused 980 nm diode laser to facilitate the loading process. Once the particle is in the trap, a 532 nm laser is turned on, adding the optical potential to the hybrid trap. The scattered light is collected with a 0.8 numerical aperture objective (OBJ) and sent to a quadrant photodiode (QPD) to detect the particle's motion. The measured signals are band-pass filtered (BPF) and sent to an FPGA, where they are further pre-processed and sent to a computer. The 532 nm laser can also excite internal transitions, in which case the collected fluorescence is sent to a light-tight box and measured with a fluorescence camera or a spectrometer.

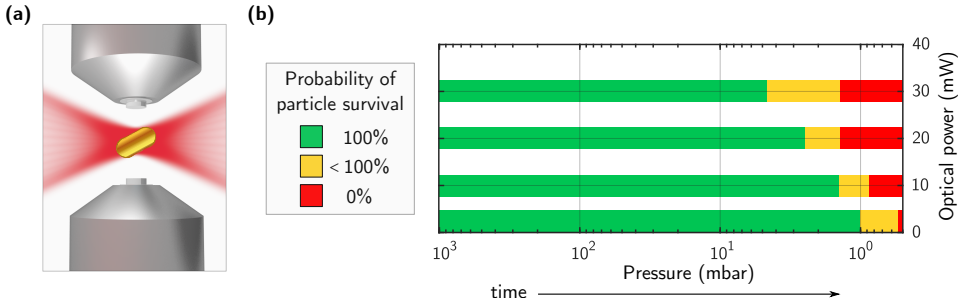

Figure 4.2: **Probability of survival of gold nanorods** (a) Sketch of a nanorod (33 nm × 63 nm in the trap. The particle can be illuminated with 532 nm or 1064 nm laser light. (b) Experimental probability of survival of a levitated gold nanorod at the focus of the hybrid trap when the pressure is progressively reduced (using 532 nm light). Green color marks that all particles achieved said pressure, yellow marks the survival of some (but not all) of the trapped particles, and red that no particle could be brought to that pressure. Most of the gold nanoparticles are lost around 1 mbar. We repeated the experiment with 1064 nm light, obtaining similar results.

At the same time, we keep the particle at the optimal position for motion detection.

4.3 Results and analysis

We have tested the hybrid trap with metallic particles, which by definition suffer from high optical absorption and hence heating. This scenario is portrayed in Fig. 4.2 (a). Gold nanorods of 33 nm × 63 nm were loaded into the trap at ambient pressure, and later on brought to vacuum to assess its survival and stability at low heat dissipation conditions. As can be seen in Fig. 4.2 (b), the particles could be safely maintained in the trap down to 10 mbar. Below this pressure, and depending on the power of the optical trap, the probability that the nanorods would disappear increased dramatically. At $\sim$ 1 mbar most of the studied particles vanished, except for low optical powers. In this last case, it was not possible to maintain a stably trapped particle, which hopped in and out of the focus intermittently and thus received a considerably lower average power. We also observed that, when the particles disappeared from the trap, the event happened rather suddenly, without clear prior changes in particle brightness. We speculate that this is due to the evaporation of the outer layer of the gold particle, which leads to a sudden change in charge to mass ratio and the ensuing particle ejection.

The CoM Langevin equation of motion of a particle in a hybrid trap can be obtained with Newton's 2nd law:

$$m\ddot{x} + m\Gamma\dot{x} - \frac{QV}{d^2}\cos\omega_{\mathrm{d}}t \cdot x + \alpha\frac{1}{2}\nabla|\mathbf{E}|^2 = \sigma\eta(t). \tag{4.1}$$

Here, $x(t)$ is the CoM motion, m is the particle mass [101] and Γ is the damping due to the interaction with residual gas molecules. From the Paul trap, ω_{d} is the trap driving frequency, Q is the particle charge, V the trap voltage and d is the characteristic size of the Paul trap. Regarding the optical trap, α is the particle polarizability and $\mathbf{E} \triangleq \mathbf{E}(x, y, z)$ is the optical field, which we approximate as a focused Gaussian Beam (see Supplemental material) to perform numerical simulations. Finally, $\sigma\eta(t)$ is a stochastic force, with $\eta(t)$ being a unit intensity Gaussian white noise and $\sigma = \sqrt{2k_{\mathrm{B}}T\gamma}$ [102].

In equation (4.1) we have not consider gravity, which is small compared to the electric force (from the Paul trap) and the gradient force (from the optical tweezers field), nor the scattering force, that can be neglected for tightly focused beams (as is our case). We have included a stochastic force to account for the thermal coupling with the environment. Since both relevant deterministic forces are gradients, the total potential will be the addition of the two individual trap potentials. However, note that by working with low optical powers, the levitated particle explores large regions of the optical trap and the dipole force cannot be approximated as a linear restoring force, as is common practice in optical tweezers experiments. The Paul trap potential, being much larger, can still be safely approximated as a quadratic (time-varying) potential.

If we consider the adiabatic approximation for the Paul trap (i.e., we approximate the time-varying potential by an effective constant potential) [86], then, at equilibrium, $x(t)$ will follow the Gibbs probability density function

$$\rho_\infty(x) = \frac{1}{Z}\exp(-\beta\Psi(x)), \tag{4.2}$$

where Z is a normalizing factor, $\beta = 1/k_{\mathrm{B}}T$, and $\Psi(x)$ is the combined hybrid potential. Hence, by estimating $\rho_\infty(x)$ and inverting Eq. (4.2), we can recover the trap potential.

This process is shown in Fig. 4.3 with simulated time traces. Here, we have studied theoretically the effects of a decrease in the optical field's intensity. The simulations reveal that when the laser power is below 8 mW, the position histograms start to deviate noticeably from a normal distribution. This is due to a reduced particle confinement, that lets the particle explore the nonlinearities away from the optical trap center. Eventually, at sufficiently low powers, the particle starts leaving and re-entering the beam focus.

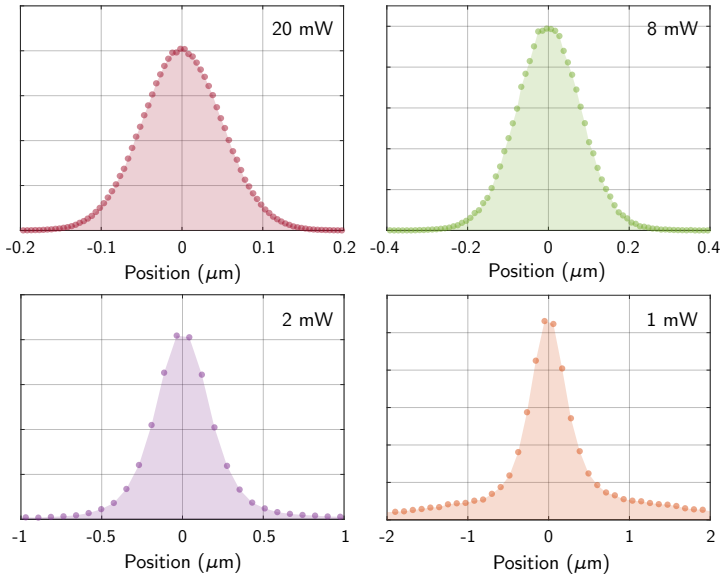

Figure 4.3: **Surge of nonlinearities at low intensities**. The plots shows numerical simulations of the position density distribution $\rho_\infty(x)$ of 100 nm dielectric nanoparticles (no absorption considered) for decreasing optical powers in the hybrid trap ($\lambda = 1064$ nm). Below 20 mW, a reduction in the laser power brings about position distributions that deviate more and more from a normal distribution (quadratic potential case, exemplified with the upper left plot). At 1 mW, the particle leaves and re-enters the beam focus intermittently, resulting in long tails in $\rho_\infty(x)$.

We observe a similar behaviour in the laboratory. Starting at a "high" intensity state (e.g., 20 mW of 532 nm laser light), a progressive reduction of the power will lead after some time to a blinking of the particle, which we interpret as the particle hopping in and out of the optical trap. Experimentally, the blinking starts at higher powers than in the simulations. However, this is to be expected, since when the particle is not perfectly centred in the Paul trap, the RF driving may push it away from the focus before than in would happen in the more ideal simulated case.

The potential reconstruction from real trapped dielectric particles is shown in Fig. 4.4, plotting the profiles obtained at different powers. The potential has the shape of a *dimple* trap [121], consisting of a large, flatter trapping volume (due to the Paul trap), superimposed to a tighter optical dipole trap, as represented in Fig. 4.4 (b).

In these time traces, we have filtered out the contribution of the driving AC field, which is never completely eliminated through field compensation

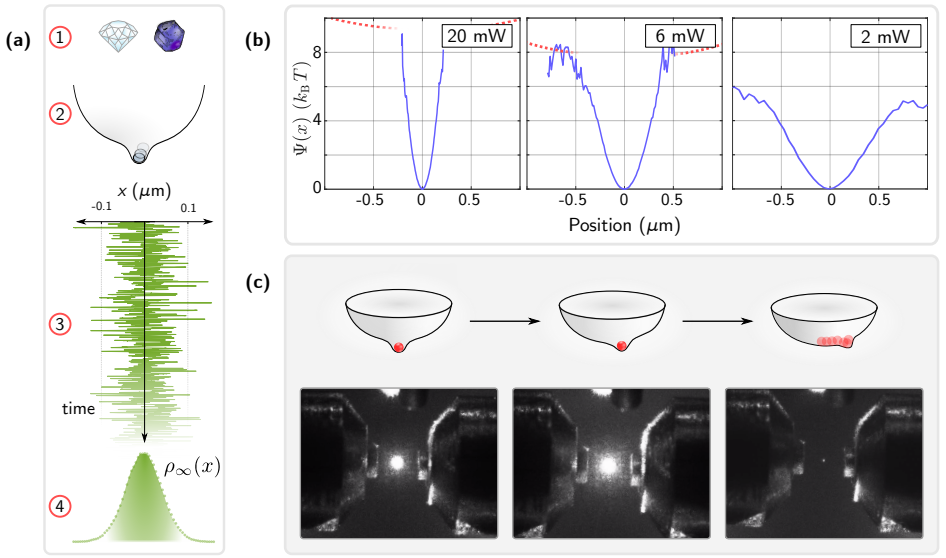

Figure 4.4: **Potential reconstruction** (a) Process of potential reconstruction. A dielectric particle (1) oscillates in the hybrid potential (2). A time trace $x(t)$ of the trapped particle is measured for a few seconds (3). From the time trace, we compute an histogram of the position (4) to estimate the Gibbs probability density function $\rho_\infty(x)$ (see Eq. (4.2)). From this density function, we may obtain $\Psi(x) = \frac{-1}{\beta} \ln(Z\rho_\infty(x))$ (b) Reconstructed trap potentials for three different powers of 532 nm laser light (blue line). The dashed red lines are only a guide to the eye for the Paul trap section of the combined potential. (c) Photographs (accompanied by sketch pictures) of the effect of a displacement between the optical and electric quadrupole field. If this displacement is small, a particle in the potential minimum (i.e., at the focus of the beam) will follow the intensity maximum. However, if the displacement is increased further, the Paul trap eventually pushes the particle back to its center and the particle's brightness decreases suddenly. The photographs portray the Paul trap moving towards the incoming beam. In this case, the maximum of the particle brightness takes place when the Paul trap and the optical trap are slightly misaligned, and the Paul trap exactly compensates the optical scattering force.

and perturbs the results. The presence of non-linearities in the detection system (i.e., in the correspondence between detected signal and position) also poses a problem for such potential reconstructions. To correct for this, in our experiment we have eliminated fractions of the recorded time traces in which it is clear that the particle is away from the trap centre, and have inverted the remaining data with the expression found in Gittes et al. [122].

4.4 Conclusions

In conclusion, we have built a hybrid nanoparticle trap by combining a Paul trap with a weak but highly focused optical beam, and we have proved its suitability as an experimental platform to trap particle species with large optical responses [98, 123, 124].

We have put our platform to the test with gold, diamond and Erbium doped nanoparticles, trapping them and detecting its signal at optical powers below 10 mW, which are low when compared to typical optical tweezers powers ($\sim$ 100 mW). We have also verified that the hybrid scheme easily allows a reduction of the vacuum pressure, even below $\sim$ 10 mbar with gold nanorods. This contrasts with previous optical levitation experiments in vacuum, where due to optical absorption of the trapped particles [60, 125], the range of materials was limited to just a few options. Moreover, we notice that there is still scope to reduce the heating, since in most experiments the presence of the optical field is only required to perform short measurements. To keep the particles in levitation the Paul trap suffices, allowing for arbitrarily long levitation times.

We have also used the measured position traces to reconstruct the effective potential with the Boltzmann–Gibbs distribution, and compared the results to numerical simulations of the stochastic equation of motion. As is intuitively expected, the trap potential has a dip in the middle, due to the optical field. Such calculations are a possible way to measure the nonlinear terms of the optical intensity series expansion, which may be of utility when trying to engineer specific trap potentials.

In the last decade, the study of levitated nanoparticles [48] has experienced a large growth. In the coming years, the field will need to adapt to regimes where other schemes find difficulties, and a particularly promising direction is the study of isolated particles that strongly interact with light, such as metals [126] or particles with internal degrees of freedom [98, 124]. Prime examples of these are diamonds with color centers, quantum dots or crystals hosting rare earth ions. Due to its versatility, the studied hybrid platform is ideally suited to investigate such small objects, which live in a domain that is mostly classical but, still, not completely free of quantum

effects.

5

Trapping and interrogation of a single NV in vacuum

Inefficient heat dissipation of optically trapped particles in vacuum is a challenge for levitation experiments aiming to study quantum physics. Most nanoobjects, even with low absorbing materials, experience photo-damage in optical traps. In this chapter we present our results of levitation in vacuum and CoM feedback cooling of a nanodiamond hosting a single nitrogen vacancy center, using a Paul trap to avoid heating issues. The feedback motion control enables us to optically interrogate and characterize the emitter response. The developed platform is applicable to a wide range of other nanoobjects and represents a promising step towards coupling internal and external degrees of freedom.
The contents of this chapter are based on Ref. [98], article published in Nano letters.

5.1 Introduction

Optomechanics offers a toolbox to investigate classical and quantum mechanical oscillators in a highly controlled way. Nevertheless, the controlled generation of arbitrary superpositions of motional states [127], which would be of high interest to both fundamental physics and quantum technology, still remains in the future due to its very demanding technical requirements. An exciting route towards these ends is the use of nanoscale mechanical resonators containing internal degrees of freedom [128, 129, 130], whose energy

levels can be coupled to the motion of the oscillator. This scheme would allow state transfer or cooling and outperform classical resonators, for instance as ultra-precise sensors [128].

In this regard, nanomechanical resonators based on nanoparticles levitated in vacuum are especially attractive, because they are highly decoupled from the environment due to the absence of clamping, and hence exhibit very large $\mathcal{Q}$-factors, even at moderate pressures. In optical traps, optical forces can be used to efficiently cool the nanoparticle center of mass (CoM) motion and thus reduce the influence of thermal noise [55, 70]. Nevertheless, one could add even further functionality and control to the platform by levitating nanoobjects with tailored specific properties. For instance, levitated particles with internal degrees of freedom (DOF), such as controllable spin systems, have the potential to be used in matter-wave interferometry [131, 132, 133].

However, the optical levitation of nanoparticles with internal DOF faces some challenges [62, 134]: on the one hand, large optical trapping powers introduce a big constraint on the type of particles that can be levitated in vacuum, since heat from residual absorption of the trapping laser cannot be efficiently dissipated at low pressures. On the other hand, high vacuum levels are necessary for maintaining motion coherence and attaining large $\mathcal{Q}$-factors. Hence, to avoid photo-damage, other methods to levitate particles with internal DOF are needed.

An alternative approach to optical trapping is the use of Paul traps [75], which have been widely applied to manipulate individual ions. The main appeal of Paul traps is the possibility to levitate charged particles without the aid of optical fields [64, 65, 66], thereby widening the range of their constitutive materials. Paul traps are thus well suited for the levitation of particles with optical defects, like nanodiamonds hosting nitrogen vacancy (NV) centers. NV centers are optical emitters formed by a nitrogen impurity and a vacancy in the crystal lattice of diamond [135]. NV centers are attractive because they are a stable source of single photons even at room-temperature, whose electron spin can be optically addressed and possesses long coherence times [136]. They have already been successfully used as a qubit [137, 138, 139] and are excellent candidates for sensing electric and magnetic fields by either using Stark or Zeeman shifts [140, 141, 142]. So far, Paul traps have been used to trap and optically interrogate small nanodiamond clusters at ambient pressures [63] and larger microdiamonds [97] hosting multiple NV centers. Nevertheless, levitation and detection of a single NV center in vacuum, in a strongly underdamped regime of the nanoparticle's oscillation, has not yet been achieved, requiring a further level of control on the particle dynamics compatible with single photon optical detection.

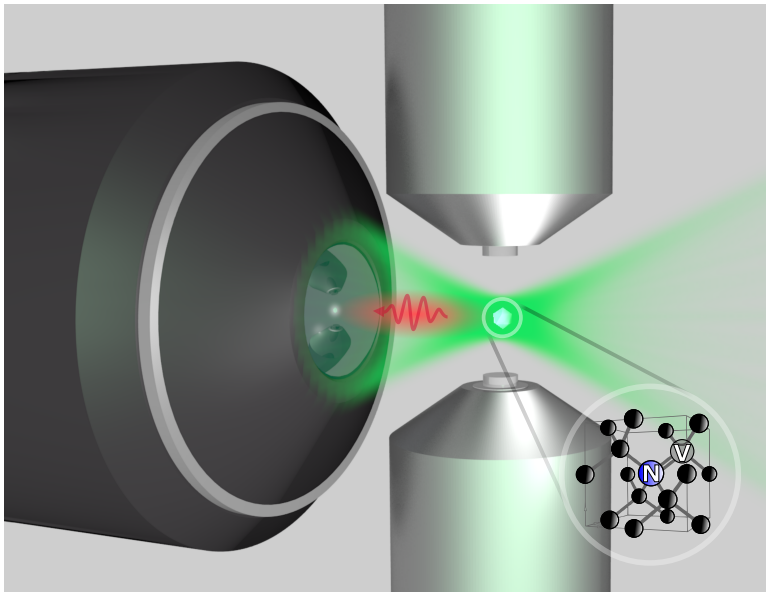

Figure 5.1: **Experiment sketch**: artistic representation of the trapping scheme. A charged nanodiamond containing a single NV center sits at the minimum of the effective potential of a Paul trap. The nanodiamond is illuminated with a continuous wave 532 nm laser with a high numerical aperture objective (OBJ) lens. The fluorescence emitted by the NV center is collected using the same OBJ. The simplified atomic structure of the NV center is also shown.

In this chapter, we detail our efforts towards coupling internal DOFs with the oscillator's CoM motion, by achieving two key experimental requirements. Firstly, we demonstrate levitation in high vacuum of a nanodiamond hosting a single NV center. By trapping with a Paul trap, we avoid particle photo-damage, and with low optical intensity are able to measure the NV single photon emission and monitor the nanodiamond's CoM motion (see Figure 5.1). Secondly, we implement a feedback scheme to reduce the effective temperature of its CoM motion (see Annex D), thus improving the particle's stability and confinement at low pressures.

5.2 The NV center

The nitrogen vacancy center, or NV^- center, is a type of point defect in the diamond lattice, consisting of a substitutional nitrogen atom adjacent to a carbon vacancy (see Figure 5.2 (a)). It is the most studied and well understood of the diamond color defects, particularly regarding its electronic energy level structure. In an NV^- the transition from the ground state to

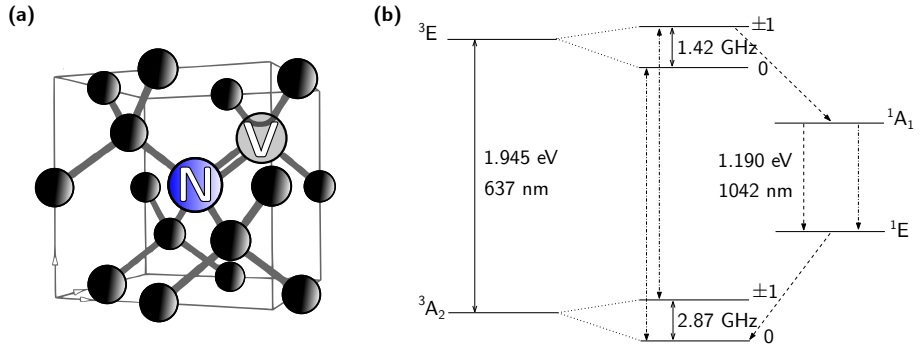

Figure 5.2: **Structure of the NV center** (a) Simplified atomic structure of the NV center. (b) Schematic energy level structure of the NV^- center, showing electron transitions and hyperfine splitting of the ground state. Values obtained from [144].

the excited state can be non-resonantly excited with a green laser, since the zero phonon line (ZPL) (consisting of $\sim 5\%$ of the total fluorescence emission at room temperature) stands at 637 nm. A schematic energy level structure of the NV^- is portrayed in Fig. 5.2 (b).

The NV center is a very convenient defect to work with in levitodynamics, since its electronic spin can be read-out and manipulated optically, vastly facilitating the realization of quantum physics experiments or of other applications in quantum information processing. This happens because the ground state of the NV^-, a triplet, has a single zero-field splitting of 2.87 GHz due to spin-spin interaction ($\pm 1 \rightarrow 0$), and the different hyperfine levels also have different luminescences depending on the spin orientation. Thus, since optical transitions must preserve the total spin, the electron spin can be measured by just monitoring the fluorescence intensity, making it easy to detect, for instance, Rabi oscillations [143].

The degeneracy between the $m_s = \pm 1$ states can be broken under the influence of a magnetic field due to the Zeeman effect, which to first order is

$$\Delta E = m_s g \mu_B B, \tag{5.1}$$

where g is the anomalous gyromagnetic ratio and μ_B the Bohr magneton. This expression suggests a way in which a magnetic field can couple the spin and a mechanical degree of freedom, such as a translational or a rotational variable, of a levitated diamond hosting a NV. The first step towards single spin quantum levitodynamics experiments is the detection of a levitated single NV in vacuum, to which we dedicate the rest of the chapter.

5.3 Trapped particle dynamics

The CoM equation of motion of a particle levitated in a revolution symmetry Paul trap can be found by calculating the force experienced by a charged particle in the Paul trap time-dependent electric potential [75]:

$$\Phi = \frac{V_0 \cos \omega t}{2d^2}(2z^2 - r^2). \tag{5.2}$$

where V_0 is the voltage amplitude, ω the driving frequency, t the time variable, d a geometric constant with length units and z, r are cylindrical coordinates. Even though the particle's CoM Hamiltonian $H(t)$ is explicitly time-dependent, under certain general conditions the motion can be averaged over the high frequency ω [12]. This is known as the adiabatic approximation and ensures that the particle is governed by an effective potential $U_{\text{eff}} = \frac{1}{2}\Omega_i^2 x_i^2$ for every axis x_i, where Ω_i is known as the secular frequency of the i-th axis; more details can be found in Chapter 2.

Therefore, for low frequencies the full equation of motion for the particle's CoM along the z axis can be simplified in the following way

$$\mathrm{d}p_z + \gamma \mathrm{d}z - \frac{2qV_0}{d^2}\cos(\omega t) z \mathrm{d}t = \sigma \mathrm{d}W_t \quad \rightarrow \quad \mathrm{d}p_z + \gamma \mathrm{d}z + k_{\text{eff}} z = \sigma \mathrm{d}W_t\,, \tag{5.3}$$

where p_z is the momentum in the z direction, γ the damping constant, q the charge of the particle, $k_{\text{eff}} = m\Omega_i^2$ the restoring force of the effective potential and $\sigma \mathrm{d}W_t$ a stochastic force with standard deviation σ, associated with the damping via the fluctuation-dissipation relation $\sigma = \sqrt{2k_{\text{B}}T\gamma}$, where k_{B} is Boltzmann's constant and T is temperature [102]. By reducing the pressure and hence γ, the motion decoherence is reduced, while the inversely proportional $\mathcal{Q}$-factor of the oscillator increases. This is why a trapping scheme capable of bringing particles to low pressures is appealing.

5.4 Experimental methods

5.4.1 Paul trap

Our trap design (see Figure 5.3b) has an endcap geometry for good optical access. It is made of two assembled steel electrodes separated by 1.4 mm mounted on a ceramic holder; the design specifics can be found in Chapter 2. These electrodes are mounted on a three axis piezoelectric stage (Figure 5.3a) and driven by a high voltage signal generated by a Field-Programmable Gate Array (FPGA) card and a high voltage amplifier (Matsusada AMT-1B60). The FPGA acts as a wave generator, and provides

a sinusoidal output at adjustable frequency and amplitude. Usual working parameters in our experiment are driving frequency $\omega/2\pi = 20$ kHz and amplitude V_0 in the range of 0.75 $\mathrm{kV_{pp}}$ to 2 $\mathrm{kV_{pp}}$. Two extra rods pointing towards the center of the trap act as compensation electrodes and are used to eliminate stray fields—thus minimizing residual micromotion driving.

5.4.2 Particle dispersion and electrospray

We have used a custom made electrospray to load particles into the trap at ambient pressure. The particles were injected with the electrospray by activating a 3 kV voltage source and then pumping the dispersion. A few milliseconds after, they would pass through the center of the trap potential, and a few of them would lose enough energy (due to air damping) to stay trapped in the potential. In fact, it was usual to trap several at once. Excess particles were pushed out of the trap by carefully reducing the voltage and, after only a single particle remained, the electrospray was removed and the vacuum chamber closed.

The charge of the trapped particles can be estimated by assuming the particle's mass, a reasonable assumption given the fact that we filtered the particles by size with a porous filter. As we have seen, in the underdamped regime (i.e., low damping by air molecules), the equation of motion for the center of mass (CoM) of the particle is described by the Mathieu [12] equation,

$$\ddot{u}(\tau) - 2q \cdot \cos(2\tau)u(\tau) = 0, \tag{5.4}$$

where

$$q \triangleq \frac{2QV}{md^2\omega^2}. \tag{5.5}$$

Here, Q is the particle charge (not to be confused with the $\mathcal{Q}$-factor), V the voltage, m the particle mass, d a geometrical parameter (which is constant and can be calculated for a given trap) and ω the driving angular frequency. Since we set the voltage and frequency, the only unknown parameter is Q. Thus, if the parameter q can be measured, we can solve equation (5.4) for Q and find the particle charge.

This parameter q can be found indirectly. Firstly, we measure the ratio between the particle secular frequency Ω and the driving frequency, $\beta = 2\frac{\Omega}{\omega}$. β is a characteristic exponent of the Mathieu's equation, and is a function of q only: $\beta(q)$. Therefore, by numerically inverting the expression $\beta(q)$ we get $q(\beta)$. Finally, by plugging the obtained value and calculating

$$Q = \frac{q(\beta)md^2\omega^2}{2V} \tag{5.6}$$

we can estimate the particle charge. Usual elementary charge numbers that we have measured this way lay in the range of 40 to 150 e^+.

The particles consisted of nanodiamonds that we bought from Adámas Nanotechnologies (40 nm in diameter, 1–4 NV), and were suspended in ethanol in a ratio of 20 μl of the commercial dispersion for every 40 ml of ethanol. To avoid particle clustering, we utilised a syringe filter with 100 nm pore size and sonicated the dispersion for 10 minutes before the experiment.

After the spraying, trapping events were monitored with a CMOS camera, using the scattering from a weakly focused 980 nm laser (Figure 5.3b). The Paul trap can be subsequently moved with the piezoelectric stages to bring the particle into the focus of a high numerical aperture (NA) microscope objective (OBJ) (Olympus LMPLFLN 100x). The OBJ is used to illuminate the nanodiamond with a 532 nm laser, thus exciting the NV transition, and also to collect the emitted fluorescence. The fluorescence light is then directed towards a light-proof box, where it is selectively analysed with an electron multiplying camera (EMCCD) (Andor iXon+ EMCCD), a spectrometer (Acton Spectrapro 2500i), or coupled into low dark-counts single photon avalanche photodiodes (APDs) (Perkin Elmer SPCM-AQR-14). When the APDs where used, single photon counting was performed with a PicoHarp 300 system. Due to the low intensity of the two laser beams, we did not detect any effect of the dipole force on the particle dynamics in the Paul trap.

5.4.3 Fluorescence detection

After trapping, we characterized the fluorescence emission of the loaded nanodiamonds at ambient pressure. For a given particle, we first collect the fluorescence with the OBJ, and with a confocal microscope and a series of filters we eliminate unwanted sources of light that would add noise to the measurements (see Annex C for details). Preliminary fluorescence imaging of the particles is performed with the EMCCD camera. If fluorescence is detected (sometimes the trapped particles have no emitters), we direct the beam to a pair of single photon detectors set up in a Hanbury, Brown and Twiss (HBT) configuration and study the emitters photon statistics [145]. This setup is used to measure the time dependent intensity correlation function, defined as

$$g^{(2)}(\tau) \triangleq \frac{\langle : I(t)I(t+\tau) : \rangle}{\langle I(t) \rangle^2}, \tag{5.7}$$

where I is the intensity operator and $\langle : \ldots : \rangle$ indicates normal ordering. For a single photon emitter, $g^{(2)}(0) = 0$ and for two or more (equal) emitters $g^{(2)}(0) \geq 0.5$. External contributions can lead to a $g^{(2)}(0) > 0$ even though

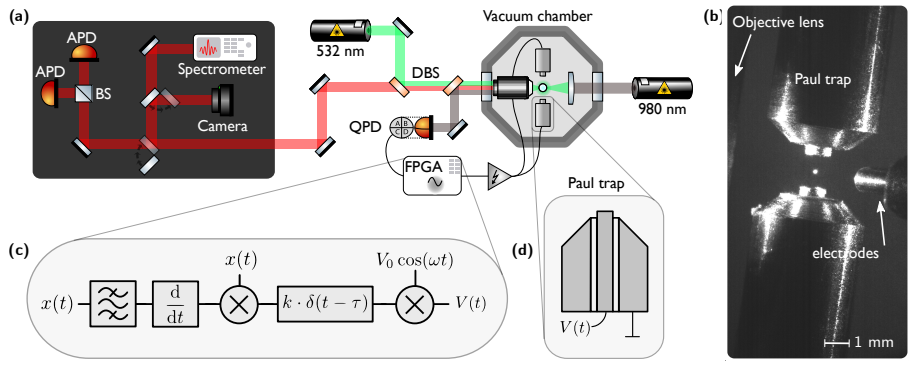

Figure 5.3: **Experimental setup**: (a) Sketch of the experimental setup. A 532 nm continuous wave laser excites the NV center. The emitted fluorescence is collected back through the same microscope objective (OBJ) (Olympus long working distance, NA 0.8), filtered, and sent to a light-proof box for fluorescence detection. The particle's motion is monitored by focusing a 980 nm laser onto the particle and detecting the forward scattered light with a quadrant photodiode (QPD). (b) Camera image of the trap viewed from above, showing the end-cap Paul trap electrodes, compensation electrodes, and the OBJ lens. (c) Signal processing blocks of the feedback system. The particle's motion $x(t)$ is digitally acquired in the FPGA and band-pass filtered to eliminate noise and unwanted modes. Then, its derivative $\dot{x}(t)$ is numerically calculated and the product $x(t)\dot{x}(t)$ is used to modulate the amplitude of the driving radio frequency signal. The modulation amplitude and delay are set to values that minimize the mode energy. (d) Cutaway of a Paul trap electrode. Particles are levitated at the trap's center of symmetry, above the inner rod. The trapping pseudo-potential is generated by grounding the outer electrodes and applying the driving radio-frequency signal $V(t)$ to the inner ones; a white alumina tube is used for electrode insulation.

the main contribution stems from a single emitter, which is ensured by $g^{(2)}(0) < 0.5$ [146]. This condition is the criterion we use to identify trapped nanodiamonds holding single NVs.

In a real experiment one never has access to the clean $g^{(2)}(\tau)$ function. Instead, for continuous excitation, we measure the joint second order correlation function of the emitter (with intensity $\langle n_s \rangle = s$) and the background noise (with intensity $\langle n_b \rangle = b$). Its expression will be

$$g^{(2)}_{sb} = \frac{\langle (s(t)+b(t))\,(s(t+\tau)+b(t+\tau))\rangle}{(s+b)^2}, \tag{5.8}$$

$$g^{(2)}_{sb} = \frac{s^2 g^{(2)}_s + b^2 + 2sb}{(s+b)^2}, \tag{5.9}$$

where $\langle \ldots \rangle$ indicate expected values, $g^{(2)}_s$ is the emitter second order correlation function and it has been assumed that

- The background noise is quantum mechanically uncorrelated with the emitter fluorescence
- The background noise has Poisson statistics, $g_b^{(2)} = 1$.

Therefore, by measuring s and b it is possible to correct $g_{sb}^{(2)}$ (which is the function measured in our single photon counting system) to obtain the emitter $g_s^{(2)}$.

Analogously, by defining $\rho = \frac{s}{s+b}$, we obtain

$$g_s^{(2)} = \frac{g_{sb}^{(2)} + \rho^2 - 1}{\rho^2}. \tag{5.10}$$

Background noise was measured to be $150 + f(I)$ counts per second, where 150 counts per second was the average dark count rate in our APDs and $f(I)$ was a pumping laser intensity dependent fluorescence contribution, due to optical elements in our setup.

After the measurements were corrected for background noise, the sets of experimental $g^{(2)}(\tau)$ functions were fitted with a least squares criterion to a modified three-level model [147]

$$g^{(2)}(\tau) = 1 + p_f^2 \left(c e^{-\frac{|\tau|}{\tau_1}} - (1+c) e^{-\frac{|\tau|}{\tau_2}} \right). \tag{5.11}$$

Since we do not measure $g^{(2)}(\tau)$ but $g^{(2)}(\tau) * h(\tau)$, where $h(\tau)$ is the APD system instrument response function, we fit the data with $g^{(2)}(\tau) * h(\tau)$ instead. With the obtained parameters, we calculate $g^{(2)}(0) = 1 - p_f^2$ to determine whether the emitter is a single photon source or not. The confidence levels for $g^{(2)}(0)$ with $\pm\sigma$ were calculated from the inferred p_f distribution. Measurements of three particles are shown in Figure 5.4.

We detected several single NVs in trapped nanodiamonds, with usual count rates of 2000 to 7000 counts per second at excitation powers between 1 mW and 5 mW. Even though the rotation of the trapped nanodiamonds has not been studied in this experiment, measuring and controlling the crystal Euler angles will be important for coupling internal and external degrees of freedom, as the spin interaction depends on the NV orientation. This control could be implemented by using elongated nanodiamonds, whose birefringence would transduce the particle's rotation into a modulation of the intensity and a change in the light polarization [126, 148, 149].

When a single NV was detected, we proceeded to eliminate stray DC fields that pushed the particle slightly away from the center of the trap. This helped to minimize the micromotion driving, and thus the stability of the particle at low pressures. The procedure consisted in sweeping a

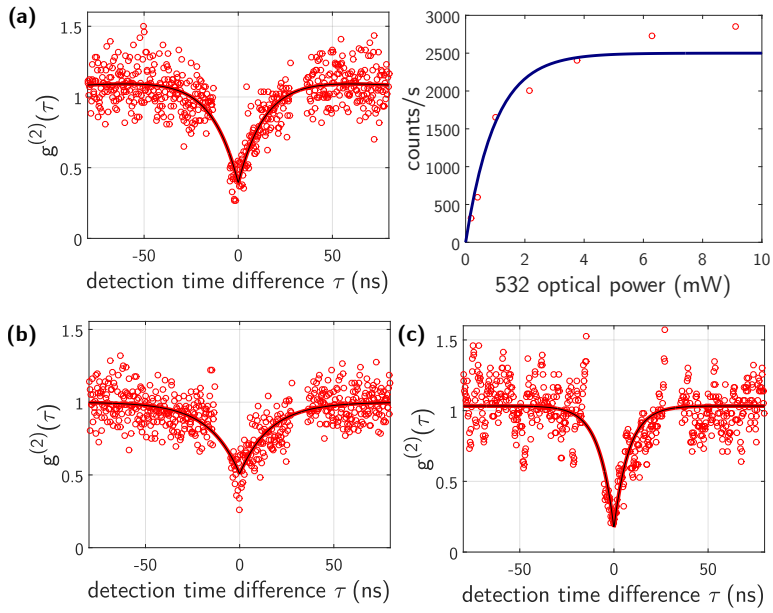

Figure 5.4: **Intensity correlation measurements**. (a) Single NV $g^{(2)}(\tau)$ measurement along with a saturation curve (taken to determine the optimal excitation power: a trade-off between photon counts and heating induced to the particle). When APDs detect a photon (i.e., an incoming photon excites an electron of the detector semiconductor to the conduction band), they often emit some fluorescence, which—depending on the wavelength and intensity—can be detected by the opposite APD. This results in wrong photon counts, since they are mixed with those of the emitter. In our experiment, one of the APDs (a PicoQuant APD) had especially intense fluorescence emission after photon detection in the visible. However, these "intruder" photons were easy to spot, since they appeared as peaks in the $g^{(2)}(\tau)$ measurements. Such fluorescence photons were detected by the APDs with always the same delay: the time required to travel the distance between the PicoQuant APD and the other APD (Perkin Elmer). This is why two sets of data—one at each side of the dip—have been deleted in the plot. The PicoQuant APD was replaced shortly after by a Perkin Elmer APD, identical to the other one (same model); this vastly reduced the problem of spurious detection. (b) and (c) show further measurements of a 2 NV and a single NV nanodiamond

range of volts (between -5 V and 5 V) for each of the three compensation electrodes, setting on the values that minimized the micromotion peak in the motion PSD. This had to be repeated for every new particle, since it was prone to drifting and sign changes; the most likely cause for this was the introduction of charged particles in the chamber during the use of the electrospray, since this could change the static electric field in the trapping region. However, by following the described compensation procedure, particles could be stably trapped at ambient pressure over very long times: some levitated nanodiamonds were kept for weeks, until they were deliberately substituted by other nanocrystals.

5.4.4 Motion PSD and feedback

At ambient pressure, the stochastic forces due to the interaction of the particle with air molecules damp oscillations and lead to overdamped Brownian dynamics, as we have seen in Chapter 3. Thus, when a trapped single NV is detected, we decrease the pressure to bring the chamber to vacuum. The voltage amplitude used to trap particles is 2 kV_{pp}, but Paschen's law (see Fig. 5.5) predicts a minimum of the breakdown voltage of air at 750 V_{pp} [150]. At the right pressure (which in our case is ~ 10 mbar), voltages above this value will ignite a plasma, leading to particle loss. Consequently, while decreasing the pressure we also reduce the voltage amplitude below 750 V_{pp}; at pressures lower than $5 \cdot 10^{-1}$ mbar the voltage amplitude can be safely increased again.

At these low pressures, under the adiabatic approximation, the power spectral density (PSD) of the particle's CoM takes the expression

$$S_x(\Omega) = \frac{\sigma^2/m^2}{\left(\frac{\Omega_i}{\mathcal{Q}}\right)^2 \Omega^2 + \left(\Omega_i^2 - \Omega^2\right)^2}, \tag{5.12}$$

where m is the particle's mass, $\sigma = \sqrt{2k_B T\gamma}$ is the Brownian noise standard deviation, Ω_i is the secular angular frequency of the oscillator and its $\mathcal{Q}$-factor represents the number of "coherent" oscillations of the particle. By introducing the normalized damping constant $\Gamma = \frac{\gamma}{m}$, which for low damping corresponds to the full width at half maximum of the oscillator transfer function, the $\mathcal{Q}$-factor is defined as $\mathcal{Q} = \frac{\Omega_i}{\Gamma}$. By fitting the measured PSD to expression (5.12), we can indirectly measure the value of $\mathcal{Q}$ and Ω_i.

For pressures below 1 mbar, the $\mathcal{Q}$-factor (or autocorrelation length) of the particle's motion is sufficiently large to activate the cooling and reduce the energy of the particle. The feedback system, described in Figure 5.3c, is a type of parametric feedback cooling (PFC) and is implemented in the following way: a 980 nm laser is focused with a low effective NA and superimposed with the focus of the trap's center. The focused light, together

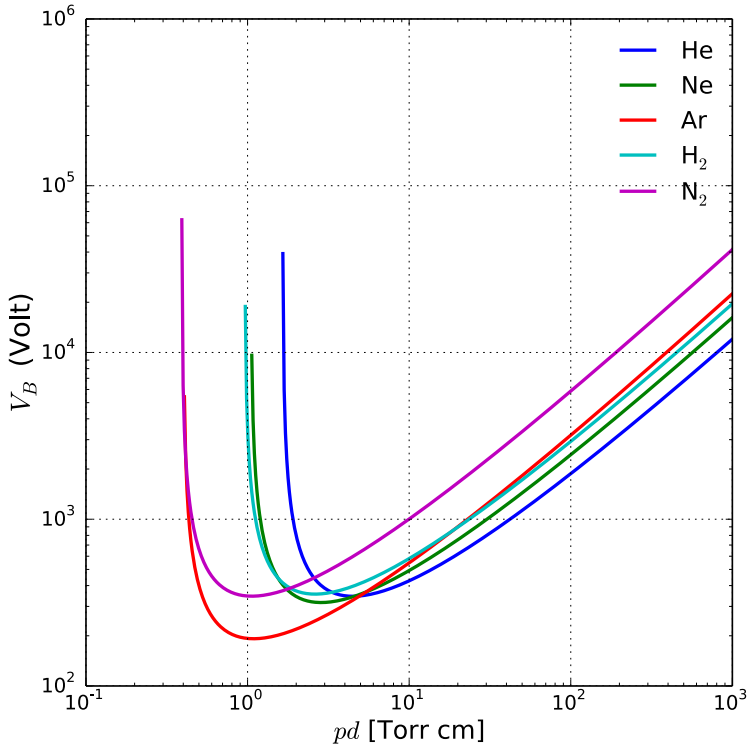

Figure 5.5: **Paschen's law**: Paschen curves obtained for helium, neon, argon, hydrogen and nitrogen. The vertical axis indicates the breakdown voltage—the minimum voltage that causes air to become a plasma (i.e., electrically conductive)—between two parallel metal plates as a function of the pressure times the distance between the plates. Image by Krishnavedala, under the Creative Commons Attribution-Share Alike 4.0 International license.

with the light scattered by the particle, are collected by the OBJ. The 980 nm light is then directed onto a quadrant photodiode (QPD), which extracts signals that are proportional to the particle's position $V_i(t) \propto x_i(t)$ for the i-th axis. For the x and y axis, this signal is obtained via differential measurements of the intensity on the quadrants. Conversely, the dynamics in z are detected from a modulation on the total intensity, resulting from the interference between the laser beam and the position dependent particle scattering (see Annex D). These signals are fed to the FPGA and processed (Figure 5.3b). Then, the FPGA modulates the amplitude of the driving voltage to cool down the energy of the CoM motion i [64]. The driving signal applied to the inner rod has the expression

$$V(t) = V_0(1 + k \cdot V_i(t)\dot{V}_i(t)) \cos(\omega t), \tag{5.13}$$

where V_0 is the driving amplitude and k is the modulation depth, which is experimentally determined.

Since the feedback is a parametric modulation, $V(t)$ will enter the equation of motion as a product with $x(t)$

$$\frac{\mathrm{d}^2x}{\mathrm{d}t^2} + \Omega^2 x = -f(t)x, \tag{5.14}$$

where $f(t) = k \cdot V(t)\dot{V}(t)$. Equation (5.14) is a simplified version of our system, but is enough to understand the idea behind parametric cooling (or, alternatively, driving). Eq. (5.14) represents a simple harmonic oscillator being driven by a signal $f(t)x$ that is proportional to its own response x. Since the particle motion $x(t)$ has a peak at Ω (corresponding to its secular frequency), $x(t) \approx A\cos\Omega t$. Therefore,

$$f(t)x(t) \propto A(\cos\Omega t + \cos 3\Omega t), \tag{5.15}$$

by a simple trigonometric identity. The $3\Omega_i$ is off-resonance of the oscillator transfer function, and this component can be neglected. In contrast, the component at Ω will be on resonance, and have a large effect on the dynamics. Thus, the parametric modulation will have approximately a driving effect on the motion of the particle: by adjusting the delay accordingly (in phase or at push-pull), we can either excite or damp the particle oscillations.

To cool the motion along the x, y and z axes with PFC, the secular frequencies of the trap need to be different for every direction. Otherwise, cooling one axis could result in heating another that shares the same frequency. This is because the motion of the translational modes is uncoupled, and therefore the phase between them is undefined.

The measurements of this chapter have been realized in a trap with perfect revolution symmetry, and thus, trapped particles had equal eigenfrequencies at the radial directions. However, this symmetry can be broken with a slightly different geometry. By modifying the electrodes—for instance, introducing a "cut" on the outer metal cylinder [64]—, the effective electric field perceived by the particle changes, separating all three frequencies.

We explored this idea by introducing cuts into the trap steel jackets, and built a new design that separated the two radial eigenfrequencies. This design is shown in Figure 5.6. Nevertheless, it was decided that a better approach to cooling would be the use of (separately controlled) compensation electrodes. This will be the topic of the next chapter.

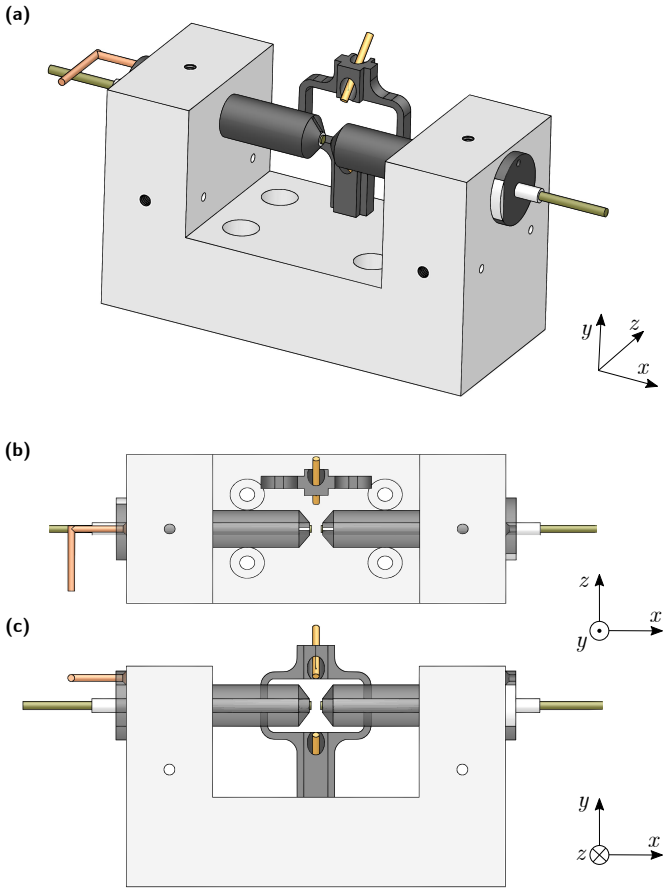

Figure 5.6: **Paul trap with broken symmetry**: (a) Perspective of the trap. It includes a small cut of the outer steel jackets along the vertical direction, resulting in a slightly smaller y eigenfrequency. (b) Plan of the trap. The rods on the left and right side of the ceramic mount are used to drive the trap's electric field. On the upper side, the compensation electrodes can be seen, forming and angle of 45° with respect to the z direction. (c) Elevation of the trap.

5.5 Results and discussion

Observed secular frequencies in the trap axis direction (for $V_{\mathrm{pp}} = 750$) are specified in Table 5.1.

Table 5.1: Secular oscillation frequencies, observed in trapped nanodiamonds.

Min. freq	Typical	Max. freq
–	(1.5 kHz, 6 kHz)	15 kHZ

Particles at low pressures were much more stable when stray fields had been cancelled with the compensation electrodes. Without 532 nm excitation light and only some weak 980 nm illumination to detect the CoM, we were able to trap nanodiamonds at pressures as low as 10^{-3} mbar, where the particle's oscillating motion attained $\mathcal{Q}$-factors above 10^3 (Figure 5.7b); at lower pressures the nanodiamonds generally became unstable. The cancellation of the stray fields was also required for feedback cooling. With it, the energy of the axial CoM mode could be reduced to a fraction of its value at thermal equilibrium

$$\left\langle m\Omega^2 x^2 \right\rangle = k_{\mathrm{B}} T, \tag{5.16}$$

expected by the equipartition theorem (see Annex D for details on the trapped particle effective temperature). Figure 5.7 shows the effect of the feedback on a nanodiamond levitated at $5 \cdot 10^{-1}$ mbar, demonstrating a reduction of energy of the eigenmode.

We thus achieved energy reductions of 6 to 9 dB at pressures between 10^{-2} mbar and 10^{-1} mbar, which corresponds to effective temperatures in the range of 75 K to 38 K. This reduction in energy is partly limited by the signal to noise ratio (SNR) from the signal measured using the QPD, but the biggest restriction is the level of vacuum. Indeed, at lower pressures the particle's motion is more predictable and the feedback performance improves.

The pressure level is, however, limited by diamond photo-degradation. Although nanodiamonds in Paul traps do not inherently suffer from heating due to optical absorption, a certain amount of optical power is required to interact with the single NV center, whether for excitation or for motion detection. As a result, laser power must be high enough for a good SNR, yet sufficiently low to avoid heating up the particle excessively. At ambient pressure, this limitation is not present since the interaction with air molecules not only damps oscillations but is also sufficiently high to keep the particle's lattice temperature at equilibrium with the environment. It

must be noticed, nevertheless, that heating is not a problem in more general scenarios. In this experiment, we have used continuous wave illumination of the nanodiamond, but once a single NV is detected, we can simply use pulsed schemes to readout and manipulate the NV spin. In this case, the laser would be off most of the time.

In order to probe the capacity of the nanodiamond to withstand heat dissipation, we performed $g^{(2)}(\tau)$ measurements at different pressures. We obtained stable fluorescence counts up until the 10^{-1} mbar to $5 \cdot 10^{-1}$ mbar range, with 1 to 3 mW of 532 nm power; no signature of quenching due to high temperatures was observed under these conditions [151]. At this point, a progressive decrease in the scattering signal was apparent, indicating a possible shrinking of the nanodiamonds.

Figure 5.8a shows the $g^{(2)}(\tau)$ measurement and spectrum of a single NV in a nanodiamond trapped at 0.5 mbar, the same on which we applied the feedback shown in Figure 5.7d. Figure 5.8b shows the fluorescence emission spectrum obtained for this NV. The two peaks at $\lambda = 620$ nm are caused by Raman scattering (OH stretching) of ethanol traces [152] present in the nanodiamonds.

5.6 Conclusions

In conclusion, we have demonstrated stable trapping of nanodiamonds and optical readout of a single NV center at pressures down to $5 \cdot 10^{-1}$ mbar. This is two orders of magnitude lower than previously attained with optical traps [62], where thermal damage limits access to higher vacuum levels. Furthermore, our platform enables us to cool down the particle's translational modes via parametric feedback.

In future experiments, the experimental setup can be improved in various ways. Firstly, to attain control over the spin system of the levitated NV center, we will need to design and add a microwave antenna in the trap. Secondly, to perform spin echo experiments, the continuous illumination with 532 nm light, that we have used in this experiment and is the major reason for particle degradation at vacuum, will not be required; instead, shorter π and $\pi/2$ pulses (necessary for initialization, driving and readout) will suffice, allowing us to work at even lower pressures. Finally, a new type of linear feedback (unlike the nonlinear parametric feedback) can be implemented by acting on the particle through the compensation electrodes. This will be the topic of the next chapter.

Having such a high level of control of a particle hosting emitters is a decisive step towards achieving strong coupling between a spin and the

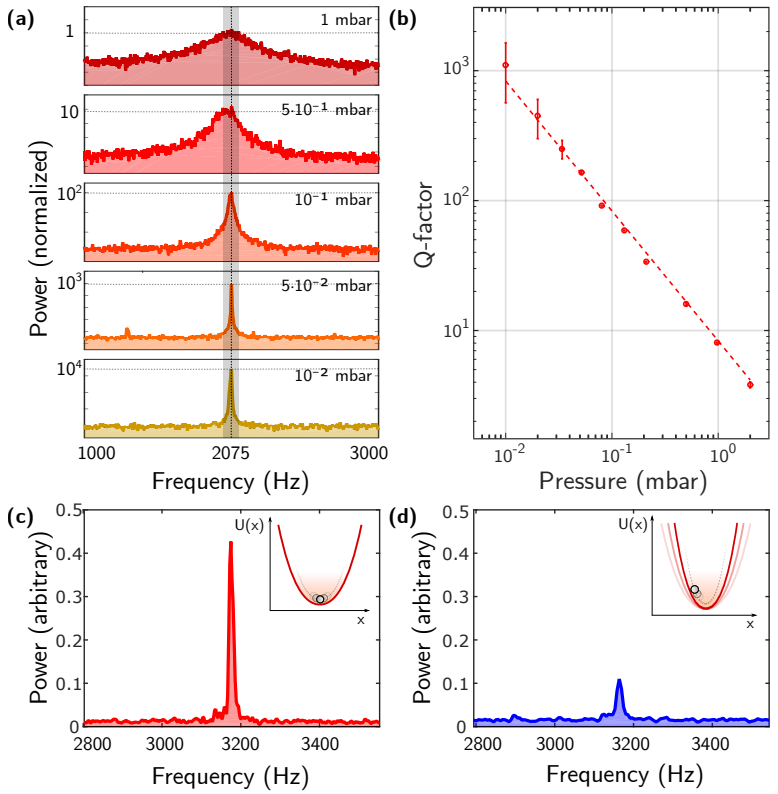

Figure 5.7: **Motion and feedback**: measurements of the particle's motion and feedback. The translational modes are driven by thermal noise, which is dominant for Brownian particles such as 40 nm nanodiamonds. (a) power spectral density (PSD) in log-scale of the particle's CoM, showing increasingly better defined resonance peaks at lower pressures. Approximate values of the powers at the peaks are normalized to the first plot maximum; the area under the curves is proportional to the particle's CoM temperature. The flat part of the spectrum is dominated by laser shot noise. (b) $\mathcal{Q}$-factor inferred by fitting the measured PSDs of a single nanodiamond at different pressures to the one expected from a harmonic oscillator driven by Brownian noise (see eq. (2.57)). The bigger error bars at low pressures are due to fitting uncertainties, since most of the oscillator response is buried in the noise floor. (c) and (d): Temperature reduction of the energy in the eigenmode by a factor of 4, corresponding to a temperature of 75 K. In panel c) the feedback is off (no potential modulation) while it is on in panel d) (potential modulated at 2Ω). The measurements are performed on a 40 nm diamond at $5 \cdot 10^{-1}$ mbar at the same time as a $g^{(2)}(\tau)$ intensity correlation measurement was being taken (see Figure 5.8).

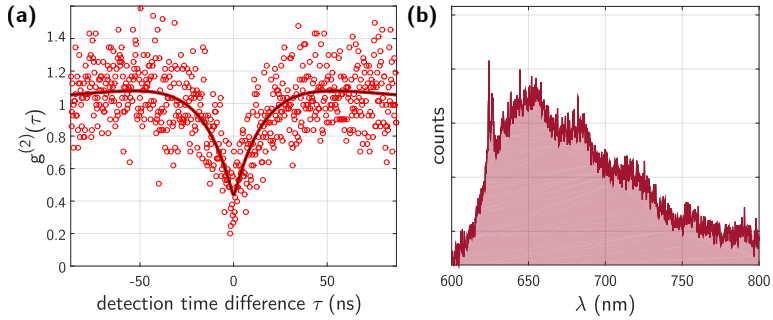

Figure 5.8: **Cooled single NV $g^{(2)}(\tau)$ measurement**. (a) $g^{(2)}(\tau)$ intensity correlation measurement of the NV^- fluorescence of a nanodiamond with applied feedback (data shown in Figure 5.7). The correlation measurement is fitted with a modified three-level model [147] convoluted with the instrument response function, with $g^{(2)}(\tau)$ showing a minimum at 0.4 ± 0.1, and thus the presence of a single NV center. Other $g^{(2)}(\tau)$ measurements for different nanodiamonds are shown in Fig. 5.4. (b) Fluorescence emission spectrum of the single NV center. The two peaks at 625 nm are due to Stokes Raman scattering, and indicate the presence of ethanol traces from the electrospray in the particle.

particle's mechanical degrees of freedom [128, 153, 154], a clear path towards observing and studying quantum phenomena at the macroscopic level.

6

Optimal control of an optically levitated particle

In this chapter we discuss the results obtained using a linear-quadratic regulator controller to cool the center of mass motion of an optically levitated nanoparticle. The feedback, with gains automatically optimized by gradient descent, exerts a Coulomb force on a charged particle with a pair of electrodes that are controlled with an FPGA. The cooling technique requires less optics than former optical feedback schemes, achieves lower CoM temperatures and has shorter transients. The technical details of the implementation on the FPGA are also discussed.
The contents of this section are based on Ref. [106], article published in Physical Review Letters.

6.1 Introduction

Levitated particles [155] are highly isolated and decoupled systems. As such, they offer new platforms to test quantum mechanics at the mesoscopic scale. However, the experimental possibilities with levitated particles go beyond those of clamped optomechanical systems, since they can be used to study internal phonons, quantized internal degrees of freedom [98, 124] and matter-wave interferometry.

As with clamped resonators, a general prerequisite of these experimental proposals is the ground state of motion, which—for levitated systems—had

not yet been achieved at the beginning of this thesis. Ongoing efforts concentrate on cavity [67, 69] and feedback [55, 70] cooling of the center of mass (CoM) motion of optically levitated particles, with parametric feedback cooling (PFC) [55] being the current standard technique for motion control and the only to report sub mK temperatures [71]. An all-electrical feedback approach for highly charged particles has also been proposed [156] based on the recent development of charge control in nanoparticles [157, 158] but, from a design point of view, it is a good idea to separate the feedback force and the trapping potential, since this will add flexibility to the system and allow for more sophisticated feedback schemes, such as optimal control (OC) protocols [159] (see Annex F for details).

For linear observable and noiseless systems, the OC law is known as the linear-quadratic regulator (LQR) and is widely utilized in larger mechanical systems [159]. It guarantees that a dynamical system will minimize its energy[1] in the fastest way possible. For a levitated nanoparticle, the LQR takes the law of a proportional-derivative controller with optimal gain coefficients. These can be determined analytically, but an additional machine learning (ML) algorithm can autonomously find the optimal gains without prior knowledge of the system parameters. The adaptiveness of the feedback is an especially relevant feature in more sophisticated schemes; for instance, the introduction of a Kalman filter [160] where the coefficients have a high degree of uncertainty, can transform the tuning of the feedback into a high dimensional optimization problem. If different particle species, pressures and regimes need to be accessed, a ML algorithm might become indispensable.

In this chapter we present the results of our experiment on feedback cooling and control of a mode of the CoM motion of an optically levitated charged nanoparticle. As the main novelty of our work, we have used a ML controlled LQR feedback, exerted by electric fields through Field-Programmable Gate Array (FPGA) controlled electrodes. This scheme is considerably easier to implement than previous optically-based feedback schemes [55, 70] and, importantly, can be included in Paul trap experiments in a completely analogous way.

With a considerably simple experimental setup, the LQR in our experiment yielded CoM temperatures that are between one and two orders of magnitude lower than PFC [55] over the 10^{-1} mbar to 10^{-7} mbar range in which we performed the experiment, and had transients 10 to 600 times faster than regular cold damping (CD). As we will discuss, the cooling is eventually limited by the detection noise floor, yielding a minimum temperature of 5 mK at 3×10^{-7} mbar.

[1] Defined in a way that will be made precise in the next section.

6.2 Theory

The CoM motion along the x-axis of an optically levitated particle can be described by the stochastic differential equation

$$\ddot{x} + \Gamma\dot{x} + \omega_0^2 x = \frac{\sigma}{m}\eta(t) + u(t), \tag{6.1}$$

where m is the particle mass [101], Γ is the normalized damping term due to the interaction with residual gas molecules, ω_0 is the oscillator's natural frequency, $\sigma\eta(t)$ is a stochastic force with zero mean and autocorrelation $R(\tau) = \sigma^2\delta(\tau)$, associated with the damping via the fluctuation-dissipation relation [102] $\sigma = \sqrt{2k_\mathrm{B}Tm\Gamma}$, and $u(t)$ is an externally applied feedback force of arbitrary form. Experimentally, the velocity $v(t) = \dot{x}(t)$ is inaccessible. We can only measure a noisy position, $z(t) = x(t) + \xi(t)$, where $z(t)$ is the *observed* position (not to be confused with the motion along the Z axis) and $\xi(t)$ is detection noise, in our case dominated by shot noise.

If equation (6.1) describes the system evolution accurately, there exists an OC law [159] $u(t)$ that minimizes the expected energy functional

$$\mathcal{J} = \mathbb{E}\left[\int_0^{\mathcal{T}} \Big(x^2(t) + \rho u^2(x(t))\Big)\,\mathrm{d}t\right], \tag{6.2}$$

where ρ is a weighting parameter and $\mathcal{T}$ is the energy integration time; both can be chosen at will, in a trade-off that the feedback designer will need to settle. The expression of $u(t)$ that minimizes $\mathcal{J}$ is given by the LQR controller[2] [159]:

$$u(t) = \mathbf{K}\cdot\begin{pmatrix}x(t)\\ v(t)\end{pmatrix}, \quad \mathbf{K} = \begin{pmatrix}k_\mathrm{p} & k_\mathrm{d}\end{pmatrix}, \tag{6.3}$$

where $\mathbf{K}$ is a constant matrix whose coefficients can be calculated numerically (see the LQG simulations section).

We can make ρ almost arbitrarily small because we don't need to worry about the energy spent on the control signal $u(t)$. It is quite intuitive to see that, the smaller the value of ρ, the better the performance of the feedback but also the higher the energy requirements. In general, however, one cannot afford to "ignore" the feedback contribution. In bigger, macroscopic feedback systems (for instance at the industrial scale) a small prefactor ρ in $u(t)$ can result in large fuel expenses or unpleasant surprises in the electricity bill.

In our experiment the only restriction is that the generated feedback signals are below the 1 V level, the maximum voltage allowed in the FPGA

[2]See Annex F for details.

(Red Pitaya STEMlab board) analog output. In practice, as observed in our simulations, this is always the case for $\rho \geq 10^{-4}$. Then, for a fixed $\mathcal{T}$, the OC law will minimize an expression that is approximately proportional to the particle energy, $\mathcal{J} \propto \langle x^2(t) \rangle$. As a corollary, a proportional-derivative controller with expression $u(t) = k_{\mathrm{p}} x(t) + k_{\mathrm{d}} v(t)$ will minimize the energy among all other possible feedback protocols $u(x(t))$, either linear or nonlinear [159]. In particular, a linear feedback scheme should outperform PFC [55], which relies on a modulation of the potential. The case where only a damping term is considered ($k_{\mathrm{p}} = 0$) is usually known as CD [161]. While the final minimal temperature for CD and LQR in most experimental conditions is the same, the LQR has significantly shorter transient times, since by definition it minimizes energy over time[3].

The optimal controller can be separated in two steps: firstly, an optimal phase state estimator, known as Kalman filter [160, 162, 163] (see Annex F), that will produce estimates of $(x(t), v(t))$ given noisy position measurements $z(t)$; secondly, an optimal feedback (LQR) based on (6.3). The combination of both is known as a linear-quadratic Gaussian regulator (LQG) controller. In our experiment, instead of a Kalman filter, we approximate the phase space coordinates as

$$(\hat{x}(t), \hat{v}(t)) = (z(t), -\omega_0 z(t - \phi/\omega_0)), \tag{6.4}$$

with $\phi = \pi/2$. Not using a Kalman filter yields higher CoM temperatures, but results in a considerably simplified digital signal processing unit. Additionally to the feedback we have implemented a ML algorithm that autonomously optimizes the parameters $(k_{\mathrm{p}}, k_{\mathrm{d}})$ by minimizing $\langle x^2(t) \rangle$, adapting itself to different experimental conditions.

6.2.1 Spectral densities and T_{eff}

Introducing the expression of $u(t)$ given by a LQR controller in the previous equation of motion (i.e., a proportional-derivative feedback controller), we obtain the stochastic differential equation

$$\ddot{x} + \Gamma \dot{x} + \omega_0^2 x = \frac{\sigma}{m} \eta(t) - k_{\mathrm{p}}(x + \xi(t)) - k_{\mathrm{d}}(v(t) + \dot{\xi}(t)), \tag{6.5}$$

where k_{p} and k_{d} are the feedback gains and $\xi(t)$ is a signal representing measurement noise. The model described by eq. (6.5) is accurate as long as the optical field is well approximated by a quadratic potential. This is usually the case at pressures above 50 mbar, where the viscous damping dominates the particle's dynamics, and is also a good description at lower pressures

[3] See Annex D for details on the temperature definition.

when the feedback $u(t)$ restricts the particle's motion to the vicinity of the optical trap center.

Taking the Fourier transform of (6.5), defining

$$\mathcal{F}(\xi(t)) = \Lambda_\xi(\omega)$$
$$\mathcal{F}(\eta(t)) = \Lambda_\eta(\omega)$$

and solving for $X(\omega)$ we get

$$X(\omega) = \frac{\sigma/m}{(\omega_0^2 + k_\mathrm{p} - \omega^2) + i\omega(\Gamma + k_\mathrm{d})}\Lambda_\eta(\omega) - \frac{(k_\mathrm{p} + ik_\mathrm{d}\omega)\Lambda_\xi(\omega)}{(\omega_0^2 + k_\mathrm{p} - \omega^2) + i\omega(\Gamma + k_\mathrm{d})}. \tag{6.6}$$

Equivalently, the Fourier transform including the measurement noise will be

$$X(\omega) + \Lambda_\xi(\omega) = \frac{\sigma/m}{(\omega_0^2 + k_\mathrm{p} - \omega^2) + i\omega(\Gamma + k_\mathrm{d})}\Lambda_\eta(\omega) + \frac{(w_0^2 - \omega^2) + i\omega\Gamma}{(\omega_0^2 + k_\mathrm{p} - \omega^2) + i\omega(\Gamma + k_\mathrm{d})}\Lambda_\xi(\omega). \tag{6.7}$$

By using $S_x(\omega) = \mathbb{E}(|X(\omega)|^2)$ and the fact that $\xi(t)$ and $\eta(t)$ are uncorrelated we find the PSDs of both the real position and the position that is measured with the IL detector:

$$S_x(\omega) = \frac{\sigma^2/m^2}{(\omega_0^2 + k_\mathrm{p} - \omega^2)^2 + (\Gamma + k_\mathrm{d})^2\omega^2} + \frac{k_\mathrm{p}^2 + k_\mathrm{d}^2\omega^2}{(\omega_0^2 + k_\mathrm{p} - \omega^2)^2 + (\Gamma + k_\mathrm{d})^2\omega^2}\sigma_\xi^2, \tag{6.8}$$

$$S_\mathrm{IL}(\omega) = \frac{\sigma^2/m^2}{(\omega_0^2 + k_\mathrm{p} - \omega^2)^2 + (\Gamma + k_\mathrm{d})^2\omega^2} + \frac{(\omega_0^2 - \omega^2)^2 + \Gamma^2\omega^2}{(\omega_0^2 + k_\mathrm{p} - \omega^2)^2 + (\Gamma + k_\mathrm{d})^2\omega^2}\sigma_\xi^2, \tag{6.9}$$

where $S_\xi(\omega) = \sigma_\xi^2$ is the detection noise level (constant at the spectral range of interest in our experiment). The second term of the PSD, absent in freely oscillating particles, is due to the introduction of noise by the feedback and becomes dominant for large k_p, k_d gains. The feedback also introduces a correlation between detection noise and position, affecting the PSD shape measured through the in-loop (IL) detector and making it differ from the real position expression in eq. (6.8). For small k_d the mentioned difference between $S_\mathrm{IL}(\omega)$ and $S_x(\omega)$ is negligible. However, for larger values of

k_d the correlation of detection noise and $x(t)$ will produce a reduction or *squashing* of the noise floor around ω_0 in $S_\mathrm{IL}(\omega)$. To avoid underestimations of the particle's energy, we introduce a second, out-of-loop (OoL), detector with uncorrelated noise. The OoL, which was omitted in previous levitodynamics feedback cooling experiments [55, 70, 71], is commonly found in optomechanics experiments with feedback-cooled clamped oscillators.

If we define $\beta(t)$ as the measurement noise in an OoL detector (i.e., not used in the feedback system), we can obtain the new measured PSD with a completely analogous derivation as before

$$S_\mathrm{OoL}(\omega) = \frac{\sigma^2/m^2}{(\omega_0^2 + k_\mathrm{p} - \omega^2)^2 + (\Gamma + k_\mathrm{d})^2\omega^2} + \frac{k_\mathrm{p}^2 + k_\mathrm{d}^2\omega^2}{(\omega_0^2 + k_\mathrm{p} - \omega^2)^2 + (\Gamma + k_\mathrm{d})^2\omega^2}\sigma_\xi^2 + \sigma_\beta^2. \tag{6.10}$$

In this experiment, however, we haven't used the real particle velocity. Instead, we have approximated

$$v(t) \simeq \omega_0 x(t - \tau), \tag{6.11}$$

where $\tau = \phi/\omega_0$ and $\phi = \pi/2$. By using the fact that $\mathcal{F}(x(t-\tau)) = e^{-i\omega\tau}X(\omega)$ we may obtain new expressions for the PSDs. Considering only a derivative gain k_d and defining

$$G(\omega) = (\omega_0^2 - k_\mathrm{d}\cos(\omega\tau) - \omega^2)^2 + (\Gamma\omega + \omega_0 k_\mathrm{d}\sin(\omega\tau))^2, \tag{6.12}$$

then the new PSD expressions will be

$$S'_x(\omega) = \frac{\sigma^2/m^2}{G(\omega)} + \frac{\omega_0^2 k_\mathrm{d}^2}{G(\omega)}\sigma_\xi^2, \tag{6.13}$$

$$S'_\mathrm{IL}(\omega) = \frac{\sigma^2/m^2}{G(\omega)} + \frac{(\omega_0^2 - \omega^2)^2 + \Gamma^2\omega^2}{G(\omega)}\sigma_\xi^2 \tag{6.14}$$

$$S'_\mathrm{OoL}(\omega) = \frac{\sigma^2/m^2}{G(\omega)} + \frac{\omega_0^2 k_\mathrm{d}^2}{G(\omega)}\sigma_\xi^2 + \sigma_\beta^2. \tag{6.15}$$

These PSDs are very similar to the ones found before for values of ω close to ω_0 as long as ϕ is exactly $\pi/2$. Nevertheless, for values smaller or larger than $\pi/2$ the resulting PSD will have a small asymmetry, very visible in the IL noise squashing. Figure 6.1 shows the resulting theoretical PSDs with a properly tuned delay, whereas the case of $\phi \neq \pi/2$ is displayed in Fig. 6.2. Experimental data with different delay values is shown in Fig. 6.3, showing good agreement with the derived expressions.

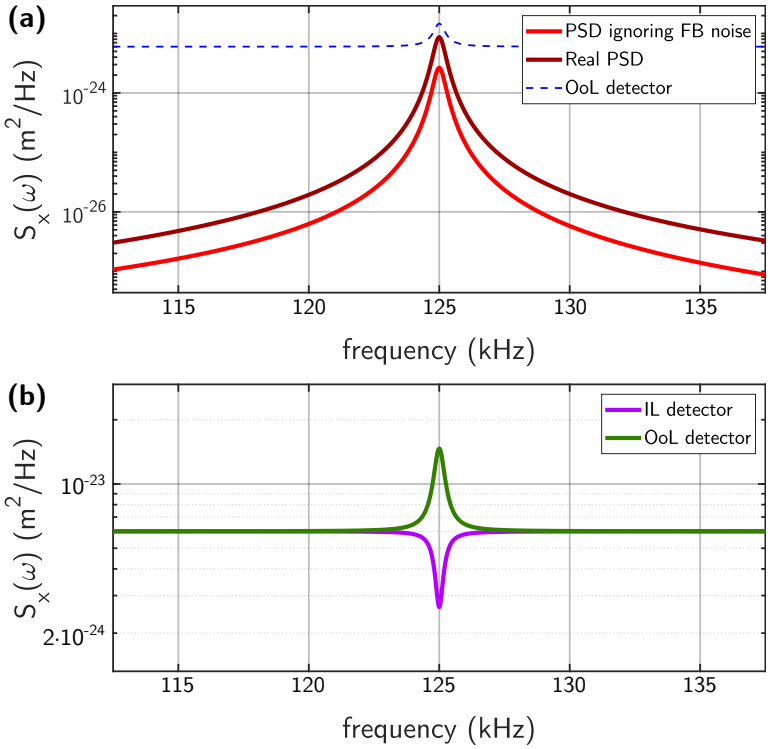

Figure 6.1: **Motion PSDs with perfect delay**. Theoretical PSD of the CoM motion in the presence of cold damping with a perfectly adjusted delay $\phi = \pi/2$. (a) The plot shows three PSDs: the particle's PSD without taking into account measurement noise, the real $S'_x(\omega)$ and the signal $S'_{\mathrm{OoL}}(\omega)$ measured in the out-of-loop. The PSD $S_x(\omega)$ would practically overlap with $S'_x(\omega)$. (b) Comparison of the PSD signals measured in the IL detector and OoL detector, showing perfect squashing symmetry in the IL.

Using the equipartition theorem, we define the mode effective temperature (see (D.23) in Annex D) as

$$T_{\mathrm{eff}} = \frac{m\omega_0^2\langle x^2\rangle}{k_{\mathrm{B}}}. \tag{6.16}$$

An expression of this temperature can be obtained integrating in the frequency domain, since the Fourier transform is unitary[4]

$$T_{\mathrm{eff}} = \frac{m\omega_0^2}{k_{\mathrm{B}}}\frac{1}{2\pi}\int_{-\infty}^{\infty} S_x(\omega)\mathrm{d}\omega. \tag{6.17}$$

[4]This result is known as Parseval's theorem.

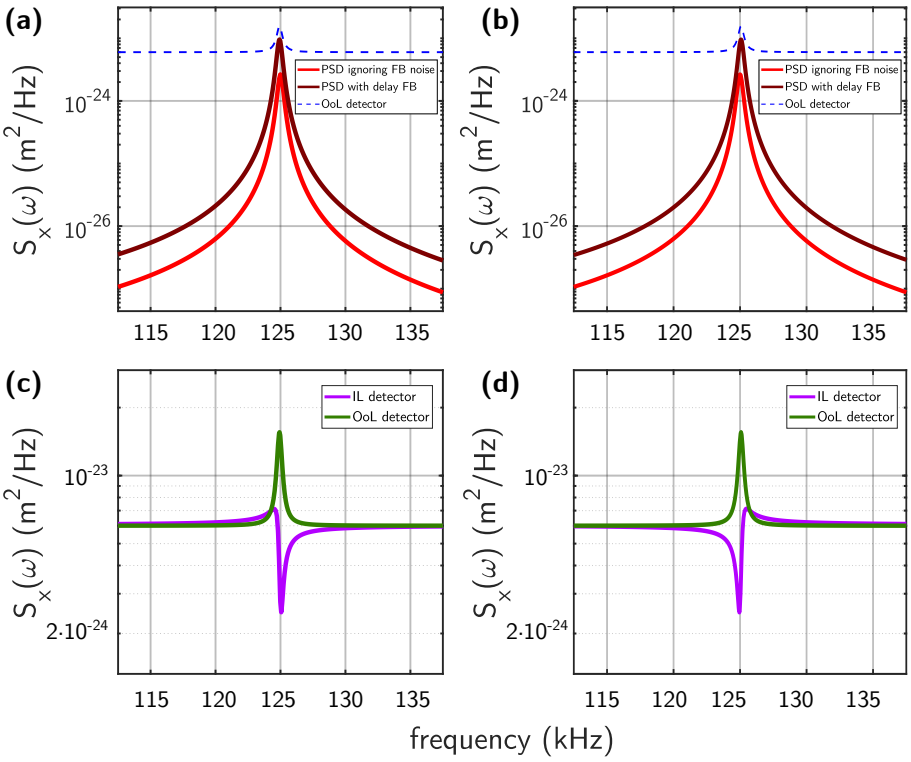

Figure 6.2: **PSDs with incorrect delay**. Theoretical PSD of the CoM motion in the presence of cold damping with a smaller/larger than $\pi/2$ delay. (a) The plot shows three PSDs: the particle's PSD without taking into account measurement noise, the real $S'_x(\omega)$ and the signal $S'_{\mathrm{OoL}}(\omega)$ measured in the out-of-loop (OoL), for a delay of $0.8 \cdot \pi/2$. (b) The plot shows three PSDs: the particle's PSD without taking into account measurement noise, the real $S'_x(\omega)$ and the signal $S'_{\mathrm{OoL}}(\omega)$ measured in the OoL, for a delay of $1.2 \cdot \pi/2$. (c) Comparison of the PSD signals measured in the IL detector and OoL detector, showing asymmetry in the IL, for a delay of $0.8 \cdot \pi/2$. (d) Comparison of the PSD signals measured in the IL detector and OoL detector, showing asymmetry in the IL, for a delay of $1.2 \cdot \pi/2$.

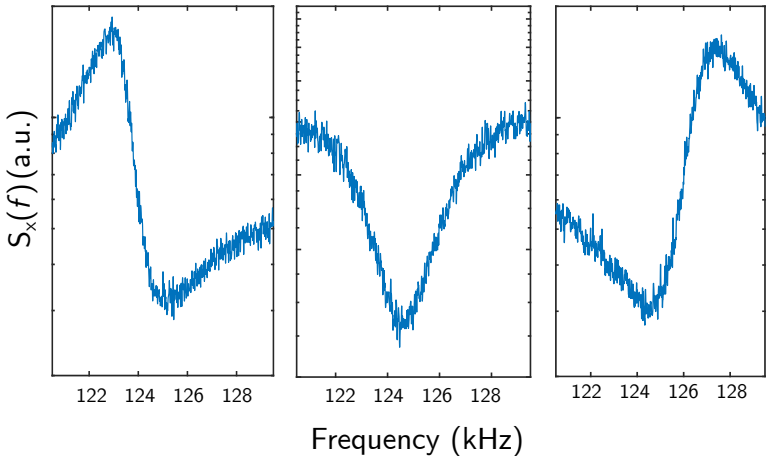

Figure 6.3: **Effect of delay in the feedback**. Experimental PSDs recorded with the IL detector for large k_d gains ($k_p = 0$), showing squashing of the noise floor. The center PSD displays a symmetrical squashing dip, corresponding to a feedback delay that is correctly tuned. Decreasing (left PSD) or increasing (right PSD) the value of the delay leads to squashing asymmetry, as predicted in equations 6.15 and plotted in Fig. 6.2.

Using the following integral expressions

$$\frac{1}{2\pi}\int_{-\infty}^{\infty}\frac{1}{(\omega^2-\omega_0^2)^2+\Gamma^2\omega^2}\mathrm{d}\omega = \frac{1}{2\omega_0^2\Gamma},$$
$$\frac{1}{2\pi}\int_{-\infty}^{\infty}\frac{\omega^2}{(\omega^2-\omega_0^2)^2+\Gamma^2\omega^2}\mathrm{d}\omega = \frac{1}{2\Gamma},$$

we find

$$T_{\mathrm{eff}} = \frac{m\omega_0^2}{2k_B}\left(\frac{\sigma^2/m^2+k_p^2\sigma_\xi^2}{(\omega_0^2+k_p)(\Gamma+k_d)}+\frac{k_d^2\sigma_\xi^2}{(\Gamma+k_d)}\right), \tag{6.18}$$

which coincides with the expression for CD found in [164] when $k_p = 0$. We use expression (6.18) to compare the measured temperatures with theoretical values in terms of k_p, k_d.

6.2.2 Simulations of the LQG

The LQG minimizes the functional

$$\mathcal{J} = \mathbb{E}\left[\int_0^T \Big(x^2(t)+\rho u^2(x(t))\Big)\,\mathrm{d}t\right], \tag{6.19}$$

but since we can make ρ arbitrarily small, then, for a fixed T,

$$\mathcal{J} \approx T\,\mathbb{E}\left[\frac{1}{T}\int_0^T x^2(t)\mathrm{d}t\right] \propto \langle x^2(t)\rangle. \tag{6.20}$$

In other words, for $\rho \ll 1$ the LQG minimizes the energy functional among all other feedback laws (a similar argument can be made for n-dimensional linear systems). Since we have used some approximations (i.e., no Kalman filter) in the actual implementation of the feedback scheme, we use simulations of the LQG as a benchmark for comparison.

The simulations of the LQG have been performed in MATLAB and consist of a three step process:

1. We generate a signal $x(t)$ to emulate the particle's position. After that we *simulate* and add a measurement noise, obtaining $z(t)$, thus taking into account the two dominant noise sources (shot noise and electronic noise) in the measured signal.

2. The signal $\hat{x}(t)$ is reconstructed from $z(t)$ by a Kalman filter.

3. We add a feedback step with a LQR. We first calculate k_p, k_d by solving the Riccati equation, as described in [165], and calculate $u(t)$ as in equation (6.3). We add $u(t)$ to the equation of motion when the simulated feedback is "turned on".

Finally, we compare the results of the LQR with the ones where different values of k_p and k_d are used.

The signal $x(t)$ simulation is performed with a Runge-Kutta method of strong order 1 [105, 166] (see Annex A). As described before, the equation of motion of the CoM of the levitated nanoparticle is

$$\mathrm{d}x_t = v_t\mathrm{d}t\ , \tag{6.21}$$

$$m\mathrm{d}v_t = -\nabla\Psi(x_t)\mathrm{d}t - m\Gamma v_t\mathrm{d}t + \sigma\mathrm{d}W_t + mu(t)\mathrm{d}t\ , \tag{6.22}$$

where

$$\Psi(x) = m\omega_0^2\left(\frac{x^2}{2}\right) \tag{6.23}$$

and higher terms of the series expansion of the optical potential have not been considered because when the feedback is on the particle's motion is restricted to the vicinity of the potential minimum.

The rest of the values needed to perform the simulations (i.e., m, Γ, σ, σ_ξ, and the electronic noise) have been calculated assuming:

- A temperature $T = 295$ K.
- A spherical silica particle of radius 117.5 nm and density 2200 kg/m^3.
- $\gamma = m\Gamma$ follows Stoke's drag force, and is linear with the pressure for moderate levels of vacuum.
- The noise intensity σ satisfies the fluctuation-dissipation relation, i.e., $\sigma = \sqrt{2k_{\mathrm{B}}Tm\Gamma}$.
- $\sigma_\xi^2 \simeq 6 \times 10^{-24}$ m^2/Hz, the noise floor of our balanced detectors.
- The Red Pitaya analog output electronic noise approximately follows a normal distribution with $\sigma_{\mathrm{RP}} = 1$ mV. The digital discretization noise has also been taken into account.

6.3 Experimental methods

6.3.1 Optical setup

The experimental setup is displayed in Fig. 6.4. A silica nanoparticle (diameter 235 ± 11 nm) is loaded at ambient pressure into a single beam optical trap inside a vacuum chamber (wavelength $\lambda = 1064$ nm, power $P \simeq 75$ mW, objective NA $= 0.8$). The charge Q of the particle, fixed to -50 net e^+ in this experiment, is controlled [101, 158] with a corona discharge on a bare electrode. Along the horizontal direction x, a pair of electrodes separated by d_{el} form a parallel-plate capacitor around the particle position (Fig. 6.4(b)). Applying a voltage $V(t)$, we create a feedback force $u(t) \approx QV(t)/d_{\mathrm{el}}$ on the particle.

Balanced photodiodes (see Annex D) monitor the oscillation of the particle over all three degrees of freedom. Along the two oscillation modes perpendicular to x we perform PFC [55] to avoid any possible cross-coupling without between different translation modes and maintaining the motion in these two directions in the linear regime. The x CoM motion is monitored with two photodiodes: the first, an IL detector, generates the feedback signal, whereas the OoL detector solely records data.

6.3.2 FPGA feedback

The IL x signal is processed in the FPGA, where it is separated into $\hat{x}(t)$ and $\hat{v}(t)$ after a $-90°$ shift, amplified with the feedback gains k_{p}, k_{d} and summed back together. The resulting $u(t)$ feedback signal is sent to the electrodes. The gains are controlled from the board CPU, either manually or with an autonomous ML algorithm that estimates the particle energy

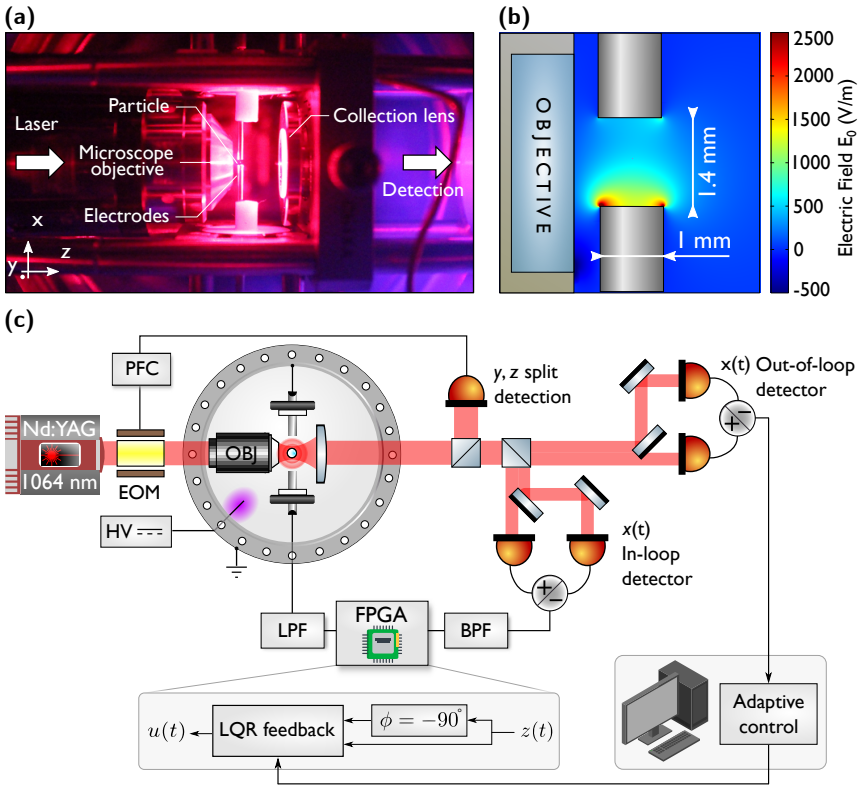

Figure 6.4: **Experimental setup** (a) Photograph of the setup inside the vacuum chamber. The purple glow on the right is a plasma generated to control the particle's charge (b) Close-up image of the trapping region with a simulation of the electric field for an applied DC voltage of 1 V. (c) Setup sketch. A microscope objective (OBJ) is used to trap a silica nanoparticle. The scattered light is collected and sent to a balanced photodiode to detect the motion. The x-motion signal is band-pass filtered (BPF) and sent to the FPGA, where the LQR signal is calculated. The output is low-pass filtered (LPF) and sent to the electrodes to cool the motion electrically. The LQR parameters are controlled with a ML routine that runs on the board CPU. PFC is used to modulate the laser light with an electro-optic modulator (EOM) and cool the two other axes during all the measurements.

from the OoL signal and uses a stochastic gradient descent technique to find the gain values that minimize it [167].

The FPGA (Red Pitaya STEMlab board) bitstream has been created in Vivado Design Suite, combining Xilinx IP cores and custom Verilog code. The feedback law (gains, delay, machine learning on/off, etc.) is controlled from the Red Pitaya CPU board with custom made C code that communicates with the FPGA through registers. Links to all the code (FPGA and CPU controller) can be found at:
→ https://github.com/gerardpc/Red-Pitaya-Levitodynamics-Feedback. It can be downloaded and freely used.

6.3.3 Machine learning algorithm

We use a form of stochastic gradient descent [167] for the adaptive feedback algorithm. The objective function to be minimized is an estimation of the particle energy, calculated as

$$L(K_\mathrm{p}, K_\mathrm{d}) = h * \left(\zeta^2(t)\right) \approx \langle x^2(t)\rangle, \tag{6.24}$$

where K_p, K_d are the constants k_p and k_d in internal FPGA units (i.e., the values introduced with the software), $\zeta(t)$ is the signal measured in the OoL detector after an analog band-pass filter, and $h[n]$ is a low-pass (LPF) digital infinite impulse response filter of order 1. This LPF is implemented in the FPGA and has a cut-off frequency $f_\mathrm{c} = 0.3$ Hz, designed to eliminate the fast fluctuations and, thus, the time dependency on L.

Experimentally, the OoL signal is fed into a second FPGA input, and L is continuously calculated. The updated values of L are written into a register at 62.5 MHz, and custom-made software designed to control the FPGA (running on the board CPU) reads the current energy value. The program decides the new values of K_p, K_d according to

$$(K_\mathrm{p}[n], K_\mathrm{d}[n]) = (K_\mathrm{p}[n-1], K_\mathrm{d}[n-1]) - \delta \nabla L, \tag{6.25}$$

where the step size δ has been chosen to ensure convergence and reasonable speeds and the gradient of L is approximated as

$$\nabla L(K_\mathrm{p}[n], K_\mathrm{d}[n]) \approx \begin{pmatrix} \frac{L(2K_\mathrm{p}[n], K_\mathrm{d}[n]) - L(K_\mathrm{p}[n], K_\mathrm{d}[n])}{K_\mathrm{p}[n]} \\ \frac{L(K_\mathrm{p}[n], 2K_\mathrm{d}[n]) - L(K_\mathrm{p}[n], K_\mathrm{d}[n])}{K_\mathrm{d}[n]} \end{pmatrix} \tag{6.26}$$

by exploring for a short time different values of K_p and K_d.

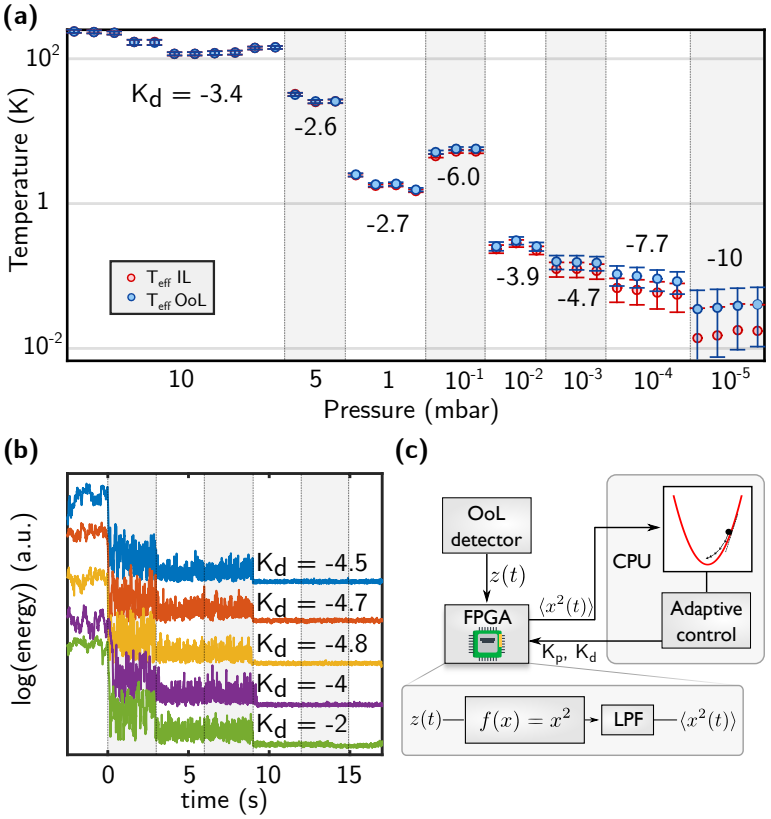

Figure 6.5: **ML algorithm** (a) ML routine adapting to the optimal k_d while the pressure in the chamber is reduced from $p = 10$ mbar to $p = 10^{-5}$ mbar. Points in the same segment are measured at constant pressure. (b) Convergence of the ML routine (started at $t = 0$) to the optimal gain in a few steps at $p = 3 \times 10^{-6}$ mbar, for five uncooled x initial conditions. All reach similar final energy values (value of k_d in FPGA units is displayed), but slightly differ in the converged gains. Each section represent 3 second iteration steps during which k_d has been left constant (for clarity). Data is smoothed with a moving average filter and separated on the vertical axis by a constant factor for readability. (c) Setup and processing details of the algorithm. The OoL signal is sent to the FPGA (through a different input than the IL feedback signal), where the mode energy is estimated. A stochastic gradient descent algorithm, running on the CPU, optimizes the values of k_p, k_d.

6.4 Results

6.4.1 Data evaluation details

We estimate the conversion factor between the FPGA software gain K_p, K_d (in arbitrary units) and k_p, k_d as defined in equation (6.3) by

$$k_\mathrm{p} \simeq \frac{55\,\mathrm{bits}}{\mathrm{nm}} \frac{10\,\mathrm{V}}{32768\,\mathrm{bits}} G_\mathrm{el} \frac{577 n\mathrm{e}^-}{m} \frac{10^9\,\mathrm{nm}}{\mathrm{m}} K_\mathrm{p} = 3.34 \times 10^8 K_\mathrm{p}, \tag{6.27}$$

$$k_\mathrm{d} \simeq \frac{3.3410^8}{\omega_0} K_\mathrm{d} = 4.26 \times 10^2 K_\mathrm{d}, \tag{6.28}$$

where G_el accounts for the electronic gain in our setup, $m \approx 2 \times 10^{-17}$ kg is the mass of the particle used throughout the chapter, e^- the electron charge and $n = 50$ the number of elementary charges in our particle.

To estimate the energy of the particle's x mode, the OoL PSD is background corrected by subtracting the detection noise floor and then the uncalibrated area of the PSD is summed up over a region of interest of approximately ± 15 kHz. The calibration (i.e., Volts to m^2/Hz conversion factor, see Annex D) is obtained by calculating the area of a PSD at 50 mbar without any feedback, assuming that it is thermalized at a room temperature of $T = 295$ K (nonlinear terms of the optical field expansion have contributions way below experimental error at this pressure). Dividing the respective areas and multiplying with the room temperature yields the effective mode temperature.

The uncertainty in the evaluation of temperature is calculated by taking into account the uncertainties of the PSD, noise floor and calibration factor. They are displayed as error bars in the figure plots.

6.4.2 Experimental results

Cold damping measurements ($k_\mathrm{p}, k_\mathrm{d}$ manually set) at pressures ranging from 10^{-2} mbar to 10^{-7} mbar are shown in Fig. 6.6. Figures 6.6(a) and 6.6(b) display the double sided PSDs $S_x^\mathrm{IL}(\omega)$ and $S_x^\mathrm{OoL}(\omega)$, measured from the IL and OoL detectors respectively. For strong feedback gains in the order of $k_\mathrm{d} = 1$ krad/s the energy of the mode becomes comparable to the noise energy. In contrast to the OoL measurement, on the IL PSDs we observe squashing of the noise floor due to the correlation of detector noise and particle signal. Noise squashing was previously observed in other systems [164, 168, 169] but never in feedback cooled levitated nanoparticles. In Fig. 6.6(c) we plot the minimum CoM temperature for different pressures, achieving temperatures between one and two orders of magnitude lower than PFC [55], since PFC is nonlinear and becomes inefficient

for small $x(t)$. Below $p < 10^{-5}$ mbar T_{eff} is not reduced as efficiently as at higher pressures, suggesting the detectors noise floor σ_ξ^2 as the main limiting factor at this pressure range. In Fig. 6.6(d) we show $T_{\text{eff}}(k_{\text{d}})$ at 3×10^{-7} mbar, achieving a minimum $T_{\text{eff}} = 5.1 \pm 0.5$ mK. The qualitative temperature behaviour agrees with theory, although the expected optimal k_{d} is a factor 3.4 larger than measured and the minimum T_{eff} is approximately 10 times larger than predicted with the theoretical expression of T_{eff} (see eq. (6.18)). Since at these temperatures the motion PSDs are close to the noise floor, this could be due to noise correlations or PFC effects unaccounted for in the model.

In Fig. 6.5 we present time traces with the ML adaptive algorithm on. Figure 6.5(a) displays the particle's temperature as pressure is reduced, showing how the algorithm adapts k_{d} to different conditions starting from a hot particle (individual data points are recorded at constant pressure while the algorithm is in standby). At 10^{-5} mbar, temperatures lie in the 10^{-2} K range, recovering the results obtained with the CD pressure scan. Figure 6.5(b) shows how the algorithm converges to similar final temperatures for five identical initial conditions. Fluctuations of the estimated energy result in a "noisy" convergence of the algorithm around the optimum, a characteristic feature of stochastic gradient descent based techniques. A block diagram of the algorithm processing details is sketched in Fig. 6.5.

Finally, introducing a k_{p} term, we investigate (Fig. 6.7) the full LQR and the difference in transient times in comparison to CD; we also compare the results with full system simulations of the LQG (see Annex F for details). An increase in k_{p} leads to faster cooling, as shown in Fig. 6.7(a). Here, the ratio of decay times between cold damping t_{CD} and OC's t_{LQR} with increasing values of k_{p} is plotted for different values of k_{d}, showing decay times a factor 10 to 600 shorter. Three experimental sample paths serve as examples in Fig. 6.7(b). Reducing the time required to transition between different thermal states is beneficial in experiments where the feedback signal needs to adapt quickly to avoid particle loss or where high repetition rates are required. However, as shown in Fig. 6.7(c), the experimental transient times that we observe are still orders of magnitude longer than the simulated LQG. We believe this is due to the introduction of the delays to approximate $v(t)$, which reduce the correlation between feedback signal and actual phase space variables.

6.5 Conclusions

In summary, we have demonstrated a novel feedback cooling technique for levitated nanoparticles based on an adaptive optimal protocol, using

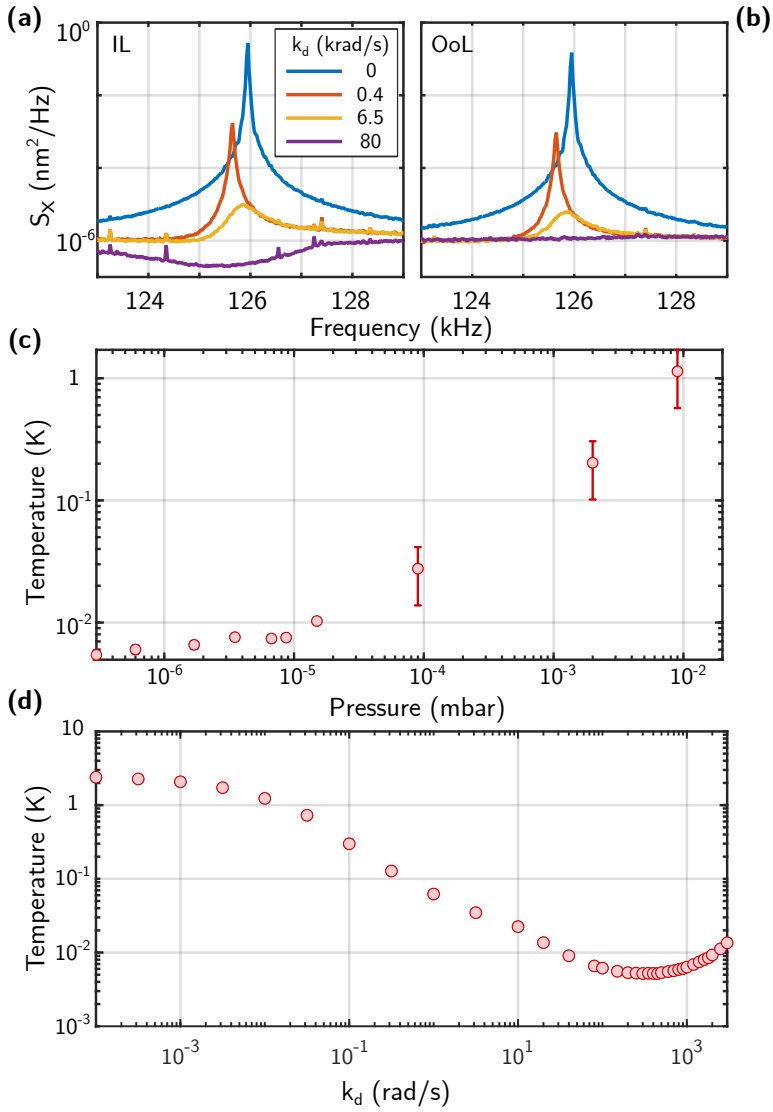

Figure 6.6: **Cold damping**: $k_p = 0$ and varying k_d. (a) PSD of the motion in the x direction recorded from the IL detector signal at various gains for a particle at $p = 10^{-5}$ mbar. For large k_d, $S_x(\omega)$ shows noise squashing. (b) PSD of the motion in the x direction simultaneously recorded with the OoL detector. Noise squashing is avoided. (c) Minimum temperature achieved at different pressures for the optimal k_d (OoL detector). The lowest temperature, $T_{eff} = 5.1 \pm 0.5$ mK, is reached at 3×10^{-7} mbar. (d) Temperature vs. k_d gain at 3×10^{-7} mbar, displaying an optimal gain minimum at $k_d \simeq 700$ rad/s, where $T_{eff} = 5.1 \pm 0.5$ mK (OoL detector). Eq. (6.18) predicts a qualitative behaviour in accordance with data, with optimal k_d a factor 3.4 larger than measured.

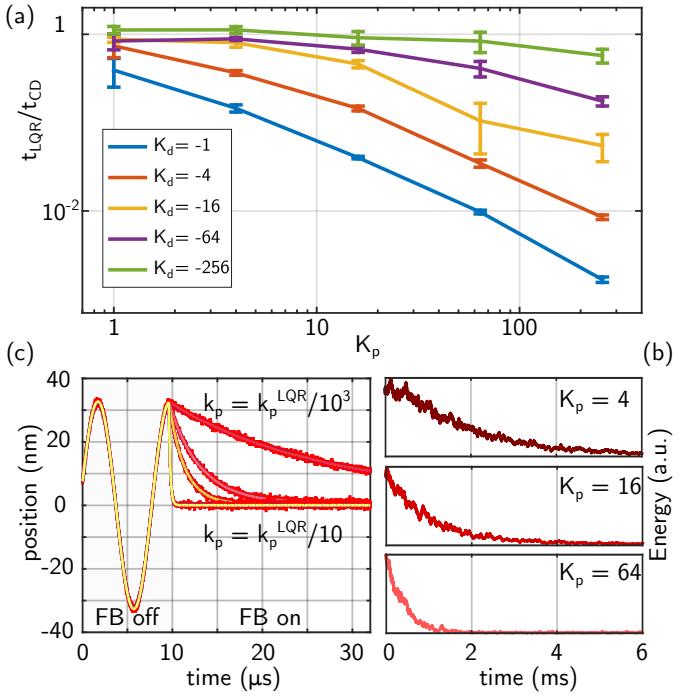

Figure 6.7: **LQR controller** (a) Ratio $t_{\mathrm{LQR}}/t_{\mathrm{CD}}$ of the decay times (energy reduced to $1/e$) of a controller having both K_{p} and K_{d} (gain values in arbitrary FPGA units) and of cold damping ($k_{\mathrm{p}} = 0$) for a pressure $p = 10^{-5}$ mbar. The figure displays how the transient times can be reduced by adding a K_{p} term to the feedback controller. Lines connecting points are added as guides to the eye. (b) Experimental sample traces of the transients after turning on the feedback ($t = 0$) for a fixed value of k_{d}. The transients are reduced by increasing k_{p}. (c) Numerical simulation of controllers approaching the $k_{\mathrm{p}}^{\mathrm{LQR}}$ optimal value. From red (smaller k_{p}) to yellow (larger and closer to $k_{\mathrm{p}}^{\mathrm{LQR}}$). The simulations show how the minimum stationary energy can be reached in a fraction of one oscillation period when k_{p} is properly tuned. In our measurements we never reach μs transients, due to the use of artificial delays to approximate $v(t)$.

electric fields to act on charged particles. Our feedback scheme, which only requires an FPGA and electrodes in the vicinity of the levitated particle, stands out for its robustness and simplicity, and can be easily extended to 3D cooling. Importantly, the usage of OoL detection addresses the limitations of prior implementations [70, 71], preventing potential energy underestimations and hence providing a more accurate temperature readout. In the present experiment we reached a temperature of 5 mK at 3×10^{-7} mbar, corresponding to an occupation number below 1000 phonons.

Shot noise and the optical setup measurement efficiency set the limit for the lowest achievable temperature. However, since detection was not optimized in our work, this leaves potential for future improvements. A possibility to improve the detection efficiency would be exploiting cavity enhanced detection schemes. If, in addition, the experiment is performed at ultra-high vacuum, occupation numbers can be brought down by a factor 10^2 or 10^3, making ground state cooling attainable [170].

In our scheme, the transients between thermal and cooled states are at least one order of magnitude shorter than in regular cold damping (CD). This feature may be important in experiments where sudden changes (such as varying optical potentials when approaching a surface or nanostructure) might lead to particle loss. Furthermore, the ML algorithm optimizes the cooling performance continuously, adapting to different regimes without requiring prior knowledge of the initial particle state within $\tau_{\mathrm{ML}} < 5$ s. This makes it especially suitable for experiments with slowly varying conditions, such as pressure or intensity, minimizing the need for continuous realignment and feedback optimization. Future extension to LQG control (see Annex F) will reduce the minimum achievable temperature two-fold, since the use of a Kalman filter will produce optimal estimates of $v(t)$ (see Annex F), reducing the effect of measurement noise, and eliminate the need for artificial delays in the system. The introduction of further parameters from the Kalman filter will make the ML algorithm indispensable, since optimization will become a high dimensional problem.

We anticipate that the presented adaptive feedback technique will be implemented in a diverse range of levitodynamics experiments, since it can be easily miniaturized and automated. It can be a significant addition in studies requiring robustness and high repetition rates, like the planned future space mission MAQRO [171], or in small devices, such as force and inertial sensors [172] based on levitated objects[5].

[5]See the last section of Annex B for details.

7

Outlook

Ten years have passed since the emergence of modern levitation of micro and nanoparticles in vacuum. During this time, several groups have joined the field, and many techniques—specific to levitated particles—have been developed; the amount of published work is today quite remarkable. A prime example of this is the recent achievement of the motional ground state in a levitated particle, a long-sought milestone [173]. With all these signs of maturity, it is now fair to reflect back on the progress, contributions and future perspectives of particle levitation. We should ask ourselves: what have we learnt? What can we study that is unique to our systems? How should we steer our future efforts?

Currently, the study of levitated objects constitutes a relatively small fraction of research in optomechanics. Still, like any scientific enterprise, there is hope that novel contributions to fundamental research will come out of it. The possibility to develop applications with an impact in everyday life is also being explored. We must keep in mind, however, that reaching the current state (and what lays ahead) requires considerable time. Recall, as recounted in the introduction, that optomechanics and nanoparticle levitation is built upon many previous scientific contributions: the ones of scientists like A. Ashkin, V. Braginsky, D. Wineland or W. Paul. Their ideas entered our collective knowledge decades ago, but at the time it was hard to imagine many of the applications that would result.

After the years of lethargy that followed the papers of Ashkin, the levitation of nanoparticles in vacuum was reinitiated by the works of T. Li [54, 70] and J. Gieseler [55, 83]. Since then, the results of this harvest haven't produced radically new insights into the laws of physics, but it would be unjust to say that the field has not advanced. In just a few years, the experimental know-how has increased tremendously, and proposals that a few years ago appeared to be hard are now within reach. In other words, levitation

optomechanics is showing signs of "ripeness", and physically novel results can be expected in the next decade.

In the following paragraphs, we present possible directions, experiments and applications of systems realized with levitated particles. We also discuss its potential impact.

7.1 Quantum mechanics with levitated particles

Levitated particles have several advantageous features when compared to clamped resonators. They naturally have a single mechanical mode per axis and are highly isolated from its environment. On top of that, in levitated systems the trapping potential can be modulated over time, and virtually any type of material or geometry can be used—something that, due to fabrication constraints, is not possible in MEMS. Being completely detached from any substrate, levitated objects allow us to envision matter-wave interference experiments at a greater scale than ever before[1]. They also offer an ideal platform to construct macroscopic cat states [52], assess the validity of collapse models [58, 59], and study quantum decoherence mechanisms [58].

By extending the range of materials, trapped nanoparticles also enable us to work with internal spins and emitters. In a recent experiment, an ensemble of internal spins was coupled to a torsional degree of freedom of a levitated microdiamond [175]; however, scaling this coupling down to the single defect level to produce pure quantum states will require more work. In this thesis [98], we have reported on the first part of this landmark by demonstrating the detection of a single levitated NV in vacuum [98]. Other degrees of freedom specific to levitated objects are Euler angles, in studies of rotation [176, 177], or lattice phonons, that due to its scale and decoupling from the environment may behave in unexpected or counter-intuitive ways [178]. All these possibilities require the realization of arbitrary quantum states and their precise control thereafter, something that, so to say, is still in the field's wish list.

The ground state of a macroscopic system was achieved for the first time ten years ago [36, 37, 38], in experiments with MEMS; these works established that quantum mechanics is a good description of reality at the "macro" scale. Hence, even though the recently achieved sideband cooling ground state of a levitated particle [173] marks an extraordinary milestone, it mostly represents a proof-of-concept of the experiments that may lie in the future. Still, this study and similar cavity-based efforts [179, 180] have

[1] So far, the heaviest objects to be used in such experiments are organic molecules [174], in the group of Markus Arndt.

demonstrated that the ground state of the motion can be achieved with a setup at room temperature. This is a technical novelty in optomechanics that can simplify the study of the classical to quantum transition.

A different path towards the ground state is feedback cooling. The approach introduced in this thesis—cooling a charged levitated particle through electric fields—has also proved to be extremely efficient and fruitful [106, 181]; less than one year after its appearance, it has already produced occupation numbers $\langle n \rangle < 10$ [182]. If particle detection is improved, the pressures are lowered to ultra-high vacuum conditions and better FPGA electronics are introduced (i.e., better boards with negligible signal delays and optimal state estimation [160]), electric feedback cooling has the potential to become the easiest and cheapest way to achieve the ground state in any physics experiment so far. Furthermore, it has the potential of being used in more general systems, such as in recently proposed levitated electromechanical systems [156].

7.2 Stochastic thermodynamics with levitated particles

For a long time, it was believed that the correlations between the phase space variables (x, v) of a Brownian process were too fast to be measurable in practice. However, more than 100 years after Einstein's seminal paper [183], the first experimental observations of these short-time correlations were achieved with optical tweezers, levitating a microsphere in vacuum [54]. This work paved the way of many more studies of stochastic processes with single levitated particles.

During these last years, many different equations of motion—including linear and nonlinear terms—and measurements of stochastic thermodynamic quantities, such as energy or work, have been realized with levitated particles [184]. Feedback control has been included often, either for automation of the experiment or to realize more complex processes.

Most of these works were carried out in the underdamped regime which, before the advent of levitated particles, was largely inaccessible. This allowed the verification of classical models for thermal noise, the comparison of different formalisms for stochastic processes[2] and also generalized the use of computer simulations to predict and check the results. Moreover, by working at the single particle level, it improved our understanding of time and noise as memory-erasing features in ergodic processes; in the past, this had been obfuscated by the need to work with ensembles.

[2]E.g. the Focker-Planck equation or stochastic calculus with the Itô integral.

With the classical thermodynamics models firmly established, an interesting research direction for statistical physics with levitated particles involves entering the quantum regime. In this domain, not only the concepts are more complex to realize on computers, but often it is not even clear what the evolution equations are. Working with *quantum* Brownian particles would allow the study of non-thermal quantum noise sources, the exploration of the constraints on the efficiency of non-Markovian quantum engines or investigating information extraction in the presence of uncertainty relations.

7.3 Sensing with levitated particles

Levitated objects are suited to perform sensing experiments or even to develop commercial sensor devices. As an example, levitated particles hosting atom-like defects in the crystal lattice have been used to perform thermometry [185]; they can also sense electromagnetic fields [141, 142], via the split of the electron energy levels. However, performing an experiment is different from developing a robust, marketable product. In technological applications one has to ponder not only whether the application is possible, but also if there is a market for it. In the latter case, perhaps there are already cheaper products that carry out the same job.

Force and acceleration sensors are often proposed as possible applications of levitated particles. Nevertheless, the two are fundamentally different cases [186]: force sensing is the detection of forces $g(t)$ acting *upon* the oscillator's mass, whereas in an accelerometer the driving acts on the housing instead of on the oscillator itself. This has consequences in the sensitivity of the device, which is ultimately limited by thermal noise and integration time. In a force sensor, the sensitivity scales with the sensor's mass m: the smaller the mass, the smaller the force that can be detected. In an accelerometer it is the other way around: the minimum acceleration that can be detected scales inversely with the mass. For this reason, when building an accelerometer, engineers include a mass that is as large as possible; in levitated particles, this mass is rather small when compared to larger devices made with MEMS.

One should notice that the sensor's sensitivity does not only depend on the mass. Eventually, it is also limited by the mechanical stability of the system, which is not accounted for in a harmonic oscillator model[3]. For instance, jitter in the resonance frequency might result in a decrease of the sensitivity or in incorrect values of the measured driving intensity. Active stabilization through feedback is a potential route towards sensors based

[3]See the last section of Annex B for details.

on levitated particles. With a "cold damping" [106], the resonance peak is broadened (reducing the relative effect of jitter), the nonlinearities are minimized and the memory of the system is shortened (i.e., signal remnants from some past event are quickly eliminated).

Due to the small masses demonstrated so far, the development of a commercial accelerometer based on levitated nanoparticles might find some initial difficulties; its prospects will improve if means to work with larger particles are found. But, even if levitation is restricted to small particles, their use as torque sensors may find some advantages over commercial devices, specially since they offer possibilities (rotation control and free fall) that are completely absent in MEMS. For example, torque could be detected as a coupling between axes during short, repeated free fall experiments. Regarding force sensing, levitated particles constitute a good compromise between a small mass and ease of use; atoms and ions have smaller masses, but are way more restrictive in the experimental conditions. To use them as force sensors, the first important question that needs to be answered is *which* force is to be measured. For instance, approaching devices in the vicinity of levitated particles can be quite complex, but if this problem is solved [187], levitated particles can open up the exploration of short-range interactions [188], such as the Casimir force. Alternatively, they can be used to measure static forces, for example by detecting displacements in the trap center [189, 190] or, again, with free fall experiments [191].

Glossary

$I(\,\cdot\,)$	Optical intensity.
Q	Charge.
$S_x(\omega)$	Power spectral density of $x(t)$.
T	Temperature.
W_t	Wiener process.
Γ	Normalized damping γ/m.
Ω	Paul trap secular frequency.
$\Phi(\,\cdot\,)$ or $V(\,\cdot\,)$	Electric potential.
$\Psi(\,\cdot\,)$	Energy potential.
ϵ_0	Electric permittivity in vacuum.
$\eta(t)$	White noise process.
γ	Damping.
$\mathbb{E}[\,\cdot\,]$ or $\langle\,\cdot\,\rangle$	Expected value, ensemble average.
$\mathcal{Q}$	Q-factor ω_0/Γ.
μ_0	Magnetic permeability in vacuum.
ω	Angular frequency variable.
ω_0	Natural angular frequency.
ω_d	Driving angular frequency.
$\propto$	"Proportional to" symbol.
σ	Noise intensity.
$\mathbf{B}(\,\cdot\,)$ or $B(\,\cdot\,)$	Magnetic field.
$\mathbf{E}(\,\cdot\,)$ or $E(\,\cdot\,)$	Electric field.
$\triangleq$	New definition.
$g^{(2)}(\tau)$	Intensity correlation.

k_{B}	Boltzmann's constant.
m	Mass.
r	Position along the radial direction.
t	Time variable.
v	Velocity.
w	Gaussian beam width.
x	Position along the x direction.
y	Position along the y direction.
z	Position along the z direction.

Acronyms

APD	avalanche photodiode. 73, 75, 76,
BPF	band pass filter. 46, 60, 96,
CD	cold damping. 86, 88, 91–93, 100, 102, 103,
CoM	center of mass. 8–12, 14, 15, 31, 39, 40, 62, 67–69, 71, 72, 77, 78, 81, 83, 85–88, 91, 92, 94, 95, 99,
EMCCD	electron multiplying camera. 73,
FPGA	Field-Programmable Gate Array. 12, 46, 48, 59, 60, 71, 74, 78, 85–87, 95–99, 102, 103,
HBT	Hanbury, Brown and Twiss. 73,
IL	in-loop. 89–93, 95, 98, 99, 101,
LIGO	Laser Interferometer Gravitational-Wave Observatory. 8,
LPF	low pass filter. 96, 97,
LQG	linear-quadratic Gaussian regulator. 87, 88, 93, 94, 100, 103,
LQR	linear-quadratic regulator. 12, 85–88, 94, 96, 100, 102,

MEMS	microelectromechanical systems. 8, 9, 106, 108, 109,
ML	machine learning. 86, 88, 95, 96, 98, 100, 103,
MSD	mean square displacement. 36,
NA	numerical aperture. 28, 29, 48, 54, 69, 73, 74, 77,
NV	nitrogen vacancy. 9, 10, 67–70, 73–77, 81, 82, 84, 106, , 115
OBJ	objective. 25, 28, 46, 48, 60, 69, 73, 74, 78, 95, 96,
OC	optimal control. 86–88, 100,
ODE	ordinary differential equation. 17, 30,
OoL	out-of-loop. 90–92, 95, 97–99, 101, 103,
OU	Ornstein-Uhlenbeck. 32, 35, 39, 40, 46, 54, 55,
PFC	parametric feedback cooling. 10, 77, 79, 86, 88, 95, 96, 99, 100,
PSD	power spectral density. 25, 33, 34, 37, 40, 46, 47, 49, 54, 55, 59, 77, 83, 89–93, 99–101,
QPD	quadrant photodiode. 46, 48, 60, 74, 78, 81,
SDE	stochastic differential equation. 32, 34,
WKB	Wentzel–Kramers–Brillouin. 39, 40, 43–45, 47, 49, 55,

List of Figures

List of publications

Publications as 1st author

1. Gerard P. Conangla, Andreas W. Schell, Raúl A. Rica, and Romain Quidant. "Motion control and optical interrogation of a levitating single NV in vacuum", *Nano letters*, 18(6):3956–3961, 2018

2. Gerard P. Conangla, Francesco Ricci, Marc T. Cuairan, Andreas W. Schell, Nadine Meyer, and Romain Quidant. "Optimal feedback cooling of a charged levitated nanoparticle with adaptive control", *Physical Review Letters*, 122(22):223602, 2019

3. Gerard P. Conangla, Dwight Nwaigwe, Jan Wehr, and Raúl A. Rica. "Overdamped dynamics of a Brownian particle levitated in a Paul trap", accepted in *Physical Review A*, 2019

4. Gerard P. Conangla, Raúl A. Rica, and Romain Quidant. "Extending levitodynamics to absorbing objects with hybrid Paul-optical traps", in preparation.

Other works

1. Francesco Ricci, Marc T. Cuairan, Gerard P. Conangla, Andreas W. Schell, and Romain Quidant. "Accurate mass measurement of a levitated nanomechanical resonator for precision force-sensing", *Nano letters*, 19(10):6711–6715, 2019

2. Gerard P. Conangla. "Sensing with the harmonic oscillator", *arXiv preprint arXiv:1905.02612*, 2019

A

Review of stochastic calculus

A.1 Stochastic calculus theory

A.1.1 The Wiener process

Given a probability space $(\Omega, \mathcal{F}, P)$ and a measurable space (S, Σ), a collection of S-valued random variables on Ω, indexed by a totally ordered set T (the "time") is called an S-valued *stochastic process*. That is, a collection of random variables representing the evolution of some system of random values over time.

A stochastic process can be characterized by several common properties:

- *Stationarity.* A stationary process is a stochastic process whose unconditional joint probability distribution does not change when shifted in time. A *wide-sense* stationary process is a process X_t such that its first two moments are constant, i.e., the expected value is constant $\mathbb{E}[X_t] = \mu$ and its autocorrelation $\mathbb{E}[X_t X_{t+\tau}] = \mathrm{R}(\tau)$ is a function of τ only.

- *Ergodicity.* A stationary random process X_t is ergodic if its time average

$$\text{avg} = \lim_{t\to\infty} \frac{1}{T} \int_0^t X_t \, \mathrm{d}t \tag{A.1}$$

  is the same as its average over the probability space $\mathbb{E}[X_t]$ (also known as its ensemble average in physics).

- The *Markovian property.* A process has the Markovian property (i.e., it is a Markov process) if, for each $A \in \Sigma$ and each $s, t \in T$ with $s < t$,

$$\mathbb{P}(X_t \in A | \mathcal{F}_s) = \mathbb{P}(X_t \in A | X_s).$$

Loosely speaking, this means that one can make predictions for the future of the process based solely on its present state just as well as one could knowing the process's full history. For this reason they are usually called memoryless processes. An important example of Markov processes are *Markov chains*, where the process undergoes transitions between a finite set of states. They can be modelled with the *master equation*

$$\frac{\mathrm{d}\vec{P}}{\mathrm{d}t} = \mathbf{A}(t)\vec{P},$$

where in this case $\mathbf{A}$ is time independent.

- The *martingale property*. A stochastic process is a martingale if

$$\mathbb{E}(X_{t_{n+1}} \mid X_{t_1}, \ldots, X_{t_n}) = X_{t_n}$$

for increasing times $t_1 < \ldots < t_n < t_{n+1}$, so the expected value of the process at any point in the future is exactly the current value of the process.

The *Wiener process*, commonly written W_t, is an important example of continuous stochastic process, since many other processes can be defined from it. It is characterised by the following properties:

1. $W_0 = 0$ almost surely.
2. $W_u - W_t$ is normally distributed with $\mu = 0$ and $\sigma^2 = u - t$.
3. W_t has independent increments: if $0 \leq s < t < u$ then $W_u - W_t$ is independent of $W_t - W_s$.
4. W_t is continuous in t with probability 1.

The process also satisfies

$$\mathrm{cov}(W_s, W_t) = \min(s, t)$$

(this follows from the fact that non-overlapping increments are independent) and has quadratic variation $[X_t, X_t] = t$. The Wiener process can also be thought of as the integral of a Gaussian white noise process, so that if $\eta(t)$ is white noise, the formal substitution $\eta(t)\mathrm{d}t = \mathrm{d}W_t$ can be made.

A.1.2 The Wiener-Khinchin theorem

The *Wiener–Khinchin theorem* relates the autocorrelation function of a wide-sense stationary stochastic process x_t

$$\mathrm{R}_{xx}(\tau) = \mathbb{E}[x(t)x(t+\tau)] \tag{A.2}$$

to the spectral density

$$S_{xx}(\omega) = \mathbb{E}\left[|\hat{x}(\omega)|^2\right], \tag{A.3}$$

via the Fourier transform

$$S_{xx}(\tau) = \int_{-\infty}^{+\infty} \mathrm{R}_{xx}(f) e^{-i2\pi f\tau}\,\mathrm{d}f, \tag{A.4}$$

by observing that

$$\begin{aligned}\mathbb{E}\left[|\hat{x}(\omega)|^2\right] &= \mathbb{E}\left[\frac{1}{T}\int_0^T x^*(t)e^{i\omega t}\,\mathrm{d}t \int_0^T x(t')e^{-i\omega t'}\,\mathrm{d}t'\right] \\ &= \frac{1}{T}\int_0^T \int_0^T \mathbb{E}\left[x^*(t)x(t')\right] e^{i\omega(t-t')}\,\mathrm{d}t\,\mathrm{d}t'. \end{aligned} \tag{A.5}$$

In the last expression, one can make the change of variables $\tau = t - t'$, and with the limits of integration approaching infinity, the resulting power spectral density $S_{xx}(\omega)$ and the autocorrelation function $\mathrm{R}_{xx}(\tau)$ become Fourier transform pairs. In this thesis, all the spectral densities are assumed to be two-sided.

Recall that the *Fourier transform* of a continuous function $x(t)$ is defined as

$$\hat{g}(f) = \int_{-\infty}^{+\infty} g(x)\ e^{-i2\pi ft}\,\mathrm{d}x.$$

This transformation replaces the time variable by a frequency variable $t \to f$. Another usual definition, and the one that we follow in this thesis, uses ω instead of $2\pi f$: in this case the inverse Fourier transform needs a $1/2\pi$ multiplying factor, and $\hat{g}(f) = \hat{g}(\frac{\omega}{2\pi})$.

A.1.3 Itô calculus

The *Itô integral* is defined as

$$\int_0^T f(W_t, t)\,\mathrm{d}W_t,$$

where $X_t = f(W_t, t)$ and the integral is interpreted as the limit of

$$\sum_{i=0}^{k-1} X_{t_i} \left(W_{t_{i+1}} - W_{t_i}\right).$$

It has the important property of producing martingales when $f(W_t, t)$ is square integrable. The *Stratonovich integral*, on the other hand, is defined as

$$\sum_{i=0}^{k-1} \frac{X_{t_{i+1}} + X_{t_i}}{2} \left(W_{t_{i+1}} - W_{t_i}\right).$$

Stratonovich integrals obey the ordinary chain rule, whereas Itô integrals obey Itô's lemma. Conversion between the two is obtained with the expression

$$\int_0^T f(W_t, t) \circ \mathrm{d}W_t = \frac{1}{2}\int_0^T \frac{\partial f}{\partial W}(W_t, t)\,\mathrm{d}t + \int_0^T f(W_t, t)\,\mathrm{d}W_t.$$

The most general stochastic differential equation takes the expression

$$\mathrm{d}X_t = b(t, X_t)\mathrm{d}t + \sigma(t, X_t)\mathrm{d}W_t,$$

where $\mathrm{d}t$ is the time differential and $\mathrm{d}W_t$ is the differential of a Wiener process. This has to be understood as an integral equation, as stochastic processes are not, in general, differentiable. The differentials notation is just a convenient (and shorter) way to express the same idea. If this is not said specifically, the integral with respect to $\mathrm{d}W_t$ will always be taken in Itô's sense.

In stochastic calculus, the equivalent of the chain rule is known as *Itô's lemma*: let $Y_t = g(t, X_t)$, where X_t is an Itô process defined by a SDE. Then, Y_t is also an Itô process and

$$\mathrm{d}Y_t = \frac{\partial g}{\partial t}(t, X_t)\mathrm{d}t + \frac{\partial g}{\partial x}(t, X_t)\mathrm{d}X_t + \frac{1}{2}\frac{\partial^2 g}{\partial x^2}(t, X_t)\cdot(\mathrm{d}X_t)^2,$$

where $(\mathrm{d}X_t)^2$ is computed according to the rules $\mathrm{d}t\cdot\mathrm{d}t = \mathrm{d}t\cdot\mathrm{d}W_t = \mathrm{d}W_t\cdot\mathrm{d}t = 0$, $\mathrm{d}W_t \cdot \mathrm{d}W_t = \mathrm{d}t$. More generally, $\mathrm{d}X_t \cdot \mathrm{d}Y_t = \mathrm{d}[X, Y]_t$.

Generally, there is no explicit solution for SDEs. However, it is possible to find one in the linear case, which has the following equation:

$$\mathrm{d}X_t = \left(A(t)X_t + a(t)\right)\mathrm{d}t + \sigma(t)\mathrm{d}W_t, \tag{A.6}$$

In the scalar case, $A(t)$ and $a(t)$ are numerical coefficients; in the general multivariate case $A(t)$ is a matrix and $a(t)$ is a vector. In the scalar case,

we may find the solution by the following transformation and Itô's lemma:

$$\begin{aligned}\mathrm{d}\left(e^{-\int A(t)\mathrm{d}t}X_t\right) &= -A(t)e^{-\int A(t)\mathrm{d}t}X_t\mathrm{d}t + e^{-\int A(t)\mathrm{d}t}\mathrm{d}X_t \\ &= e^{-\int A(t)\mathrm{d}t}\left(-A(t)X_t\mathrm{d}t + \mathrm{d}X_t\right).\end{aligned}$$

Therefore

$$\begin{aligned}e^{\int A(t)\mathrm{d}t}\cdot\mathrm{d}\left(e^{-\int A(t)\mathrm{d}s}X_t\right) = \\ \mathrm{d}X_t - A(t)X_t\mathrm{d}t = a(t)\mathrm{d}t + \sigma(t)\mathrm{d}W_t\end{aligned}$$

and

$$\mathrm{d}\left(e^{-\int A(t)\mathrm{d}t}X_t\right) = e^{-\int A(t)\mathrm{d}t}\left(a(t)\mathrm{d}t + \sigma(t)\mathrm{d}W_t\right),$$

so an explicit solution to the SDE will be

$$\begin{aligned}X_t = e^{\int_0^t A(t)\mathrm{d}t}\cdot X_0 + e^{\int_0^t A(t)\mathrm{d}t} \\ \cdot\left(\int_0^t e^{-\int A(s)\mathrm{d}s}a(s)\mathrm{d}s + \int_0^t e^{-\int A(s)\mathrm{d}s}\sigma(s)\mathrm{d}W_s\right).\end{aligned} \tag{A.7}$$

In what follows we mention some remarkable SDEs:

- *Standard Brownian motion*

  $$\mathrm{d}X_t = \sigma\mathrm{d}W_t$$

  so $X_t = \sigma W_t$. In physics, $\mathbb{E}(X_t^2) = 2Dt$, where D is known as the diffusion constant or diffusivity. Therefore, in this case $\sigma^2 = 2D$.

- *Ornstein-Uhlenbeck process*

  $$\mathrm{d}X_t = \theta(\mu - X_t)\,\mathrm{d}t + \sigma\,\mathrm{d}W_t,$$

  which is the only non-trivial, Gaussian, stationary and Markovian process. The solution of the SDE is

  $$X_t = X_0e^{-\theta t} + \mu(1 - e^{-\theta t}) + e^{-\theta t}\int_0^t \sigma e^{\theta s}\,\mathrm{d}W_s.$$

  This process is used to describe the evolution of a free Brownian particle

  $$\begin{aligned}\mathrm{d}x &= v\mathrm{d}t, \\ \mathrm{d}v &= \frac{1}{m}\left(-\gamma v\mathrm{d}t + \sigma\mathrm{d}W_t\right).\end{aligned}$$

Since the process must satisfy the equipartition theorem, it can be seen that $\sigma = \sqrt{2\gamma k_{\mathrm{B}} T}$. This relation is known as the *fluctuation-dissipation* theorem, and similar expressions can be obtained for other systems and degrees of freedom (such as electric circuits). From $\mathbb{E}(X_t^2) = 2Dt$, we obtain the following result

$$D = \frac{k_{\mathrm{B}} T}{\gamma},$$

sometimes known as Stokes-Einstein relation.

- *Itô diffusions* are SDEs where the functions $b(X_t)$ and $\sigma(X_t)$ don't have explicit t dependence

  $$\mathrm{d}X_t = b(X_t)\,\mathrm{d}t + \sigma(X_t)\,\mathrm{d}W_t.$$

  Itô diffusions are always Markov processes (since they have the strong Markov property).

During calculations with stochastic processes defined by SDEs, it is common to use the following identities and theorems:

- Let $X_t = \int_0^t f(s)\mathrm{d}W_s$. If $f(s)$ is deterministic, then X_t will follow a zero mean normal distribution with variance

  $$\mathbb{E}(X_t^2) = \int_0^t f(s)^2\,\mathrm{d}s$$

  so, in particular, the expected value of the integral of a deterministic function by $\mathrm{d}W_s$ will always be zero.

- The time change formula for Itô integrals is

  $$\int_0^{\alpha_t} v(s,\omega)\,\mathrm{d}W_s = \int_0^t v(\alpha_r,\omega)\sqrt{\alpha_r'}\,\mathrm{d}W_r,$$

  where α_r' is the derivative with respect to r of $\alpha(r,\omega) = s$.

- *Itô's isometry*: let X_t be a predictable process (al continuous processes are predictable). Then

  $$\mathbb{E}\left[\left(\int_0^T X_t\,\mathrm{d}W_t\right)^2\right] = \mathbb{E}\left[\int_0^T X_t^2\,\mathrm{d}t\right].$$

  By applying the polarization identity we get the more general result

  $$\mathbb{E}\left[\int_0^T f(u)\,\mathrm{d}W_u \int_0^S g(v)\,\mathrm{d}W_v\right] = \mathbb{E}\left[\int_0^{\min(T,S)} f(u)g(u)\,\mathrm{d}u\right],$$

  where $f(t)$ and $g(t)$ are stochastic processes. The Itô isometry is often used to calculate covariances of stochastic processes.

- By Fubini's theorem,

$$\mathrm{d}\,\mathbb{E}(f(X_t)) = \mathbb{E}(\mathrm{d}f(X_t)).$$

  This needs to be understood in the integral sense, and can be used to calculate statistical moments (e.g., $f(X_t) = X_t^2$).

A.1.4 Advanced topics

It is fundamental for many applications to associate a second order partial differential operator (i.e., a 2nd order differential equation) to Itô diffusions. For an Itô diffusion $(X_t)_{t\geq 0}$, with $X_0 = x$, we define the *generator* A by

$$Af(x) = \lim_{t\downarrow 0} \frac{\mathbb{E}^x(f(X_t)) - f(x)}{t}. \tag{A.8}$$

In this equation $f(x)$ is introduced without much intuition, but as it will be seen later, it is used to study the moments of the process and its probability density function. By Taylor's formula, equation (A.8) can be understood as

$$\mathbb{E}^x f(X_t) \approx f(x) + tAf(x)$$

for small $t \geq 0$, so the generator essentially describes the movement of the process in an infinitesimal time interval. The set of all functions f for which this limit exists at a point x is denoted $D_A(x)$, while D_A denotes the set of all f for which the limit exists for all $x \in \mathbb{R}$. One can show that all compactly-supported C^2 functions belong to D_A and

$$Af(x) = \sum_i b_i(x)\frac{\partial f}{\partial x_i}(x) + \frac{1}{2}\sum_{i,j}\left(\sigma(x)\sigma(x)^\top\right)_{i,j}\frac{\partial^2 f}{\partial x_i\,\partial x_j}(x).$$

Several important results and theorems use the concept of the generator:

- *Dynkin's formula*: Let X_t be a $\mathbb{R}$ valued Itô diffusion, let τ be a stopping time with $\mathbb{E}^x(\tau) < \infty$, and let f be C^2 with compact support. Then

$$\mathbb{E}^x[f(X_\tau)] = f(x) + \mathbb{E}^x\left[\int_0^\tau Af(X_s)\,\mathrm{d}s\right].$$

  Dynkin's formula can be seen as a stochastic generalisation of the fundamental theorem of calculus.

- *Kolmogorov's backward equation*: the Kolmogorov backward equation describes the evolution of the statistics (i.e., moments) of a stochastic process. Let X_t be a Markov process, such as an Itô diffusion. If we define $u(t,x) = \mathbb{E}^x(f(X_t))$, with $f \in C^2(\mathbb{R}^n)$, then

$$\begin{aligned} \frac{\partial u}{\partial t} &= Au \qquad t > 0,\, x \in \mathbb{R}^n \\ u(0,x) &= f(x) \qquad x \in \mathbb{R}^n \end{aligned}$$

  This equation is usually seen with an end condition and a negative sign in front of the time derivative. This can be recovered by performing the change $t \to T - t$.

$$\begin{aligned} -\frac{\partial u}{\partial t} &= Au \qquad t > 0,\, x \in \mathbb{R}^n \\ u(T,x) &= f(x) \qquad x \in \mathbb{R}^n \end{aligned}$$

  This equation can be particularised when f is the indicator function I_B of some set B. Then

$$u(r,y) = \mathbb{E}_{r,y}(I_B(X_T)) = \mathbb{P}(X_T \in B | X_r = y)$$

  by the properties of the indicator function. Thus, the backward Kolmogorov equation can be written for transition probabilities

$$\begin{aligned} -\frac{\partial P}{\partial t} &= AP \qquad 0 < t < T,\, x \in \mathbb{R}^n \\ P(T,x) &= I_B(x) \qquad x \in \mathbb{R}^n \end{aligned}$$

  with $P(t,x) = \mathbb{P}(X_T \in B | X_t = x)$, and also as densities, if they exist.

- *Kolmogorov's forward equation*, also known as the Fokker-Planck equation, is a partial differential equation that describes the time evolution of the probability density function (if it exists) of a stochastic process. Let A^* be the adjoint operator of A, defined by

$$A^* f(x) = -\sum_i \frac{\partial}{\partial x_i}(b_i f(x)) + \frac{1}{2}\sum_{i,j} \frac{\partial^2}{\partial x_i\, \partial x_j}(a_{ij} f(x)),$$

  where $a_{ij} = \sum_k \sigma_{ik}\sigma_{jk}$. Then, the forward Kolmogorov equation for a Markov process is

$$\begin{aligned} \frac{\partial p(t,x)}{\partial t} &= A^* p(t,x) \qquad t > 0,\, x \in \mathbb{R}^n \\ p(0,x) &= f(x) \qquad x \in \mathbb{R}^n \end{aligned}$$

- Let X_t be an Itô diffusion satisfying the SDE

$$\mathrm{d}X_t = -\nabla\Psi(X_t)\,\mathrm{d}t + \sqrt{2\beta^{-1}}\,\mathrm{d}W_t,$$

where $\beta > 0$ plays the role of an inverse temperature and $\Psi : \mathbb{R}^n \to \mathbb{R}$ is a scalar potential satisfying suitable smoothness and growth conditions. Then, the Fokker-Planck equation has a unique stationary solution (an invariant measure, or density distribution without time dependency) known as the *Gibbs distribution*:

$$\rho_\infty(x) = Z^{-1}\exp(-\beta\Psi(x))$$

where Z is the *partition function* and is given by

$$Z = \int_{\mathbf{R}^n} \exp(-\beta\Psi(x))\,\mathrm{d}x.$$

- *Feynman-Kac formula*: the Feynman-Kac formula is a slight generalisation of the Kolmogorov backward equation. Let X_t be a Markov process (notice that usually Markov processes are Itô diffusions) satisfying

$$\mathrm{d}X_t = b(X_t, t)\,\mathrm{d}t + \sigma(X_t, t)\,\mathrm{d}W_t.$$

Then the conditional expectation

$$u(x,t) = \mathbb{E}\left[\int_t^T e^{-\int_t^r V(X_\tau,\tau)\,\mathrm{d}\tau} f(X_r, r)\mathrm{d}r + e^{-\int_t^T V(X_\tau,\tau)\,d\tau}\psi(X_T)\middle| X_t = x\right]$$

satisfies the following PDE

$$\begin{aligned}&\frac{\partial u}{\partial t} + b(x,t)\frac{\partial u}{\partial x} + \tfrac{1}{2}\sigma^2(x,t)\frac{\partial^2 u}{\partial x^2} - V(x,t)u + f(x,t) = 0\\ &u(x,T) = \psi(x) \qquad x \in \mathbb{R}\end{aligned}$$

A.2 Simulation of stochastic differential equations

The fundamental idea behind all techniques for simulating SDEs is the fact that variances are additive, while standard deviations are not. Therefore, since $W_t \sim \sqrt{t}\cdot N(0,1)$, after a discretization $\mathrm{d}t$ in the time variable has been introduced,

$$\mathrm{d}W_t \simeq \sqrt{\mathrm{d}t}\cdot\mathcal{N}(0,1).$$

In other words, the differential of the Wiener process is proportional to $\sqrt{\mathrm{d}t}$ instead of proportional to $\mathrm{d}t$, which at first sight would seem more intuitive.

To see that this is indeed the case, let us take a process defined by the recursive equation $X_{i+1} = X_i + R_{i+1}\sqrt{\Delta t}$, where R_i are independent identically distributed normal random variables. After two steps, we have

$$X_2 = X_0 + (R_1 + R_2)\sqrt{\Delta t}.$$

But $R_1 + R_2$ is normal with variance 2, so we can write it as $\sqrt{2}R$, where $R_{12} \sim R_i$. Thus, we get

$$X_2 = X_0 + \sqrt{2}R_{12}\sqrt{\Delta t} = X_0 + R_{12}\sqrt{2\Delta t},$$

which is exactly the same as taking a single time step of twice the length. This doesn't happen if one takes the stochastic component to be $R_i \Delta t$ instead, since the variances add up linearly. After n time steps we will have accumulated a variance of $n\sigma^2$.

Now, assume X_n is an approximation (which we obtained by whatever means) of a continuous time process X_t defined by a SDE, which at discrete time steps takes the values $X(t_n)$. Clearly, both X_n and $X(t_n)$ are random variables, so in what sense does $|X_n - X(t_n)| \to 0$ as $\Delta t \to 0$?

There are many, non-equivalent, definitions of convergence for sequences of random variables, but the two most common and useful in numerical SDEs are

- Weak convergence, which captures the error of the mean. A method is said to be weakly convergent if

  $$\lim_{\Delta t \to 0} |\mathbb{E}(X_n) - \mathbb{E}(X(t_n))| = 0.$$

  Weak convergence captures the average behaviour.

- Strong convergence, which captures the mean of the error:

  $$\lim_{\Delta t \to 0} \mathbb{E}|X_n - X(t_n)| = 0.$$

  Strong convergence is important to follow paths accurately: that means that, given a certain W_t driving the process of the SDE, a method using a discretization of *the same Wiener process* will converge to the original, time-continuous, sample path.

Strong and weak convergence orders (which we will call p and q) do not need to be the same, but strong convergence always implies weak convergence, so $p \leq q$.

A.2.1 Methods for SDEs

The Euler–Maruyama method (also called the Euler method) is the most basic numerical method for SDEs. It is a simple generalization of the Euler method for ordinary differential equations to stochastic differential equations[1], and has a weak order of 1 and a strong order of 1/2. Consider the SDE

$$\mathrm{d}X_t = a(X_t)\,\mathrm{d}t + b(X_t)\,\mathrm{d}W_t,$$

with initial condition X_0, and suppose that we wish to solve this SDE on an interval of time $[0, T]$. Then, the Euler–Maruyama approximation to the true solution X_t is the Markov chain defined as

$$Y_{n+1} = Y_n + a(Y_n)\,\Delta t + b(Y_n)\,\Delta W_n,$$

where

$$\Delta W_n = W_{\tau_{n+1}} - W_{\tau_n}.$$

and the time variable t has been discretized in Δt segments. The random variables $\Delta W_n \sim \mathcal{N}(0, \Delta t)$ are independent and identically distributed normal variables.

Several generalizations to SDEs exist for deterministic Runge-Kutta methods, although they become increasingly convoluted for moderate orders. A method of strong order 1 is detailed here, which reduces to the Improved Euler scheme for deterministic ODEs[105].

Consider the vector stochastic process $\mathbf{X}(t) \in \mathbb{R}^n$ that satisfies the general Itô SDE

$$\mathrm{d}\mathbf{X} = \mathbf{a}(t, \mathbf{X})\,\mathrm{d}t + \mathbf{b}(t, \mathbf{X})\,\mathrm{d}W,$$

where drift $\mathbf{a}$ and diffusion $\mathbf{b}$ are sufficiently smooth functions of their arguments. Given a time step Δt and the value $\mathbf{X}(t_k) = \mathbf{X}_k$, then $\mathbf{X}(t_{k+1})$ is calculated recursively with

$$\begin{aligned}
\mathbf{K}_1 &= \mathbf{a}(t_k, \mathbf{X}_k)\Delta t + (\Delta W_k - S_k\sqrt{\Delta t}) \cdot \mathbf{b}(t_k, \mathbf{X}_k), \\
\mathbf{K}_2 &= \mathbf{a}(t_{k+1}, \mathbf{X}_k + \mathbf{K}_1)\Delta t + (\Delta W_k + S_k\sqrt{\Delta t}) \cdot \mathbf{b}(t_{k+1}, \mathbf{X}_k + \mathbf{K}_1), \\
\mathbf{X}_{k+1} &= \mathbf{X}_k + \frac{1}{2}(\mathbf{K}_1 + \mathbf{K}_2),
\end{aligned}$$

where ΔW_k is calculated as detailed above, and $S_k = \pm 1$, each with probability 1/2. Setting $S_k = 0$ will approximate X_t in the Stratonovich sense.

[1] Beware: this means that, for small noise, this method can be expected to behave as the Euler method for deterministic ODEs, i.e., converge very slowly. In such cases, strong methods of higher order should be used.

B

The harmonic oscillator model

B.1 Linear time-invariant systems

A linear constant-coefficient ordinary differential equation, defined by a linear polynomial in the unknown function $x(t)$ and its derivatives, takes the form

$$f\left(x, x', x'', \ \ldots, \ x^{(n)}\right) = g(t), \tag{B.1}$$

where $f(\ldots)$ is a linear function and we added a non-homogeneous term $g(t)$. If we now Fourier transform both sides of the equation, we get

$$p(i\omega)X(\omega) = G(\omega),$$

where $p(i\omega)$ is the characteristic polynomial of the differential equation and $X(\omega)$ and $G(\omega)$ are the Fourier transforms of $x(t)$ and $g(t)$ respectively. Therefore

$$X(\omega) = \frac{1}{p(i\omega)}G(\omega) = H(\omega) \cdot G(\omega),$$

where we defined the frequency response (or transfer function) $H(\omega) = \frac{1}{p(i\omega)}$. By the convolution theorem, if we apply the inverse Fourier transform we obtain

$$\begin{aligned} \mathcal{F}^{-1}\left(X(\omega)\right) &= \mathcal{F}^{-1}\left(H(\omega) \cdot G(\omega)\right) \\ x(t) &= h(t) * g(t). \end{aligned}$$

Here, $h(t)$ is known as the *impulse response* of the system, and is used to find $x(t)$ for an arbitrary driving $g(t)$.

B.2 The harmonic oscillator

The harmonic oscillator is a 2nd order constant coefficient linear ODE that can be used as a first approximation or a paradigmatic model of most simple oscillatory systems. In the most general case, starting from Newton's second law, the equation reads

$$m\ddot{x} + m\Gamma\dot{x} + kx = F(t),$$

where $m\Gamma\dot{x}$ is a damping force, kx is a restoring force[1] (of arbitrary origin) and $F(t)$ a driving force.

Conserved quantities

When $\Gamma = F(t) = 0$, the system is Hamiltonian, and its energy takes the form

$$H = \frac{p^2}{2m} + \frac{1}{2}m\omega_0^2 x^2,$$

where $\omega_0 = \sqrt{\frac{k}{m}}$; it can be proved that this is the only conserved quantity of the system (Hamiltonian systems with $2n$ degrees of freedom can have, at most, n constants of motion). The equality between energy and Hamiltonian is justified because H doesn't explicitly depend on t.

The first summand is the kinetic energy, and the second the (restoring force) potential energy. When feedback is introduced to the system, $H \equiv H(t)$, energy conservation cannot be taken for granted, as in general feedback can lead to cooling, heating, chaotic motion, etc.

Deterministic solution

Damped harmonic oscillator: If $F(t)$ is zero, we define the *natural frequency* $\omega_0 = \sqrt{\frac{k}{m}}$, the *damping ratio*

$$\zeta = \sqrt{\frac{m}{k}}\frac{\Gamma}{2} = \frac{\Gamma}{2\omega_0}$$

and the *quality factor*

$$\mathcal{Q} = \frac{\omega_0}{\Gamma} = \frac{1}{2\zeta}.$$

[1] For now we are ignoring the fact that a damping force leads to a Brownian random force, due to the fluctuation-dissipation theorem. Since this force scales with $\sqrt{m}$, the randomness doesn't need to be taken into account for large oscillator masses, but will be relevant in micro and nanoparticles.

The $\mathcal{Q}$-factor can be understood in different (but mostly equivalent) manners. One way, that will be discussed later, is as the number of "coherent" oscillations of the system. A different definition is as the fraction of the energy E stored in the system versus the energy dissipated ΔE in a period τ_0 of the oscillation, as

$$\mathcal{Q} = \frac{2\pi E}{\Delta E} = \frac{2\pi}{1 - e^{-\Gamma t_0}} \approx \frac{\omega_0}{\Gamma}.$$

The last approximation comes from an order one Taylor expansion, so when Γ is small one recovers the previous quality factor definition. Using these parameters, the ODE now takes the form

$$\frac{\mathrm{d}^2 x}{\mathrm{d}t^2} + \Gamma \frac{\mathrm{d}x}{\mathrm{d}t} + \omega_0^2 x = 0.$$

The value of the damping ratio ζ critically determines the behaviour of the system. A damped harmonic oscillator can be

- Overdamped, $\mathcal{Q} \leq 0.5$. The system exponentially decays to zero without oscillating. The case $\mathcal{Q} = 0.5$ is usually called critically damped and is the boundary between oscillation and no oscillation.
- Underdamped, $\mathcal{Q} > 0.5$. The system oscillates at $\omega_1 = \omega_0 \sqrt{1 - \mathcal{Q}^2/4}$, so the smaller the damping the closer the oscillation frequency to the natural frequency of the oscillator. The sinusoid has an exponential decay of $\lambda = \frac{\omega_0}{2\mathcal{Q}} = \frac{\Gamma}{2}$.[2]

Driven harmonic oscillator: In the case of a sinusoidal driving force:

$$\frac{\mathrm{d}^2 x}{\mathrm{d}t^2} + \Gamma \frac{\mathrm{d}x}{\mathrm{d}t} + \omega_0^2 x = \frac{1}{m} F_0 \sin(\omega t),$$

where F_0 is the driving amplitude and ω is the driving frequency for a sinusoidal driving mechanism[3].

The general solution is a sum of a transient term that depends on initial conditions, and a steady state that is independent of initial conditions and depends only on the driving amplitude F_0, driving frequency ω, natural angular frequency ω_0, and Γ. The transient solutions are the same as the unforced ($F_0 = 0$) harmonic oscillator and represent the systems response to other events that occurred previously. However, they typically die out rapidly enough that they can be ignored.

[2] The characteristic time is $\tau = 1/\lambda$.

[3] This type of system appears in AC driven inductor-capacitor systems and in driven spring systems having internal mechanical resistance or external, like a particle in an optical trap.

The steady-state solution is proportional to the driving force with an induced phase change of ϕ:

$$x(t) = \frac{F_0}{Z_m}\sin(\omega t + \phi),$$

where

$$Z_m = m\sqrt{(2\omega_0\zeta)^2\omega^2 + (\omega_0^2 - \omega^2)^2} = m\sqrt{\left(\frac{\omega_0}{\mathcal{Q}}\right)^2\omega^2 + (\omega_0^2 - \omega^2)^2}$$
$$= m\sqrt{\Gamma^2\omega^2 + (\omega_0^2 - \omega^2)^2}$$

is the absolute value of the linear response function, and

$$\phi = \arctan\left(\frac{2\omega\omega_0\zeta}{\omega^2 - \omega_0^2}\right)$$

is the phase of the oscillation relative to the driving force, if the arctan(·) value is taken to be between -180 degrees and 0 (that is, it represents a phase lag, for both positive and negative values of the arctan argument).

These last two expressions are obtained from the complex transfer function

$$H(\omega) = \frac{1}{m(\omega_0^2 - \omega^2 + i\omega\Gamma)},$$

the power transfer function being

$$|H(\omega)|^2 = \frac{1/m^2}{\Gamma^2\omega^2 + (\omega_0^2 - \omega^2)^2}.$$

For a particular driving frequency, called the resonance or resonant frequency

$$\omega_r = \omega_0\sqrt{1 - 2\zeta^2} = \omega_0\sqrt{1 - \frac{1}{2\mathcal{Q}^2}},$$

the amplitude of $x(t)$ (for a fixed F_0) becomes maximum, and

$$|H(\omega_r)|^2 = \frac{4\mathcal{Q}^4}{m^2(4\mathcal{Q}^2 - 1)\omega_0^4} \simeq \frac{\mathcal{Q}^2}{m^2\omega_0^4}.$$

The last approximation only holds for large $\mathcal{Q}$ factors; notice that the ratio between the power transfer function at ω_r and at zero is $H(\omega_r)^2/H(0)^2 \simeq Q^2$.

The resonance effect only occurs when $\mathcal{Q} > \sqrt{2}/2$, i.e., for significantly underdamped systems. For strongly underdamped systems the value of the amplitude can become quite large near the resonance frequency.

We can calculate the half width half maximum (HWHM) by imposing Z_m^2 to be half of the value at resonance. The angular frequencies thus obtained are

$$\omega_i = \sqrt{\omega_r^2 \pm \frac{\omega_0^2}{\mathcal{Q}^2}\sqrt{\mathcal{Q}^2 - \frac{1}{4}}}$$

and by approximating $\sqrt{\mathcal{Q}^2 - \frac{1}{4}} \simeq \mathcal{Q}$, $\omega_r \simeq \omega_0$ and applying the Taylor series expansion of the square root in $\omega_0\sqrt{1 \pm \frac{1}{\mathcal{Q}}}$, we obtain

$$\begin{aligned}\text{HWHM} = \frac{\omega_2 - \omega_1}{2} &\simeq \frac{\omega_0}{2}\left(1 + \frac{1}{2\mathcal{Q}} - \frac{1}{8\mathcal{Q}^2} - 1 + \frac{1}{2\mathcal{Q}} + \frac{1}{8\mathcal{Q}^2} + \mathcal{O}\left(\frac{1}{\mathcal{Q}^3}\right)\right) \\ &= \frac{\omega_0}{2\mathcal{Q}} = \frac{\Gamma}{2}.\end{aligned}$$

This shows that increasing $\mathcal{Q}$ (or, equivalently, decreasing Γ) reduces the width of the frequency response of the oscillator. Therefore, a high $\mathcal{Q}$ is particularly important when trying to detect frequency shifts.

B.3 Sensing with the harmonic oscillator

B.3.1 Principles of force sensing

The harmonic oscillator is a 2nd order constant coefficient linear ordinary differential equation. In the most general case, the equation reads

$$m\ddot{x} + m\Gamma\dot{x} + m\omega_0^2 x = g(t), \tag{B.2}$$

where $m\Gamma\dot{x}$ is a damping force, $m\omega_0^2 x$ is a restoring force and $g(t)$ is an (external) driving force. Force sensing is the detection of these forces $g(t)$ acting *upon* the oscillator's mass[4]. Since the harmonic oscillator is a linear time-invariant system (see the LTI section), the response of the system to a deterministic (arbitrary) driving function $g(t)$ will be

$$x(t) = h(t) * g(t), \tag{B.3}$$

where $h(t)$ is the impulse response of the system. By the convolution theorem, $X(\omega) = H(\omega) \cdot G(\omega)$, where the capital letters indicate Fourier transforms. Recall the transfer function of the harmonic oscillator is

$$H(\omega) = \frac{1/m}{\omega_0^2 - \omega^2 + i\omega\Gamma^2}.$$

[4]This section is based in the article [186]

If the driving function is stochastic, but wide sense stationary[5], this equality still holds in the power spectral density (PSD) sense

$$S_{xx}(\omega) = |H(\omega)|^2 \cdot S_{gg}(\omega).$$

Therefore, given a certain experimentally measurable $x(t)$, to obtain its originating S_{gg} we would need to calculate

$$S_{gg}(\omega) = |H(\omega)|^{-2} \cdot S_{xx}(\omega). \tag{B.4}$$

In a more realistic scenario, the oscillator will be driven by thermal noise[6], a stochastic driving that can be modelled as a white noise $w(t)$ with zero mean and autocorrelation function $R_w(\tau) = \sigma_1^2\delta(\tau)$. There will also be a random noise $u(t)$ originating from our measuring device, that we can consider additive Gaussian white noise (AGWN) (with $R_u(\tau) = \sigma_2^2\delta(\tau)$), summed *after* the harmonic oscillator frequency response. Therefore, the measured power spectral density of a driving force $g(t)$ is

$$S_{xx} = |H(\omega)|^2 S_{gg} + |H(\omega)|^2 S_{ww} + S_{uu} = |H(\omega)|^2 S_{gg} + |H(\omega)|^2\sigma_1^2 + \sigma_2^2,$$

and our estimate of S_{gg} will be

$$\begin{aligned} |H(\omega)|^{-2} \cdot S_{xx} &= |H(\omega)|^{-2} \left(|H(\omega)|^2 S_{gg} + |H(\omega)|^2\sigma_1^2 + \sigma_2^2\right) \\ &= S_{gg} + \sigma_1^2 + |H(\omega)|^{-2}\sigma_2^2. \end{aligned} \tag{B.5}$$

In this expression S_{gg} is deterministic, σ_1^2 comes from the thermal noise and is independent of ω and $|H(\omega)|^{-2}\sigma_2^2$ has explicit ω dependency. The signal to noise ratio (SNR), defined as the square root[7] of the ratio of the signal and noise powers, will thus take the expression

$$\text{SNR} = \sqrt{\frac{S_{gg}}{\sigma_1^2 + |H(\omega)|^{-2}\sigma_2^2}}.$$

This expression is bounded by $\sqrt{\frac{S_{gg}}{\sigma_1^2}}$: this is a hard limit that cannot be improved with this system and assumptions. However, the $|H(\omega)|^{-2}\sigma_2^2$ term can be minimised by using ω at resonance.

[5] This assumption is important, since the following expressions assume no transient behaviours. When $\Gamma \ll 1$, past transients can contaminate the signal, leading to worse signal to noise ratio (SNR) than expected.

[6] As can be seen by the fluctuation-dissipation theorem (D.20). The engineer/scientist should decide whether this Brownian noise can be neglected or should be taken into account, depending on the harmonic oscillator's mass.

[7] We use the square root to work with force units, instead of power units. This is, of course, arbitrary.

In any case, to get the minimum measurable force $g(t)$ we have to set a limit to what we can detect: usually this limit is SNR > 1[8]. From this inequality we can obtain a bound for $g(t)$, which is where the minimum sensitivity expressions come from. Using the fluctuation-dissipation relationship $\sigma_1 = \sqrt{2m\Gamma k_{\mathrm{B}}T}$ and $|H(\omega)|^2$ at its maximum (i.e., at resonance) we get

$$\begin{aligned}\sqrt{S_{gg}} &> \sqrt{\sigma_1^2 + |H(\omega)|^{-2}\sigma_2^2} \\ &= \sqrt{2m\Gamma k_{\mathrm{B}}T + \sigma_2^2 \frac{m^2(4\mathcal{Q}^2-1)\omega_0^4}{4\mathcal{Q}^4}} \simeq \sqrt{2m\Gamma k_{\mathrm{B}}T + \sigma_2^2 m^2 \omega_0^2 \Gamma^2},\end{aligned} \tag{B.6}$$

where after the inequality we assumed resonance, and the last equality is a good approximation for large enough $\mathcal{Q}$. Whether we are measuring at resonance or not, if the measuring noise is very small compared to the thermal noise, the second term in the square root may be negligible, in which case we obtain the following expression for the amplitude spectral density (ASD)

$$\mathrm{ASD} = \sqrt{2m\Gamma k_{\mathrm{B}}T}. \tag{B.7}$$

The "minimum resolvable" [192] force or force sensitivity is hence defined as the root mean square of the noise power spectral density (i.e., the ASD is just the square root of the PSD[9]). Notice that *smaller* sensitivity values are *better*, since the benchmark is the smallest signal that can be detected.

Expression (B.7) is useful to get an intuition of how the sensitivity scales with the oscillator parameters. For example, a smaller mass results in a better sensitivity[10]. Bear in mind, however, that (B.7) is just an approximation and the full sensitivity has ω dependency,

$$\mathrm{ASD} = \sqrt{\sigma_1^2 + |H(\omega)|^{-2}\sigma_2^2}. \qquad (\mathrm{N}/\sqrt{\mathrm{Hz}}) \tag{B.8}$$

If we further integrate the power only on an interval of length Δf in the Fourier domain[11], we obtain

$$g_{\min} = \sqrt{2\Delta f S_{gg}} > \sqrt{4m\Gamma\Delta f k_{\mathrm{B}}T}.$$

[8] Again, this limit is arbitrary: in principle if the system is ergodic and the driving force periodic, signals of any SNR can be detected.

[9] For reference, check the LISA Pathfinder paper.

[10] Assuming, of course, that noise has no m dependency. For instance, with optically levitated nanoparticles, decreasing the mass increases the measurement noise, since smaller particles scatter less light. Thus, to obtain a signal that is comparable to that of bigger particles, we will need to amplify the measured signal, hence also amplifying measurement noise.

[11] As is done in ref. [193].

This expression of $g_{\min}$ is also sometimes known as the force sensitivity of the system. Nevertheless, the previous ASD definition can (and is) also used under the same name. In general, the use of the force sensitivity defined as the ASD (and not as this $g_{\min}$) should always be preferred, since its value doesn't depend on how long the measurement is, it doesn't make any assumptions on the bandwidth of the signal and any information of different sensitivities at different ω values is not lost.

It is worth pointing out that if one assumes that measurement noise can be neglected, the sensitivity is the same for all frequencies: it doesn't matter if one measures at resonance or out of it[12]. This happens because the oscillator gain affects thermal noise and driving signal equally and the SNR stays constant. Therefore, for a fixed m, the obvious knobs for reducing the ASD are decreasing the temperature T and/or Γ.

B.3.2 The case of a harmonic oscillator with jitter

If the response function of the harmonic oscillator jitters (i.e., is not constant with time), we can model the sensitivity in probabilistic terms. Assume the jittering is due to a stochastic natural frequency of the oscillator Ω[13], that now fluctuates with time, but has a certain stationary, well-known probability density function $f_\Omega(u)$. Then, the value of the ASD from (B.8) will also be stochastic, but we can still calculate its statistical moments. In particular, the expected value of the sensitivity will be

$$\mathbb{E}[\mathrm{ASD}(\omega)] = \mathbb{E}\left(\sqrt{\sigma_1^2 + |H(\omega)|^{-2}\sigma_2^2}\right) \tag{B.9}$$

$$= \int_{-\infty}^{\infty} \sqrt{\sigma_1^2 + |H(\omega)|^{-2}\sigma_2^2} \cdot f_\Omega(u)\,\mathrm{d}u. \tag{B.10}$$

Clearly this value depends on ω, since the expected sensitivity will not be the same for every frequency. However, if, as before, measurement noise can be neglected, then

$$\mathbb{E}[\mathrm{ASD}(\omega)] = \int_{-\infty}^{\infty} \sqrt{\sigma_1^2 + |H(\omega)|^{-2}\sigma_2^2} \cdot f_\Omega(u)\,\mathrm{d}u \tag{B.11}$$

$$\simeq \int_{-\infty}^{\infty} \sqrt{\sigma_1^2} \cdot f_\Omega(u)\,\mathrm{d}u. = \sigma_1, \tag{B.12}$$

recovering the expression of (B.7). Intuitively, this means that if the natural frequency Ω jitters only in a region where thermal noise is still dominant (for

[12] In fact, measuring at resonance may be a bad idea if the driving signal has a big bandwidth, since the phase response changes a lot around the resonance peak.

[13] In contrast with the previous ω_0.

instance the standard deviation of the natural frequency, σ_Ω, is less than $\Gamma/2$), the sensitivity is not affected, even if the force amplitude fluctuates due to the jitter. *However*, the actual value of the measured force will be affected if one naively uses equation (B.4) without taking into account that $H(\omega)$ is stochastic. To calculate the real expected force, we will need to, again, find the expected value of $H(\omega)$

$$\sqrt{S_{gg}(\omega)} = \sqrt{\mathbb{E}(|H(\omega)|^{-2}) \cdot S_{xx}(\omega)}, \tag{B.13}$$

which can be thought of as an effective response function obtained by averaging the instantaneous responses at different times.

Real oscillators, and especially small ones (which are more susceptible to perturbations), will always have some jitter. The importance of the effect depends on the parameters of the oscillator: for instance, the effect can be neglected when the damping is large and the oscillator's width is much broader than the jitter (i.e., $\Gamma \gg \sigma_\Omega$). However, for strongly underdamped systems—which have a very narrow response peak—, jitter needs to be taken into account. Beyond the probabilistic treatment that we just described, it is advisable to have some way of artificially increasing the damping in the harmonic oscillator. As long as this extra damping does not induce additional noise (i.e., it is a *cold damping* [106]), this has several advantages:

- Since the peak is broadened, the relative effect of jitter is reduced.
- As long as thermal noise is still considerably larger than measurement noise, the SNR (i.e., the sensitivity) will not be affected.
- It will reduce the effect of non-linearities in the oscillator. Low dissipation systems with narrow resonances are prone to large oscillation amplitudes: in this case, non-linearities can dominate[14].
- It will also reduce the memory of the system. Recall that, the lower the damping, the longer the memory of the impulse response. In practical terms, this means that if no additional damping is included we will keep measuring signal remnants from some past event long after the driving has stopped.

One possibility to implement this damping is by adding a feedback force $F = -mk_d\dot{x}$. The equation of motion becomes

$$m\ddot{x} + m\Gamma\dot{x} + m\omega_0^2 x = -mk_d\dot{x}, \tag{B.14}$$

[14]The video of an oscillating bridge is a classical example.

resulting in a new transfer function

$$H(\omega) = \frac{1/m}{\omega_0^2 - \omega^2 + i\omega(\Gamma + k_d)^2},$$

which has a bigger effective damping than before, while the thermal noise will still have spectral density $\sqrt{2k_{\mathrm{B}}Tm\Gamma}$. Real feedback systems will never be completely noise-free, but for small gains the effect of this noise is negligible (see Chapter 4 or the supplementary material of [106]).

B.3.3 Sensing a perfectly sinusoidal force

Assume now the force $g(t)$ we want to measure is a sinusoid, with a constant phase relation to a controlled reference signal (i.e., it is a *perfect* sinusoid). In this case, the sensitivity to this signal can be greatly increased if instead of working with PSDs one averages the Fourier transform measurements (note that this gives $(\mathrm{N}/\sqrt{\mathrm{Hz}})$ units directly). The argument is described in what follows: the measured signal $m(t)$ will take the expression

$$m(t) = (g(t) + w(t)) * h(t) + u(t)$$

where, as before, $g(t)$ is the driving force, $w(t)$ is a white thermal noise and $u(t)$ is an AWGN from the measuring device. By assumption, $g(t) = \cos w_d t$. Then, if we take the Fourier transform of the previous expression we get

$$\begin{aligned}\mathcal{F}\left((g(t) + w(t)) * h(t) + u(t)\right) &= \mathcal{F}\left(g(t) * h(t)\right) + \mathcal{F}\left(w(t) * h(t)\right) + \mathcal{F}\left(u(t)\right) \\ &= \pi(\delta(\omega - \omega_d) + \delta(\omega + \omega_d)) \cdot H(\omega) + \mathcal{F}\left(u(t)\right) + \\ &\mathcal{F}\left(\left(\cos\sqrt{a}t \sin\sqrt{a}t/\sqrt{a}\right) \cdot \int_0^t b e^{\frac{\Gamma}{2}(r-t)} \cdot \begin{pmatrix} -\sin\sqrt{a}r/\sqrt{a} \\ \cos\sqrt{a}r \end{pmatrix} \mathrm{d}W_r\right),\end{aligned}$$

where we have used the properties of the Fourier transform, in the second summand we have substituted by the solution of a thermally driven harmonic oscillator (see Chapter 2 for the derivation), $a = \omega_0^2 - \Gamma^2/4$ and W_r is a Wiener process parametrized by the time r. Finally, taking expected values

$$\begin{aligned}\mathbb{E}[\mathcal{F}\left((g(t) + w(t)) * h(t) + u(t)\right)] &= \mathbb{E}[\pi(\delta(\omega - \omega_d) + \delta(\omega + \omega_d)) \cdot H(\omega) + \\ \mathcal{F}\left(\left(\cos\sqrt{a}t \sin\sqrt{a}t/\sqrt{a}\right) \cdot \int_0^t b e^{\frac{\Gamma}{2}(r-t)} \cdot \begin{pmatrix} -\sin\sqrt{a}r/\sqrt{a} \\ \cos\sqrt{a}r \end{pmatrix} \mathrm{d}W_r\right) &+ \mathcal{F}\left(u(t)\right)] \\ &= \pi(\delta(\omega - \omega_d) + \delta(\omega + \omega_d)) \cdot H(\omega) + \\ \mathcal{F}\left(\left(\cos\sqrt{a}t \sin\sqrt{a}t/\sqrt{a}\right) \cdot \mathbb{E}\left[\int_0^t b e^{\frac{\Gamma}{2}(r-t)} \cdot \begin{pmatrix} -\sin\sqrt{a}r/\sqrt{a} \\ \cos\sqrt{a}r \end{pmatrix} \mathrm{d}W_r\right]\right) &\\ + \mathcal{F}\left(\mathbb{E}[u(t)]\right) = \pi(\delta(\omega - \omega_d) + \delta(\omega + \omega_d)) \cdot H(\omega),&\end{aligned}$$

since the expected values of an Itô integral and $u(t)$ are zero. If we are perfectly rigorous, Fubini's theorem can't be applied with delta distributions; nonetheless, the calculation can be repeated in complete analogy with sinc functions instead. Sinc functions appear as the Fourier transforms of finite rectangular windows, and are unavoidable in actual measurements[15].

Thus, defining the SNR as the ratio between expected driving signal amplitude and expected noise amplitude in the frequency domain, we find that the value goes to infinity. A more accurate analysis should compare not the ratio of the expected values but the ratio of the signal and noise random variables themselves (which, to a good approximation, should follow a Cauchy distribution[16]). However, this section is enough to show that if more information about the driving force is known (in this case, the fact that the force is sinusoidal), we don't need to restrict ourselves to the sensitivity described in eq. (B.8) and more intelligent approaches might exist.

B.4 Accelerometers

In the last section we saw the expressions for the sensitivity and response of the harmonic oscillator when subjected to an external driving. In a situation where the driving acts on the housing of the oscillator instead of on the oscillator itself, the equation of motion for the harmonic oscillator is modified to

$$m\ddot{x} + m\Gamma\dot{x} + m\omega_0^2 x = 0 \rightarrow m\ddot{x} + m\Gamma(\dot{x} - \dot{y}) + m\omega_0^2(x - y) = 0 \quad \text{(B.15)}$$

where $y(t)$ is the motion of the housing. By rewriting the equation in terms of $z \equiv x - y$, which is the quantity that we will measure, we obtain the equation

$$m\ddot{z} + m\Gamma\dot{z} + m\omega_0^2 z = -m\ddot{y}. \quad \text{(B.16)}$$

Therefore, the transfer function for $y(t)$, as compared with a regular harmonic oscillator, will take the modified expression

$$H(\omega) = \frac{-\omega^2}{\omega_0^2 - \omega^2 + i\omega\Gamma^2}. \quad \text{(B.17)}$$

[15]Since every real measurement will be a *finite* time measurement. Therefore, the measured signal of an arbitrary $f(t)$ will in fact be $f(t) \cdot \Pi(t)$ ($\Pi(t)$ being a rectangular window), and by the convolution theorem the Fourier transform of the measurement will be $F(\omega) * \mathrm{sinc}(\omega)$. This avoids the infinite values from the delta distribution.

[16]The Cauchy distribution appears as the ratio of two normally distributed random variables and has undefined (i.e., going to infinity) statistical moments.

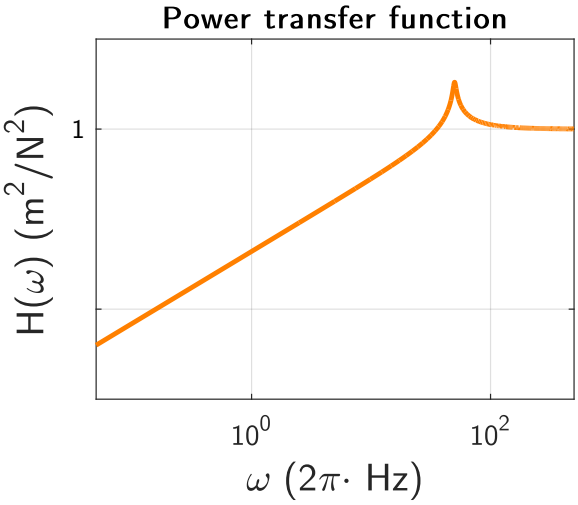

Figure B.1: Oscillator response $H(f)$, for arbitrary ω_0 and Γ, to a housing motion $y(t)$ (seismometer regime).

Note that, for large values of ω, $H(\omega) \simeq 1$. Therefore, for frequencies significantly above resonance, the accelerometer has a flat response and behaves approximately as a Dirac delta:

$$Z(\omega) = H(\omega)Y(\omega) =_{\omega \gg \omega_0} Y(\omega)$$

so

$$z(t) \simeq y(t).$$

In this range of operation, the oscillator behaves as a *seismometer*: it measures the displacement of the housing (see Fig. B.1).

To understand the *accelerometer* regime, lets assume we have an arbitrary housing motion $y(t)$. The response in terms of the power spectral densities will be

$$S_{zz}(\omega) = \frac{\omega^4}{(\omega_0^2 - \omega^2)^2 + \Gamma^2\omega^2} \cdot S_{yy}(\omega). \tag{B.18}$$

But since $-\omega^2 Y(\omega) = A(\omega)$, where $Y(\omega)$ and $A(\omega)$ are the Fourier transforms of $y(t)$ and the acceleration $a(t) = \ddot{y}(t)$, the response to an acceleration $\ddot{y}(t)$ will be

$$S_{zz}(\omega) = \frac{\omega^4}{(\omega_0^2 - \omega^2)^2 + \Gamma^2\omega^2} \cdot S_{yy}(\omega) = \frac{1}{(\omega_0^2 - \omega^2)^2 + \Gamma^2\omega^2} \cdot S_{aa}(\omega). \tag{B.19}$$

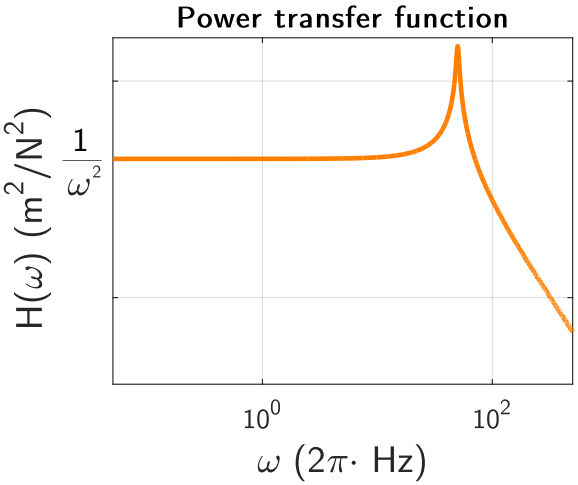

Figure B.2: Oscillator response $H(f)$, for arbitrary ω_0 and Γ, to the acceleration of the housing $a(t)$ (accelerometer regime).

In other words, the response of $z(t)$ to an acceleration of the housing is, except for the missing $1/m^2$ factor, the same as the response of a force acting on the harmonic oscillator, as plotted in Fig. B.2. Now, the response of the harmonic oscillator is flat at low frequencies (i.e., below resonance)

$$H(\omega)_{\omega\to 0} = \frac{1}{\omega_0^2},$$

and this is the frequency band where most of the accelerometers work. Like in seismometers, this is a relevant point: working in a regime where the impulse response is approximately a Dirac delta is necessary when the driving force isn't restricted to a small bandwidth (otherwise, to recover $a(t)$ out of $z(t)$, some sort of deconvolution may be needed, which is an ill-posed problem that should be avoided if possible).

Assuming the housing mass is large enough, the stochastic component of $y(t)$ due to Brownian noise can be neglected. However, Brownian noise will still drive the harmonic oscillator itself[17]

$$m\ddot{z} + m\Gamma\dot{z} + m\omega_0^2 z = \omega(t).$$

Therefore, repeating the analysis of the force sensing section we obtain

$$S_{zz} = m^2 \cdot |H(\omega)|^2 S_{aa} + |H(\omega)|^2 \sigma_1^2, \tag{B.20}$$

[17]Note that an important approximation is being done here: we assume that the acceleration leaves the statistical properties of Brownian noise unchanged. For large accelerations this approximation may not hold.

where $H(\omega)$ is the response of the harmonic oscillator including the $1/m^2$ factor. Thus, neglecting the measurement noise, $\text{SNR} = \sqrt{\frac{S_{aa}m^2}{\sigma_1^2}}$ so

$$\text{ASD} = \sqrt{S_{aa}} = \sqrt{\frac{2k_\text{B}T\Gamma}{m}}. \tag{B.21}$$

This means that larger masses will push down the value of the minimum detectable accelerations.

C

Review of optics

C.1 Ray optics and basic concepts

Lenses

A lens is a transmissive optical device that focuses or disperses a light beam by means of refraction. If the lens is convex, a collimated beam of light passing through the lens converges to a spot (a *focus*) behind the lens. In this case, the lens is called a positive or converging lens. The distance from the lens to the spot is the focal length of the lens, which is commonly abbreviated f in diagrams and equations. A lens can focus light from and object to form an image.

If distances from the object to the lens and from the lens to the image are d_o and d_i respectively, for a lens of negligible thickness, in air, the distances

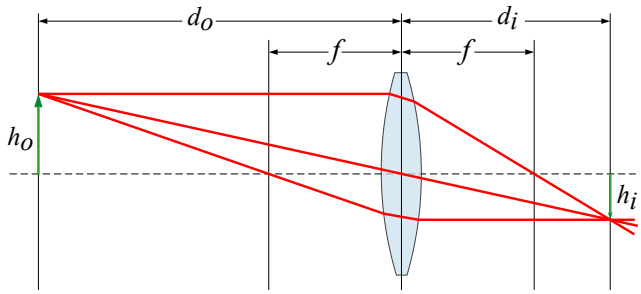

Figure C.1: **Thin lens**: sketch of a lens focusing an object to an image plane, with the relevant parameter names and light lines for ray tracing.

are related by the thin lens formula

$$\frac{1}{d_o} + \frac{1}{d_i} = \frac{1}{f},$$

Hence, an image will be formed at the plane d_i (since every point from the object plane will be focused in a point of the image plane). This can be seen by putting a sheet of paper at the image plane: if the object is bright enough (for instance, it is illuminated), then an image will be projected on the sheet. Putting the sheet at any other position will result in a blurred image.

Two relevant cases of the thin lens formula are the following

- If the object is at infinity, the image will be formed at exactly the focal plane, $d_o = f$ (and vice versa).
- If the object is at distance $2f$, the image will also be formed at $2f$.

Magnification

In an optical system where and object is imaged, magnification is defined as the ratio of the image height with respect to the object height

$$M = \frac{h_i}{h_o}.$$

For a single lens, the magnification will be

$$M = -\frac{d_i}{d_o} = \frac{f}{f - d_o}.$$

For a system of several lenses, the image of a lens will become the object of the following lens. By induction, this means that the combined magnification will be the product of magnifications,

$$M = \prod_i M_i.$$

Both the single thins lens formula and the magnification formula will be specially relevant when designing an imaging system (such as a microscope). The product of the total magnification by the size of the object will need to fit (i.e., be smaller than, but not too much) the camera chip where the image will be formed.

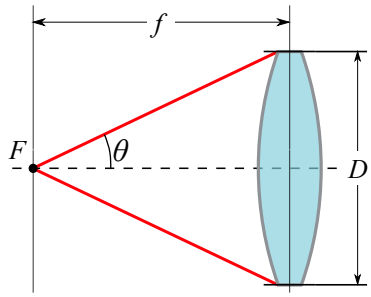

Figure C.2: θ and NA of a thin lens.

Numerical aperture

In most areas of optics, the numerical aperture of an optical system such as an objective is defined by

$$\mathrm{NA} = n \sin \theta,$$

where n is the refractive index of the medium in which the lens is working (1 for air, 1.33 for water, 1.5 for a glass or immersion oil) and θ is the maximal half-angle of the cone of light that can enter or exit the lens.

The use of a high NA lens will result in the collection of a high fraction of the cone of light emitted by the point source in the focus. For a given half angle θ, the fraction of the light collected will be

$$\frac{1 - \cos \theta}{2}.$$

For instance, a lens with NA = 0.9 (resp. 0.8, 0.7, 0.5) will collect 0.28 (0.2, 0.14, 0.07) of the light.

In photography the f-number or N is used instead, defined as $N = \frac{f}{D}$, with f the lens focal length and D its diameter. As can be seen with a first order Taylor approximation, $N \approx \frac{1}{2\mathrm{NA}}$[1]. The depth of field (DOF)[2] decreases by either increasing the NA (which can be modified by adding an aperture after the objective lens) or increasing the image magnification.

Objectives

An objective is an optical element that gathers light from a close object. Objectives can be a single lens or mirror, or combinations of several optical

[1]This expression, which ignored higher order terms of the expansion of the sin and arctan functions, is often the right one when the lens is corrected for coma and spherical aberration.

[2]The DOF is the distance about the Plane of Focus (POF) where objects appear acceptably sharp in an image.

elements, and are used in microscopes, telescopes, cameras, etc[3]. What sets them apart from other simple lenses is their degree of correction for different kinds of optical aberration (mainly spherical and chromatic). Depending on their characteristics (from cheaper to more expensive), they are classified as

1. Achromat: corrected for spherical aberration at 1 wavelength, for chromatic aberration at 2. Not corrected for field curvature.

2. Plan Achromat: like an achromat but with field curvature correction.

3. Fluorite (or semi-apochromat): corrected in 2-3 colors both in spherical and chromatic aberration. Not corrected for field curvature.

4. Plan Fluorite: like a fluorite but with field curvature correction.

5. Plan Apochromat: chromatic aberration correction at 4 wavelengths and spherical aberration correction usually at 3 wavelengths.

Microscope objectives are characterized by two parameters: magnification and numerical aperture (defined as in the previous section). The magnification typically ranges from 4× to 100×, and is multiplied with the magnification of the eyepiece to determine the overall magnification. However, not all objectives make an image of an object at a fixed focal length: in fact, this is a constraint that severely limits the size of the microscope and prevents the use of other optical elements after it. Newer (and better) objectives are *infinity corrected*, and have an image distance that is set to infinity (i.e., they collimate the light emitted at the focal plane). Therefore, they require a tube lens[4], placed within the body tube between the objective and the eyepieces, to produce the intermediate image[5]. The Infinity optical system allows auxiliary components (such as illuminators, polarizers, etc.) to be added into the parallel optical path between the objective and the tube lens with only a minimal effect on focus.

Microscopy basics

A microscope is an instrument used to see objects that are too small to be seen by the naked eye. A microscope system usually places the sample to be studied at the focal plane of the first optical component.

[3]Main manufacturers are Olympus, Nikon, Meiji, Leica and Zeiss.

[4]The position of which depends on the objective manufacturer, but lies in the range of 180 mm.

[5]Since, of course, if there is no image, magnification can't be calculated.

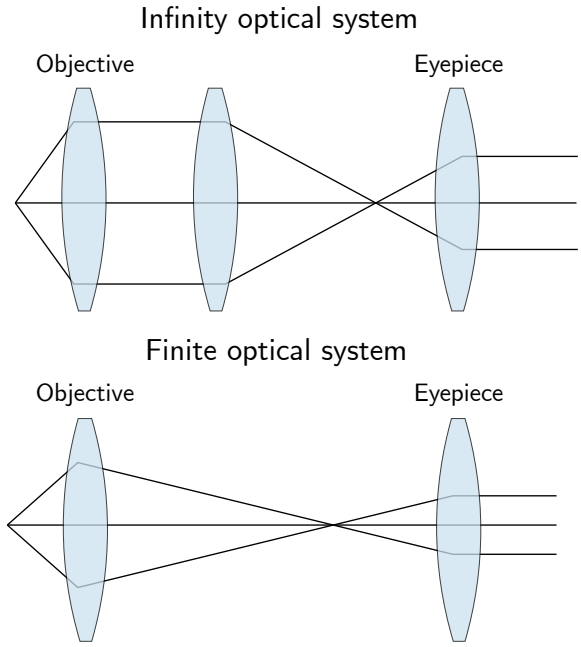

Figure C.3: **Infinity corrected system**. Comparison between finite and infinity corrected objectives. For an infinity corrected system, the light from the object plane is perfectly collimated, and therefore the optical system can be of arbitrary length. For a finite system, the microscope tube is fixed to the objective conjugate focal length.

In order to improve specimen contrast or highlight certain structures in a sample, different techniques must be used. Some of them are listed in the following:

- Bright field: sample contrast comes from absorbance of light in the sample.
- Dark field: sample contrast comes from light scattered by the sample.
- Phase contrast illumination: sample contrast comes from interference of different path lengths of light through the sample.
- Confocal microscopy: it uses a scanning point of light and a pinhole to prevent out of focus light from reaching the detector (only light emitted in the focal volume[6] is collected). Compared to full sample illumination, confocal microscopy gives higher resolution, and significantly improves optical sectioning. It is commonly used where 3D

[6]See the Gaussian beam section.

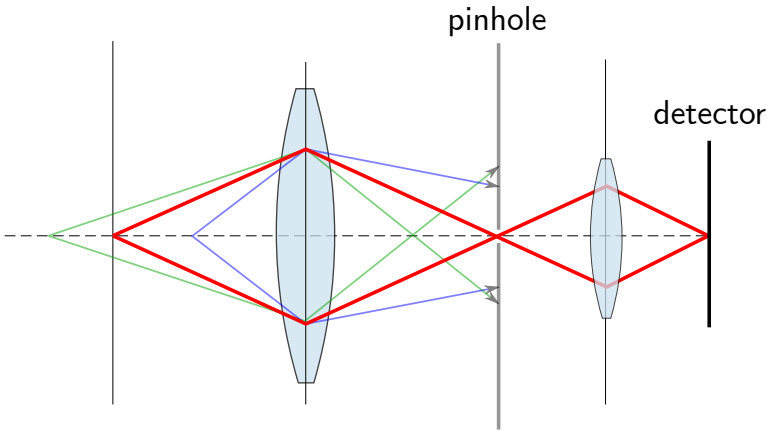

Figure C.4: **Principle of confocal microscopy**: a spatial pinhole blocks out-of-focus light in image formation.

structure is important. See Fig. C.1 for a sketch of the optical setup in a confocal microscope.

C.2 Fourier optics

Fourier optics is the study of classical optics using Fourier transforms (FTs), in which the wave is regarded as a superposition of plane waves that are not related to any identifiable sources; instead they are the natural modes of the propagation medium itself. Any curved phase front may be synthesized from an infinite number of these "natural modes".

Light can be described as a waveform propagating through free space (vacuum) or a material medium (such as air or glass). The (real valued) amplitude of one wave component is represented by a scalar wave function u that depends on both space and time:

$$u = u(\mathbf{r}, t),$$

where

$$\mathbf{r} = (x, y, z)$$

represents position in three dimensional space, and t represents time. The wave equation satisfied by these waveforms is

$$\left(\nabla^2 - \frac{1}{c^2}\frac{\partial^2}{\partial t^2}\right) u(\mathbf{r}, t) = 0.$$

If one assumes the waveforms have a fixed frequency, i.e.,

$$u(\mathbf{r},t) = \mathrm{Re}\left\{\psi(\mathbf{r})e^{j\omega t}\right\},$$

then the wave equation yields the time-independent form of the wave equation, also known as the Helmholtz equation:

$$\left(\nabla^2 + k^2\right)\psi(\mathbf{r}) = 0$$

where $k = \frac{\omega}{c} = \frac{2\pi}{\lambda}$ is the wave number and $\psi(\mathbf{r})$ is the time-independent, complex-valued component of the propagating wave. Note that the propagation constant, k, and the frequency, ω, are linearly related to one another, a typical characteristic of transverse electromagnetic (TEM) waves in homogeneous media.

A general solution to the Helmholtz equation in rectangular coordinates for a wave that propagates along z may be formed as a weighted superposition of all possible elementary plane wave solutions as:

$$\psi(x,y,z) = \int_{-\infty}^{+\infty}\int_{-\infty}^{+\infty} \Psi_0(k_x,k_y)\; e^{j(k_x x + k_y y)}\; e^{\pm jz\sqrt{k^2-k_x^2-k_y^2}}\; \mathrm{d}k_x \mathrm{d}k_y.$$

Next, let $\psi_0(x,y) = \psi(x,y,z)|_{z=0}$. Then

$$\psi_0(x,y) = \int_{-\infty}^{+\infty}\int_{-\infty}^{+\infty} \Psi_0(k_x,k_y)\; e^{j(k_x x + k_y y)}\; \mathrm{d}k_x \mathrm{d}k_y.$$

This plane wave spectrum representation of the electromagnetic field is the basic foundation of Fourier optics, because when $z = 0$, the equation above simply becomes a Fourier transform (FT) relationship between the field and its plane wave content. Thus $\Psi_0(k_x,k_y) = \mathcal{F}\{\psi_0(x,y)\}$.

Note that when $k_x^2 + k_y^2 > k^2$ the plane waves are evanescent (decaying), so that any spatial frequency content in an object plane transparency which is finer than one wavelength will not be transferred over to the image plane, simply because the plane waves corresponding to that content cannot propagate.

Diffraction limit

The resolution of an optical imaging system (a microscope, telescope, or camera) can be limited by factors such as imperfections in the lenses, misalignment or seeing. However, there is a fundamental maximum to the resolution of any optical system which is due to diffraction. This limit requires a formalism (Fourier optics) that goes beyond ray optics, where there is no such limit.

An optical system with the ability to produce images with angular resolution as good as the instrument's theoretical limit is said to be diffraction limited[7]. Using the Fraunhofer diffraction equation, we see that if a monochromatic plane wave is incident on a circular aperture (and almost any optical system will have that kind of aperture), an Airy diffraction pattern spot will be formed at infinity[8], with size

$$\varphi = \frac{1.22 \cdot \lambda}{D},$$

where φ is the angle between the optical axis and the first minima, λ is the wavelength, D is the lens or aperture diameter and the 1.22 factor arises from the Bessel functions. This angle, according to *Rayleigh's criterion*[9], is the angular resolution of our system, since two point sources separated by less than φ will appear as the same. We can transform this angular resolution to a spatial resolution by considering that the diffraction spot is at distance f from the aperture, where it has been focused by a lens[10]. By approximating $\frac{D}{2f} \simeq \mathrm{NA}$ and $\theta \cdot 2f \simeq d$, where d is the diameter of the spot, we find

$$d = \frac{1.22 \cdot \lambda}{\mathrm{NA}}.$$

As will be seen later (see equation (C.1)), this diameter is not the same as the spot size of a Gaussian Beam, even though it is of a similar size. This should be expected, however, since we assumed a plane wave was illuminating the aperture. For a collimated laser beam, in order to make use of the full NA of a lens, the incident field has to fill or overfill the back-aperture (as a rule of thumb, an overfilling factor of 2 is enough); if the lens is not completely filled, the size of the spot can be considerably larger than the expected diffraction limit. If the back aperture is infinitely filled, locally the illumination will be a plane wave, and the diffraction limit spot will be exactly recovered.

[7] It is worth noting that this is a *physical* limit. This means that, even though there is a limitation to the minimum size a focused spot can have, once a image of it is taken, it can be digitally deconvolved with the point spread function of the system to increase the image resolution (sometimes by a factor 10 or more).

[8] Here infinity means $\frac{W^2}{l\lambda} \ll 1$, where W is the aperture or slit size, l is the distance from the aperture and λ the wavelength.

[9] Which is an arbitrary limit, but is quite close to the minimum resolution humans can discern.

[10] A lens is also an aperture, and since at the focus all plane waves have the same phase, this is equivalent to viewing the wave at infinity as in Fraunhofer's diffraction.

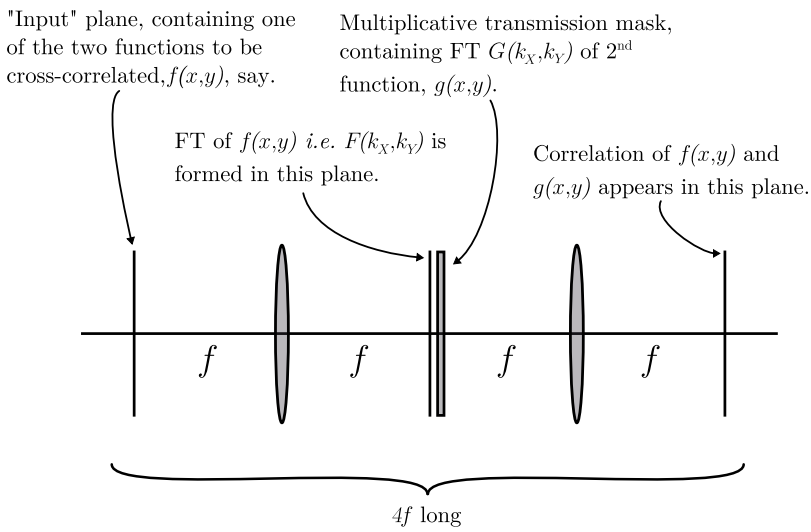

Figure C.5: $4f$ **system**: scheme of a $4f$ correlator, with explanation of the effect for every. Image by Rswarbrick, under the Creative Commons CC0 1.0 license.

Optical systems in Fourier optics

Under this formalism, an optical system will consist of an input plane, and output plane, and a set of components that transforms the image f formed at the input into a different image g formed at the output. The output image is related to the input image by convolving the input image with the optical impulse response, h (known as the point-spread function, for focused optical systems). The impulse response uniquely defines the input-output behaviour of the optical system. By convention, the optical axis of the system is taken as the z-axis. As a result, the two images and the impulse response are all functions of the transverse coordinates, x and y.

$$g(x, y) = h(x, y) * f(x, y).$$

The impulse response of an optical imaging system can be determined by measuring the output plane field which is produced when an ideal mathematical point source of light is placed in the input plane (usually on-axis).

Two simple types of system stand out

1. **Simple lens**: if a transmissive object is placed one focal length in front of a lens, then its Fourier transform will be formed one focal length behind the lens.

2. $4f$ **system**: a $4f$ system with two identical lenses can be used to control the angle of incidence of a beam at $z = 4f$ (see figure C.5), as for instance the angle of illumination of the back aperture of an objective. By shining a laser beam on a mirror at $z = 0$, an image will be formed at $z = 4f$ at the same height and angle as the one in the mirror. However, the ray optics formalism is enough to see that this will be the case; $4f$ systems can also be used as correlators, and for this Fourier optics are needed. A plane wave is assumed incident from the left and a transparency containing one 2D function, $f(x, y)$, is placed in the input plane of the correlator, located one focal length in front of the first lens. The transparency spatially modulates the incident plane wave in magnitude and phase, and in so doing, produces a spectrum of plane waves corresponding to the FT of the transmittance function. That spectrum is then formed as an image one focal length behind the first lens, as shown in figure C.5. A transmission mask containing the FT of the second function, $g(x, y)$, is placed in this same plane, one focal length behind the first lens, causing the transmission through the mask to be equal to the product, $F(k_x, k_y) \cdot G(k_x, k_y)$. This product now lies in the input plane of the second lens (one focal length in front), so that the FT of this product (i.e., the convolution of $f(x, y)$ and $g(x, y)$), is formed in the back focal plane of the second lens.

C.3 The Gaussian beam

The Gaussian beam is a transverse electromagnetic (TEM) mode, a solution to the paraxial Helmholtz equation. The interest in this family of solutions arises in problems involving compact beams, where the optical power is rather closely confined along an axis as with laser beams.

Its intensity takes the expression

$$I(r, z) = \frac{|\operatorname{Re}(\mathbf{E} \times \mathbf{H}^*)|}{2} = \frac{|E(r, z)|^2}{2\eta} = I_0 \left(\frac{w_0}{w(z)} \right)^2 \exp\left(\frac{-2r^2}{w(z)^2} \right),$$

where r is the radial distance from the center axis of the beam, z is the axial distance from the beam's focus and $w(z) = w_0 \sqrt{1 + \left(\frac{z}{z_\mathrm{R}}\right)^2}$ is the radius at which the field amplitude (resp. intensity) decays to $1/e$ (resp. $1/e^2$). The Rayleigh range z_R is defined as the distance where the intensity has decayed to half of the intensity at $z = 0$ (and therefore the area of the cross section has doubled since, by energy conservation, total intensity should be constant

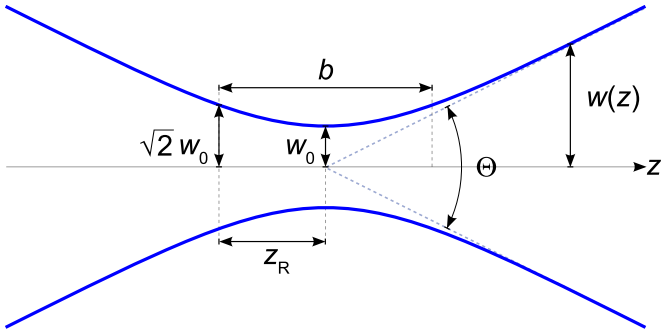

Figure C.6: **Gaussian beam**: width $w(z)$ as a function of the distance z along the beam. In the picture, w_0 is the beam waist, b the depth of focus and z_R the Rayleigh range, Θ total angular spread.

for every plane):

$$z_R = \frac{\pi w_0^2}{\lambda}.$$

The depth of focus is usually defined as $2z_R$.

The numerical aperture of the beam is also defined as $\mathrm{NA} = \sin\theta$[11]. Then we also have

$$w_0 = \frac{\lambda}{\pi \cdot \mathrm{NA}} \tag{C.1}$$

The spot size can be measured in several different ways, but the definition is always proportional to the waist size w_0. The FWHM is related to this via

$$w(z) = \frac{\mathrm{FWHM}}{\sqrt{2\ln 2}} \Rightarrow 2 \cdot w_0 = d \simeq 1.7 \cdot \mathrm{FWHM}.$$

Coupling light into fibers

We distinguish two cases, depending on the fiber type:

- **Multimode fiber**: coupling light into a multimode fiber is straightforward. The focused spot needs to be comparable (or smaller) to the core size of the MM fiber, and the incident cone angle should be equal or smaller to the acceptance cone (input NA < fiber NA).

[11] In this case this factor doesn't come from a lens; instead, it is characteristic of each Gaussian beam, since every θ will generate a different solution to the paraxial Helmholtz equation. However, this is sometimes assumed to be the case: experimentally, we can calculate our w_0 and z_R by plugging in the NA of our focusing objective.

- **Single mode fiber**: for a single mode fiber, to maximize the coupling, the incident field distribution should match the fiber mode distribution. This can be checked by illuminating the fiber from the other side and comparing the sizes of the input and output beams. It can also be calculated as follows for a step index fiber: w_0 can be approximated by

$$w_0 = r\left(0.65 + \frac{1.619}{V^{1.5}} + \frac{2.879}{V^6}\right),$$

where r is the fiber core *radius* and

$$V = \frac{2\pi a}{\lambda}\sqrt{{n_1}^2 - {n_2}^2} = \frac{2\pi a}{\lambda}\mathrm{NA}$$

is the V-number of the fiber (n_1 is the core refractive index and n_2 is the cladding refractive index of the fiber). Therefore, applying equation (C.1), we will need a lens with NA

$$\mathrm{NA} = \frac{\lambda}{\pi w_0}$$

to match the fiber. Equivalently, given a certain lens with focal length f, we will need an incident beam of radius

$$R \simeq \frac{\lambda f}{\pi w_0}.$$

C.4 Detection techniques

Homodyne and heterodyne detection are methods for extracting signals encoded as a modulation (of either phase, frequency or both) of electromagnetic radiation. Although in this section it is assumed that the carrier wave is in the visible spectrum, the exact same principles apply for electric and radiowave signals.

Keep in mind that optical detectors, such as a photodiode, detect intensities, $I(t) \propto E^2(t)$, instead of pure electromagnetic fields. In other words, optical detectors measure the squares of the electromagnetic fields. Thus, the signal acquires a component at double the field's frequency (which is not detected, since it is always out of the detector bandwidth), and a component close to zero frequency, which is converted into an electric signal.

C.4.1 Homodyne detection

Homodyne detection (Fig. C.7) is used to extract a signal $\theta(t)$ encoded as modulation of the phase by comparing the modulated signal with

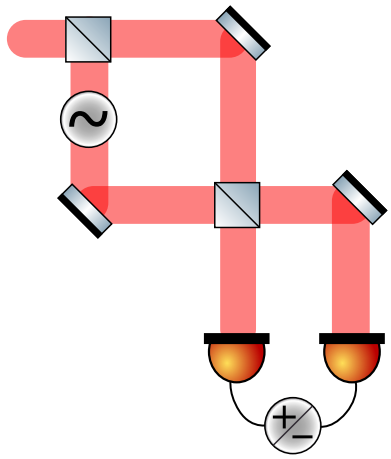

Figure C.7: **Homodyne detection**. Sketch of a homodyne detector, where the modulated field signal $E_s(t)$ is created after passing through an oscillator, marked with a "$\sim$" symbol.

a standard oscillation that would be identical to the signal if it carried null information.

In homodyne detection, the field signal $E_s(t) = E_s \cos(\omega t + \theta(t))$ and the local oscillator signal field $E_h(t) = E_h \cos(\omega t)$ are overlapped at a 50% reflecting beam splitter, and the two interfered fields are detected at two different photodiodes and subtracted. Notice that the two fields E_h and E_s need not have the same amplitude. The fields after the beam splitter are

$$E_1 = \frac{E_\mathrm{h} + E_\mathrm{s}}{\sqrt{2}},$$
$$E_2 = \frac{E_\mathrm{h} - E_\mathrm{s}}{\sqrt{2}}.$$

Thus, after subtraction (and some basic trigonometry) the detected signal will be

$$I \propto \frac{1}{2} E_s E_h \cos(\theta(t)).$$

C.4.2 Heterodyne detection

In heterodyne detection (Fig. C.8), the incoming signal is compared with a standard or reference signal from a "local oscillator" (LO), which would have a fixed offset in frequency and phase from the signal if the

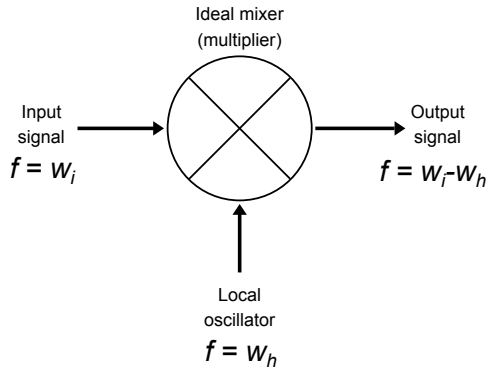

Figure C.8: **Heterodyne detection**. Sketch of a heterodyne mixer, which multiplies the incoming and local oscillator signals. Heterodyning is almost universally used to down-convert the frequency of the signal: for this reason only the $\omega_i - \omega_h$ term (and not the $\omega_i + \omega_h$ term) is considered; the second is usually filtered out.

latter carried null information (i.e., if the carrier were a pure sinusoid). "Heterodyne" signifies more than one frequency, in contrast to the single frequency employed in homodyne detection.

In heterodyne detection, the amplitude of the down-mixed difference frequency can be larger than the amplitude of the original signal itself

$$\begin{aligned} I &\propto \left[E_{\mathrm{i}} \cos(\omega_{\mathrm{i}} t + \theta(t)) + E_h \cos(\omega_h t)\right]^2 \\ &\propto \frac{1}{2} E_{\mathrm{i}}^2 + \frac{1}{2} E_h^2 + 2 E_h E_{\mathrm{i}} \cos(\omega_{\mathrm{i}} t + \theta(t)) \cos(\omega_h t). \end{aligned}$$

The first two terms of the detected signal are proportional to the average (DC) energy flux absorbed. The third term is time varying and creates the sum and difference frequencies and, as can be seen, the larger the LO amplitude, the larger the difference-frequency amplitude (hence, there is gain in the conversion process itself). In the optical regime, the sum frequency will be too high to pass through the subsequent electronics, and only the difference frequency (containing the useful phase information) and DC components will be detected.

D

Trapped particles techniques

D.1 Position detection

The motion of trapped particles can be obtained with a quadrant photodiode (QPD); other motion detector schemes, such as balanced photodiodes, use essentially the same technique, although the measuring apparatus is in a different configuration.

The QPD is divided in four quadrants (A, B, C and D) and has three different outputs:

- $X = (A + D) - (B + C)$,
- $Y = (A + B) - (C + D)$,
- SUM $= A + B + C + D$.

The particle scatters laser beam light in the Rayleigh/Mie regime, and this light, jointly with the remaining unscattered light from the laser, is collimated and projected into the QPD. To first order, the scattering profiles calculated in the QPD (X, Y and SUM) are linear with the particle's position (x, y, z) in a region close to its center, as long as the beam is well aligned and other conditions are fulfilled[1]. This means that if the particle doesn't move "too much", staying in a mostly linear operation region, the measured electrical signals are proportional to the position, $V(t) = S \cdot x(t)$.

The *Signal calibration* section details the procedure to obtain the calibration factor S.

[1] See "Optical Tweezers" [82], by G. Volpe et. al., for more details.

D.2 Particle statistics

D.2.1 The Canonical ensemble

The *Gibbs distribution* (or Boltzmann-Gibbs distribution, or Gibbs measure) is the probability distribution that gives the probability of a certain state as a function of that state's energy and temperature (the temperature of the thermal bath)[2]. It takes the expression

$$P(X = x) = \frac{1}{Z} \exp(-\beta H(p, q)), \tag{D.1}$$

where Ω is the variable space domain, Z

$$Z = \int_{\mathbf{\Omega}} \exp(-\beta H(p, q)) \tag{D.2}$$

is a normalizing factor (the partition function or "state counting function" in the discrete case), $\beta = \frac{1}{k_{\mathrm{B}} T}$ and $E(x)$ is the energy of the state x; in the discrete case, the number of particles N also enters the expression of Z. This is the basic distribution of the Canonical ensemble: almost every relevant quantity that describes the system statistics can be derived from this expression.

In the case of a trapped particle, the distribution represents the probability density that a particle is in position x, given its trapping potential $\Psi(x)$:

$$\rho_\infty(x) = \frac{1}{Z} \exp(-\beta \Psi(x)). \tag{D.3}$$

This expression can also be obtained as the invariant measure of an Itô diffusion defined by a gradient flow (see the SDE section [LINK]). In other words, given a gradient flow, the probability density function $\rho_\infty(x)$ of the equation variable $x(t)$ will *converge* towards (D.3), rightfully earning the name of *equilibrium*.

This is a especially relevant fact for particles trapped in a potential: it implies that, other than the particle dynamics being well described by a (stochastic) gradient flow, the canonical ensemble doesn't require any further assumptions. In particular, ergodicity is a corollary of the type of system, not a different requirement. For instance, in the linear equation case, the dynamics form a (multivariate) Ornstein-Uhlenbeck model, which is provably [194] geometrically ergodic.

[2]Interestingly, this distribution arises in machine learning as the equilibrium solution of a stochastic gradient descent. A way to derive it is to write the SDE of a gradient flow and apply the Feynman-Kac or Kolmogorov backward equation. See Annex A.

D.2.2 Equipartition theorem

As we have seen, the canonical ensemble is normalized such that

$$\frac{1}{Z}\int e^{-\beta H(p,q)}d\Gamma = 1. \tag{D.4}$$

Using integration by parts for a phase-space variable x_k, the above can be written as,

$$\frac{1}{Z}\int e^{-\beta H(p,q)}d\Gamma = \frac{1}{Z}\int d[x_k e^{-\beta H(p,q)}]d\Gamma_k - \frac{1}{Z}\int x_k \frac{\partial e^{-\beta H(p,q)}}{\partial x_k}d\Gamma, \tag{D.5}$$

where $\mathrm{d}\Gamma_k = \mathrm{d}\Gamma/\mathrm{d}x_k$, i.e., the first integration is not carried out over x_k. Performing the first integral between two limits a and b and simplifying the second integral yields the equation

$$\frac{1}{Z}\int \left[e^{-\beta H(p,q)}x_k\right]_{x_k=a}^{x_k=b} d\Gamma_k + \frac{1}{Z}\int e^{-\beta H(p,q)}x_k\beta\frac{\partial H}{\partial x_k}d\Gamma = 1. \tag{D.6}$$

The first term is usually zero, either because x_k is zero at the limits, or because the energy goes to infinity at those limits. In that case, the *equipartition theorem* for the canonical ensemble follows immediately

$$\frac{1}{Z}\int e^{-\beta H(p,q)}x_k\frac{\partial H}{\partial x_k}\,d\Gamma = \left\langle x_k\frac{\partial H}{\partial x_k}\right\rangle = \frac{1}{\beta} = k_{\mathrm{B}}T. \tag{D.7}$$

The general expression of the equipartition theorem is then

$$\left\langle x_m\frac{\partial H}{\partial x_n}\right\rangle = \delta_{mn}k_{\mathrm{B}}T. \tag{D.8}$$

Here, the averaging symbolized by $\langle\ldots\rangle$ is the ensemble average taken over the canonical ensemble. The ensemble average can be calculated over the phase space (different samples) or over time as long as the system is *ergodic*[3], as is the case for the OU particle model.

For a particle in a quadratic potential, the Hamiltonian is

$$H = \frac{1}{2}mv^2 + \Psi(x) = \frac{1}{2}mv^2\frac{1}{2}m\omega_0^2x^2. \tag{D.9}$$

Therefore,

$$\left\langle x\frac{\partial H}{\partial x}\right\rangle = \left\langle m\omega_0^2x^2\right\rangle = k_{\mathrm{B}}T, \tag{D.10}$$

$$\left\langle v\frac{\partial H}{\partial v}\right\rangle = \left\langle mv^2\right\rangle = k_{\mathrm{B}}T, \tag{D.11}$$

which are the classic expressions of the equipartition theorem.

[3]This condition is usually close to impossible to prove (often one just assumes this is the case).

D.2.3 Signal calibration

At equilibrium, by the equipartition theorem

$$\langle V^2 \rangle = S^2 \langle x^2 \rangle = \frac{k_\mathrm{B} T}{m\omega^2}, \tag{D.12}$$

where T is the ambient temperature, m is the mass particle (that can be calculated by several methods)[4] and ω can be measured from the PSD. Therefore

$$S^2 = \frac{k_\mathrm{B} T}{m\omega^2 \langle V^2 \rangle}, \tag{D.13}$$

providing a way to transform between voltage and position.

D.2.4 Fluctuation-dissipation theorem

A free Brownian particle satisfies the following equation of motion

$$\begin{aligned} \mathrm{d}x &= v\mathrm{d}t, \\ \mathrm{d}v &= \frac{1}{m}\left(-\gamma v \mathrm{d}t + \sigma \mathrm{d}W_t\right). \end{aligned}$$

Given the mass m and the drag γ, it is possible to determine the value of σ by forcing the system to obey the equipartition theorem. To solve for σ we only need to focus on the second equation, since it is decoupled from the first one:

$$m\dot{v} + \gamma v = \sigma \eta(t), \tag{D.14}$$

or, in Itô's notation,

$$\mathrm{d}v_t = -a v_t \,\mathrm{d}t + b\,\mathrm{d}W_t, \tag{D.15}$$

with $a = \frac{\gamma}{m} > 0$, $b = \frac{\sigma}{m}$. The solution of this SDE is

$$v_t = v_0 e^{-at} + b\int_0^t e^{-a(t-s)} \mathrm{d}W_s, \tag{D.16}$$

and applying Itô's isometry

$$\mathbb{E}[v_t^2] = \frac{b^2}{2a}\left(1 - e^{-2at}\right). \tag{D.17}$$

[4]For instance, using the provider's density and radius, calculating the radius from autocorrelation/PSD measurements and obtaining m with the density, or following the procedure described in section "Determination of the mass".

For long times

$$\lim_{t\to\infty} \mathbb{E}[v_t^2] = \frac{b^2}{2a} = \frac{\sigma^2}{2\gamma m}, \tag{D.18}$$

and, since by the equipartition theorem

$$\langle v^2 \rangle = \frac{k_\mathrm{B}T}{m}, \tag{D.19}$$

we find

$$\sigma = \sqrt{2k_\mathrm{B}T\gamma}, \tag{D.20}$$

known as the *fluctuation-dissipation* theorem because it relates the fluctuation force with the dissipation or drag.

D.2.5 COM temperature and phonons

Strictly speaking, the thermodynamic temperature is only defined when the particle is in thermodynamic equilibrium, where the quantum state is of the Gibbs form

$$\rho = \frac{e^{-H/k_\mathrm{B}T}}{\mathrm{Tr}\left(e^{-H/k_\mathrm{B}T}\right)}. \tag{D.21}$$

Here, H is the Hamiltonian and T is the temperature. However, in general a cold trapped atom or particle will not be in thermodynamic equilibrium.

A more interesting quantity that does not require a thermodynamic equilibrium is the average number of vibrational excitations of the particle motion. This is also known as the phonon occupation number, and is often denoted by $\bar{n}$ or $\langle n \rangle$. When the atom/nanoparticle is close to the potential minimum of a deep trap, the oscillations can be treated as approximately harmonic. In that case, the average number of vibrational excitations at thermal equilibrium is given by the Bose-Einstein statistics,

$$\frac{\langle E \rangle}{\hbar\omega} = \frac{1}{2} + \langle n \rangle_\mathrm{eq} = \frac{1}{2} + \frac{1}{e^{\hbar\omega/k_\mathrm{B}T} - 1}, \tag{D.22}$$

where $\omega/2\pi$ is the frequency of harmonic oscillations[5]. In the limit of high temperature this reduces to the equipartition expression (via first order Taylor expansion)

$$\langle E \rangle = \hbar\omega \langle n \rangle_\mathrm{eq} \approx k_\mathrm{B}T, \tag{D.23}$$

[5]Note that the energy E_n is proportional to n plus a constant $1/2$ factor: this constant factor makes no contribution to any statistical properties and can be ignored.

where $\langle E \rangle$ is the average energy. Therefore, given an experimentally determined $\langle n \rangle$, one can obtain an effective temperature according to the above formulae, whether or not the system is truly at equilibrium.

In the limit of low temperatures the previous expression reduces to $\bar{E} = \frac{1}{2}\hbar\omega$, the ground-state energy of the quantum harmonic oscillator.

D.3 Determination of the mass

To determine the mass of an optically trapped particle, we follow the procedure described in F. Ricci et. al. [101]. The method requires setting the net number of charges of the trapped particle to a known value, which we achieve with the creation of a plasma discharge[6]. The mass can be obtained by comparing the ratio of two different effects on the particle dynamics: the (stochastic) thermal driving and the force created by a finely calibrated electric field.

Since the motion of the particle in the optical trap without any driving is purely thermal, its PSD $S_v(\omega)$ is well approximated by a Lorentzian function

$$S_v(\omega) = \frac{\sigma^2/m^2}{(\omega^2 - \omega_0^2)^2 + \Gamma^2\omega^2}. \tag{D.24}$$

From an experimental measurement of $S_v^{\mathrm{th}}(\omega)$ we can extract the value of $S_v^{\mathrm{th}}(\omega_{\mathrm{dr}})$ and perform maximum likelihood estimation to obtain the values of ω_0 and Γ as fitting parameters. Introducing an electric driving, we determine the magnitude of the driven resonance $S_v(\omega_{\mathrm{dr}})$ and calculate the electrical contribution $S_v^{\mathrm{el}}(\omega_{\mathrm{dr}}) = S_v(\omega_{\mathrm{dr}}) - S_v^{\mathrm{th}}(\omega_{\mathrm{dr}})$.

The mass of the particle can ultimately be calculated considering the ratio $R_S = \frac{S_v^{\mathrm{el}}(\omega_{\mathrm{dr}})}{S_v^{\mathrm{th}}(\omega_{\mathrm{dr}})} = \frac{S_v - S_v^{\mathrm{th}}}{S_v{}^{\mathrm{th}}}\Big|_{\omega=\omega_{\mathrm{dr}}}$. Note that S_v^{el} scales as m^{-1} while S_v^{th} scales as m^{-2}. Thus, from their ratio we obtain:

$$m = \frac{n_q^2\ q_e^2\ E_0^2\ \mathcal{T}}{8\ k_{\mathrm{B}} T\ \Gamma\ R_S}\ , \tag{D.25}$$

where n_q is the number of elementary charges, q_e the electron charge, E_0 the electric field amplitude, $\mathcal{T}$ the trace integration time, k_{B} Boltzmann's constant, Γ the damping and R_S the previously calculated ratio.

[6] We control the charges as in Ref. [158]: after the plasma is created, the charge is monitored with single electron precision by driving the particle at a specific frequency ω_{dr} and looking at the amplitude jumps.

E

WKB calculations

E.1 First small parameter

We study the dynamics of a trapped particle, satisfying the equation of motion

$$m\ddot{y} + \gamma\dot{y} - \epsilon\cos(\omega_{\mathrm{d}}t)y = \sigma\eta_t. \tag{E.1}$$

Here, γ, ϵ, ω_{d} and σ are constants and η_t denotes a unit intensity white noise; γ is related to the Γ of the main text by $\gamma = \Gamma m$. m is the particle's mass and we are interested in small values of m. We are thus going to conduct an asymptotic analysis of the solutions to (E.1) as $m \to 0$. The primary object of study is the variance of the particle's position, i.e., the expected value of $(y(t) - \mu_t)^2$ where μ_t denotes the expected value of $y(t)$. In the case when $y(0) = \dot{y}(0) = 0$, we have $\mu_t = 0$ and the variance is equal to the second moment $\mathbb{E}\left[y(t)^2\right]$. Here (and in all the text) $\mathbb{E}$ denotes expected value.

First, we are going to study the homogeneous equation:

$$m\ddot{y} + \gamma\dot{y} - \epsilon\cos(\omega_{\mathrm{d}}t)y = 0. \tag{E.2}$$

This second-order equation has two linearly independent solutions. We want to find their approximate expressions, in order to study the solution of the randomly perturbed equation (E.1). To do this we first postulate that $y(t)$ has the form

$$y(t) = \exp\left(-\frac{\gamma}{2m}t\right)u(t) \tag{E.3}$$

and substitute into (E.2) obtaining

$$m\ddot{u} = \left(\frac{\gamma^2}{4m} + \epsilon\cos(\omega_{\mathrm{d}}t)\right)u. \tag{E.4}$$

Multiplying both sides by m, we rewrite (E.4) as

$$m^2\ddot{u} = \left(\frac{\gamma^2}{4} + m\epsilon\cos(\omega_{\mathrm{d}}t)\right)u. \tag{E.5}$$

We will study the last equation, by the WKB method. Using the ansatz

$$u(t) = \exp\left(\frac{1}{m}S_0(t) + S_1(t) + mS_2(t) + \dots\right) \tag{E.6}$$

we get

$$\ddot{u} = \left(\frac{1}{m}\ddot{S}_0 + \ddot{S}_1 + m\ddot{S}_2 + \dots\right)u + \left(\frac{1}{m}\dot{S}_0 + \dot{S}_1 + m\dot{S}_2 + \dots\right)^2 u. \tag{E.7}$$

Substituting this formula into equation (E.5) and dividing by u we obtain

$$m^2\left(\frac{1}{m}\ddot{S}_0 + \ddot{S}_1 + m\ddot{S}_2 + \dots\right) + m^2\left(\frac{1}{m}\dot{S}_0 + \dot{S}_1 + m\dot{S}_2 + \dots\right)^2 = \frac{\gamma^2}{4} + m\epsilon\cos(\omega_{\mathrm{d}}t). \tag{E.8}$$

We now compare the coefficients of the same powers of m on both sides of this equation. In order m^0 we obtain

$$\left(\dot{S}_0\right)^2 = \frac{\gamma^2}{4}. \tag{E.9}$$

This equation has two solutions, $\dot{S}_0 = \frac{\gamma}{2}$ and $\dot{S}_0 = -\frac{\gamma}{2}$. Let us start from the first case, so that

$$S_0(t) = \frac{\gamma}{2}t. \tag{E.10}$$

Comparing the terms proportional to m^1 on both sides of (E.8), we obtain

$$\ddot{S}_0 + 2\dot{S}_0\dot{S}_1 = \epsilon\cos(\omega_{\mathrm{d}}t). \tag{E.11}$$

Substituting $S_0(t)$ from (E.10) we obtain

$$S_1(t) = \frac{\epsilon}{\gamma\omega_{\mathrm{d}}}\sin(\omega_{\mathrm{d}}t). \tag{E.12}$$

Next, comparing the terms proportional to m^2 on both sides of (E.8), we find

$$\ddot{S}_1 + \left(\dot{S}_1\right)^2 + 2\dot{S}_0\dot{S}_2 = 0. \tag{E.13}$$

Substituting the calculated expressions for S_0 and S_1 from (E.10) and (E.12) and solving for $\dot{S}_2$ we obtain

$$\dot{S}_2 = \frac{\epsilon\omega_\mathrm{d}}{\gamma^2}\sin(\omega_\mathrm{d}t) - \frac{\epsilon^2}{2\gamma^3}\left(1+\cos(2\omega_\mathrm{d}t)\right), \tag{E.14}$$

and after integration

$$S_2(t) = -\frac{\epsilon}{\gamma^2}\cos(\omega_\mathrm{d}t) - \frac{\epsilon^2}{2\gamma^3}t - \frac{\epsilon^2}{4\gamma^3\omega_\mathrm{d}}\sin(2\omega_\mathrm{d}t). \tag{E.15}$$

Substituting the derived expressions for S_0, S_1 and S_2 into (E.6) and neglecting the higher order terms of the series in the exponent, we obtain for the first of two linearly independent solutions of (E.5) the approximate formula

$$\begin{aligned} u(t) \approx \exp\Bigg[\left(\frac{\gamma}{2m} - \frac{m\epsilon^2}{2\gamma^3}\right)t + \frac{\epsilon}{\gamma\omega_\mathrm{d}}\sin(\omega_\mathrm{d}t) - \\ \frac{m\epsilon}{\gamma^2}\cos(\omega_\mathrm{d}t) - \frac{m\epsilon^2}{4\gamma^3\omega_\mathrm{d}}\sin(2\omega_\mathrm{d}t)\Bigg]. \end{aligned} \tag{E.16}$$

We now multiply $u(t)$ by $\exp\left(-\frac{\gamma}{2m}t\right)$ and drop from the expression in the exponent of (E.16) the periodic terms proportional to m (a fuller justification of this step will be given below) to obtain an approximate expression for the first of two linearly independent solutions of the equation (E.2):

$$y_1(t) \approx \exp\left[\left(-\frac{m\epsilon^2}{2\gamma^3}\right)t + \frac{\epsilon}{\gamma\omega_\mathrm{d}}\sin(\omega_\mathrm{d}t)\right]. \tag{E.17}$$

An approximation of the second one follows from the choice

$$S_0 = -\frac{\gamma}{2}t \tag{E.18}$$

instead of (E.10). A calculation fully analogous to the one presented above leads to

$$y_2(t) \approx \exp\left[\left(-\frac{\gamma}{m} + \frac{m\epsilon^2}{2\gamma^3}\right)t - \frac{\epsilon}{\gamma\omega_\mathrm{d}}\sin(\omega_\mathrm{d}t)\right]. \tag{E.19}$$

Our approximate formulae are in agreement with Floquet theory, according to which two linearly independent solutions of eqn. Eq. (E.2) can be chosen in the form

$$y_j(t) = \exp(\lambda_j t)\, P_j(t) \tag{E.20}$$

for $j = 1, 2$, where P_j are $\frac{2\pi}{\omega_\mathrm{d}}$-periodic functions. λ_1 and λ_2 are the *characteristic exponents* of the equation. The above statement is true whenever the characteristic exponents are distinct, which is clearly the case here. In what follows, only the values of λ_j are going to play a role, since the periodic factors P_j are bounded. This is the reason why we could omit corrections of order m to the exponents in (E.17) and (E.17). Explicitly, we have seen that, according to the WKB approximation:

$$\lambda_1 \approx -\frac{m\epsilon^2}{2\gamma^3}, \tag{E.21}$$

$$\lambda_2 \approx -\frac{\gamma}{m} + \frac{m\epsilon^2}{2\gamma^3}, \tag{E.22}$$

$$P_1(t) = \exp\left(\frac{\epsilon}{\gamma\omega_\mathrm{d}}\sin(\omega_\mathrm{d}t)\right), \tag{E.23}$$

$$P_2(t) = \exp\left(-\frac{\epsilon}{\gamma\omega_\mathrm{d}}\sin(\omega_\mathrm{d}t)\right). \tag{E.24}$$

We now use these values to study the behaviour of solutions to the randomly perturbed equation (E.1). This can be done directly, using variation of constants method for the inhomogeneous second order equation (E.1). According to this method, (E.1) has a particular solution equal to

$$y(t) = \int_0^t \Delta(s)^{-1}\left[y_1(s)y_2(t) - y_1(t)y_2(s)\right]\frac{\sigma}{m}\eta_s\,\mathrm{d}s \tag{E.25}$$

where

$$\Delta(s) = y_1(s)\dot{y}_2(s) - \dot{y}_1(s)y_2(t). \tag{E.26}$$

Below we derive the same expression in a different way. First, we rewrite our equation as a system:

$$\dot{y} = v, \tag{E.27}$$

$$\dot{v} = \frac{\epsilon}{m}y - \frac{\gamma}{m}v + \frac{\sigma}{m}\eta_t. \tag{E.28}$$

Introducing the vector of dynamical variables

$$\mathbf{x} = \begin{pmatrix} y \\ v \end{pmatrix}, \tag{E.29}$$

the matrix

$$\mathbf{A}(t) = \begin{pmatrix} 0 & 1 \\ \frac{\epsilon}{m}\cos(\omega_\mathrm{d}t) & -\frac{\gamma}{m} \end{pmatrix} \tag{E.30}$$

and the noise vector

$$\mathbf{h}(t) = \begin{pmatrix} 0 \\ \frac{\sigma}{m}\eta_t \end{pmatrix} \tag{E.31}$$

we can rewrite the above system as

$$\dot{\mathbf{x}}(t) = \mathbf{A}(t)\mathbf{x}(t) + \mathbf{h}(t). \tag{E.32}$$

If y_1 and y_2 are two linearly independent solutions of the homogeneous equation (E.2), then the matrix

$$\mathbf{Q}(t) = \begin{pmatrix} y_1(t) & y_2(t) \\ \dot{y}_1(t) & \dot{y}_2(t) \end{pmatrix} \tag{E.33}$$

is a fundamental matrix of the homogeneous system

$$\dot{\mathbf{x}}(t) = \mathbf{A}(t)\mathbf{x}(t) \tag{E.34}$$

i.e., $\mathbf{Q}(t)$ satisfies the matrix ODE

$$\dot{\mathbf{Q}}(t) = \mathbf{A}(t)\mathbf{Q}(t). \tag{E.35}$$

The solution of the inhomogeneous system can be written as

$$\mathbf{x}(t) = \mathbf{Q}(t)\mathbf{Q}(0)^{-1}\mathbf{x}(0) + \int_0^t \mathbf{Q}(t)\mathbf{Q}(s)^{-1}\mathbf{h}(s)\,\mathrm{d}s \tag{E.36}$$

This follows from the variation of constants formula and can be easily verified by direct differentiation. Note that because both characteristic exponents are negative, the entries of $\mathbf{Q}(t)$ decay exponentially, and so does the first term in the above formula. Note also, that if the particle is initially at $y = 0$ with zero velocity, than $\mathbf{x}(0) = 0$ and this first term vanishes. In any case, the asymptotic behaviour of the solution is determined by the second term.

We have

$$\mathbf{Q}(t) = \begin{pmatrix} P_1(t)e^{\lambda_1 t} & P_2(t)e^{\lambda_2 t} \\ \dot{P}_1(t)e^{\lambda_1 t} + \lambda_1 P_1(t)e^{\lambda_1 t} & \dot{P}_2(t)e^{\lambda_2 t} + \lambda_2 P_2(t)e^{\lambda_2 t} \end{pmatrix}. \tag{E.37}$$

Hence

$$\begin{aligned} &\Delta(t) \triangleq \det\{\mathbf{Q}\}(t) \\ &= -e^{(\lambda_1+\lambda_2)t}\left[(\lambda_1 - \lambda_2)\,P_1(t)P_2(t) - \left(P_1(t)\dot{P}_2(t) - \dot{P}_1(t)P_2(t)\right)\right]. \end{aligned} \tag{E.38}$$

To leading order, we thus have

$$\Delta(t) \approx -(\lambda_1 - \lambda_2)e^{(\lambda_1+\lambda_2)t}P_1(t)P_2(t) \sim -\frac{\gamma}{m}\exp\left(-\frac{\gamma}{m}t\right). \tag{E.39}$$

Now,

$$\mathbf{Q}(s)^{-1} = \Delta(s)^{-1}\begin{pmatrix} \dot{P}_2(s)e^{\lambda_2 s} + \lambda_2 P_2(s)e^{\lambda_2 s} & -P_2(s)e^{\lambda_2 s} \\ -\dot{P}_1(s)e^{\lambda_1 s} - \lambda_1 P_1(s)e^{\lambda_1 s} & P_1(s)e^{\lambda_1 s} \end{pmatrix}. \tag{E.40}$$

We want to study the first component of the vector $\mathbf{x}(t)$ in (30) Since the first component of the noise vector $\mathbf{h}(s)$ in (25) equals 0, to calculate the first component of the integral in (E.36), we need to multiply the $(1,2)$-element of the matrix $\mathbf{Q}(t)\mathbf{Q}(s)^{-1}$ by $\frac{\sigma}{m}\eta_s$ and integrate over s from 0 to t. The $(1,2)$-matrix element of $\mathbf{Q}(t)\mathbf{Q}(s)^{-1}$ equals

$$\left(\mathbf{Q}(t)\mathbf{Q}(s)^{-1}\right)_{1,2} = \Delta(s)^{-1}\left[-P_1(t)P_2(s)e^{\lambda_1 t+\lambda_2 s} + P_2(t)P_1(s)e^{\lambda_2 t+\lambda_1 s}\right]. \tag{E.41}$$

Approximating $\Delta(s)$ by its leading term, according to (E.39), we obtain

$$\left(\mathbf{Q}(t)\mathbf{Q}(s)^{-1}\right)_{1,2} \approx \frac{m}{\gamma}\left[\frac{P_1(t)}{P_1(s)}e^{\lambda_1(t-s)} - \frac{P_2(t)}{P_2(s)}e^{\lambda_2(t-s)}\right]. \tag{E.42}$$

The factors $P_1(t)/P_1(s)$ and $P_2(t)/P_2(s)$ are of order 1 and, in fact, quite close to 1, since for the considered values of the parameters, $\frac{\epsilon}{\gamma\omega_{\mathrm{d}}}$ is of the order of 10^{-3} (see (E.21)). Of the two exponential factors, $e^{\lambda_1(t-s)}$ and $e^{\lambda_2(t-s)}$, the second decays much faster with $t-s$ and is negligible for small m. We are thus left with the following approximation to $y(t)$ (for simplicity we consider the initial conditions $y(0) = v(0) = 0$):

$$y(t) \approx \frac{\sigma}{\gamma}\int_0^t e^{\lambda_1(t-s)}\eta_s\,\mathrm{d}s = \frac{\sigma}{\gamma}\int_0^t e^{\lambda_1(t-s)}\,dW_s, \tag{E.43}$$

where the last expression is a stochastic integral with respect to the Wiener process W_t, formally (and in the sense of distribution theory) satisfying $\frac{\mathrm{d}W_t}{\mathrm{d}t} = \eta_t$. The Itô isometry implies that

$$\mathbb{E}\left[y(t)^2\right] \approx \left(\frac{\sigma}{\gamma}\right)^2\int_0^t e^{2\lambda_1(t-s)}\,\mathrm{d}s. \tag{E.44}$$

Extending the integral on the right-hand side of the above equation to infinity, we obtain an approximate bound

$$\mathbb{E}\left[y(t)^2\right] \lesssim \frac{\sigma^2}{2\gamma^2|\lambda_1|} = \frac{\sigma^2\gamma}{m\epsilon^2}. \tag{E.45}$$

Rather than substituting specific values of the physical parameters, we compare (the square root of) this result to the experimental value of the standard deviation in order to estimate the value of the particle's actual mass.

We note that, since the exponent λ_1 is very close to zero, for small times t the integrand $e^{2\lambda_1 t}$ is close to 1 and the approximate value of the variance is

$$\mathbb{E}\left[y(t)^2\right] \approx \frac{\sigma^2}{\gamma^2} t. \tag{E.46}$$

This is a good approximation (first term of the Taylor expansion) as long as $\lambda_1 t \ll 1$, thus introducing a time scale $\tau = \frac{1}{\lambda_1}$. For times much smaller than τ the variance grows approximately linearly with t, so the equation describes diffusion; for times larger than τ, localization effects become pronounced.

It is interesting to compare the results of the above calculation with those obtained from a different limit, used in the reference [91].

E.2 Second small parameter

We rewrite eq. (3.1) as

$$\kappa^2 \ddot{y} + \kappa \dot{y} - \beta' \cos(2\tau) y = \frac{m\sigma}{\gamma^2} \sqrt{\frac{\omega_\mathrm{d}}{2}} \eta(\tau), \tag{E.47}$$

which is a reformulation of (3.1) where $\tau = \frac{\omega_\mathrm{d} t}{2}$ as before, $\beta' = \frac{m\epsilon}{\gamma^2}$ and $\kappa = \frac{m\omega_\mathrm{d}}{2\gamma}$ is the new small parameter. With this new small parameter, we start by dividing eq. (E.47) by κ^2 and transforming it into the system

$$\vec{\dot{x}}(\tau) = \mathbf{A}(\tau)\vec{x} + \vec{f}(\tau), \tag{E.48}$$

where

$$\vec{x} = \begin{pmatrix} x(t) \\ \dot{x}(t) \end{pmatrix}, \quad \mathbf{A} = \begin{pmatrix} 0 & 1 \\ \beta' \cos(2\tau)/\kappa^2 & -1/\kappa \end{pmatrix},$$
$$\vec{f}(\tau) = \begin{pmatrix} 0 \\ \frac{4\sigma}{m\omega_\mathrm{d}^2} \sqrt{\frac{\omega_\mathrm{d}}{2}} \eta(\tau) \end{pmatrix}.$$

Let $\mathbf{\Phi}(\tau)$ be a principal fundamental matrix solution when $\vec{f}(\tau) = \vec{0}$. Then the general solution is

$$\vec{x}(\tau) = \mathbf{\Phi}(\tau)\vec{x}(0) + \int_0^\tau \mathbf{\Phi}(\tau)\mathbf{\Phi}(s)^{-1} \vec{f}(s)\, \mathrm{d}s. \tag{E.49}$$

From the previous derivation, the two linearly independent solutions of (E.47) are

$$x_{1,2}(\tau) = \left(\frac{1}{4} + \beta' \cos(2\tau)\right)^{-\frac{1}{4}} \cdot \exp\left(-\frac{\tau}{2\kappa} \pm \frac{1}{\kappa}\int_0^\tau \sqrt{\frac{1}{4} + \beta' \cos(2\tau)}\,\mathrm{d}\tau\right). \tag{E.50}$$

Taylor expanding this expression[1] gives

$$x_{1,2}(\tau) = \left(\frac{1}{4}\right)^{-\frac{1}{4}} \cdot \exp\left(-\frac{\tau}{2\kappa}\right) \cdot \exp\left(\pm\frac{1}{\kappa}\int_0^\tau \left(\frac{1}{2} + \beta' \cos(2\tau) - \beta'^2 \frac{1+\cos(4\tau)}{2}\,\mathrm{d}\tau\right)\right). \tag{E.51}$$

This results in

$$x_{1,2}(\tau) = \left(\frac{1}{4}\right)^{-\frac{1}{4}} \cdot \exp\left(-\frac{\tau}{2\kappa}\right) \cdot \exp\left(\pm\left(\frac{\tau}{2\kappa} + \frac{\beta' \sin(2\tau)}{2\kappa} - \frac{\beta'^2\tau}{2\kappa} - \frac{(\beta')^2 \sin(4\tau)}{8\kappa}\right)\right). \tag{E.52}$$

Using $\tau = \frac{\omega_\mathrm{d} t}{2}, \beta' = \frac{m\epsilon}{\gamma^2}, \kappa = \frac{m\omega_\mathrm{d}}{2\gamma}$, and substituting into eq. (E.52), we find (approximate) explicit expressions for the two fundamental solutions,

$$x_1 = \left(\frac{1}{4}\right)^{-\frac{1}{4}} \cdot \exp\left(\frac{\epsilon \sin(\omega_\mathrm{d} t)}{\omega_\mathrm{d}\gamma} - \frac{m\epsilon^2 t}{\gamma^3}\right) \tag{E.53}$$

and

$$x_2 = \left(\frac{1}{4}\right)^{-\frac{1}{4}} \cdot \exp\left(-\frac{\gamma t}{m} - \frac{\epsilon \sin(\omega_\mathrm{d} t)}{\omega_\mathrm{d}\gamma}\right). \tag{E.54}$$

If $P_1(\tau)e^{\lambda_1\tau}$, $P_2(\tau)e^{\lambda_2\tau}$ represent two linearly independent solutions of the homogeneous equation, then

$$\left(\mathbf{\Phi}(\tau)\mathbf{\Phi}^{-1}(s)\right)_{1,2} = \frac{e^{\lambda_2(\tau-s)}P_2(\tau)P_1(s) - e^{\lambda_1(\tau-s)}P_1(\tau)P_2(s)}{P_1(s)(P_2'(s) + \lambda_2 P_2(s)) - P_2(s)(P_1'(s) + \lambda_1 P_1(s))} \approx \frac{m\omega_\mathrm{d}}{2\gamma} e^{\frac{-m\epsilon^2(\tau-s)}{\omega_\mathrm{d}\gamma^3}}. \tag{E.55}$$

[1] This is justified because $\beta' \ll 1$.

We still need to solve the inhomogeneous equation, for which we compute

$$\begin{aligned}
&\int_0^\tau \left(\mathbf{\Phi}(\tau)\eta(s)\mathbf{\Phi}(s)^{-1}\right)_{1,2} f_2(s)\eta(s)\,\mathrm{d}s \\
&\quad\approx \int_0^\tau \frac{m\omega_\mathrm{d}}{2\gamma}\frac{4\sigma}{m\omega_\mathrm{d}^2}\sqrt{\frac{\omega_\mathrm{d}}{2}}\eta(s)e^{\frac{-m\epsilon^2(\tau-s)}{\omega_\mathrm{d}\gamma^3}}\eta(s)\,\mathrm{d}s \\
&\quad= \int_0^\tau \frac{\sigma}{\gamma}\sqrt{\frac{2}{\omega_\mathrm{d}}}e^{\frac{-m\epsilon^2(\tau-s)}{\omega_\mathrm{d}\gamma^3}}\eta(s)\,\mathrm{d}s. \qquad \text{(E.56)}
\end{aligned}$$

This provides us with an explicit solution of the process $x(t)$ in terms of elementary functions, and we may use it to calculate the variance of the process [2] Applying the Itô isometry to eq. (E.56), we get

$$\mathbb{E}\left[\int_0^\tau \frac{\sigma}{\gamma}\sqrt{\frac{2}{\omega_\mathrm{d}}}e^{\frac{-m\epsilon^2(\tau-s)}{\omega_\mathrm{d}\gamma^3}}\mathrm{d}W_s\right]^2 \qquad \text{(E.57)}$$

$$= \int_0^\tau \frac{\sigma^2}{\gamma^2}\frac{2}{\omega_\mathrm{d}}e^{\frac{-2m\epsilon^2(\tau-s)}{\omega_\mathrm{d}\gamma^3}}\mathrm{d}s. \qquad \text{(E.58)}$$

Using $s = \frac{\omega_\mathrm{d}t}{2}$, we finally obtain

$$\mathbb{E}[y^2(t)] \simeq \left(\frac{\sigma}{\gamma}\right)^2 \int_0^{\frac{2t}{\omega_\mathrm{d}}} e^{\frac{-m\epsilon^2 t}{\gamma^3}}\mathrm{d}s. \qquad \text{(E.59)}$$

This is in agreement with what was obtained from the small mass limit.

[2] The first moment is $\mathbb{E}[x(t)] = 0$, by the properties of the Itô integral with respect to a Wiener process.

F

Control theory

F.1 Introduction

Assume we have a time series (i.e., data indexed by time), generated by some underlying system, and that this data may contain additional statistical noise or other inaccuracies. In the context of state space representation, we may suppose that our system is well modelled by the equations

$$\frac{d}{dt}\mathbf{x}(t) = \mathbf{A}(t)\mathbf{x}(t) + \mathbf{B}(t)\mathbf{u}(t) + \mathbf{w}(t), \tag{F.1}$$

$$\mathbf{z}(t) = \mathbf{H}(t)\mathbf{x}(t) + \mathbf{v}(t), \tag{F.2}$$

where $\mathbf{x}(t)$ is the state vector (the true state of the system), $\mathbf{z}(t)$ is the observation vector (the observed state of the system, or "output"), $\mathbf{u}(t)$ is the control vector (the "input" to our system), $\mathbf{A}(t)$ is the state transition matrix (a model for the underlying dynamical system), $\mathbf{B}(t)$ is the control-input matrix (how we can *act* on the system), $\mathbf{H}(t)$ is the observation model (what we observe out of $\mathbf{x}(t)$) and $\mathbf{w}(t)$ and $\mathbf{v}(t)$ are the process and observation noise, respectively[1].

The state of a deterministic system completely describes the system at any given time. In particular, no information on the past of a system is needed to help in predicting the future, if the states at the present time are known and all current and future values of the control variables (those whose values can be chosen) are also known. In essence, it is an initial value problem, and the initial values completely determine the system evolution.

State space models can be given in three completely equivalent forms:

[1]The system has been modelled as a continuous, differential equation in this example. For this case, the associated Kalman filter is known as the Kalman-Bucy filter. However, everything can be rewritten for discrete processes in a totally analogous way.

- Differential equation form, with all its variants (continuous time and discrete time).
- Transfer function form, in the Laplace or z transform domains.
- Impulse response form, by undoing the Laplace or z transforms.

F.2 Observability

A system is said to be *observable* if, for any possible sequence of state and control vectors (the latter being variables whose values one can choose), the current state $\mathbf{x}(t)$ can be determined in finite time using only the outputs $\mathbf{z}(t)$. Less formally, this means that one can determine the behaviour of the entire system from the system's outputs, even in the case where $\mathbf{z}(t)$ is of lower dimension than $\mathbf{x}(t)$.

A continuous time-invariant linear state-space model is observable if and only if

$$\operatorname{rank} \begin{bmatrix} \mathbf{H} \\ \mathbf{H} \cdot \mathbf{A} \\ \vdots \\ \mathbf{H} \cdot \mathbf{A}^{n-1} \end{bmatrix} = n, \tag{F.3}$$

where rank is the number of linearly independent rows in a matrix, and where n is the number of state variables.

F.3 Controllability

Roughly, the concept of controllability denotes the ability to move a system around its configuration space using only certain admissible manipulations. The controllability property plays a crucial role in many control problems, such as stabilization of unstable systems by feedback, or optimal control.

The state controllability condition implies that it is possible—by the admissible inputs $\mathbf{u}(t)$—to steer the states $\mathbf{x}(t)$ from any initial value $\mathbf{x}_0$ to any final value within some finite time window. A continuous time-invariant linear state-space model is *controllable* if and only if

$$\begin{bmatrix} \mathbf{B} & \mathbf{A} \cdot \mathbf{B} & \cdots & \mathbf{A}^{n-1} \cdot \mathbf{B} \end{bmatrix} = n. \tag{F.4}$$

Controllability and observability are dual aspects of the same problem.

F.4 The Kalman filter

The *Kalman filter* is a recursive algorithm that uses the observed data $\mathbf{z}(t)$ and the (assumed) dynamical model $\mathbf{A}(t)$, and provides estimates of the state of the process, in a way that minimizes the mean of the squared error[2].

In most applications, the internal state is much larger (more degrees of freedom) than the few observable parameters which are measured. However, by combining a series of measurements, the Kalman filter can estimate the entire internal state. In other words, the Kalman filter is a full state estimator (and the best at it, in the L^2 sense). It requires, however, that the system is observable, as defined before. If the system has unobservable states, the filter will simply not work.

The Kalman filter allows us to

- Compute the sequence of distributions of the current state (i.e., taking into account all uncertainties), given all observations until now, for each time period. This gives us an estimate of the unobservable state $\mathbf{x}(t)$ in a way that doesn't depend on future data. Intuitively, the Kalman filter helps recover $\mathbf{x}(t)$ from $\mathbf{z}(t)$ and reduces the measurement noise.

- Compute the likelihood of the data. This allows us to perform maximum likelihood estimation and fit the model.

The Kalman filter is an extension of the sequential minimum mean square error (MMSE) estimator[3], in which instead of a fixed parameter, we may have time-varying parameters: the price to pay is that a dynamical model of the system must be known[4]. It is also a recursive estimator: this means that only the estimated state from the previous time step and the current measurement are needed to compute the estimate for the current state.

Below, some properties of the Kalman filter are listed:

- It is a time-varying filter (the Kalman gain changes with n).

[2]For a nice, visual introduction to this filter, follow this link.

[3]In the linear case, the MMSE estimator (or LMMSE) is also known as the Wiener filter. The Wiener filter can only be applied to wide-sense stationary signals, whereas the Kalman filter applies also to non-stationary signals that can be characterized by a dynamical model.

[4]The block diagrams of both (Kalman and MMSE estimator) are nearly identical except for the Az^{-1} feedback box in the Kalman filter, which for the MMSE estimator is just a z^{-1} box. A is the dynamical model's state-transition matrix

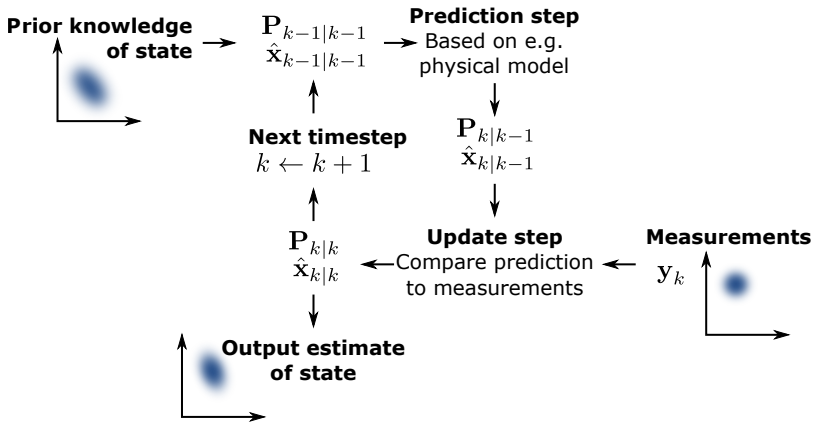

Figure F.1: **A step of the Kalman filter**. The Kalman filter keeps track of the estimated state of the system and the variance or uncertainty of the estimate. The estimate is updated using a state transition model and measurements. $\hat{x}_{k|k-1}$ denotes the estimate of the system's state at time step k before the k-th measurement y_k has been taken into account. $P_{k|k-1}$ is the corresponding uncertainty. Image by Petteri Aimonen, under the Creative Commons CC0 1.0 license.

- The Kalman filter computes and uses its performance measure $M[n|n]$.
- The prediction increases the error, the update decreases the error.
- As $n \to \infty$, the Kalman filter reaches a "steady-state" and becomes a linear, time invariant filter (i.e., $K[n]$ constant, $\mathbf{P}[n|n]$ constant).
- If a) the model perfectly matches the real system, b) the entering noise is white (uncorrelated) and c) the covariances of the noise are exactly known, then the KF is the optimal (MMSE) state estimator. In the non-Gaussian case, the KF is still the best *linear* LMMSE.
- $M[n|n-1]$, $M[n|n]$, $K[n]$ can be computed off-line (ahead of time).

F.4.1 Kalman equations

The state of the filter is represented by two variables: $\hat{\mathbf{x}}_{k|k}$ is the posteriori state estimate at time k given observations up to and including at time k, and $\mathbf{P}_{k|k}$ is the posteriori error covariance matrix (a measure of the estimated accuracy of the state estimate).

The Kalman filter can be written as a single equation, but it is most often conceptualized as two distinct phases: "predict" and "update". The

predict phase uses the state estimate from the previous time step to produce an estimate of the state at the current time step. This predicted state estimate is also known as the a priori state estimate because, although it is an estimate of the state at the current time step, it does not include observation information from the current time step. In the update phase, the current a priori prediction is combined with current observation information to refine the state estimate. This improved estimate is termed the a posteriori state estimate.

Typically, the two phases alternate, with the prediction advancing the state until the next scheduled observation, and the update incorporating the observation. However, this is not necessary; if an observation is unavailable for some reason, the update may be skipped and multiple prediction steps performed. Likewise, if multiple independent observations are available at the same time, multiple update steps may be performed (typically with different observation matrices $\mathbf{H}_k$.

Filter steps

Initialization In order to start using the Kalman filter, one must model the process in accordance with the framework of the Kalman filter. This means specifying the following matrices:

1. $\mathbf{A}_k$, the state-transition model.
2. $\mathbf{H}_k$, the observation model.
3. $\mathbf{Q}_k$, the covariance of the process noise.
4. $\mathbf{R}_k$, the covariance of the observation noise.
5. $\mathbf{B}_k$, the control-input model, for each time-step as described below.

Prediction The prediction phase advances the state estimate until the next scheduled observation.

1. Predict the state estimate:

$$\hat{\mathbf{x}}_{k|k-1} = \mathbf{A}_k \hat{\mathbf{x}}_{k-1|k-1} + \mathbf{B}_k \mathbf{u}_k. \tag{F.5}$$

2. Predict the error covariance:

$$\mathbf{P}_{k|k-1} = \mathbf{A}_k \mathbf{P}_{k-1|k-1} \mathbf{A}_k^{\mathrm{T}} + \mathbf{Q}_k. \tag{F.6}$$

Update The update incorporates the observation to improve the estimates.

1. Innovation (pre-fit residual):
$$\tilde{\mathbf{y}}_k = \mathbf{z}_k - \mathbf{H}_k\hat{\mathbf{x}}_{k|k-1}. \tag{F.7}$$
2. Innovation covariance:
$$\mathbf{S}_k = \mathbf{R}_k + \mathbf{H}_k\mathbf{P}_{k|k-1}\mathbf{H}_k^{\mathrm{T}}. \tag{F.8}$$
3. Optimal Kalman gain:
$$\mathbf{K}_k = \mathbf{P}_{k|k-1}\mathbf{H}_k^{\mathrm{T}}\mathbf{S}_k^{-1}. \tag{F.9}$$
4. Updated state estimate:
$$\hat{\mathbf{x}}_{k|k} = \hat{\mathbf{x}}_{k|k-1} + \mathbf{K}_k\tilde{\mathbf{y}}_k. \tag{F.10}$$
5. Updated estimate covariance:
$$\mathbf{P}_{k|k} = (\mathbf{I} - \mathbf{K}_k\mathbf{H}_k)\mathbf{P}_{k|k-1}(\mathbf{I} - \mathbf{K}_k\mathbf{H}_k)^T + \mathbf{K}_k\mathbf{R}_k\mathbf{K}_k^T. \tag{F.11}$$
The formula for the updated estimate covariance above is valid for any gain $\mathbf{K}_k$. For the optimal Kalman gain the formula further simplifies to
$$\mathbf{P}_{k|k} = (\mathbf{I} - \mathbf{K}_k\mathbf{H}_k)\mathbf{P}_{k|k-1}, \tag{F.12}$$
in which form it is most widely used in applications. However, one must keep in mind that it is valid only for the optimal gain that minimizes the residual error.
6. Post-fit residual:
$$\tilde{\mathbf{y}}_{k|k} = \mathbf{z}_k - \mathbf{H}_k\hat{\mathbf{x}}_{k|k}. \tag{F.13}$$

Invariants If the model is accurate, and the values for $\hat{\mathbf{x}}_{0|0}$ and $\mathbf{P}_{0|0}$ accurately reflect the distribution of the initial state values, then the following invariants are preserved:
$$\mathbb{E}[\mathbf{x}_k - \hat{\mathbf{x}}_{k|k}] = \mathbb{E}[\mathbf{x}_k - \hat{\mathbf{x}}_{k|k-1}] = 0$$
$$\mathbb{E}[\tilde{\mathbf{y}}_k] = 0.$$
That is, all estimates have a mean error of zero. Also
$$\mathbf{P}_{k|k} = \mathrm{cov}(\mathbf{x}_k - \hat{\mathbf{x}}_{k|k})$$
$$\mathbf{P}_{k|k-1} = \mathrm{cov}(\mathbf{x}_k - \hat{\mathbf{x}}_{k|k-1})$$
$$\mathbf{S}_k = \mathrm{cov}(\tilde{\mathbf{y}}_k),$$
so covariance matrices accurately reflect the covariance of estimates.

F.4.2 Estimation of the noise covariances $\mathbf{Q}_k$ and $\mathbf{R}_k$

Practical implementation of the Kalman Filter is often difficult due to the difficulty of getting a good estimate of the noise covariance matrices $\mathbf{Q}_k$ and $\mathbf{R}_k$. One practical approach to do this is the autocovariance least-squares (ALS).

F.5 Optimal control

Optimal control deals with the problem of finding a control law $\mathbf{u}(t)$ for a given system such as the one described in eqs. (F.1), such that a certain optimality criterion is achieved. Optimal control problems include a cost functional $\mathcal{J}$—which is a function of the state and control variables—that needs to be minimized among all the possible trajectories by choosing the adequate control law $\mathbf{u}(t)$.

A special case of the the deterministic optimal control problem is the linear quadratic optimal control problem. The LQ problem arises when trying to minimize the quadratic continuous-time cost functional

$$\mathcal{J} = \frac{1}{2}\mathbf{x}^{\mathsf{T}}(t_f)\mathbf{S}_f\mathbf{x}(t_f) + \tfrac{1}{2}\int_{t_0}^{t_f} [\,\mathbf{x}^{\mathsf{T}}(t)\mathbf{Q}(t)\mathbf{x}(t) + \mathbf{u}^{\mathsf{T}}(t)\mathbf{R}(t)\mathbf{u}(t)\,]\,\mathrm{d}t. \quad \text{(F.14)}$$

F.5.1 LQR controller

A particular form of the LQ problem that arises in many control system problems is that of the *linear quadratic regulator* (LQR), where all of the matrices are constant, the initial time is arbitrarily set to zero, and the terminal time is taken in the limit $t_f \to \infty$ (known as infinite horizon). The cost functional then becomes

$$\mathcal{J} = \tfrac{1}{2}\int_0^{\infty} [\,\mathbf{x}^{\mathsf{T}}(t)\mathbf{Q}\mathbf{x}(t) + \mathbf{u}^{\mathsf{T}}(t)\mathbf{R}\mathbf{u}(t)\,]\,\mathrm{d}t, \quad \text{(F.15)}$$

subject to the first-order dynamic constraints of (F.1).

In the finite-horizon case, the matrices $\mathbf{Q}$ and $\mathbf{R}$ are positive semi-definite and positive definite, respectively. In the infinite-horizon case, however, they are not only positive-semidefinite and positive-definite, respectively, but are also constant. Furthermore, in order to ensure that the cost function is bounded, the system must be controllable.

Note that, if $\mathbf{Q}$ and $\mathbf{R}$ are identity matrices (possibly times a constant), the functional becomes

$$\mathcal{J} = \frac{1}{2}\int_0^{T} \|\mathbf{x}\|^2 + \rho\,\|\mathbf{u}\|^2\,\mathrm{d}t, \quad \text{(F.16)}$$

since, by linearity, we can rescale the functional and be left only with the parameter $\rho \in \mathbb{R}$. Therefore, minimizing $\mathcal{J}$ can be thought of physically as attempting to minimize a weighted sum of the system and control energies.

It has been shown [195] that the LQ (or LQR) optimal control has the feedback form

$$\mathbf{u}(t) = -\mathbf{K}(t)\mathbf{x}(t), \tag{F.17}$$

where $\mathbf{K}(t)$ is a properly dimensioned matrix, given by

$$\mathbf{K}(t) = \mathbf{R}^{-1}\mathbf{B}^{\mathsf{T}}\mathbf{S}(t), \tag{F.18}$$

and $\mathbf{S}(t)$ is the solution of the differential Riccati equation. The differential Riccati equation is given as

$$\dot{\mathbf{S}}(t) = -\mathbf{S}(t)\mathbf{A} - \mathbf{A}^{\mathsf{T}}\mathbf{S}(t) + \mathbf{S}(t)\mathbf{B}\mathbf{R}^{-1}\mathbf{B}^{\mathsf{T}}\mathbf{S}(t) - \mathbf{Q}. \tag{F.19}$$

For the infinite horizon LQR problem, the differential Riccati equation is replaced with the algebraic Riccati equation, with expression

$$\mathbf{0} = -\mathbf{S}\mathbf{A} - \mathbf{A}^{\mathsf{T}}\mathbf{S} + \mathbf{S}\mathbf{B}\mathbf{R}^{-1}\mathbf{B}^{\mathsf{T}}\mathbf{S} - \mathbf{Q}. \tag{F.20}$$

F.5.2 LQG controller

The *linear–quadratic–Gaussian* (LQG) control problem concerns linear systems driven by additive white Gaussian noise. As in the previous deterministic case, the problem is to determine a feedback law that is optimal, in the sense of minimizing the expected value of a quadratic cost criterion, $\mathbb{E}[\mathcal{J}]$. In this stochastic version of the problem, not only the dynamics are driven by noise, but output measurements are also assumed to be corrupted by Gaussian noise.

Under these assumptions, the control law which minimizes $\mathbb{E}[\mathcal{J}]$ is known as the LQG controller, is unique and it happens to be simply a combination of a Kalman filter together with a linear–quadratic regulator (LQR); this is a very strong and practical result[5], because it is not obvious at all that the solution to the general problem should be the combination of the solutions of the two restricted problems (optimal estimation and optimal feedback). The separation principle states that the state estimator and the state feedback can be designed independently, which from an engineering point of view is very convenient.

However, unlike the LQR, the LQG may become unstable if there is uncertainty (and therefore error) in the system parameters used in designing the control law. This was proved by J. Doyle in [196][6] and lead to the development of the field of Robust control [197].

[5] And also very cool.

[6] With the shortest abstract I have ever seen, namely "There aren't any".

Bibliography

[1] Max Planck. Über das gesetz der energieverteilung im normalspektrum. Number 2, pages 237–345. Springer, 1901.

[2] Albert Einstein. Über einen die erzeugung und verwandlung des lichtes betreffenden heuristischen gesichtspunkt. *Annalen der physik*, 322(6):132–148, 1905.

[3] Niels Bohr. On the constitution of atoms and molecules. *The London, Edinburgh, and Dublin Philosophical Magazine and Journal of Science*, 26(153):476–502, 1913.

[4] Werner Heisenberg. Über quantentheoretische umdeutung kinematischer und mechanischer beziehungen. *Zeitschrift für Physik*, 33(1):870–893, 1925.

[5] Erwin Schrödinger. Quantisierung als eigenwertproblem. *Annalen der physik*, 385(13):437–490, 1926.

[6] Paul Adrien Maurice Dirac. *The principles of quantum mechanics*. Oxford university press, 1930.

[7] John Von Neumann. *Mathematical foundations of quantum mechanics: New edition*. Sprinter, 1932.

[8] Mario Bertolotti. *Masers and lasers: an historical approach*. Crc Press, 2015.

[9] Erwin Schrödinger. Die gegenwärtige situation in der quantenmechanik. *Naturwissenschaften*, 23(50):844–849, 1935.

[10] Erwin Schrödinger. Are there quantum jumps? part ii. *The British Journal for the Philosophy of science*, 3(11):233–242, 1952.

[11] D Wineland, Phil Ekstrom, and H Dehmelt. Monoelectron oscillator. *Physical review letters*, 31(21):1279, 1973.

[12] Fouad G Major, Viorica N Gheorghe, and Günther Werth. *Charged particle traps: physics and techniques of charged particle field confinement*, volume 37. Springer Science & Business Media, 2006.

[13] W Neuhauser, M Hohenstatt, PE Toschek, and H Dehmelt. Localized visible ba+ mono-ion oscillator. *Physical Review A*, 22(3):1137, 1980.

[14] DJ Wineland and Wayne M Itano. Spectroscopy of a single mg+ ion. *Physics Letters A*, 82(2):75–78, 1981.

[15] W Neuhauser, M Hohenstatt, P Toschek, and H Dehmelt. Optical-sideband cooling of visible atom cloud confined in parabolic well. *Physical Review Letters*, 41(4):233, 1978.

[16] David J Wineland, Robert E Drullinger, and Fred L Walls. Radiation-pressure cooling of bound resonant absorbers. *Physical Review Letters*, 40(25):1639, 1978.

[17] D. J. Wineland and Hans Dehmelt. Proposed 1014 delta upsilon less than upsilon laser fluorescence spectroscopy on t1+ mono-ion oscillator iii. In *Bulletin of the American Physical Society*, volume 20, 1975.

[18] F Diedrich, JC Bergquist, Wayne M Itano, and DJ Wineland. Laser cooling to the zero-point energy of motion. *Physical Review Letters*, 62(4):403, 1989.

[19] JC Bergquist, Randall G Hulet, Wayne M Itano, and DJ Wineland. Observation of quantum jumps in a single atom. *Physical review letters*, 57(14):1699, 1986.

[20] John Stewart Bell. Are there quantum jumps? *John S. Bell on the foundations of quantum mechanics*, page 172, 2001.

[21] Arthur Ashkin. Acceleration and trapping of particles by radiation pressure. *Physical review letters*, 24(4):156, 1970.

[22] Arthur Ashkin. Trapping of atoms by resonance radiation pressure. *Physical Review Letters*, 40(12):729, 1978.

[23] Alan L Migdall, John V Prodan, William D Phillips, Thomas H Bergeman, and Harold J Metcalf. First observation of magnetically trapped neutral atoms. *Physical Review Letters*, 54(24):2596, 1985.

[24] Steven Chu, Leo Hollberg, John E Bjorkholm, Alex Cable, and Arthur Ashkin. Three-dimensional viscous confinement and cooling of atoms by resonance radiation pressure. *Physical review letters*, 55(1):48, 1985.

[25] Steven Chu, JE Bjorkholm, A Ashkin, and Alex Cable. Experimental observation of optically trapped atoms. *Physical review letters*, 57(3):314, 1986.

[26] Arthur Ashkin, James M Dziedzic, JE Bjorkholm, and Steven Chu. Observation of a single-beam gradient force optical trap for dielectric particles. *Optics letters*, 11(5):288–290, 1986.

[27] Arthur Ashkin, James M Dziedzic, and T Yamane. Optical trapping and manipulation of single cells using infrared laser beams. *Nature*, 330(6150):769–771, 1987.

[28] Arthur Ashkin and James M Dziedzic. Optical trapping and manipulation of viruses and bacteria. *Science*, 235(4795):1517–1520, 1987.

[29] Karel Svoboda and Steven M Block. Biological applications of optical forces. *Annual review of biophysics and biomolecular structure*, 23(1):247–285, 1994.

[30] John Bell. Against 'measurement'. *Physics world*, 3(8):33, 1990.

[31] Richard P Feynman. There's plenty of room at the bottom. *California Institute of Technology, Engineering and Science magazine*, 1960.

[32] John Bardeen and Walter Hauser Brattain. The transistor, a semiconductor triode. *Physical Review*, 74(2):230, 1948.

[33] Kahng Dawon. Electric field controlled semiconductor device, August 27 1963. US Patent 3,102,230.

[34] Markus Aspelmeyer, Tobias J Kippenberg, and Florian Marquardt. Cavity optomechanics. *Reviews of Modern Physics*, 86(4):1391, 2014.

[35] Andrew Addison Houck, DI Schuster, JM Gambetta, JA Schreier, BR Johnson, JM Chow, L Frunzio, J Majer, MH Devoret, SM Girvin, et al. Generating single microwave photons in a circuit. *Nature*, 449(7160):328–331, 2007.

[36] Aaron D O'Connell, Max Hofheinz, Markus Ansmann, Radoslaw C Bialczak, Mike Lenander, Erik Lucero, Matthew Neeley, Daniel Sank, H Wang, and Ms Weides. Quantum ground state and single-phonon control of a mechanical resonator. *Nature*, 464(7289):697–703, 2010.

[37] Jasper Chan, TP Mayer Alegre, Amir H Safavi-Naeini, Jeff T Hill, Alex Krause, Simon Gröblacher, Markus Aspelmeyer, and Oskar Painter. Laser cooling of a nanomechanical oscillator into its quantum ground state. *Nature*, 478(7367):89–92, 2011.

[38] JD Teufel, Tobias Donner, Dale Li, JW Harlow, MS Allman, Katarina Cicak, AJ Sirois, Jed D Whittaker, KW Lehnert, and Raymond W Simmonds. Sideband cooling of micromechanical motion to the quantum ground state. *Nature*, 475(7356):359–363, 2011.

[39] Ewold Verhagen, Samuel Deléglise, Stefan Weis, Albert Schliesser, and Tobias J Kippenberg. Quantum-coherent coupling of a mechanical oscillator to an optical cavity mode. *Nature*, 482(7383):63–67, 2012.

[40] James Bateman, Stefan Nimmrichter, Klaus Hornberger, and Hendrik Ulbricht. Near-field interferometry of a free-falling nanoparticle from a point-like source. *Nature communications*, 5:4788, 2014.

[41] Ralf Riedinger, Andreas Wallucks, Igor Marinković, Clemens Löschnauer, Markus Aspelmeyer, Sungkun Hong, and Simon Gröblacher. Remote quantum entanglement between two micromechanical oscillators. *Nature*, 556(7702):473, 2018.

[42] Igor Marinković, Andreas Wallucks, Ralf Riedinger, Sungkun Hong, Markus Aspelmeyer, and Simon Gröblacher. Optomechanical bell test. *Physical review letters*, 121(22):220404, 2018.

[43] Tolga Bagci, Anders Simonsen, Silvan Schmid, Luis G Villanueva, Emil Zeuthen, Jürgen Appel, Jacob M Taylor, A Sørensen, Koji Usami, Albert Schliesser, et al. Optical detection of radio waves through a nanomechanical transducer. *Nature*, 507(7490):81–85, 2014.

[44] B Lassagne, D Garcia-Sanchez, A Aguasca, and A Bachtold. Ultrasensitive mass sensing with a nanotube electromechanical resonator. *Nano letters*, 8(11):3735–3738, 2008.

[45] Julien Chaste, A Eichler, J Moser, G Ceballos, R Rurali, and A Bachtold. A nanomechanical mass sensor with yoctogram resolution. *Nature nanotechnology*, 7(5):301–304, 2012.

[46] BP Abbott, R Abbott, TD Abbott, F Acernese, K Ackley, C Adams, T Adams, P Addesso, RX Adhikari, et al. Gw170104: observation of a 50-solar-mass binary black hole coalescence at redshift 0.2. *Physical Review Letters*, 118(22):221101, 2017.

[47] Arthur Ashkin. Applications of laser radiation pressure. *Science*, 210(4474):1081–1088, 1980.

[48] James Millen, Tania Scheel Monteiro, Robert Pettit, and Nick Vamivakas. Optomechanics with levitated particles. *Reports on Progress in Physics*, 2019.

[49] A Ashkin and JM Dziedzic. Optical levitation in high vacuum. *Applied Physics Letters*, 28(6):333–335, 1976.

[50] A Ashkin and JM Dziedzic. Feedback stabilization of optically levitated particles. *Applied Physics Letters*, 30(4):202–204, 1977.

[51] Darrick E Chang, CA Regal, SB Papp, DJ Wilson, J Ye, O Painter, H Jeff Kimble, and P Zoller. Cavity opto-mechanics using an optically levitated nanosphere. *Proceedings of the National Academy of Sciences*, 107(3):1005–1010, 2010.

[52] Oriol Romero-Isart, Mathieu L Juan, Romain Quidant, and J Ignacio Cirac. Toward quantum superposition of living organisms. *New Journal of Physics*, 12(3):033015, 2010.

[53] PF Barker and MN Shneider. Cavity cooling of an optically trapped nanoparticle. *Physical Review A*, 81(2):023826, 2010.

[54] Tongcang Li, Simon Kheifets, David Medellin, and Mark G Raizen. Measurement of the instantaneous velocity of a brownian particle. *Science*, 328(5986), 2010.

[55] Jan Gieseler, Bradley Deutsch, Romain Quidant, and Lukas Novotny. Subkelvin parametric feedback cooling of a laser-trapped nanoparticle. *Physical review letters*, 109(10):103603, 2012.

[56] Mingyun Yuan, Martijn A Cohen, and Gary A Steele. Silicon nitride membrane resonators at millikelvin temperatures with quality factors exceeding 108. *Applied Physics Letters*, 107(26):263501, 2015.

[57] Yeghishe Tsaturyan, Andreas Barg, Eugene S Polzik, and Albert Schliesser. Ultracoherent nanomechanical resonators via soft clamping and dissipation dilution. *Nature nanotechnology*, 12(8):776, 2017.

[58] Angelo Bassi, Kinjalk Lochan, Seema Satin, Tejinder P Singh, and Hendrik Ulbricht. Models of wave-function collapse, underlying theories, and experimental tests. *Reviews of Modern Physics*, 85(2):471, 2013.

[59] A Vinante, A Pontin, M Rashid, M Toroš, PF Barker, and H Ulbricht. Testing collapse models with levitated nanoparticles: Detection challenge. *Physical Review A*, 100(1):012119, 2019.

[60] J Millen, T Deesuwan, P Barker, and Janet Anders. Nanoscale temperature measurements using non-equilibrium brownian dynamics of a levitated nanosphere. *Nature nanotechnology*, 9(6):425, 2014.

[61] Levi P Neukirch, Jan Gieseler, Romain Quidant, Lukas Novotny, and A Nick Vamivakas. Observation of nitrogen vacancy photoluminescence from an optically levitated nanodiamond. *Optics letters*, 38(16):2976–2979, 2013.

[62] Levi P Neukirch, Eva Von Haartman, Jessica M Rosenholm, and A Nick Vamivakas. Multi-dimensional single-spin nano-optomechanics with a levitated nanodiamond. *Nature Photonics*, 9(10):653–657, 2015.

[63] Alexander Kuhlicke, Andreas W Schell, Joachim Zoll, and Oliver Benson. Nitrogen vacancy center fluorescence from a submicron diamond cluster levitated in a linear quadrupole ion trap. *Applied Physics Letters*, 105(7):073101, 2014.

[64] Pavel Nagornykh, Joyce E Coppock, and BE Kane. Cooling of levitated graphene nanoplatelets in high vacuum. *Applied Physics Letters*, 106(24):244102, 2015.

[65] Irene Alda, Johann Berthelot, Raúl A Rica, and Romain Quidant. Trapping and manipulation of individual nanoparticles in a planar paul trap. *Applied Physics Letters*, 109(16):163105, 2016.

[66] J Millen, PZG Fonseca, T Mavrogordatos, TS Monteiro, and PF Barker. Cavity cooling a single charged nanoparticle. *Physical Review Letters*, 114(2), 2015.

[67] Nikolai Kiesel, Florian Blaser, Uroš Delić, David Grass, Rainer Kaltenbaek, and Markus Aspelmeyer. Cavity cooling of an optically levitated submicron particle. *Proceedings of the National Academy of Sciences*, 110(35):14180–14185, 2013.

[68] Peter Asenbaum, Stefan Kuhn, Stefan Nimmrichter, Ugur Sezer, and Markus Arndt. Cavity cooling of free silicon nanoparticles in high vacuum. *Nature communications*, 4(1):1–7, 2013.

[69] Pau Mestres, Johann Berthelot, Marko Spasenović, Jan Gieseler, Lukas Novotny, and Romain Quidant. Cooling and manipulation of a levitated nanoparticle with an optical fiber trap. *Applied Physics Letters*, 107(15):151102, 2015.

[70] Tongcang Li, Simon Kheifets, and Mark G Raizen. Millikelvin cooling of an optically trapped microsphere in vacuum. *Nature Physics*, 7:527–530, 2011.

[71] Vijay Jain, Jan Gieseler, Clemens Moritz, Christoph Dellago, Romain Quidant, and Lukas Novotny. Direct measurement of photon recoil from a levitated nanoparticle. *Physical Review Letters*, 116:243601, Jun 2016.

[72] Günter Werth, Viorica N Gheorghe, and Fouard G Major. *Charged particle traps II*. Springer, 2009.

[73] Edmond De Hoffmann. Mass spectrometry. *Kirk-Othmer Encyclopedia of Chemical Technology*, 2000.

[74] David Kielpinski, Chris Monroe, and David J Wineland. Architecture for a large-scale ion-trap quantum computer. *Nature*, 417(6890):709, 2002.

[75] Wolfgang Paul. Electromagnetic traps for charged and neutral particles. *Reviews of modern physics*, 62(3):531, 1990.

[76] William D Phillips. Nobel lecture: Laser cooling and trapping of neutral atoms. *Reviews of Modern Physics*, 70(3):721, 1998.

[77] Jan Eric Sträng. On the characteristic exponents of floquet solutions to the mathieu equation. *arXiv preprint math-ph/0510076*, 2005.

[78] Michael Nasse and Christopher Foot. Influence of background pressure on the stability region of a paul trap. *European Journal of Physics*, 22(6):563, 2001.

[79] M Brownnutt, M Kumph, P Rabl, and R Blatt. Ion-trap measurements of electric-field noise near surfaces. *Reviews of modern Physics*, 87(4):1419, 2015.

[80] VS Letokhov, VG Minogin, and BD Pavlik. Cooling and trapping of atoms and molecules by a resonant laser field. *Optics Communications*, 19(1):72–75, 1976.

[81] Lukas Novotny and Bert Hecht. *Principles of nano-optics*. Cambridge university press, 2012.

[82] Philip H Jones, Onofrio M Maragò, and Giovanni Volpe. *Optical tweezers: Principles and applications*. Cambridge University Press, 2015.

[83] Jan Gieseler, Lukas Novotny, and Romain Quidant. Thermal nonlinearities in a nanomechanical oscillator. *Nature physics*, 9(12):806–810, 2013.

[84] Ioannis Karatzas and Steven E Shreve. Brownian motion. In *Brownian Motion and Stochastic Calculus*, pages 47–127. Springer, 1998.

[85] Carl M Bender and Steven A Orszag. *Advanced mathematical methods for scientists and engineers I: Asymptotic methods and perturbation theory*. Springer Science & Business Media, 2013.

[86] Gerard P Conangla, Dwight Nwaigwe, Jan Wehr, and Raúl A Rica. Overdamped dynamics of a brownian particle levitated in a paul trap. *arXiv preprint arXiv:1912.11317*, 2019.

[87] David J Wineland. Nobel lecture: Superposition, entanglement, and raising schrödinger's cat. *Reviews of Modern Physics*, 85(3):1103, 2013.

[88] R Blatt, P Zoller, G Holzmüller, and I Siemers. Brownian motion of a parametric oscillator: A model for ion confinement in radio frequency traps. *Zeitschrift für Physik D Atoms, Molecules and Clusters*, 4(2):121–126, 1986.

[89] E Joos and A Lindner. Langevin equation for the parametric oscillator: a model for ion confinement in a radio frequency trap. *Zeitschrift für Physik D Atoms, Molecules and Clusters*, 11(4):295–300, 1989.

[90] A Maitra, D Leibfried, D Ullmo, and H Landa. Far-from-equilibrium noise-heating and laser-cooling dynamics in radio-frequency paul traps. *Physical Review A*, 99(4):043421, 2019.

[91] Alexander F Izmailov, Stephen Arnold, Stephen Holler, and Allan S Myerson. Microparticle driven by parametric and random forces: Theory and experiment. *Physical Review E*, 52(2):1325, 1995.

[92] Bastian Höltkemeier, Pascal Weckesser, Henry López-Carrera, and Matthias Weidemüller. Dynamics of a single trapped ion immersed in a buffer gas. *Physical Review A*, 94(6):062703, 2016.

[93] Ulrich K Krieger, Claudia Marcolli, and Jonathan P Reid. Exploring the complexity of aerosol particle properties and processes using single particle techniques. *Chemical Society Reviews*, 41(19):6631–6662, 2012.

[94] James F Davies, Allen E Haddrell, and Jonathan P Reid. Time-resolved measurements of the evaporation of volatile components from single aerosol droplets. *Aerosol Science and Technology*, 46(6):666–677, 2012.

[95] David M Bell, Collin R Howder, Ryan C Johnson, and Scott L Anderson. Single cdse/zns nanocrystals in an ion trap: charge and mass determination and photophysics evolution with changing mass, charge, and temperature. *ACS nano*, 8(3):2387–2398, 2014.

[96] Collin R Howder, Bryan A Long, David M Bell, and Scott L Anderson. Thermally brightened cdse/zns quantum dots as noncontact probes for surface chemistry studies of dark nanoparticles trapped in the gas phase. *The Journal of Physical Chemistry C*, 119(26):14561–14570, 2015.

[97] Tom Delord, Louis Nicolas, Lucien Schwab, and Gabriel Hétet. Electron spin resonance from nv centers in diamonds levitating in an ion trap. *New Journal of Physics*, 19(3):033031, 2017.

[98] Gerard P Conangla, Andreas W Schell, Raúl A Rica, and Romain Quidant. Motion control and optical interrogation of a levitating single nitrogen vacancy in vacuum. *Nano letters*, 18(6):3956–3961, 2018.

[99] CM Bender. M. & orszag, sa, 1978. *Advanced Mathematical Methods for Scientists and Engineers*, 85.

[100] Bernt Oksendal. *Stochastic differential equations: an introduction with applications*. Springer Science & Business Media, 2013.

[101] Francesco Ricci, Marc T Cuairan, Gerard P Conangla, Andreas W Schell, and Romain Quidant. Accurate mass measurement of a levitated nanomechanical resonator for precision force-sensing. *Nano letters*, 19(10):6711–6715, 2019.

[102] Rep Kubo. The fluctuation-dissipation theorem. *Reports on progress in physics*, 29(1):255, 1966.

[103] Jae Hyun Park and Predrag S Krstić. Thermal noise in aqueous quadrupole micro-and nano-traps. *Nanoscale research letters*, 7(1):156, 2012.

[104] Édgar Roldán, Ignacio A Martínez, Luis Dinis, and Raúl A Rica. Measuring kinetic energy changes in the mesoscale with low acquisition rates. *Applied Physics Letters*, 104(23):234103, 2014.

[105] AJ Roberts. Modify the improved euler scheme to integrate stochastic differential equations. *arXiv preprint arXiv:1210.0933*, 2012.

[106] Gerard P Conangla, Francesco Ricci, Marc T Cuairan, Andreas W Schell, Nadine Meyer, and Romain Quidant. Optimal feedback cooling of a charged levitated nanoparticle with adaptive control. *Physical Review Letters*, 122(22):223602, 2019.

[107] William B Whitten, Peter TA Reilly, and J Michael Ramsey. High-pressure ion trap mass spectrometry. *Rapid communications in mass spectrometry*, 18(15):1749–1752, 2004.

[108] LD Landau and EM Lifshitz. Classical mechanics, 1959.

[109] OL Muskens, V Giannini, José A Sánchez-Gil, and J Gómez Rivas. Strong enhancement of the radiative decay rate of emitters by single plasmonic nanoantennas. *Nano letters*, 7(9):2871–2875, 2007.

[110] Fetah Benabid, JC Knight, and P St J Russell. Particle levitation and guidance in hollow-core photonic crystal fiber. *Optics express*, 10(21):1195–1203, 2002.

[111] Sabina Santesson and Staffan Nilsson. Airborne chemistry: acoustic levitation in chemical analysis. *Analytical and bioanalytical chemistry*, 378(7):1704–1709, 2004.

[112] BE Kane. Levitated spinning graphene flakes in an electric quadrupole ion trap. *Physical Review B*, 82(11):115441, 2010.

[113] Ralph F Wuerker, Haywood Shelton, and RV Langmuir. Electrodynamic containment of charged particles. *Journal of Applied Physics*, 30(3):342–349, 1959.

[114] S Schlemmer, S Wellert, F Windisch, M Grimm, S Barth, and D Gerlich. Interaction of electrons and molecules with a single trapped nanoparticle. *Applied Physics A*, 78(5):629–636, 2004.

[115] Michael Grimm, Burkhard Langer, Stephan Schlemmer, Toralf Lischke, Uwe Becker, Wolf Widdra, Dieter Gerlich, Roman Flesch, and Eckart Rühl. Charging mechanisms of trapped element-selectively excited nanoparticles exposed to soft x rays. *Physical review letters*, 96(6):066801, 2006.

[116] David G Grier. A revolution in optical manipulation. *Nature*, 424(6950):810–816, 2003.

[117] Jen-Feng Hsu, Peng Ji, Charles W Lewandowski, and Brian D'Urso. Cooling the motion of diamond nanocrystals in a magneto-gravitational trap in high vacuum. *Scientific reports*, 6:30125, 2016.

[118] Bradley R Slezak, Charles W Lewandowski, Jen-Feng Hsu, and Brian D'Urso. Cooling the motion of a silica microsphere in a magneto-gravitational trap in ultra-high vacuum. *New Journal of Physics*, 20(6):063028, 2018.

[119] JP Houlton, ML Chen, MD Brubaker, KA Bertness, and CT Rogers. Axisymmetric scalable magneto-gravitational trap for diamagnetic particle levitation. *Review of Scientific Instruments*, 89(12):125107, 2018.

[120] PZG Fonseca, EB Aranas, J Millen, TS Monteiro, and PF Barker. Nonlinear dynamics and strong cavity cooling of levitated nanoparticles. *Physical review letters*, 117(17):173602, 2016.

[121] Tino Weber, Jens Herbig, Michael Mark, Hanns-Christoph Nägerl, and Rudolf Grimm. Bose-einstein condensation of cesium. *Science*, 299(5604):232–235, 2003.

[122] Frederick Gittes and Christoph F Schmidt. Interference model for back-focal-plane displacement detection in optical tweezers. *Optics letters*, 23(1):7–9, 1998.

[123] Poul Martin Hansen, Vikram Kjøller Bhatia, Niels Harrit, and Lene Oddershede. Expanding the optical trapping range of gold nanoparticles. *Nano letters*, 5(10):1937–1942, 2005.

[124] ATM Anishur Rahman and PF Barker. Laser refrigeration, alignment and rotation of levitated yb 3+: Ylf nanocrystals. *Nature Photonics*, 11(10):634–638, 2017.

[125] Erik Hebestreit, René Reimann, Martin Frimmer, and Lukas Novotny. Measuring the internal temperature of a levitated nanoparticle in high vacuum. *Physical Review A*, 97(4):043803, 2018.

[126] Andreas W Schell, Alexander Kuhlicke, Günter Kewes, and Oliver Benson. "flying plasmons": Fabry-pérot resonances in levitated silver nanowires. *ACS Photonics*, 4(11):2719–2725, 2017.

[127] AD Armour, MP Blencowe, and Keith C Schwab. Entanglement and decoherence of a micromechanical resonator via coupling to a cooper-pair box. *Physical Review Letters*, 88(14):148301, 2002.

[128] Peter Rabl, P Cappellaro, MV Gurudev Dutt, Liang Jiang, JR Maze, and Mikhail D Lukin. Strong magnetic coupling between an electronic spin qubit and a mechanical resonator. *Physical Review B*, 79(4):041302, 2009.

[129] J Teissier, A Barfuss, P Appel, E Neu, and P Maletinsky. Strain coupling of a nitrogen-vacancy center spin to a diamond mechanical oscillator. *Physical review letters*, 113(2):020503, 2014.

[130] Donghun Lee, Kenneth W Lee, Jeffrey V Cady, Preeti Ovartchaiyapong, and Ania C Bleszynski Jayich. Topical review: Spins and mechanics in diamond. *Journal of Optics*, 19(3):033001, 2017.

[131] M. Scala, M. S. Kim, G. W. Morley, P. F. Barker, and S. Bose. Matter-wave interferometry of a levitated thermal nano-oscillator induced and probed by a spin. *Physical Review Letters*, 111:180403, Oct 2013.

[132] Andreas Albrecht, Alex Retzker, and Martin B Plenio. Testing quantum gravity by nanodiamond interferometry with nitrogen-vacancy centers. *Physical Review A*, 90(3):033834, 2014.

[133] Zhang-qi Yin, Tongcang Li, Xiang Zhang, and LM Duan. Large quantum superpositions of a levitated nanodiamond through spin-optomechanical coupling. *Physical Review A*, 88(3):033614, 2013.

[134] ATMA Rahman, AC Frangeskou, MS Kim, S Bose, GW Morley, and PF Barker. Burning and graphitization of optically levitated nanodiamonds in vacuum. *Scientific reports*, 6:21633, 2016.

[135] Igor Aharonovich, Dirk Englund, and Milos Toth. Solid-state single-photon emitters. *Nature Photonics*, 10(10):631, 2016.

[136] Nir Bar-Gill, Linh M Pham, Andrejs Jarmola, Dmitry Budker, and Ronald L Walsworth. Solid-state electronic spin coherence time approaching one second. *Nature communications*, 4:1743, 2013.

[137] Emre Togan, Yiwen Chu, AS Trifonov, Liang Jiang, Jeronimo Maze, Lilian Childress, MV Gurudev Dutt, Anders Søndberg Sørensen, PR Hemmer, Alexander S Zibrov, et al. Quantum entanglement between an optical photon and a solid-state spin qubit. *Nature*, 466(7307):730–734, 2010.

[138] Wolfgang Pfaff, BJ Hensen, Hannes Bernien, Suzanne B van Dam, Machiel S Blok, Tim H Taminiau, Marijn J Tiggelman, Raymond N Schouten, Matthew Markham, Daniel J Twitchen, et al. Unconditional quantum teleportation between distant solid-state quantum bits. *Science*, 345(6196):532–535, 2014.

[139] Bas Hensen, Hannes Bernien, Anaïs E Dréau, Andreas Reiserer, Norbert Kalb, Machiel S Blok, Just Ruitenberg, Raymond FL Vermeulen, Raymond N Schouten, Carlos Abellán, et al. Loophole-free bell inequality violation using electron spins separated by 1.3 kilometres. *Nature*, 526(7575):682–686, 2015.

[140] JM Taylor, P Cappellaro, L Childress, L Jiang, D Budker, PR Hemmer, A Yacoby, R Walsworth, and MD Lukin. High-sensitivity diamond magnetometer with nanoscale resolution. *Nature Physics*, 4(10):810–816, 2008.

[141] Liam T Hall, Jared H Cole, Charles D Hill, and Lloyd CL Hollenberg. Sensing of fluctuating nanoscale magnetic fields using nitrogen-vacancy centers in diamond. *Physical review letters*, 103(22):220802, 2009.

[142] Florian Dolde, Helmut Fedder, Marcus W Doherty, Tobias Nöbauer, Florian Rempp, Gopalakrishnan Balasubramanian, Thomas Wolf, Friedemann Reinhard, Lloyd CL Hollenberg, Fedor Jelezko, et al. Electric-field sensing using single diamond spins. *Nature Physics*, 7(6):459–463, 2011.

[143] R Hanson, VV Dobrovitski, AE Feiguin, O Gywat, and DD Awschalom. Coherent dynamics of a single spin interacting with an adjustable spin bath. *Science*, 320(5874):352–355, 2008.

[144] MW Doherty, F Dolde, H Fedder, Fedor Jelezko, J Wrachtrup, NB Manson, and LCL Hollenberg. Theory of the ground-state spin of the nv- center in diamond. *Physical Review B*, 85(20):205203, 2012.

[145] R Hanbury Brown and Richard Q Twiss. Correlation between photons in two coherent beams of light. *Nature*, 177(4497):27–29, 1956.

[146] Crispin Gardiner and Peter Zoller. *Quantum noise: a handbook of Markovian and non-Markovian quantum stochastic methods with applications to quantum optics*, volume 56. Springer Science & Business Media, 2004.

[147] Christian Kurtsiefer, Sonja Mayer, Patrick Zarda, and Harald Weinfurter. Stable solid-state source of single photons. *Physical Review Letters*, 85:290–293, Jul 2000.

[148] Stephen H Simpson, David C Benito, and Simon Hanna. Polarization-induced torque in optical traps. *Physical Review A*, 76(4):043408, 2007.

[149] Yoshihiko Arita, Michael Mazilu, and Kishan Dholakia. Laser-induced rotation and cooling of a trapped microgyroscope in vacuum. *Nature communications*, 4:2374, 2013.

[150] Friedrich Paschen. Ueber die zum funkenübergang in luft, wasserstoff und kohlensäure bei verschiedenen drucken erforderliche potentialdifferenz. *Annalen der Physik*, 273(5):69–96, 1889.

[151] DM Toyli, DJ Christle, A Alkauskas, BB Buckley, CG Van de Walle, and DD Awschalom. Measurement and control of single nitrogen-vacancy center spins above 600 k. *Physical Review X*, 2(3):031001, 2012.

[152] Tatiana A. Dolenko, Sergey A. Burikov, Sergey A. Dolenko, Alexander O. Efitorov, Ivan V. Plastinin, Viktor I. Yuzhakov, and Svetlana V. Patsaeva. Raman spectroscopy of water–ethanol solutions: The estimation of hydrogen bonding energy and the appearance of clathrate-like structures in solutions. *The Journal of Physical Chemistry A*, 119(44):10806–10815, 2015.

[153] Yue Ma, Thai M. Hoang, Ming Gong, Tongcang Li, and Zhang-qi Yin. Proposal for quantum many-body simulation and torsional matter-wave interferometry with a levitated nanodiamond. *Physical Review A*, 96:023827, Aug 2017.

[154] T. Delord, L. Nicolas, Y. Chassagneux, and G. Hétet. Strong coupling between a single nitrogen-vacancy spin and the rotational mode of diamonds levitating in an ion trap. *Physical Review A*, 96:063810, Dec 2017.

[155] Zhang-Qi Yin, Andrew A Geraci, and Tongcang Li. Optomechanics of levitated dielectric particles. *International Journal of Modern Physics B*, 27(26):1330018, 2013.

[156] Daniel Goldwater, Benjamin A Stickler, Lukas Martinetz, Tracy E Northup, Klaus Hornberger, and James Millen. Levitated electromechanics: all-electrical cooling of charged nano-and micro-particles. *Quantum Science and Technology*, 4(2):024003, 2019.

[157] David C Moore, Alexander D Rider, and Giorgio Gratta. Search for millicharged particles using optically levitated microspheres. *Physical review letters*, 113(25):251801, 2014.

[158] Martin Frimmer, Karol Luszcz, Sandra Ferreiro, Vijay Jain, Erik Hebestreit, and Lukas Novotny. Controlling the net charge on a nanoparticle optically levitated in vacuum. *Physical Review A*, 95(6):061801, 2017.

[159] Huibert Kwakernaak and Raphael Sivan. *Linear optimal control systems*, volume 1. Wiley-Interscience New York, 1972.

[160] Ashley Setter, Marko Toroš, Jason F Ralph, and Hendrik Ulbricht. Real-time kalman filter: Cooling of an optically levitated nanoparticle. *Physical Review A*, 97(3):033822, 2018.

[161] Pavel Bushev, Daniel Rotter, Alex Wilson, François Dubin, Christoph Becher, Jürgen Eschner, Rainer Blatt, Viktor Steixner, Peter Rabl, and Peter Zoller. Feedback cooling of a single trapped ion. *Physical review letters*, 96(4):043003, 2006.

[162] Rudolph Emil Kalman. A new approach to linear filtering and prediction problems. *Journal of basic Engineering*, 82(1):35–45, 1960.

[163] Rudolph Emil Kalman and Richard S Bucy. New results in linear filtering and prediction theory. *Journal of basic engineering*, 83(1):95–108, 1961.

[164] M. Poggio, C. L. Degen, H. J. Mamin, and D. Rugar. Feedback cooling of a cantilever's fundamental mode below 5 mk. *Physical Review Letters*, 99:017201, Jul 2007.

[165] Gregory C Chow. *Analysis and control of dynamic economic systems*. Wiley, 1975.

[166] Andreas Rößler. Second order runge–kutta methods for itô stochastic differential equations. *SIAM Journal on Numerical Analysis*, 47(3):1713–1738, 2009.

[167] Jerome Friedman, Trevor Hastie, and Robert Tibshirani. *The elements of statistical learning*, volume 1. Springer series in statistics New York, NY, USA:, 2001.

[168] Pierre-François Cohadon, Antoine Heidmann, and Michel Pinard. Cooling of a mirror by radiation pressure. *Physical Review Letters*, 83(16):3174, 1999.

[169] DJ Wilson, Vivishek Sudhir, Nicolas Piro, Ryan Schilling, Amir Ghadimi, and Tobias J Kippenberg. Measurement-based control of a mechanical oscillator at its thermal decoherence rate. *Nature*, 524(7565):325, 2015.

[170] Massimiliano Rossi, David Mason, Junxin Chen, Yeghishe Tsaturyan, and Albert Schliesser. Measurement-based quantum control of mechanical motion. *Nature*, 563(7729):53, 2018.

[171] Rainer Kaltenbaek, Gerald Hechenblaikner, Nikolai Kiesel, Oriol Romero-Isart, Keith C Schwab, Ulrich Johann, and Markus Aspelmeyer. Macroscopic quantum resonators (maqro). *Experimental Astronomy*, 34(2):123–164, 2012.

[172] Neil Barbour and George Schmidt. Inertial sensor technology trends. *IEEE sensors journal*, 1(4):332–339, 2001.

[173] Uroš Delić, Manuel Reisenbauer, Kahan Dare, David Grass, Vladan Vuletić, Nikolai Kiesel, and Markus Aspelmeyer. Cooling of a levitated nanoparticle to the motional quantum ground state. *Science*, 367(6480):892–895, 2020.

[174] Yaakov Y Fein, Philipp Geyer, Patrick Zwick, Filip Kiałka, Sebastian Pedalino, Marcel Mayor, Stefan Gerlich, and Markus Arndt. Quantum superposition of molecules beyond 25 kda. *Nature Physics*, 15(12):1242–1245, 2019.

[175] T Delord, P Huillery, L Nicolas, and G Hétet. Spin-cooling of the motion of a trapped diamond. *Nature*, pages 1–4, 2020.

[176] Muddassar Rashid, Marko Toroš, Ashley Setter, and Hendrik Ulbricht. Precession motion in levitated optomechanics. *Physical review letters*, 121(25):253601, 2018.

[177] Benjamin A Stickler, Birthe Papendell, Stefan Kuhn, Björn Schrinski, James Millen, Markus Arndt, and Klaus Hornberger. Probing macroscopic quantum superpositions with nanorotors. *New Journal of Physics*, 20(12):122001, 2018.

[178] Daniel Hümmer, René Lampert, Katja Kustura, Patrick Maurer, Carlos Gonzalez-Ballestero, and Oriol Romero-Isart. Acoustic and optical properties of a fast spinning dielectric nanoparticle. *arXiv preprint arXiv:1912.08537*, 2019.

[179] Nadine Meyer, Andrés De los Rios Sommer, Pau Mestres, Jan Gieseler, Vijay Jain, Lukas Novotny, and Romain Quidant. Resolved-sideband cooling of a levitated nanoparticle in the presence of laser phase noise. *Physical review letters*, 123(15):153601, 2019.

[180] Dominik Windey, Carlos Gonzalez-Ballestero, Patrick Maurer, Lukas Novotny, Oriol Romero-Isart, and René Reimann. Cavity-based 3d cooling of a levitated nanoparticle via coherent scattering. *Physical review letters*, 122(12):123601, 2019.

[181] Felix Tebbenjohanns, Martin Frimmer, Andrei Militaru, Vijay Jain, and Lukas Novotny. Cold damping of an optically levitated nanoparticle to microkelvin temperatures. *Physical review letters*, 122(22):223601, 2019.

[182] Felix Tebbenjohanns, Martin Frimmer, Vijay Jain, Dominik Windey, and Lukas Novotny. Motional sideband asymmetry of a nanoparticle optically levitated in free space. *Physical Review Letters*, 124(1):013603, 2020.

[183] Albert Einstein. Über die von der molekularkinetischen theorie der wärme geforderte bewegung von in ruhenden flüssigkeiten suspendierten teilchen. *Annalen der physik*, 322(8):549–560, 1905.

[184] Jan Gieseler and James Millen. Levitated nanoparticles for microscopic thermodynamics—a review. *Entropy*, 20(5):326, 2018.

[185] T Delord, L Nicolas, M Bodini, and G Hétet. Diamonds levitating in a paul trap under vacuum: Measurements of laser-induced heating via nv center thermometry. *Applied Physics Letters*, 111(1):013101, 2017.

[186] Gerard P Conangla. Sensing with the harmonic oscillator. *arXiv preprint arXiv:1905.02612*, 2019.

[187] Rozenn Diehl, Erik Hebestreit, René Reimann, Felix Tebbenjohanns, Martin Frimmer, and Lukas Novotny. Optical levitation and feedback cooling of a nanoparticle at subwavelength distances from a membrane. *Physical Review A*, 98(1):013851, 2018.

[188] George Winstone, Robert Bennett, Markus Rademacher, Muddassar Rashid, Stefan Buhmann, and Hendrik Ulbricht. Direct measurement of the electrostatic image force of a levitated charged nanoparticle close to a surface. *Physical Review A*, 98(5):053831, 2018.

[189] David Hempston, Jamie Vovrosh, Marko Toroš, George Winstone, Muddassar Rashid, and Hendrik Ulbricht. Force sensing with an optically levitated charged nanoparticle. *Applied Physics Letters*, 111(13):133111, 2017.

[190] Chris Timberlake, Marko Toroš, David Hempston, George Winstone, Muddassar Rashid, and Hendrik Ulbricht. Static force characterization with fano anti-resonance in levitated optomechanics. *Applied Physics Letters*, 114(2):023104, 2019.

[191] Erik Hebestreit, Martin Frimmer, René Reimann, and Lukas Novotny. Sensing static forces with free-falling nanoparticles. *Physical review letters*, 121(6):063602, 2018.

[192] Michele Armano, Heather Audley, Gerard Auger, JT Baird, Massimo Bassan, et al. Sub-femto-g free fall for space-based gravitational wave observatories: Lisa pathfinder results. *Physical review letters*, 116(23):231101, 2016.

[193] Gambhir Ranjit, David P Atherton, Jordan H Stutz, Mark Cunningham, and Andrew A Geraci. Attonewton force detection using microspheres in a dual-beam optical trap in high vacuum. *Physical Review A*, 91(5):051805, 2015.

[194] Eva Löcherbach. Ergodicity and speed of convergence to equilibrium for diffusion processes. *Unpublished manuscript, June*, 2013.

[195] Robert F Stengel. Stochastic optimal control: theory and application. *New York*, 1986.

[196] John C Doyle. Guaranteed margins for lqg regulators. *IEEE Transactions on automatic Control*, 23(4):756–757, 1978.

[197] Kemin Zhou and John Comstock Doyle. *Essentials of robust control*, volume 104. Prentice hall Upper Saddle River, NJ, 1998.